

# **Development of the Direct Borohydride Fuel Cell Anode**

by

Vincent Wai Sang Lam

B.A.Sc., The University of British Columbia, 2004

A THESIS SUBMITTED IN PARTIAL FULFILLMENT OF THE  
REQUIREMENTS FOR THE DEGREE OF

DOCTOR OF PHILOSOPHY

in

The Faculty of Graduate Studies

(Chemical and Biological Engineering)

THE UNIVERSITY OF BRITISH COLUMBIA  
(Vancouver)

June 2012

© Vincent Wai Sang Lam, 2012

## Abstract

Direct borohydride fuel cells (DBFC) are a promising technology for meeting increasing energy demands of portable electronic applications. The objective of this dissertation was to contribute to the understanding of borohydride ( $\text{BH}_4^-$ ) electro-oxidation and the development of the DBFC anode; a component which can influence both the performance and cost of a DBFC system. The first part of the investigation involves the elucidation of the  $\text{BH}_4^-$  electro-oxidation mechanism on Pt. The  $\text{BH}_4^-$  electro-oxidation mechanism was studied by correlating the results obtained by the electrochemical quartz crystal microbalance technique (EQCM) and the rotating disk electrode technique (RDE) with density functional theory (DFT) calculations from the literature. It was found that  $\text{BH}_4^-$  electro-oxidation on Pt resulted in the adsorption of reaction intermediates, such as  $\text{BH}_2\text{OH}_{\text{ad}}$  and  $\text{BOH}_{\text{ad}}$ , which required high oxidizing potentials to desorb/ oxidize from the catalyst surface. It was also found that the  $\text{BH}_4^-$  oxidation mechanisms (Langmuir – Hinshelwood versus Eley – Rideal) were dictated by the availability of Pt-sites and the competitive adsorption of  $\text{OH}^-$  and  $\text{BH}_4^-$ .

The second part involves an investigation of the performance of three different carbon black supported anode catalysts: Pt, PtRu, and Os, with a focus on Os catalysts. Fundamental electrochemical methods combined with fuel cell experiments revealed that osmium nanoparticles are kinetically superior and stable catalysts for  $\text{BH}_4^-$  electro-oxidation compared to Pt and PtRu. It was also found that supported Os electrocatalysts appear to favour the direct oxidation of  $\text{BH}_4^-$  in comparison to Pt, and PtRu electrocatalysts. The final section of this dissertation focuses on the effect of electrocatalyst support and anode design on the performance of the DBFC anode. It was

found that the Vulcan<sup>®</sup> XC-72 supported catalyst alleviated mass transfer related problems associated with hydrogen generation from  $\text{BH}_4^-$  hydrolysis. The most significant improvement was obtained when using the graphite substrate supported catalysts (three-dimensional anodes). Fuel cell studies revealed power densities of 103  $\text{mW cm}^{-2}$  to 130  $\text{mW cm}^{-2}$  achieved by 1.7  $\text{mg cm}^{-2}$  Os and  $\sim 1$   $\text{mg cm}^{-2}$  PtRu three-dimensional electrodes respectively at 333 K, using an  $\text{O}_2$  oxidant at 4.4 atm (abs), and a 0.5 M  $\text{NaBH}_4$  – 2 M  $\text{NaOH}$  anolyte composition.

## Preface

The following papers were published based on the work presented in this dissertation:

A version of chapter 2 is published in:

- V.W.S. Lam, D.C.W. Kannangara, A. Alfantazi, and E.L. Gyenge, *Electrochemical Quartz Crystal Microbalance Study of Borohydride Electro-Oxidation on Pt: the Effect of Borohydride Concentration and Thiourea Adsorption*. J. Phys. Chem. C 115 (2011) 2727.
- V.W.S. Lam, D.C.W. Kannangara, A. Alfantazi, and E.L. Gyenge, *Reply to Comment on: “Electrochemical Quartz Crystal Microbalance Study of Borohydride Electro-Oxidation on Pt: the Effect of Borohydride Concentration and Thiourea Adsorption,”* J. Phys. Chem. C 115 (2011) 10312.
- V. W. S. Lam, D. Kannangara, A. Alfantazi, and E. L. Gyenge, *Borohydride Electrooxidation on Polycrystalline Pt Electrodes* (Regional Electrochemistry Meeting of South-East Asia, Thailand, November 17, 2010)

Where all of the experiments were performed by Vincent W.S. Lam with laboratory recommendations by Dhanesh C.W. Kannangara. The manuscripts were co-authored with Előd L. Gyenge with support from Akram Alfantazi.

A version of chapter 3 is published in:

- V.W.S. Lam, E.L. Gyenge, *High Performance Osmium Nanoparticle Electrocatalyst for Direct Borohydride PEM Fuel Cell Anodes*, J. Electrochem. Soc. 155 (2008) B1155.

Where all of the experiments were performed by Vincent W.S. Lam and the manuscript was co-authored with Előd L. Gyenge.

A version of chapter 4 is published in:

- V.W.S. Lam, A. Alfantazi, E.L. Gyenge, *The Effect of Catalyst Support on the Performance of PtRu in Direct Borohydride Fuel Cell Anodes*, J. Appl. Electrochem. 39 (2009) 1763.

Where the experiments were performed by Vincent W.S. Lam and the manuscript was co-authored with Előd L. Gyenge with support from Akram Alfantazi.

A version of chapter 5 is published in:

- V.W.S. Lam, D.C.W. Kannangara, A. Alfantazi, and E.L. Gyenge, *Electrodeposited Osmium Three-Dimensional Anodes for Direct Borohydride Fuel Cells*, J. Power Sources 212 (2012) 57.

Where the experiments were performed by Vincent W.S. Lam with laboratory recommendations by Dhanesh C.W. Kannangara, and the manuscript was co-authored with Előd L. Gyenge with support from Akram Alfantazi.

# Table of Contents

Abstract.....	ii
Preface.....	iv
Table of Contents.....	vi
List of Tables.....	ix
List of Figures.....	x
List of Symbols.....	xviii
List of Greek Symbols.....	xxi
List of Constants.....	xxiii
List of Abbreviations.....	xxiv
Acknowledgements.....	xxvi
Dedication.....	xxvii
1 Introduction.....	1
1.1 Physicochemical Properties of Borohydride.....	8
1.1.2 Borohydride Synthesis.....	8
1.1.3 Borohydride Stability.....	10
1.1.4 Borohydride Hydrolysis.....	14
1.2 Direct Borohydride Fuel Cell Performance.....	20
1.2.1 Effect of Temperature on $\text{BH}_4^-$ Electro-Oxidation.....	20
1.2.2 Anolyte Composition.....	23
1.2.3 Crossover.....	32
1.2.4 Oxidant Pressure.....	33
1.2.5 Anolyte Flow Rate.....	34
1.2.6 Direct Borohydride Fuel Cell Design Characteristics.....	37
1.3 Anode Catalysts.....	42
1.3.1 Platinum.....	42
1.3.2 Gold.....	46
1.3.3 Osmium.....	52
1.3.4 Silver.....	55
1.3.5 Zinc.....	57
1.3.6 Nickel.....	60
1.3.7 Palladium.....	64
1.3.8 Hydrogen Storage Alloys.....	67

1.3.9	Rhodium and Rh-Ir Alloys.....	69
1.3.10	Catalyst Summary.....	71
1.4	Objectives.....	73
2	Sodium Borohydride Electro-oxidation Mechanism on Polycrystalline Platinum*.	74
2.1	Experimental Procedure.....	75
2.1.1	Rotating Disk Electrode (RDE) and Cyclic Voltammetry (CV) .....	75
2.1.2	Electrochemical Quartz Crystal Microbalance Experiments.....	76
2.2	Pt Rotating Disk Electrode Studies .....	78
2.3	Electrochemical Quartz Crystal Microbalance Study of Pt in 2 M NaOH .....	85
2.4	Electrochemical Quartz Crystal Microbalance Study of $\text{BH}_4^-$ on Pt in 2 M NaOH .....	93
2.5	Electrochemical Quartz Crystal Microbalance Study of Thiourea on Pt in 2 M NaOH.....	107
2.6	Electrochemical Quartz Crystal Microbalance Study of the Thiourea effect on $\text{BH}_4^-$ on Pt in 2 M NaOH .....	110
2.7	Summary for Chapter 2.0.....	114
3	Anode Catalyst Investigation: Os/ C, Pt/ C, and PtRu/ C*.....	116
3.1	Experimental Procedure.....	117
3.1	Half-Cell Studies.....	121
3.2	Fuel Cell Experiments.....	130
3.3	Summary for Chapter 3.0.....	134
4	The Effect of Catalyst Support on Direct Borohydride Fuel Cell Performance* ...	136
4.1	Experimental Procedure.....	138
4.1.1	Catalyst Ink Preparation.....	138
4.1.2	Fuel Cell Experiments.....	138
4.1.3	PtRu Electrodeposition on Graphite Felt.....	139
4.1.4	Characterization of the PtRu on Graphite Felt.....	140
4.2	Effect of Support.....	140
4.3	Effect of the Anode Structure in Relation to PtRu electrocatalysts: Three-Dimensional Graphite Felt Support .....	146
4.3.1	Characterization of PtRu Supported on Graphite Felt .....	146
4.3.2	PtRu on Graphite Felt Anode Performance in DBFC.....	149
4.4	Summary for Chapter 4.0.....	151
5	Development of Osmium Three-Dimensional Anodes*.....	154
5.1	Experimental Procedure.....	154

5.2	Pretreatment of the Fibrous Carbon Substrates by Potential Cycling in 2M NaOH .....	157
5.3	Os Electrodeposition and Structural Characterization of Os Three-Dimensional Electrodes.....	159
5.4	Cyclic Voltammetry Investigation of $\text{BH}_4^-$ Oxidation on the Electrodeposited Three-Dimensional Os Electrodes .....	164
5.5	Direct Borohydride Fuel Cell Experiments.....	168
5.6	Summary for Chapter 5.0 .....	181
6	Thesis Concluding Remarks .....	182
7	Recommendations.....	187
	Bibliography .....	190
Appendix A	Electrochemical Surface Area Calculation .....	204
Appendix B	Electrochemical Quartz Crystal Microbalance .....	208
B.1	Electrochemical Quartz Crystal Microbalance Cell Setup.....	209
Appendix C	Determination of the Sauerbrey Constant .....	212
Appendix D	Surface Coverage Estimation .....	218
Appendix E	Standard Error Calculation.....	221
Appendix F	Os Electrochemical Surface Area .....	222
Appendix G	XRD Scans on GF-S3 and AvCarb™ P75 Blank Substrates.....	226
Appendix H	Fuel Cell Setup .....	228
Appendix I	Effect of Diaphragms, and Anion and Cation Exchange Membranes on Direct Borohydride Fuel Cell Performance .....	230
I.1	Procedure.....	231
I.1.1	Electrode Preparation.....	231
I.1.2	Fuel Cell Tests .....	231
I.2	Discussion .....	232
Appendix J	Recyclability of Sodium Borate .....	236

## List of Tables

Table 1. Hydrogen liberated from NaBH <sub>4</sub> pellets containing a solid homogeneous hydrolysis catalyst. Starting conditions: T: 298 K, and pH: 7. Modified with permission from [52], Copyright 1953, American Chemical Society.....	17
Table 2. Effect of fuel composition on DBFC performance. Temperature = 358 K. Other conditions as in Figure 6. Reprinted with permission from [6], Copyright 2006, Elsevier. ....	25
Table 3. Effect of NaBH <sub>4</sub> concentration on peak power density and fuel utilization. Anode: 10 wt% Pd/ C, 0.30 mg cm <sup>-2</sup> , cathode: 10 wt% Pt/ C, 0.30 mg cm <sup>-2</sup> , membrane: Nafion <sup>®</sup> 117, Temperature: 298 K, humidified air (RH: 65%) flow rate: 0.15 SLPM, P <sub>air</sub> : 1 atm (abs), fuel flow rate: 2 ml min <sup>-1</sup> . Modified with permission from [72], Copyright 2010, Elsevier. ....	26
Table 4. Effect of oxidant composition and pressure. T: 358 K, anode: Au/ C, 2 mg cm <sup>-2</sup> , cathode: Pt/ C, 2 mg cm <sup>-2</sup> , membrane: Nafion <sup>®</sup> 117, anolyte: 5 wt% NaBH <sub>4</sub> - 10 wt% NaOH, anolyte flow rate: 10 ml min <sup>-1</sup> , O <sub>2</sub> pressure: 1 atm (abs), O <sub>2</sub> flow rate: 0.2 SLPM. Modified with permission from [6], Copyright 2006, Elsevier. ....	34
Table 5. Top five performing anode catalysts in DBFC using an Air or O <sub>2</sub> oxidant. ....	72
Table 6. Calculated number of electrons for BH <sub>4</sub> <sup>-</sup> electro-oxidation on Pt/ C in 3 M NaOH at 298 K [140].....	84
Table 7. Elemental analysis of deposition substrates before and after electrochemical pretreatment in weight percentage. ....	158
Table 8. Calculation of the effective ionic ( $\kappa'$ ) and electronic ( $\sigma'$ ) conductivity ratios of the GF-S3 to AvCarb <sup>™</sup> P75 three-dimensional electrodes under the employed experimental conditions.....	170
Table 9. van der Waals volumes and cross-sectional areas for selected relevant molecules and molecular fragments [2,3]. ....	219
Table 10. Properties of various separators. AEM: anion exchange embrane, CEM: cation exchange membrane.....	230
Table 11. Performance comparison of separators under the conditions of Figure 83. ...	235

## List of Figures

- Figure 1. Total cost of DBFC and DMFC system at 20 W power output. Modified with permission from [8], Copyright 2006, Elsevier. .... 3
- Figure 2. Schematic of the  $\text{BH}_4^-$  electro-oxidation reaction mechanisms including both Faradaic and non-Faradaic thermocatalytic pathways. Modified with permission from [10], Copyright 2011, American Chemical Society..... 5
- Figure 3. DBFC A) cation exchange membrane (CEM) electrode assembly and B) anion exchange membrane (AEM) electrode assembly. .... 7
- Figure 4. Schematic of the Brown and Schlesinger process. Modified with permission from [43], Copyright 2004, U.S. Department of Energy. .... 9
- Figure 5.  $\text{NaBH}_4$  decomposition. T: 295 K,  $\text{NaBH}_4\text{:H}_2\text{O}$  molar ratio: 1:5, NaOH: (1) 3 wt%, (2) 5 wt%, (3) 10 wt%. Reprinted with permission from [46], Copyright 2008, Springer..... 13
- Figure 6. Temperature dependence of polarization and power curves. Anode: Au/ C; 2  $\text{mg cm}^{-2}$ ; Area: 4  $\text{cm}^2$ . Anolyte: 5 wt%  $\text{NaBH}_4$  – 10 wt% NaOH.  $\text{O}_2$ : 0.2 SLPM; 1 atm (abs). Cathode: 2  $\text{mg cm}^{-2}$ ; Pt/ C. Separator: Nafion<sup>®</sup> 117. Flow field: parallel flow pattern. Figure notes: Temperature is in  $^\circ\text{C}$ . E = Polarization Curve, P = Power Curve. Reprinted with permission from [6], Copyright 2006, Elsevier. .... 21
- Figure 7. A picture of carbonate precipitation on the cathode current collector after up to 475 hours of operation in 1 M NaOH electrolyte. Reprinted with permission from [73], Copyright 2009, Elsevier. .... 28
- Figure 8. Borohydride electro-oxidation on 1 mm diameter Pt disk. Electrolyte: 0.03 M  $\text{NaBH}_4$  – 2 M NaOH, T: 295 K, scan rate: 25  $\text{mV s}^{-1}$ . Inset: 2 M NaOH blank scan on 1 mm diameter Pt disk. Modified with permission from [9], Copyright 2004, Elsevier. ... 29
- Figure 9. Borohydride electro-oxidation on 1 mm diameter Pt disk with TU. Electrolyte: 0.03 M  $\text{NaBH}_4$  – 2 M NaOH – 1.5 x 10<sup>-3</sup> M TU, T: 295 K, scan rate: 50  $\text{mV s}^{-1}$  (—), 100  $\text{mV s}^{-1}$  (- - -). Inset: 2 M NaOH – 1.5 x 10<sup>-3</sup> M TU blank scan on 1 mm diameter Pt disk. Modified with permission from [9], Copyright 2004, Elsevier. .... 30
- Figure 10. DBFC polarization curves. Anode: 5  $\text{mg cm}^{-2}$  Au/ C, anolyte: 2 M  $\text{NaBH}_4$  – 2 M NaOH, cathode: 4  $\text{mg cm}^{-2}$  Pt/ C,  $\text{O}_2$  flow rate: 0.2 SLPM,  $\text{O}_2$  pressure: 2.7 atm (abs). Modified with permission from [15], Copyright 2006, Elsevier. .... 36
- Figure 11. DBFC polarization curves. Anode: 5  $\text{mg cm}^{-2}$  Au-Pt/ C, anolyte: 2 M  $\text{NaBH}_4$  – 2 M NaOH, cathode: 4  $\text{mg cm}^{-2}$  Pt/ C,  $\text{O}_2$  flow rate: 0.2 SLPM,  $\text{O}_2$  pressure: 2.7 atm (abs). Modified with permission from [15], Copyright 2006, Elsevier. .... 37

Figure 12. Diagram of MEA configurations by Wang et al.. A) MEA configuration MEA-A where both the anode and cathode active layers are sectioned into two halves but only one half of each side contains catalysts. B) MEA configuration MEA-B where both the anode and cathode active layers are sectioned into two halves, and one half of the anode active layer is hydrophobic with 40% Pt/ C for H<sub>2</sub> electro-oxidation. C) Experimental cell setup. Reprinted with permission from [79], Copyright 2010, Elsevier. .... 39

Figure 13. Qineti Q tubular cell with a 0.8 mg cm<sup>-2</sup> Au/ Ni grid anode and an MnO<sub>2</sub> cathode. Reprinted with permission from [22], Copyright 2008, Elsevier. .... 40

Figure 14. DBFC stack operating under passive and ambient conditions powering a small television. The anolyte composition was 5 wt% NaBH<sub>4</sub> – 20 wt% NaOH, and the Ni powder to Pd/ C to Nafion<sup>®</sup> anode ratio was 0.75:0.3:0.1 with a 20 mg cm<sup>-2</sup> metal loading. Reprinted with permission from [80], Copyright 2008, Elsevier. .... 41

Figure 15. Cyclic voltammogram on 1 mm diameter Au disk electrode. Electrolyte: 0.03 M NaBH<sub>4</sub> – 2 M NaOH, T: 295 K. Modified with permission from [9], Copyright 2004, Elsevier. .... 47

Figure 16. Chronoamperometry on Au and Pt/TU at 293 K. Electrolyte: NaBH<sub>4</sub> – 2 M NaOH, TU concentration: 1.5 x 10<sup>-3</sup> M, potential step: -0.6 V to 0.2 V. Modified with permission from [9], Copyright 2004, Elsevier. .... 49

Figure 17. Chronopotentiometry on Pt and various 1:1 atomic ratio binary catalysts. electrolyte: 0.5 M NaBH<sub>4</sub> – 2 M NaOH, T: 298 K. Current step from 0 to 10 mA/ cm<sup>2</sup>. Modified with permission from [18], Copyright 2006, The Electrochemical Society. .... 51

Figure 18. DBFC polarization curves of Pt and various 1:1 atomic ratio 5 mg cm<sup>-2</sup> binary catalysts. Anolyte: 2 M NaBH<sub>4</sub> – 2 M NaOH, anolyte flow rate: 50 ml min<sup>-1</sup> at STP, O<sub>2</sub> flow rate: 0.2 SLPM, O<sub>2</sub> pressure = 2.7 atm (abs), T: 298K, cathode: 4 mg cm<sup>-2</sup> Pt/ C. Modified with permission from [18], Copyright 2006, The Electrochemical Society. .... 52

Figure 19. Cyclic voltammogram of freshly prepared 20% Os/ C by modified Bönmeman method. Load: 30 µg cm<sup>-2</sup>, electrolyte: 0.03 M NaBH<sub>4</sub> – 2 M NaOH, blank scan electrolyte: 2 M NaOH, T: 295 K, scan rate: 100 mV s<sup>-1</sup>. Modified with permission from [109], Copyright 2005, The Laboratory of New Materials for Energy and Electrochemistry Systems. .... 54

Figure 20. Chronoamperometry of freshly prepared 20% Os/ C by modified Bönmeman method. Load: 30 µg cm<sup>-2</sup>, electrolyte: NaBH<sub>4</sub> – 2 M NaOH, T: 295 K. Potential step from -0.6 V to 0.5 V. Modified with permission from [109], Copyright 2005, The Laboratory of New Materials for Energy and Electrochemistry Systems. .... 55

Figure 21. Zinc cyclic voltammogram. Electrolyte: 1 M NaBH<sub>4</sub> – 4 M NaOH, scan rate: 0.05 V s<sup>-1</sup>, T: 295 K. Modified with permission from [120], Copyright 2010, The Electrochemical Society. .... 59

- Figure 22. Power density curves of supported Pt, Ni, and Pt-Ni alloys. Anode loading: 1 mg cm<sup>-2</sup> metal, anolyte: 5 wt% NaBH<sub>4</sub> – 10 wt% NaOH, anolyte flow rate: 1 mL min<sup>-1</sup>, T: 333 K, cathode loading: 1 mg cm<sup>-2</sup> Pt/ C, oxidant: O<sub>2</sub>, P<sub>O<sub>2</sub></sub>: 2atm (abs), oxidant flow rate: 0.1 SLPM. Modified with permission from [124], Copyright 2008, Elsevier..... 62
- Figure 23. Cyclic voltammograms of (a) Ni/ C and (b) 41:1 Ni-Pt/ C. Anolyte: 0.2 M NaBH<sub>4</sub> – 2 M NaOH, scan rate: 50 mV s<sup>-1</sup>, rotation rate: 1600 rpm, T: 293 K. Modified with permission from [124], Copyright 2008, Elsevier. .... 64
- Figure 24. Calculated number of electrons exchanged on Pd/ C, Au/ C, and Pd-Au/ C alloys. Electrolyte: 1 x 10<sup>-2</sup> M NaBH<sub>4</sub> – 1 M NaOH – N<sub>2</sub> saturated, T: 293 K. Modified with permission from [128], Copyright 2009, American Chemical Society. .... 65
- Figure 25. Hydrogen generation on ◆ Pd/ C, ● Au/ C, and ■ Pd<sub>0.7</sub>Au<sub>0.3</sub>/ C catalysts. Hydrogen was measured by water displacement in a column at ambient conditions. Electrolyte: 0.124 M NaOH – 0.136 M NaBH<sub>4</sub>, T: 293 K, P: 1 atm (abs), Metal loading: 0.4 mg cm<sup>-2</sup>, Electrode Area: 2.42 cm<sup>2</sup>. Modified with permission from [128], Copyright 2009, American Chemical Society. .... 67
- Figure 26. Single and multi-cell stack performance using bipolar stainless steel plates. Anode: 150 mg cm<sup>-2</sup> Zr-Ni alloy with Ni powder and PTFE binder, anolyte: 10 wt% NaBH<sub>4</sub> – 5 wt% NaOH, anolyte flow rate: cell number x 150 mL min<sup>-1</sup>, T: 333 K, cathode: 1 mg cm<sup>-2</sup> 50% Pt/ C, oxidant: air, oxidant flow rate: cell number x 5 SLPM, P<sub>air</sub>: not reported. Modified with permission from [129], Copyright 2008, Elsevier..... 69
- Figure 27. Rh-Ir/ C anode catalyst DBFC polarization curve at 298 K and 333 K. Anode: 0.5 mg cm<sup>-2</sup> Rh-Ir/ C, anolyte: 2.64 M NaBH<sub>4</sub> – 2 M NaOH, anolyte flowrate: 1.5 L min<sup>-1</sup>, cathode: 2 mg cm<sup>-2</sup> Pt/ C, catholyte: 2.2 M H<sub>2</sub>O<sub>2</sub> – 1.5 M H<sub>2</sub>SO<sub>4</sub>, catholyte flow rate: 2.1 L min<sup>-1</sup>. Modified with permission from [134], Copyright 2010, The Electrochemical Society..... 71
- Figure 28. Cyclic voltammogram of 0.5 mM NaBH<sub>4</sub> – 2 M NaOH on Pt at 0 rpm and 298 K. Scan rate: 10 mV s<sup>-1</sup>. .... 79
- Figure 29. Levich plot of 0.1 mM NaBH<sub>4</sub> – 2 M NaOH electro-oxidation on Pt at 298 K. Scan rate: 10 mV s<sup>-1</sup>. .... 80
- Figure 30. Effect of rotation rate for 0.1 mM NaBH<sub>4</sub> – 2 M NaOH at 298 K. Scan rate: 10 mV s<sup>-1</sup>. .... 81
- Figure 31. Effect of NaBH<sub>4</sub> concentration on calculated number of electrons from Pt RDE studies. T: 298 K, electrolyte: NaBH<sub>4</sub> – 2 M NaOH. .... 83
- Figure 32. Surface mass changes of the Pt resonator electrode during cyclic voltammetry in 2 M NaOH after 11 scans. T: 293 K; scan rate: 10 mV s<sup>-1</sup>. Reproduced with permission from [104], Copyright 2011, American Chemical Society. .... 86

Figure 33. Surface mass changes (a) of the Pt resonator electrode during consecutive cyclic voltammetry scans in 2 M NaOH (b). Consecutive Pt cyclic voltammograms in 2 M NaOH. T: 293 K; scan rate: 10 mV s <sup>-1</sup> . Reproduced with permission from [104], Copyright 2011, American Chemical Society. ....	90
Figure 34. Surface mass changes of the Pt resonator electrode during cyclic voltammetry in 2 M NaOH after A) 100 scans and B) 200 scans. T: 293 K; scan rate: 10 mV s <sup>-1</sup> . ....	91
Figure 35. Effect of BH <sub>4</sub> <sup>-</sup> concentration on the stationary cyclic voltammograms on Pt disk. All the scans started in the anodic direction. Inset: BH <sub>4</sub> <sup>-</sup> electro-oxidation peak current density versus BH <sub>4</sub> <sup>-</sup> concentration. Supporting Electrolyte: 2 M NaOH; T: 298 K; scan rate: 100 mV s <sup>-1</sup> . Reproduced with permission from [104], Copyright 2011, American Chemical Society. ....	94
Figure 36. Cyclic voltammetry and surface mass changes of a Pt resonator electrode in 10 mM NaBH <sub>4</sub> - 2 M NaOH. T: 293 K; scan rate: 10 mV s <sup>-1</sup> . Reproduced with permission from [104], Copyright 2011, American Chemical Society. ....	95
Figure 37. Cyclic voltammetry and surface mass changes of a Pt resonator electrolyte in 60 mM NaBH <sub>4</sub> - 2 M NaOH; T: 293 K; scan rate: 10 mV s <sup>-1</sup> . Reproduced with permission from [104], Copyright 2011, American Chemical Society. ....	96
Figure 38. Effect of the switching potential on the cyclic voltammetry behaviour of BH <sub>4</sub> <sup>-</sup> on Pt disk electrode. All scans started in the anodic direction. Anolyte: 20 mM NaBH <sub>4</sub> - 2 M NaOH; T: 293 K; scan rate: 10 mV s <sup>-1</sup> . Reproduced with permission from [104], Copyright 2011, American Chemical Society. ....	104
Figure 39. Effect of TU on the cyclic voltammogram and surface mass changes of a Pt resonator electrode in 2 M NaOH - 1.5 mM TU. 293 K, scan rate: 10 mV s <sup>-1</sup> . Reproduced with permission from [104], Copyright 2011, American Chemical Society. ....	108
Figure 40. Effect of TU concentration on the cyclic voltammetry of BH <sub>4</sub> <sup>-</sup> on a Pt resonator electrode. Electrolyte: 30 mM NaBH <sub>4</sub> - 2 M NaOH; T: 293 K; scan rate: 10 mV s <sup>-1</sup> . Reproduced with permission from [104], Copyright 2011, American Chemical Society. ....	111
Figure 41. Effect of TU on surface mass changes of a Pt resonator electrode during cyclic voltammetry in BH <sub>4</sub> <sup>-</sup> solution. Electrolyte: 30 mM NaBH <sub>4</sub> - 2 M NaOH; T: 293 K; scan rate: 10 mV s <sup>-1</sup> . Reproduced with permission from [104], Copyright 2011, American Chemical Society. ....	112
Figure 42. TEM image of Os/ C prepared by a modified Bönnerman method. ....	118
Figure 43. Distribution of Os/ C particle sizes as observed by TEM. ....	119

Figure 44. XPS spectra of Os/ C prepared by the modified Bönnehan method. Reproduced with permission from [165], Copyright 2008, The Electrochemical Society.

..... 120

Figure 45. Cyclic voltammograms of A) Pt/ C, C) PtRu/ C, and E) Os/ C in 0.05 M NaBH<sub>4</sub> – 2 M NaOH, and B) Pt/ C, D) PtRu/ C, and F) Os/ C in 2 M NaOH. T: 293 K, scan rate: 50 mV s<sup>-1</sup>. Reproduced with permission from [165], Copyright 2008, The Electrochemical Society.

..... 122

Figure 46. 20% Os/ C cyclic voltammograms at varied scan rates. Inset: Potential at peak current density (E<sub>p</sub>) versus logarithm of scan rate. Electrolyte: 0.05 M NaBH<sub>4</sub> – 2 M NaOH, T: 293 K.

..... 125

Figure 47. Chronoamperometry curves for BH<sub>4</sub><sup>-</sup> oxidation on a) Pt/ C, b) PtRu/ C and c) Os/ C catalysts. Potential step from open circuit to -0.6 V, -0.5 V, and -0.4 V, respectively. Electrolyte: 0.05 M NaBH<sub>4</sub> – 2 M NaOH, T: 293 K. Reproduced with permission from [165], Copyright 2008, The Electrochemical Society.

..... 127

Figure 48. Chronopotentiometry profiles for BH<sub>4</sub><sup>-</sup> oxidation on 20% Pt/ C, PtRu/ C and Os/ C catalysts. Anolyte: 0.05 M NaBH<sub>4</sub> – 2 M NaOH, T: 293 K, P: 1 atm (abs), i: 10 mA cm<sup>-2</sup>. Reproduced with permission from [165], Copyright 2008, The Electrochemical Society.

..... 130

Figure 49. Direct borohydride fuel cell polarization curves using 20% Pt/ C, 20% PtRu/ C and 20% Os/ C anode catalysts with a load of 1 mg cm<sup>-2</sup>. Cathode catalyst Pt black 4 mg cm<sup>-2</sup>. a) T: 298 K, b) T: 333 K. Anolyte: 0.5 M NaBH<sub>4</sub> – 2 M NaOH, anolyte flow rate: 10 ml min<sup>-1</sup>, oxidant: O<sub>2</sub>, oxidant flowrate: 1.25 SLPM, oxidant pressure: 4.4 atm (abs). Reproduced with permission from [165], Copyright 2008, The Electrochemical Society.

..... 131

Figure 50. 20% Pt/ C, PtRu/ C, and Os/ C direct fuel cell longevity tests over 3 hours at a constant current of 120 mA cm<sup>-2</sup>. Anode catalysts with a load of 1 mg cm<sup>-2</sup>. Cathode catalyst Pt black 4 mg cm<sup>-2</sup>. T: 333 K, anolyte: 0.5 M NaBH<sub>4</sub> – 2 M NaOH, anolyte flow rate: 10 mL min<sup>-1</sup>, oxidant: O<sub>2</sub>, oxidant flow rate: 1.25 SLPM, oxidant pressure: 4.4 atm (abs).

..... 133

Figure 51. Effect of Os dispersion on the carbon support on the DBFC polarization curves. Anode catalysts with a load of 1 mg cm<sup>-2</sup>. Cathode catalyst Pt black 4 mg cm<sup>-2</sup>. T: 333 K, anolyte: 0.5 M NaBH<sub>4</sub> – 2 M NaOH, anolyte flow rate: 10 mL min<sup>-1</sup>, oxidant: O<sub>2</sub>, oxidant flow rate: 1.25 SLPM, oxidant pressure: 4.4 atm (abs). Reproduced with permission from [165], Copyright 2008, The Electrochemical Society.

..... 134

Figure 52. Non-supported Pt black and PtRu black anode catalyst comparison for DBFC. A) Power density curves B) Polarization curves. Anode loading: 1 mg cm<sup>-2</sup>, cathode loading: 4 mg cm<sup>-2</sup> Pt black, anolyte: 0.5 M NaBH<sub>4</sub> – 2 M NaOH, anolyte flow rate: 10 mL min<sup>-1</sup>, O<sub>2</sub> flow rate: 1.25 SLPM, O<sub>2</sub> pressure: 4.4 atm (abs); T: 333K. Reproduced with permission from [186], Copyright 2009, Springer.

..... 141

Figure 53. Comparison of 20% PtRu/ C and PtRu black catalyst performance. Anode loading:  $1 \text{ mg cm}^{-2}$ , cathode loading:  $4 \text{ mg cm}^{-2}$  Pt black, anolyte:  $0.5 \text{ M NaBH}_4 - 2 \text{ M NaOH}$ , anolyte flow rate:  $10 \text{ ml min}^{-1}$ ,  $\text{O}_2$ , flow rate: 1.25 SLPM,  $\text{O}_2$  pressure: 4.4 atm (abs), T: 333K. Reproduced with permission from [186], Copyright 2009, Springer... 142

Figure 54. Heterogeneous catalysis of  $\text{BH}_4^-$  hydrolysis without electrode polarization.  $1 \text{ mg cm}^{-2}$  PtRu black and 20 wt%  $1 \text{ mg cm}^{-2}$  PtRu/ C. Catalyst sprayed on Toray carbon paper with 60 wt% Nafion<sup>®</sup> binder. Anolyte:  $0.5 \text{ M NaBH}_4 - 2 \text{ M NaOH}$ ; T: 293K. Reproduced with permission from [186], Copyright 2009, Springer. .... 145

Figure 55. TEM picture of PtRu electrodeposited on compressed graphite felt. A)  $3 \times 10^5$  magnification. B)  $6 \times 10^5$  magnification. Reproduced with permission from [186], Copyright 2009, Springer..... 147

Figure 56. XRD spectra of PtRu electrodeposited on GF-S3. XRD scan of GF-S3 without Os deposit is shown in Appendix G. Reproduced with permission from [186], Copyright 2009, Springer..... 149

Figure 57. Effect of the three-dimensional anode structure on the DBFC. A) power density curves B) polarization curves. Cathode loading:  $4 \text{ mg cm}^{-2}$  Pt black, anolyte:  $0.5 \text{ M NaBH}_4 - 2 \text{ M NaOH}$ ; anolyte flow rate:  $10 \text{ ml min}^{-1}$ ;  $\text{O}_2$  flow rate: 1.25 SLPM; oxidant pressure: 4.4 atm (abs); T: 333 K. Reproduced with permission from [186], Copyright 2009, Springer..... 151

Figure 58. Deconvoluted XPS narrow scan on C 1s spectra. A) Untreated AvCarb<sup>™</sup> P75, B) pretreated AvCarb<sup>™</sup> P75, C) untreated GF-S3, D) pretreated GF-S3. .... 158

Figure 59. Cathode potential profile during Os electrodeposition on AvCarb<sup>™</sup> P75 substrate at  $4 \text{ mA cm}^{-2}$  and 341 K. Inset: shows the cathode potential profile during the first 120 s of deposition. The bath was composed of  $10 \text{ mM } (\text{NH}_4)_2\text{OsCl}_6$  with 12.5 vol% of Triton-X 102. Typical  $E_{\text{OCP}} \sim 0.66 \text{ V}$ . .... 160

Figure 60. SEM images of A) AvCarb<sup>™</sup> P75 without deposit, B) GF-S3 without deposit, and Os electrodeposited on: C) AvCarb<sup>™</sup> P75 and D) GF-S3 substrates..... 161

Figure 61. SEM Images of A) AvCarb<sup>™</sup> P75 electrodeposited with Os and B) GF-S3 electrodeposited with Os..... 162

Figure 62. TEM images of Os deposits on: A) AvCarb<sup>™</sup> P75 and B) GF-S3 substrates. .... 163

Figure 63. XRD wide scan of Os electrodeposited onto AvCarb<sup>™</sup> P75 (Os loading:  $0.3 \text{ mg cm}^{-2}$ ) and GF-S3 (Os loading  $0.2 \text{ mg cm}^{-2}$ ). XRD scan of AvCarb<sup>™</sup> P75 without Os deposit is shown in Appendix G. .... 164

Figure 64. Cyclic voltammogram of: A) Os/ AvCarb<sup>™</sup> P75 in  $10 \text{ mM NaBH}_4 - 2 \text{ M NaOH}$ , B) Os/ AvCarb<sup>™</sup> P75 in  $2 \text{ M NaOH}$ , C) Os/ GF-S3 in  $10 \text{ mM NaBH}_4 - 2 \text{ M NaOH}$ .

NaOH, D) Os/ GF-S3 in 2 M NaOH, Os loading for each electrode:  $0.2 \text{ mg cm}^{-2}$ . T: 298 K, scan rate:  $10 \text{ mV s}^{-1}$  ..... 165

Figure 65. A) XPS wide scan of Os/ AvCarb™ P75 and B) XPS narrow scan of the same sample. .... 168

Figure 66. Comparison of DBFC performance with Os/ GF-S3 and Os/ AvCarb™ P75 anodes. Os loading:  $0.2 \text{ mg cm}^{-2}$  for both anodes. T: 333 K. Cathode catalyst:  $4 \text{ mg cm}^{-2}$  Pt, O<sub>2</sub> pressure: 4.4 atm (abs), O<sub>2</sub> flow rate 0.25 SLPM, anolyte: 0.5 M NaBH<sub>4</sub> – 2 M NaOH, anolyte flow rate  $10 \text{ mL min}^{-1}$  ..... 169

Figure 67. Effect of temperature on DBFC operation with Os/ AvCarb™ P75 anode with  $0.2 \text{ mg cm}^{-2}$  Os loading. Cathode catalyst:  $4 \text{ mg cm}^{-2}$  Pt, O<sub>2</sub> pressure: 4.4 atm (abs), O<sub>2</sub> flow rate 0.25 SLPM, anolyte: 0.5 M NaBH<sub>4</sub> – 2 M NaOH, anolyte flow rate  $10 \text{ ml min}^{-1}$ . .... 175

Figure 68. Effect of Os loading on the DBFC performance with Os/ AvCarb™ P75 anode. The Os loading was increased by repeating the electrodeposition process a number of times on the same substrate. Legend: (1x): single deposition, Os loading:  $0.3 \text{ mg cm}^{-2}$ , (2x): double deposition, Os loading:  $0.9 \text{ mg cm}^{-2}$ , (4x): quadruple deposition, Os loading:  $1.7 \text{ mg cm}^{-2}$ , T: 333 K, cathode catalyst:  $4 \text{ mg cm}^{-2}$  Pt, O<sub>2</sub> pressure: 4.4 atm (abs), O<sub>2</sub> flow rate 1.25 SLPM, anolyte: 0.5 M NaBH<sub>4</sub> – 2 M NaOH, flow rate  $10 \text{ ml min}^{-1}$  ..... 177

Figure 69. Reproducibility of the BFC performance with Os/ AvCarb™ P75 anode prepared by the quadruple (4x) deposition procedure. Error bars represent the standard error of the mean with 90% confidence level. T: 333 K, Cathode catalyst:  $4 \text{ mg cm}^{-2}$  Pt, O<sub>2</sub> pressure: 4.4 atm (abs), O<sub>2</sub> flow rate 1.25 SLPM, anolyte: 0.5 M NaBH<sub>4</sub> – 2 M NaOH, anolyte flow rate  $10 \text{ ml min}^{-1}$  ..... 178

Figure 70. Longer-term performance evaluation of the DBFC with Os/ AvCarb™ P75 anode prepared by the quadruple (4x) deposition procedure. Os loading:  $1.7 \text{ mg cm}^{-2}$ . The DBFC was held at a constant current output of  $290 \text{ mA cm}^{-2}$ . T: 333 K, cathode catalyst:  $4 \text{ mg cm}^{-2}$  Pt, oxygen pressure: 4.4 atm (abs), oxygen flow rate 1.25 SLPM, anolyte: 0.5 M NaBH<sub>4</sub> – 2 M NaOH, anolyte flow rate  $10 \text{ mL min}^{-1}$ . .... 179

Figure 71. H-UPD on 0.5 cm diameter polycrystalline Pt disk. T: 298 K, Electrolyte: 0.5 M H<sub>2</sub>SO<sub>4</sub>, scan rate:  $20 \text{ mV s}^{-1}$  ..... 206

Figure 72. EQCM experimental setup. .... 210

Figure 73. EQCM A) original cell design B) improved vertical cell design c) Pt resonator. .... 211

Figure 74. Cyclic voltammetry scan of Pt in 0.1 M H<sub>2</sub>SO<sub>4</sub> (20<sup>th</sup> scan) and the Cu stripping curve. T: 293 K, scan rate:  $10 \text{ mV s}^{-1}$ . Reproduced with permission from [6], Copyright 2011, American Chemical Society. .... 214

Figure 75. EQCM mass response from Cu stripping. Reproduced with permission from [6], Copyright 2011, American Chemical Society.....	215
Figure 76. Change of resonator frequency versus change in Cu stripping charge. ....	216
Figure 77. Three-dimensional Os electrode cyclic voltammogram in 0.5 M H <sub>2</sub> SO <sub>4</sub> . T: 298 K, scan rate: 30 mV s <sup>-1</sup> .....	224
Figure 78. XRD scan of GF-S3 blank substrate. ....	226
Figure 79. XRD scan of AvCarb™ P75 blank substrate. ....	227
Figure 80. Schematic of DBFC cell used for single cell tests. ....	228
Figure 81. DBFC system testing setup .....	229
Figure 82. Stainless steel flowfield plate .....	229
Figure 83. Polarization curves of diaphragms. T: 333 K, anode catalyst: 1 mg cm <sup>-2</sup> Pt/ C, cathode catalyst: 1 mg cm <sup>-2</sup> Pt/ C, oxidant: O <sub>2</sub> , oxidant pressure: 4.4 atm (abs), oxidant flow rate: 1.25 SLPM, anolyte: 0.5 M NaBH <sub>4</sub> – 2 M NaOH, anolyte flow rate: 10ml min <sup>-1</sup> .....	235

## List of Symbols

Symbol	Definition	SI Units	In Text
$A$	Electrochemical area	$\text{m}^2$	$\text{cm}^2$
$A_s$	Specific surface area	$\text{m}^2 \text{kg}^{-1}$	$\text{cm}^2 \text{kg}^{-1}$
$a_i$	Activity	---	---
$a'$	Lattice parameter	Å	Å
$b$	Tafel slope	$\text{V dec}^{-1}$	$\text{V dec}^{-1}$
$C_o$	Bulk concentration	$\text{mol m}^{-3}$	$\text{mol cm}^{-3}$
$C^o$	Arbitrary reference state	$\text{mol m}^{-3}$	$\text{mol L}^{-1}$
$C_f$	Sauerbrey constant	$\text{Hz m}^2 \text{kg}^{-1}$	$\text{Hz cm}^2 \text{g}^{-1}$
$C$	Molar concentration	$\text{mol m}^{-3}$	$\text{mol L}^{-1}$
$C_{\pm}$	Mean molar concentration	$\text{mol m}^{-3}$	$\text{mol L}^{-1}$
$D$	Effective diffusivity	$\text{m}^2 \text{s}^{-1}$	$\text{cm}^2 \text{s}^{-1}$
$D_o$	Diffusivity	$\text{m}^2 \text{s}^{-1}$	$\text{cm}^2 \text{s}^{-1}$
$d_m$	Hydrogen monolayer density	$\text{atoms m}^{-2}$	$\text{atoms cm}^{-2}$
$d$	Particle diameter	m	nm
$E$	Potential	V	V
$E_p$	Peak potential	$\text{V}_{\text{SHE}}$	$\text{V}_{\text{SHE}}$
$E_T^o$	Standard potential	$\text{V}_{\text{SHE}}$	$\text{V}_{\text{SHE}}$
$E_{e,\text{cell}}$	Equilibrium potential	$\text{V}_{\text{SHE}}$	$\text{V}_{\text{SHE}}$
$E_{\text{OCP}}$	Open Circuit Potential	$\text{V}_{\text{SHE}}$	$\text{V}_{\text{SHE}}$
$f$	Activity coefficient	---	---
$f_{\pm}$	Mean molar activity coefficient	---	---
$\Delta f$	Change in frequency	Hz	Hz
$\Delta G^o$	Free energy	$\text{J mol}^{-1}$	$\text{J mol}^{-1}$
$\Delta H_c^o$	Enthalpy of combustion	$\text{J mol}^{-1}$	$\text{J mol}^{-1}$
$I$	Current	A	mA
$I_p$	Peak current	A	mA

## List of Symbols (Continued)

Symbol	Definition	SI Units	In Text
$i$	Current density	A m <sup>-2</sup>	mA cm <sup>-2</sup>
$i_c$	Crossover current density	A m <sup>-2</sup>	mA cm <sup>-2</sup>
$i_l$	Limiting current density	A m <sup>-2</sup>	mA cm <sup>-2</sup>
$J$	Molar ionic strength	---	---
$k$	Rate constant	m s <sup>-1</sup>	cm s <sup>-1</sup> or m s <sup>-1</sup>
$k'$	Rate constant	s <sup>-1</sup>	hr <sup>-1</sup>
$k^\circ$	Standard heterogeneous rate constant	m s <sup>-1</sup>	m s <sup>-1</sup>
$MW$	Molar mass	kg kmol <sup>-1</sup>	g mol <sup>-1</sup>
$\Delta m$	Change in mass	kg	ng
$m$	Mass	kg	mg
$N$	Total number of atoms	atoms	atoms
$n$	Electron number	mol e <sup>-</sup>	mol e <sup>-</sup>
$n_a$	Number of electrons for rate determining step	---	---
$n'$	Number of data points in population	---	---
$p$	Partial pressure	atm	atm
$P_{Total}$	Total gas pressure	atm	atm
$Q$	Cu stripping charge	C	C
$Q_d$	Hydrogen monolayer charge density	C m <sup>-2</sup>	C cm <sup>-2</sup>
$Q_{d,real}$	Actual hydrogen monolayer charge density	C m <sup>-2</sup>	C cm <sup>-2</sup>
$Q_{DL}$	Double layer charge	C	C
$Q'$	Reaction quotient	---	---
$Q_V$	Volumetric flow rate	m <sup>3</sup> s <sup>-1</sup>	L s <sup>-1</sup>
$r$	Apparent molecular radius or atomic van der Waals radius	Å	Å
$r'$	Hydrated radius of ionic species	m	cm

## List of Symbols (Continued)

Symbol	Definition	SI Units	In Text
$\Delta S$	Entropy	$\text{J mol}^{-1} \text{K}^{-1}$	$\text{J mol}^{-1} \text{K}^{-1}$
$s$	Standard deviation	---	---
$T$	Temperature	K	K
$t$	Time	s	s or hr
$t_{1/2}$	Half life	s	min
$t_{\alpha/2}$	Critical value for a t-distribution of data points	---	---
$\hat{V}_{vdW}$	van der Waals volume	$\text{\AA}^3 \text{ molecule}^{-1}$	$\text{\AA}^3 \text{ molecule}^{-1}$
$x$	Atomic fraction	---	---
$y$	Reaction rate order	---	---
$z$	Net charge of ionic species	---	---
$z'$	Data point	---	---
$\bar{z}'$	Mean of a sample population	---	---

## List of Greek Symbols

Symbol	Definition	SI Units	In Text
$\alpha$	Transfer coefficient	---	---
$\alpha_{DH}$	Debye-Hückel parameter	---	---
$\beta$	Full width at half maximum	Rad	Rad
$\beta_{DH}$	Debye-Hückel parameter	---	---
$\gamma_i$	Stoichiometric coefficient	---	---
$\varepsilon$	Effective porosity	---	---
$\varepsilon_o$	Porosity	---	---
$\eta$	Current efficiency	---	---
$\eta_Q$	Faradaic efficiency	---	---
$\eta_f$	Fuel utilization efficiency	---	---
$\eta'$	Thermodynamic efficiency	---	---
$\theta$	Angle at the maximum peak	Rad	Rad
$\theta'$	Molecular surface coverage	$\text{m}^2_{\text{molecule}} \text{m}^{-2}_{\text{surface}}$	$\text{cm}^2_{\text{molecule}} \text{cm}^{-2}_{\text{surface}}$
$\kappa$	Effective ionic conductivity	$\text{S m}^{-1}$	$\text{S m}^{-1}$
$\kappa_o$	Ionic conductivity	$\text{S m}^{-1}$	$\text{S m}^{-1}$
$\kappa'$	Ratio of the effective ionic conductivities	---	---
$\mu$	Mean of total population	---	---
$\nu$	Kinematic viscosity	$\text{m}^2 \text{s}^{-1}$	$\text{cm}^2 \text{s}^{-1}$
$\nu'$	Scan rate	$\text{V s}^{-1}$	$\text{V s}^{-1}$
$\xi$	Percentage of degradation by mass	%	%
$\rho'$	Gravimetric energy density	$\text{J kg}^{-1}$	$\text{J kg}^{-1}$
$\sigma$	Electronic conductivity of a porous matrix	$\text{S m}^{-1}$	$\text{S m}^{-1}$
$\sigma'$	Ratio of electronic conductivities	---	---
$\hat{\sigma}$	Surface area occupied per molecule	$\text{\AA}^2 \text{molecule}^{-1}$	$\text{\AA}^2 \text{molecule}^{-1}$
$\tau$	Time	s	days

## List of Greek Symbols (Continued)

Symbol	Definition	SI Units	In Text
$\tau'$	Compressed matrix thickness	m	$\mu\text{m}$
$\tau'_o$	Uncompressed matrix thickness	m	$\mu\text{m}$
$\phi$	Coefficient equal to 0.88	---	---
$\omega$	Rotation rate	Rad s <sup>-1</sup>	Rad s <sup>-1</sup>

## List of Constants

Symbol	Definition	Units
$F$	Faraday's number = 96485	C (mol e <sup>-</sup> ) <sup>-1</sup>
$N_A$	Avogadro's number = 6.022x10 <sup>23</sup>	molecules mol <sup>-1</sup>
$R$	Universal gas constant = 8.314	J mol <sup>-1</sup> K <sup>-1</sup>

## List of Abbreviations

---

<b>Symbol</b>	<b>Definition</b>
AEM	Anion Exchange Membrane
CEM	Cation Exchange Membrane
CCM	Catalyst Coated Membrane
CL	Catalyst Layer
DBFC	Direct Borohydride Fuel Cell
DFT	Density Functional Theory
DMFC	Direct Methanol Fuel Cell
EQCM	Electrochemical Quartz Crystal Microbalance
FWHM	Full Width at Half Maximum
GDL	Gas Diffusion Layer
GF	Graphite Felt
H-UPD	Hydrogen Under Potential Deposition
IBFC	Indirect Borohydride Fuel Cell
MEA	Membrane Electrode Assembly
ML	Monolayer
NMR	Nuclear Magnetic Resonance
OCV	Open Circuit Voltage
PEM	Polymer Electrolyte Membrane
PEMFC	Polymer Electrolyte Membrane Fuel Cell
PTFE	Polytetrafluoroethylene (Teflon <sup>®</sup> )
RDE	Rotating Disk Electrode
RH	Relative Humidity
RPM	Rotations Per Minute
SEM	Scanning Electron Microscope
SHE	Standard Hydrogen Electrode
STP	Standard Temperature and Pressure

---

## List of Abbreviations (Continued)

Symbol	Definition
SLPM	Standard Litres Per Minute
TEM	Transmission Electron Microscope
TU	Thiourea
XPS	X-Ray Photoelectron Spectroscopy
XRD	X-Ray Diffraction

**NOTE TO READER:** All electrode potentials in this dissertation are presented versus the standard hydrogen electrode reference potential.

## Acknowledgements

*My mother Josephine, for her encouragement and ever lasting support*

*My sisters Pearl and Persis, for always being there for me*

*Sarah, for believing that I could be better than I was, and better than I am*

*Elöd, for his trust, his patience, and his guidance*

*Dhanesh, for her wisdom and her kindness*

*Akram, for his generosity and support*

*My colleagues and friends for their friendship, our conversations, and our laughter*

*The members of my committee for their critical thoughts*

*For being a part of my life, you have made me a better person, and for that, I am forever grateful.*

*To my family*

# 1 Introduction

Direct borohydride fuel cells (DBFC) are among the newest fuel cell types, having being first proposed in the early 1960s by Indig and Snyder [1] and Jasinski [2]. The potential of DBFC's arises from its high theoretical gravimetric energy density (9.3 Wh  $\text{g}_{\text{NaBH}_4}^{-1}$  versus 6.1 Wh  $\text{g}_{\text{CH}_3\text{OH}}^{-1}$ ), competitive volumetric energy density, and high theoretical energy efficiency (0.91 versus 0.83 for a PEMFC at 298 K) [3]; see equations (1) and (2).

$$\rho' = \frac{|\Delta G^o|}{MW_{\text{NaBH}_4}} = \frac{|-nFE_{e,cell}|}{MW_{\text{NaBH}_4}} \quad n = 8 \text{ for equation (5)} \quad (1)$$

$$\eta' = \frac{\Delta G^o}{\Delta H_c^o} = \frac{-nFE_{e,cell}}{\Delta H_c^o} \quad (2)$$

The desirability for liquid fuels for fuel cells is a result of complications related to hydrogen storage and distribution. Hydrogen has a low volumetric energy density at atmospheric pressure and conventional means of increasing its energy density through liquefaction or compression are either costly or simply impractical for small scale portable electronic applications. Sodium borohydride ( $\text{NaBH}_4$ ) may be fed to the fuel cell as a liquid solution at room temperature, thus having a clear advantage over compressed hydrogen fuel for PEMFC in terms of volumetric energy density (i.e. 1.86 kWh  $\text{L}^{-1}$  for a 20 wt%  $\text{NaBH}_4$  solution, and 0.54 kWh  $\text{L}_{\text{H}_2}^{-1}$  for  $\text{H}_2$  gas compressed at 200 atm and 298 K).

Current developments in DBFC performance are comparable to those of direct methanol fuel cells (DMFC), although DBFC are theoretically and practically superior in

many ways [3,4]. Firstly, the absence of carbon in the fuel should hypothetically simplify a great deal the anode kinetics of the DBFC, since  $\text{CO}_{\text{ad}}$  poisoning of Pt based catalysts is not an issue. As a fuel,  $\text{CH}_3\text{OH}$  is toxic, combustible, and produces  $\text{CO}_2$  as a by-product. Perhaps the most pertinent setbacks for DMFC's are i) anode catalyst poisoning by the inevitably formed  $\text{CO}_{\text{ad}}$ , and ii)  $\text{CH}_3\text{OH}$  crossover to the cathode ( $7.5 \times 10^{-4} \text{ mol}_{\text{CH}_3\text{OH}} \text{ m}^{-2} \text{ s}^{-1}$  for 1 M  $\text{CH}_3\text{OH}$  using Nafion<sup>®</sup> 115 at 333 K [5]). In general, organic fuels suffer from low electro-oxidation catalytic activity [6]. Commercialization of direct organic PEM fuel cells are presently hampered by a prohibitively high ratio of total Pt load per peak power, e.g., typically above  $30 \text{ g}_{\text{Pt}} \text{ kW}^{-1}$  at 333 K for direct methanol, ethanol and formic acid fuel cells [7].

A comparative 20 W fuel cell study on DBFC and DMFC by Wee, demonstrated that DBFC is superior to DMFC in terms of cell size per power output and fuel consumption [8]. However due to the high cost of  $\text{NaBH}_4$  ( $\$2081 \text{ kmol}_{\text{NaBH}_4}^{-1}$  versus  $\$333 \text{ kmol}_{\text{MeOH}}^{-1}$ ), DBFC's become uneconomical for applications that require long operation times (Figure 1). From Figure 1, it is observed that the  $8e^-$  DBFC system is more economical than the DMFC system at operation times less than 280 hours when considering the costs associated with the loss of fuel utilization efficiency to fuel crossover. Therefore, as long as the  $\text{BH}_4^-$  fuel price remains high, DBFC systems are limited to applications that run for less than 280 hours.

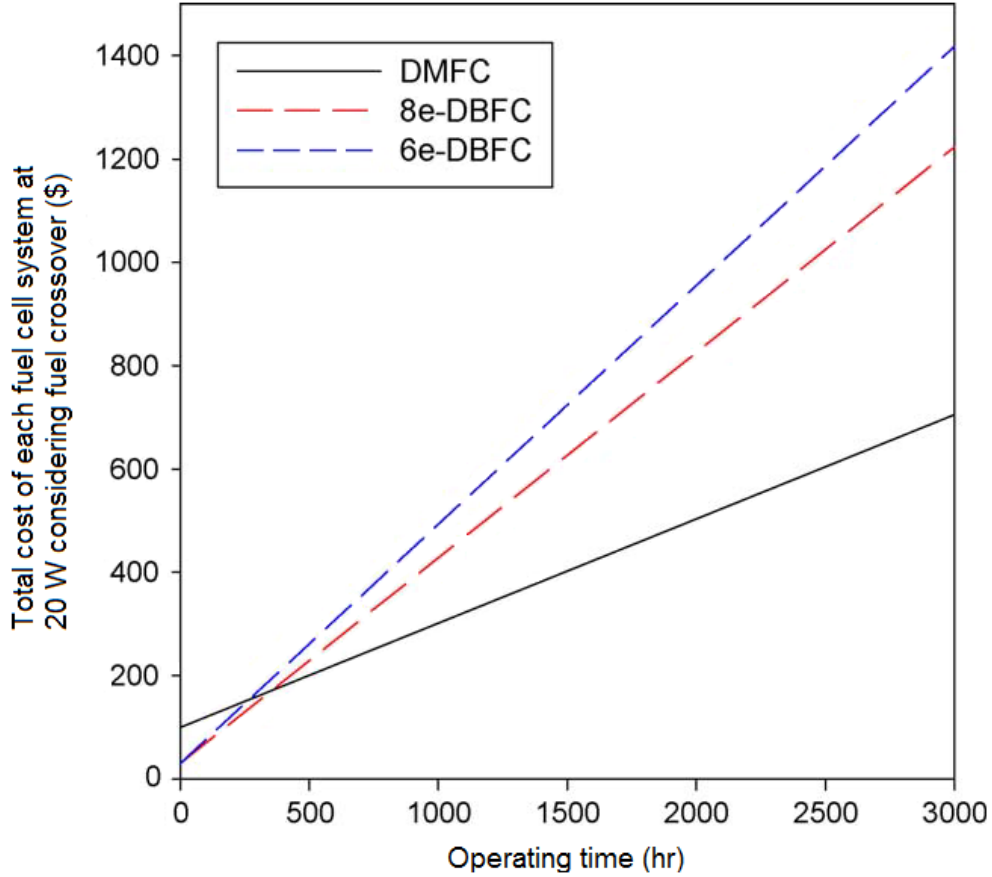
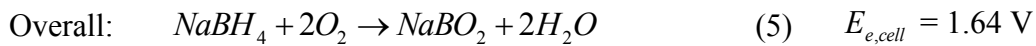


Figure 1. Total cost of DBFC and DMFC system at 20 W power output. Modified with permission from [8], Copyright 2006, Elsevier.

The principal direct  $\text{BH}_4^-$  redox reactions are as follows:



Depending on the catalyst composition and operating conditions, the reaction mechanisms may vary. For instance, on Pt catalysts, the direct oxidation of  $\text{NaBH}_4$  must

compete with the hydrolysis reaction (6), however on Au catalysts the hydrolysis reaction is less significant [9].



The hydrolysis reaction does pose some problems for the DBFC system if the anode design does not account for its occurrence; as will be explained in later chapters. In reality the  $BH_4^-$  electro-oxidation reaction mechanism is complex, often involving the formation of many different reaction intermediates between the extremes of reaction (3) and reaction (6) as represented by Figure 2. There is also interest however, in optimizing the hydrolysis reaction for the application of indirect  $BH_4^-$  fuel cells (IBFC) where the hydrogen released by reaction (6) is fed to a PEMFC. Further discussion regarding IBFC's can be found in section 1.1.4.

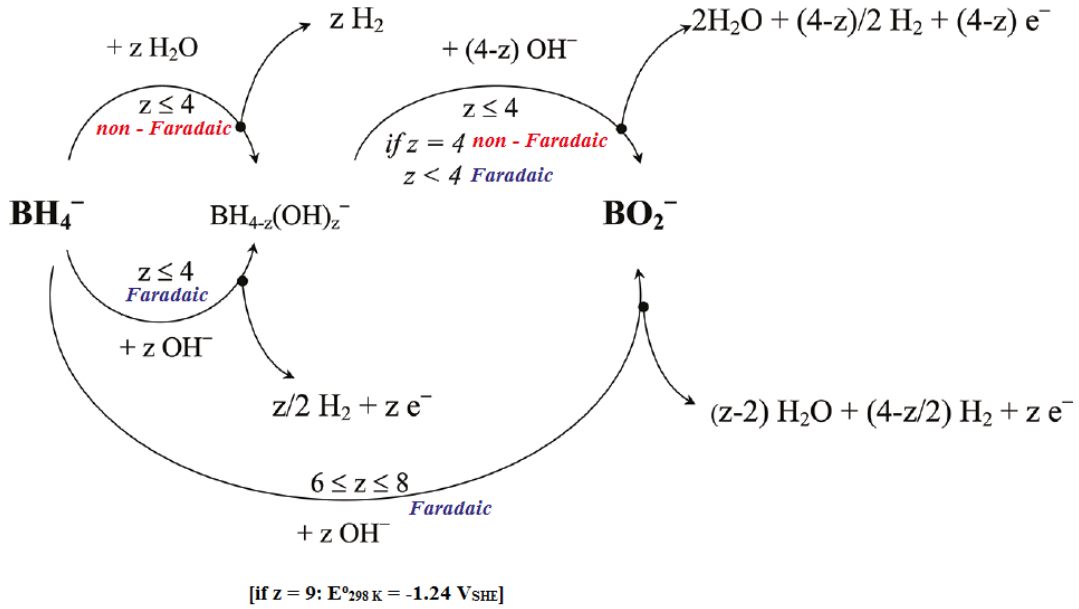


Figure 2. Schematic of the  $\text{BH}_4^-$  electro-oxidation reaction mechanisms including both Faradaic and non-Faradaic thermocatalytic pathways. Modified with permission from [10], Copyright 2011, American Chemical Society.

With respect to the direct electro-oxidation of  $\text{BH}_4^-$  in a PEMFC, there are three principal models according to the employed electrolyte. The electrolyte will determine the charge carrier and direction of ion conductance through the electrolyte (Figure 3). Investigations by Liu et al. comparing the performance effect of anion versus cation ionomers in DBFC's do not rule out the use of either membrane [11], however there are some distinct disadvantages associated with each type of membrane. It would appear from the literature [11--13] that anion exchange membranes exhibit poor chemical resistance and mechanical stability in strong alkaline environments in comparison to cation exchange membranes; Nafion<sup>®</sup> in particular. In addition, by nature, anion exchange membranes are more susceptible to  $\text{BH}_4^-$  migration to the cathode compartment, also known as crossover, although there are no reported values for  $\text{BH}_4^-$  crossover in commercial anion exchange membranes. Cation exchange membranes may

impede  $\text{BH}_4^-$  crossover, however there does not appear to be a commercially available cation exchange membrane that is impervious to  $\text{BH}_4^-$  crossover. Lakeman et al. [14] measured the  $\text{BH}_4^-$  flux across a Nafion<sup>®</sup> 117 membrane to be  $4.01 \times 10^{-3} \text{ mol}_{\text{NaBH}_4} \text{ m}^{-2} \text{ s}^{-1}$  at an assumed temperature of 298 K (not specified) and using an anolyte composed of 30 wt%  $\text{NaBH}_4$  and 6 M  $\text{NaOH}$ . Further discussion regarding  $\text{BH}_4^-$  crossover can be found in section 1.2.3. Another weakness of cation exchange membranes is the chemical imbalance of the DBFC system. Cation exchange membranes impede the transport of hydroxide ions produced at the cathode to the anode compartment, therefore the hydroxide concentration in the anolyte would continually decrease over time, according to equation (3), which could decrease the  $\text{BH}_4^-$  stability. Furthermore, the excess of hydroxide in the cathode compartment can lead to the formation of carbonates should the system be exposed to  $\text{CO}_{2(\text{g})}$ , and the hydroxides may even crystallize in the pores of the cathode gas diffusion layer (GDL) and catalyst layer (CL) thus creating mass transport issues.

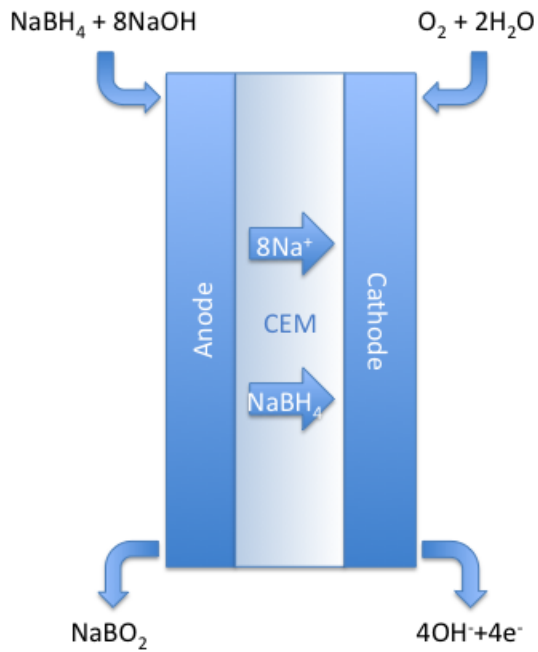
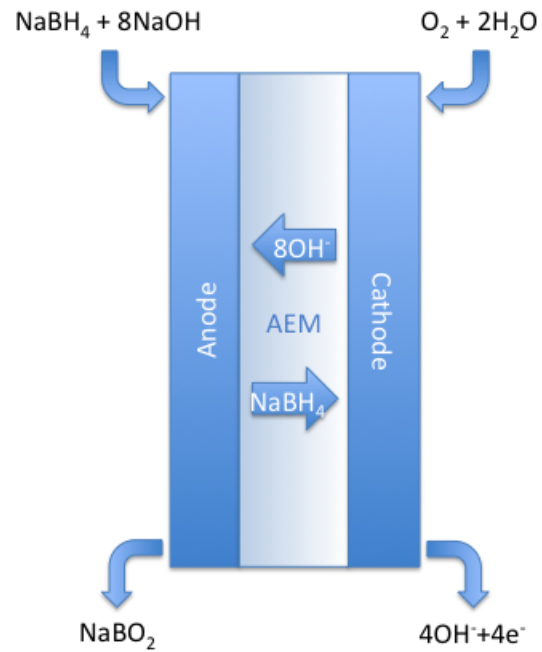
**A)****B)**

Figure 3. DBFC A) cation exchange membrane (CEM) electrode assembly and B) anion exchange membrane (AEM) electrode assembly.

Some of the most costly components for all fuel cell types in general are catalysts and ionomer materials. Similar to  $\text{H}_2$  PEMFC, Pt catalysts, and Nafion<sup>®</sup> membranes have proven to be excellent materials for DBFC, however they are neither the only nor necessarily the best choices available. Many non-Pt anodic catalyst materials such as gold (Au) and its alloys, nickel (Ni) and its alloys, osmium (Os), platinum-ruthenium (Pt-Ru), and binary or alloyed iridium (Ir) catalysts have been investigated for DBFC [9,15--21]. Non-platinum cathodic catalysts have also been investigated such as  $\text{MnO}_2$  [22],  $\text{LaNiO}_3$  [23],  $\text{La}_{1-x}\text{Sr}_x\text{CoO}_3$  [24],  $\text{LaCoO}_3$  [25],  $\text{Eu}_2\text{O}_3$  [26], and  $\text{CoPc}$  [27].

## 1.1 Physicochemical Properties of Borohydride

Borohydride compounds have been developed for a multitude of applications including: uranium  $\text{BH}_4^-$  as a potential alternative for uranium enrichment compounds,  $\text{H}_2$  signal balloons, and rocket fuel [28]. In the late 1940's it was realized that  $\text{BH}_4^-$  was an effective reductant of specific organic compounds such as the carbonyl group of aldehydes, ketones, and acid chlorides; thereafter  $\text{BH}_4^-$  has been an important reagent for chemical synthesis in organic chemistry [29]. In the 1960's the concept of a DBFC was introduced [1,2], but their development was practically abandoned until the last decade or so. The primary market for the use of  $\text{BH}_4^-$  compounds is still in the synthesis of organic compounds, and the "in-house" synthesis of sodium hydrosulfite for the paper and textile industries [28,30].

### 1.1.2 Borohydride Synthesis

There are a number of methods in which  $\text{BH}_4^-$  may be synthesized through chemical synthesis [31--41]. The basis of these methods is the hydrogenation of boron-oxides, commercially known as borax, and the addition of an alkali metal. The most widely used process for the manufacture of  $\text{NaBH}_4$  since the 1950's is the Schlesinger process [42]. The overall reaction for  $\text{NaBH}_4$  synthesis from this process is shown by reaction (7).



Figure 4 shows a schematic of the Schlesinger process, summarizing the process in 7 basic steps [42]:

- Step 1: Hydrogen production through steam reforming of methane
- Step 2: Sodium production through sodium chloride electrolysis
- Step 3: Conversion of boron oxides into boric acid
- Step 4: Production of trimethylborate from boric acid and methanol
- Step 5: Production of sodium hydride from sodium and hydrogen
- Step 6: Production of sodium borohydride from sodium hydride
- Step 7: Recycling of by-products to reproduce methanol

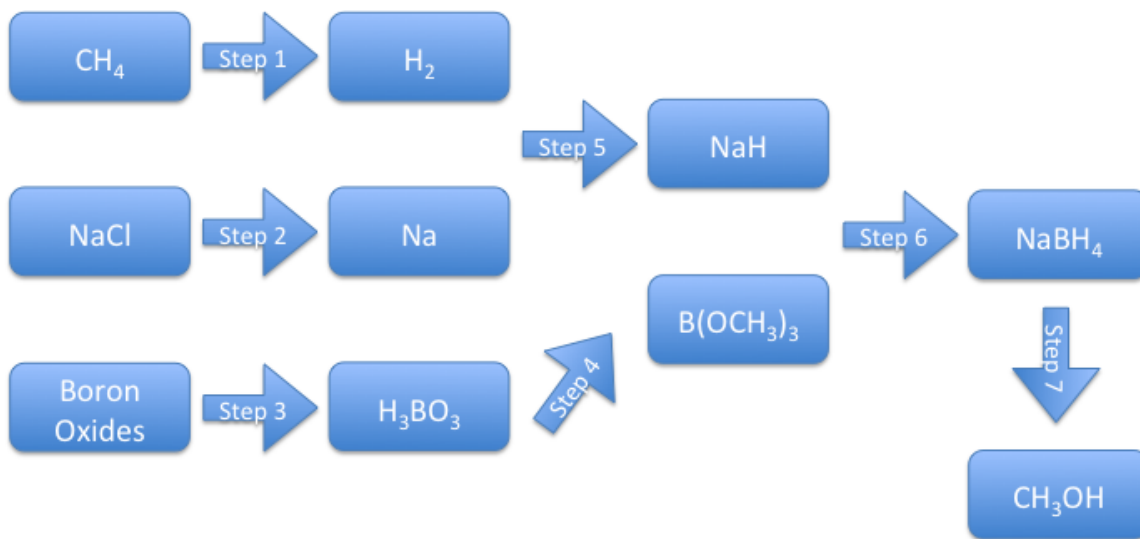
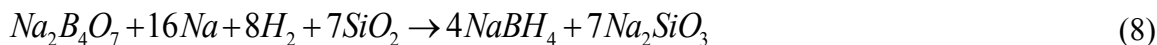


Figure 4. Schematic of the Brown and Schlesinger process. Modified with permission from [43], Copyright 2004, U.S. Department of Energy.

In addition to the Brown and Schlesinger process, another commercial process for NaBH<sub>4</sub> production is the Bayer process, which has been used by the Bayer corporation

itself [31,32,43]. In the Bayer process, NaBH<sub>4</sub> is synthesized via a batch process at 1073 K where the overall reaction is shown below:



Borohydride manufacturing is an energy intensive process, and the key to its cost reduction lies in process efficiency improvement or reduction in power consumption via new methods. Reduction in cost may also be obtained through mass production and improved recycling processes of the sodium borate product. In 2006 the price of NaBH<sub>4</sub> was \$55 kg<sub>NaBH<sub>4</sub></sub><sup>-1</sup>[28], recently the price of NaBH<sub>4</sub> has been reduced to \$20 - \$30 kg<sub>NaBH<sub>4</sub></sub><sup>-1</sup> [44].

### 1.1.3 Borohydride Stability

Alkali BH<sub>4</sub><sup>-</sup> compounds are soluble in water; however, in aqueous solutions, a basic environment is required to mitigate significant degradation through hydrolysis according to reaction (6). Brown and Svensson conducted a comprehensive study on the stability of KBH<sub>4</sub> in Ca(OH)<sub>2</sub> solution [29]. Borohydride content was measured over time at a constant pH of 12.45 and a constant temperature of 298 K. A relationship between BH<sub>4</sub><sup>-</sup> degradation and time was devised (equations (9) to (11)). Fitting their experimental data to equation (11), this relationship is represented in equation (12), where the rate constant  $k^o$  was calculated to be equal to 1.45 x 10<sup>-3</sup> hr<sup>-1</sup>. Over several trial runs, the average rate constant was 1.41 x 10<sup>-3</sup> hr<sup>-1</sup>. It should be noted that equation (12) is written in terms of mass of KBH<sub>4</sub> used in Brown and Svensson's experiments.

Brown and Svensson also found that the logarithm of the degradation rate constant is linearly dependent on pH. Equation (13) shows this relationship from a pH of 12 to a pH of 14. At lower pH values (pH = 7 to 10), the slope of this linear dependency decreases [29]. Comparing their data to the work of Jensen [45], Brown and Svensson also found that the  $\text{BH}_4^-$  decomposition in hydroxide solutions, at a certain pH, is non-specific to alkali metal ions such as  $\text{Na}^+$  and  $\text{K}^+$ . This was more recently confirmed by Minika et al. [46].

$$\frac{-d(m_{\text{BH}_4^-})}{dt} = k' m_{\text{BH}_4^-} \quad (9)$$

$$\ln(m_{\text{BH}_4^-}) = \ln(m_{\text{BH}_4^-}^o) - k' t \quad (10)$$

$$\log(m_{\text{BH}_4^-}) = \log(m_{\text{BH}_4^-}^o) - \frac{k'}{2.303} t \quad (11)$$

$$\log(m_{\text{KBH}_4}) = 2.7 - 6.3 \times 10^{-4} t \quad \begin{array}{l} \text{mg KBH}_4 \text{ in 100 mL Ca(OH)}_2 \text{ solution} \\ \text{pH} = 12.45, k' = 1.45 \times 10^{-3} \text{ hr}^{-1} \end{array} \quad (12)$$

$$-\log(k') = -2.3 + 0.4 \text{ pH} \quad \text{T} = 298 \text{ K}, 12 < \text{pH} < 14 \quad (13)$$

A longevity test conducted by Brown and Svensson found that in a span of 451 hours and 30 minutes, approximately 53% of the total  $\text{BH}_4^-$  content from a fresh  $\text{KBH}_4$  and  $\text{Ca(OH)}_2$  solution at 298 K and a pH of 12.45 decomposed [29]. Colominas et al. also found a significant degradation of  $\text{NaBH}_4$  in a  $\text{NaOH}$  solution adjusted to a pH of 12

[47]. Through equation (14), the half life of  $\text{BH}_4^-$  was calculated to be 4.3 days at a pH of 12 and 426.2 days at a pH of 14 [48,49].

$$\text{Log}(t_{1/2}) = \text{pH} - (0.034T - 1.92) \quad (14)$$

Where  $t_{1/2}$  is the  $\text{BH}_4^-$  half-life in minutes, and T is the temperature in K.

More recent studies indicate that the stability of  $\text{NaBH}_4$  is greater than initially thought. Using a hermetically sealed reactor, Minkina et al. [46] measured the liberated  $\text{H}_{2(\text{g})}$  from a  $\text{NaBH}_4 - \text{NaOH}$  solution, through measurement of the volume of  $\text{H}_{2(\text{g})}$  or the change in reactor pressure. Their procedure involved two vital assumptions. The most important assumption being that the formation of intermediate  $\text{BH}_4^-$  hydrolysis compounds is negligible. Non-negligible amounts of intermediate compounds would result in faulty  $\text{NaBH}_4$  assay calculations. Lastly, that the hydrogen did not appreciably absorb into the stainless steel reactor walls. The importance of these assumptions is emphasized by the fact that the experiments were conducted over an extended period of time. Figure 5 shows the calculated results of their investigation, where  $\xi$  is the percentage of  $\text{BH}_4^-$  degradation by mass. Less than 1 wt% of the  $\text{NaBH}_4$  degraded over a period of 50 days when using a NaOH concentration of 10 wt% at 295 K.

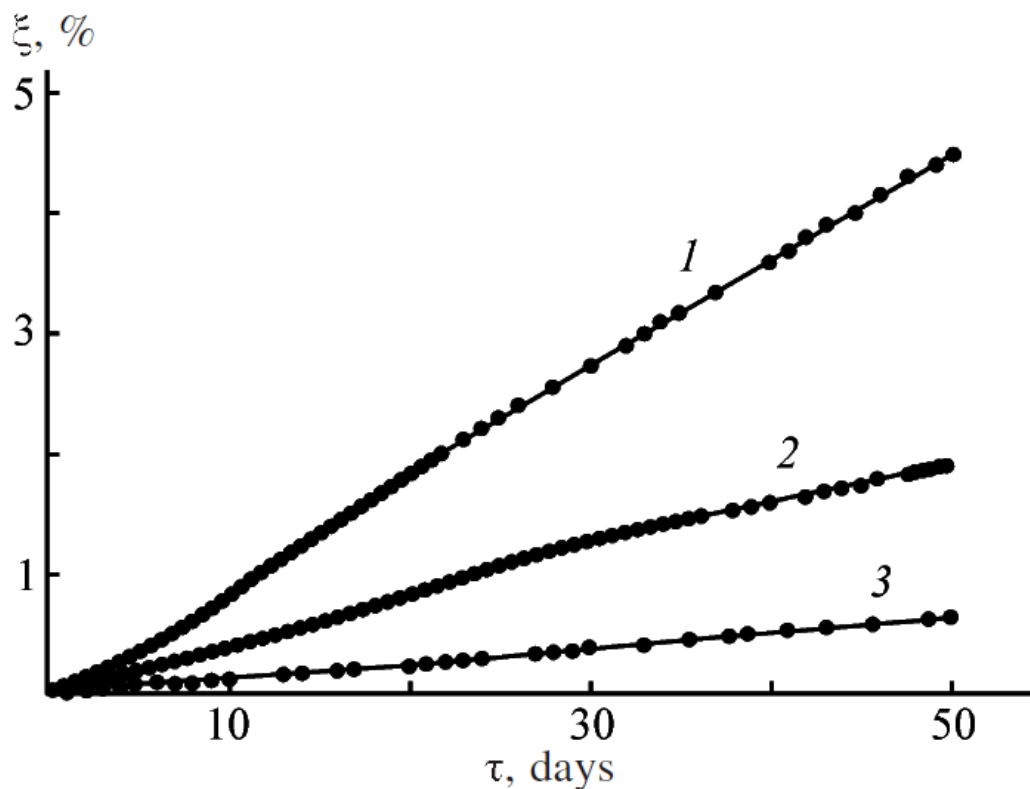


Figure 5. NaBH<sub>4</sub> decomposition. T: 295 K, NaBH<sub>4</sub>:H<sub>2</sub>O molar ratio: 1:5, NaOH: (1) 3 wt%, (2) 5 wt%, (3) 10 wt%. Reprinted with permission from [46], Copyright 2008, Springer.

The stability of the NaBH<sub>4</sub> decreased appreciably at high temperatures or when the NaOH concentration was low. At 323 K, using a 6.9 wt% NaBH<sub>4</sub> – 90.1 wt% H<sub>2</sub>O – 3 wt% NaOH solution, nearly 100 wt% of the NaBH<sub>4</sub> hydrolyzed after 50 hours. Clearly, NaBH<sub>4</sub> alkaline solutions cannot be stored at high temperatures. Using a NaBH<sub>4</sub> – 5H<sub>2</sub>O molar ratio and 10 wt% NaOH composition, approximately 50 wt% of the NaBH<sub>4</sub> decomposed after 350 days at 323 K. At 303 K using the same NaBH<sub>4</sub> – H<sub>2</sub>O composition with 5 wt% NaOH, approximately 30 % of the NaBH<sub>4</sub> hydrolyzed after 350 days. High concentrations of NaOH are generally favoured for the stability of NaBH<sub>4</sub>, but it can also lead to environmental problems associated with its disposal or recycling of

spent  $\text{BH}_4^-$  fuel. Sodium hydroxide concentrations of 3 to 5 wt% was reported by Zhang et al. to be sufficient to achieve the desired fuel stability for their IBFC system [50].

Despite the requirement for a high  $\text{OH}^-$  to  $\text{BH}_4^-$  concentration ratio to stabilize aqueous  $\text{BH}_4^-$  solutions, there is some conflicting evidence that an increased amount of  $\text{BH}_4^-$  content may also lead to improved stability. Using a composition of 44 wt%  $\text{NaBH}_4$ , 55.8 wt%  $\text{H}_2\text{O}$ , and 0.2 wt%  $\text{NaOH}$ , Lumsden and Evans reported only 10%  $\text{NaBH}_4$  degradation after 272 days at 298 K [30].

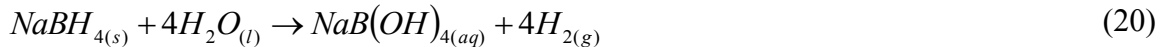
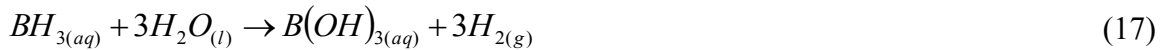
Furthermore, a presentation given by Air Liquide in 2005 shows findings that a  $\text{NaBH}_4$  concentration of  $\sim 31$  wt% was much more stable than a  $\text{NaBH}_4$  concentration of  $\sim 7$  wt% using a fixed concentration of 3 wt%  $\text{NaOH}$  at 323 K [51]. Studies by Minkina et al. [46] on  $\text{NaBH}_4$  – alkaline suspensions with low water content, do show an increased stability of  $\text{NaBH}_4$ , however, a viscous suspension of  $\text{NaBH}_4$  may also lead to practical issues for DBFC operation depending on the system design [46]. The increased stability of  $\text{NaBH}_4$  with increased  $\text{NaBH}_4$  concentration may be due to the alkalinity of  $\text{NaBH}_4$  itself. As the concentration of  $\text{NaBH}_4$  increases, the pH of the solution also increases as shown by Rohm and Haas, where they found that 0.01 M  $\text{NaBH}_4$  resulted in a solution pH of  $9.56 \pm 0.02$  and 1 M  $\text{NaBH}_4$  resulted in a solution pH of  $10.48 \pm 0.02$  [48,49,52].

#### **1.1.4 Borohydride Hydrolysis**

Until a method has been devised to effectively utilize the hydrogen generated in-situ by  $\text{BH}_4^-$  hydrolysis, for the most part,  $\text{BH}_4^-$  hydrolysis is undesired during the operation of a DBFC system. There have been interests in using  $\text{NaBH}_4$  as a hydrogen storage media, where  $\text{NaBH}_4$  is hydrolyzed according to reaction (6) to supply hydrogen

to a H<sub>2</sub> PEMFC. These systems are also known as IBFC. In the case of IBFC, promotion of the hydrolysis reaction is desired during operation of the H<sub>2</sub> PEMFC.

Gonçalves et al. [53,54] proposed a model for the hydrolysis reaction mechanism (reactions (15) to (20)) and confirmed the accuracy of their model with experimental results. Reaction (15) is the initial dissociation of NaBH<sub>4</sub>, reactions (16) and (17) are responsible for the production of hydrogen, and reaction (19) results in the increase in solution pH during hydrolysis. The combination of reactions (14) to (17) results in a new overall hydrolysis reaction (20) as opposed to reaction (6).<sup>11</sup>B-NMR studies [55] confirm the formation of NaB(OH)<sub>4</sub> as a stable product. The hydrolysis activation energy was calculated to be approximately 100 ± 35 kJ mol<sup>-1</sup>[56--62]. A more recent investigation [55] confirmed the activation energy to be 98 ± 10 kJ mol<sup>-1</sup> over a temperature range of 303 K to 353 K and a NaBH<sub>4</sub> concentration range of 0.63 to 6.19 mol L<sup>-1</sup>.



In alkaline media, reaction (16) becomes the rate limiting due to the decrease of H<sup>+</sup> concentration in solution, thus explaining the NaBH<sub>4</sub> stabilizing effect of basic solutions. Andrieux et al. measured the solution pH over time during NaBH<sub>4</sub> hydrolysis

and compared their data against calculated pH values based on reaction (19). A close fit was found between their theoretical and actual data for NaBH<sub>4</sub> conversions above 22%. At the initial stages of NaBH<sub>4</sub> hydrolysis (NaBH<sub>4</sub> to H<sub>2</sub> conversions lower than 22%), the formed B(OH)<sub>4</sub><sup>-</sup> did not appear to have a significant contribution to the change in solution pH.

The hydrolysis reaction can be accelerated using several methods including: heterogeneous catalysis, increasing the temperature of the solution, and acidification of a BH<sub>4</sub><sup>-</sup> solution. Hydrolysis through catalysis and acidification of the solution have been pursued in particular for IBFC. One practical way of implementing these methods is by pelletizing BH<sub>4</sub><sup>-</sup> with either a solid acid, or with a catalyst precursor. The earliest work in this area was that of Schlesinger et al. [52], where they tested the effectiveness of many different compositions of pelletized NaBH<sub>4</sub> for hydrogen generation (Table 1).

Table 1. Hydrogen liberated from NaBH<sub>4</sub> pellets containing a solid homogeneous hydrolysis catalyst. Starting conditions: T: 298 K, and pH: 7. Modified with permission from [52], Copyright 1953, American Chemical Society.

Hydrolysis accelerant	Concentration of hydrolysis catalyst in NaBH <sub>4</sub> pellet (wt%)	Hydrogen liberated after 10 minutes (wt% of total hydrogen content)
Calcium Chloride	50	0
Sodium Borofluoride	50	15
Phthalic Acid	43	54
Salicylic Acid	50	54
Alum	50	64
Benzoic Acid	50	64
Phthalic Anhydride	42.9	65
Sulfamic Acid	37.5	69
Ammonium Alum	50	74
Ammonium Chloride	50	75
Maleic Anhydride	50	76
Sodium Acid Sulfate	50	78
Sodium Diacid Phosphate	50	80
Aluminum Sulfate	50	82
Maleic Acid	50	85
Ammonium Carbonate	50	90
Oxalic Acid	37.5	95
Oxalic Acid	42.9	Violent Reaction
Oxalic Acid	50	Violent Reaction
Succinic Acid	37.5	95
Succinic Acid	42.9	99
Succinic Acid	50	Very Fast
Malonic Acid	37.5	94
Citric Acid	37.5	85
Citric Acid	42.9	90
Citric Acid	50	100
Tartaric Acid	37.5	83
Tartaric Acid	50	100
Malic Acid	42.9	95
Boric Oxide	42.9	89
Boric Oxide	50	97.5
Mucic Acid	50	95
Iron (II) Chloride	5	53
Cobalt (II) Chloride	5	97
Nickel (II) Chloride	5	74
Copper (II) Chloride	5	43

Among the acid accelerants tested, oxalic acid appeared to produce the greatest reaction rate, however the reaction was described as being violent. In addition, preparation of the oxalic acid –  $\text{BH}_4^-$  pellets was dangerous as the risk of catching fire was high. Boric oxide was assessed to be the best candidate, with a good pellet temperature and moisture stability, and minimal solution foaming during reaction. The disadvantage of the boric oxide is the non-linear hydrogen generation due to increasing solution pH attributed to  $\text{BO}_2^-$  formation, the large amount of boric oxide required to facilitate an appreciable hydrolysis rate, and finally the precipitation of sodium tetraborate, which must be eventually removed from the reactor.

Of the catalyst precursors tested, Schlesinger et al. [52] found that cobalt salts (specifically  $\text{CoCl}_2$ ) generated the greatest hydrolysis rate. While the pellet dissolved in solution,  $\text{Co}_2\text{B}$  was formed which further catalyzed the hydrolysis reaction. In comparison to the boric oxide, only 5 wt%  $\text{CoCl}_2$  in the pellet composition was required to hydrolyze the  $\text{BH}_4^-$  at a comparable rate to 50 wt% boric oxide. Furthermore the hydrolysis rate was virtually constant when using the cobalt salt and was independent of the increasing pH of the solution. The disadvantages of the  $\text{CoCl}_2$  include foaming of the product solution, and high pH of the product solution.

The pelletized delivery of  $\text{NaBH}_4$  fuel can be categorized as solid  $\text{NaBH}_4$  fuel delivery. The advantage of this system is that it has the potential of having very high gravimetric hydrogen storage capacities [63]. The disadvantages of this method are the additional fuel costs added due to the necessity of homogeneous hydrolysis catalysts (acids and catalyst precursors), the difficulty in controlling hydrogen production rates on

demand, and the difficulty in controlling the heat generated from the exothermic hydrolysis reaction.

An alternative to the solid fuel delivery method are aqueous NaBH<sub>4</sub> solutions, in which NaBH<sub>4</sub> is dissolved in an alkaline solution and hydrolysis of the NaBH<sub>4</sub> is facilitated by contact of the fuel with a heterogeneous catalyst. There have been many different types of non-noble and noble metal catalysts investigated for NaBH<sub>4</sub> hydrolysis for hydrogen generation [63]. Of the non-noble metal catalysts, Co-B nano-particles appeared to be the most effective with an activity of 26 L<sub>H2</sub> min<sup>-1</sup> g<sub>cat</sub><sup>-1</sup> at 303 K [64]. Of the noble metal catalysts Ru nanoclusters demonstrated one of the greatest catalytic activities producing 96.8 L<sub>H2</sub> min<sup>-1</sup> g<sub>cat</sub><sup>-1</sup> at 298 K [65].

The greatest advantage of the heterogeneous catalysis method is the ability to control the hydrolysis rate by controlling the amount of contact between the catalyst and the NaBH<sub>4</sub> solution. Another advantage is the ability for the NaBH<sub>4</sub> solution to act as a thermal buffer for heat released by the exothermic hydrolysis reaction. The greatest hurdle of this method however, is the solubility of NaBH<sub>4</sub> and NaBO<sub>2</sub> in aqueous solutions and subsequently the current inability to meet the U.S. Department of Energy (DOE) targets for gravimetric hydrogen storage capacities [63,66].

At this point, it is unclear if it is advantageous to use NaBH<sub>4</sub> in a IBFC system or a DBFC system. Wee [28] made a direct comparison of the two in terms of system production costs, fuel costs, and costs associated with fuel crossover, per power generated from the fuel cell system (\$ W<sup>-1</sup>). The IBFC is more economical than DBFC when taking into account the Faradaic efficiency (equation (21)) and the fuel utilization efficiency (equation (22)) of the respective systems. However, they also demonstrated

that in the scenario where a DBFC is operated with no fuel crossover and at high faradaic efficiencies (6 to 8 electron oxidation of NaBH<sub>4</sub>), the DBFC was more economical.

$$\eta_Q = \frac{n_{actual}}{n_{theoretical}} \quad (21)$$

$$\eta_f = \frac{iA}{n_{theoretical} F Q_V C_{NaBH_4}} \quad (22)$$

## 1.2 Direct Borohydride Fuel Cell Performance

Due to the physicochemical properties of NaBH<sub>4</sub>, the conditions in which one operates the DBFC, the catalyst material and its structure, and the anode design can greatly affect its performance. In this section, the effect of the DBFC system operating conditions on its performance will be discussed.

### 1.2.1 Effect of Temperature on BH<sub>4</sub><sup>-</sup> Electro-Oxidation

On a carbon supported gold anode (Au/ C), it was found that an increase of temperature resulted in lower open circuit voltages (OCV) but higher peak power densities and higher limiting currents (Figure 6) [6].

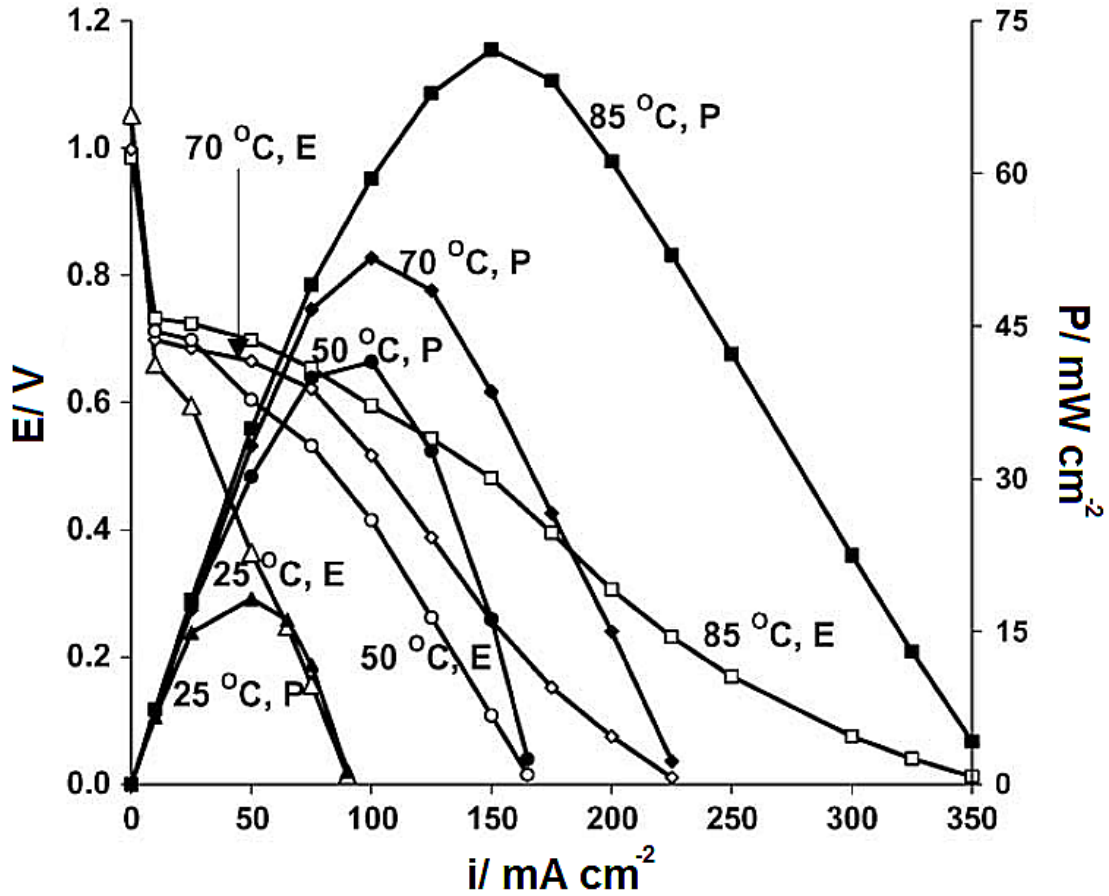


Figure 6. Temperature dependence of polarization and power curves. Anode: Au/ C; 2 mg cm<sup>-2</sup>; Area: 4 cm<sup>2</sup>. Anolyte: 5 wt% NaBH<sub>4</sub> – 10 wt% NaOH. O<sub>2</sub>: 0.2 SLPM; 1 atm (abs). Cathode: 2 mg cm<sup>-2</sup>; Pt/ C. Separator: Nafion<sup>®</sup> 117. Flow field: parallel flow pattern. Figure notes: Temperature is in °C. E = Polarization Curve, P = Power Curve. Reprinted with permission from [6], Copyright 2006, Elsevier.

A decrease in the open circuit voltage is expected in the DBFC system when considering the thermodynamic relationship between potential and temperature represented by equations (23) and (26).

$$E_{e,cell} = E_T^{\circ} - \frac{RT}{nF} \ln(Q') \quad (23)$$

$$E_T^o = \frac{-\Delta G}{nF} \quad (24)$$

$$\left( \frac{\delta E_T^o}{\delta T} \right)_a = \frac{\Delta S^o}{nF} \quad (25)$$

Using the boundary conditions:  $E_T^o = E_{298K}^o$  at  $T = 298$  K:

$$E_T^o = E_{298K}^o + \Delta S_{298K}^o \frac{(T - 298)}{nF} \quad T < 373 \text{ K} \quad (26)$$

where  $E_{e,cell}$  is the equilibrium cell potential,  $E_T^o$  is the standard potential at the temperature  $T$  where  $T > 298$  K,  $n$  is the electron number,  $F$  is Faraday's constant,  $Q'$  is the reaction quotient,  $\Delta G$  is the free energy of the system, and  $\Delta S_{298K}^o = -418.1 \text{ J mol}^{-1}$

$\text{K}^{-1}$  is the entropy of the reaction. The calculated value for  $\left( \frac{\delta E_T^o}{\delta T} \right)_a$  is  $-5.42 \times 10^{-4} \text{ V K}^{-1}$ .

Atwan et al. tested the effect of temperature on a variety of Pt alloys and Au alloys from 298K to 333K and also found an increase in overall fuel cell performance [15,16,18]. Various groups have observed the same temperature dependence on other catalysts [4,20,67--69]. Verma and Basu found that the performance temperature dependence on a Pt/ C anode with a 2M  $\text{NaBH}_4$  and 3M KOH fuel solution was optimal below 358 K [67]. An increase of the operating temperature results in an increase of homogeneous and heterogeneous  $\text{BH}_4^-$  hydrolysis as well as an increase in fuel crossover [6]. The increased  $\text{BH}_4^-$  hydrolysis rate can decrease the OCV of the DBFC. Subsequently, the fuel cell would behave as a mix of a DBFC and a PEMFC which has a lower equilibrium potential ( $\sim 1.2$  V versus 1.64 V for a DBFC). An increased

temperature is also important for the air/ O<sub>2</sub> cathode, due to relatively slow oxygen reduction reaction rate.

The rate of BH<sub>4</sub><sup>-</sup> electro-oxidation kinetics can be explained as [70]:

$$r = \frac{i_a}{nF} = k_a C_{BH_4^-}^y \quad (27)$$

where r is the electrochemical reaction rate, k<sub>a</sub> is the heterogeneous rate constant, C<sub>BH<sub>4</sub><sup>-</sup></sub> is the BH<sub>4</sub><sup>-</sup> concentration, and y is the order of the reaction.

The dependence of the electron reaction rate on temperature can be found in the equation of the heterogeneous reaction rate constants[70]:

$$k_a = k_a^o \exp\left(\frac{\alpha_a F (E - E_{BH_4^- / BO_2^-}^o)}{RT}\right) \quad (28)$$

where k<sub>a</sub><sup>o</sup> is the standard heterogeneous rate constant, α<sub>a</sub> is the anodic transfer coefficient, F is Faraday's constant, E is the anode potential, R is the universal gas constant, and T is the temperature.

### 1.2.2 Anolyte Composition

As previously discussed, the DBFC performance is sensitive to the anolyte composition. Different compositions of BH<sub>4</sub><sup>-</sup> and supporting electrolyte (i.e. NaOH or KOH) can affect the anode equilibrium half-cell potential (equation (29)), the Faradaic efficiency (equation (21)), and the fuel utilization efficiency (equation (22)) of the system depending on the active material composition and operating conditions. Qualitatively

speaking, high  $\text{BH}_4^-$  concentrations correspond to improved mass transfer and reaction kinetics at the anode. However, high  $\text{BH}_4^-$  concentrations would also trigger high crossover rates to the cathode, and potentially high rates of  $\text{NaBH}_4$  hydrolysis; ultimately leading to low faradaic and fuel utilization efficiencies.

$$E_{e,\text{NaBH}_4} = E_{\text{NaBH}_4}^o - \frac{RT}{nF} \ln \frac{a_{\text{NaBH}_4} a_{\text{OH}^-}^8}{a_{\text{NaBO}_2}} \quad (29)$$

Following the general formula:  $A_{\gamma_+} B_{\gamma_-} \leftrightarrow \gamma_+ A^{z_+} + \gamma_- B^{z_-}$  and  $\gamma_+ + \gamma_- = \gamma$ , the total number of ions formed in dissociation. The activities are calculated as follows:

$$a_i = \left( f_{\pm,i}^{\gamma} \left( \frac{C_{\pm,i}}{C^o} \right)^{\gamma} \right) \quad \text{for NaBH}_4 \text{ and NaBO}_2 \quad (30)$$

and,

$$a_{\text{OH}^-} = \left( f_{\text{OH}^-} \frac{C_{\text{OH}^-}}{C^o} \right) \quad (31)$$

where  $a_i$  is the activity,  $C_i$  is the concentration in M,  $C^o$  is the concentration of an arbitrary reference state taken to be equal to 1 M,  $f_i$  is the activity coefficient, and  $f_{\pm,i}$  is the mean molar activity coefficient.  $f_i$  and  $f_{\pm,i}$  can be calculated by the Debye-Hückel equation and a modified version of the Debye-Hückel equation, respectively as follows:

$$\log(f_i) = \frac{-\alpha_{DH} z_i^2 \sqrt{J}}{1 + \beta_{DH} r_i' \sqrt{J}} \quad (32)$$

$$\log(f_{\pm,i}) = \frac{-\alpha_{DH} |z_+ z_-| \sqrt{J}}{1 + \sqrt{J}} + 0.1 |z_+ z_-| J \quad \text{For } C_i < 0.1 \text{ M} \quad (33)$$

where  $\alpha_{DH}$  and  $\beta_{DH}$  are parameters from the Debye-Hückel theory,  $z_i$  is the charge in dilute solution ( $C_i < 0.1 \text{ M}$ ),  $r_i$  is the hydrated radius of species  $i$ , and  $J$  is the molar ionic strength of the solution expressed as  $J = \frac{1}{2} \sum_i z_i^2 C_i$ .

Cheng and Scott's investigation into the effect of DBFC fuel composition using a Au/ C anode and a Pt/ C cathode is summarized in Table 2 [6]. Three observations can be made: firstly, the OCV decreased with increasing  $\text{BH}_4^-$  concentration due to  $\text{BH}_4^-$  crossover (discussed in more detail in section 1.2.3), secondly, both the peak power densities and current densities increased with increasing concentration, and lastly, an increase in supporting electrolyte concentration with a constant  $\text{BH}_4^-$  concentration had no appreciable effect on DBFC performance in their study.

Table 2. Effect of fuel composition on DBFC performance. Temperature = 358 K. Other conditions as in Figure 6. Reprinted with permission from [6], Copyright 2006, Elsevier.

NaBH <sub>4</sub> (wt%)	NaOH (wt%)	OCV (V)	P <sub>p</sub> * (mW cm <sup>-2</sup> )	i <sub>max</sub> ** (mA cm <sup>-2</sup> )
3	10	1.0	57	260
5	10	0.99	72	350
8	10	0.98	74	360
10	10	0.97	79	375
5	5	0.99	71	320
5	20	1.0	69	315

\*peak power density, \*\*sustained maximum current density

Liu et al. [71] found that the ratio of  $\text{OH}^-$  to  $\text{BH}_4^-$  can also affect the Faradaic efficiency of the DBFC system even when employing electro-oxidation catalysts that do not favour  $\text{NaBH}_4$  hydrolysis, such as Au and Ag. Using a  $[\text{OH}^-]/[\text{BH}_4^-]$  ratio of 1, three out of a possible eight electrons was observed, which is uncharacteristic of either electrocatalysts. It was suggested that the low faradaic efficiency was caused by a competition between  $\text{H}_2\text{O}$  and  $\text{OH}^-$  species. When the concentration of  $\text{OH}^-$  is low,  $\text{BH}_4^-$  may react with water forming  $\text{BH}_3\text{OH}^-$  and  $\text{H}_2$  (equation (34)).  $\text{BH}_3\text{OH}^-$  then proceeds to react via a 3 electron process (equation (45)). Higher ratios of anolyte compositions ( $[\text{OH}^-]/[\text{BH}_4^-] \geq 5$ ) can achieve a near 8 electron process on Au [71].



In a system employing a Pd/ C anode, and a Pt/ C cathode, Celik et al. confirmed that fuel utilization (equation (22)), decreased with increased  $\text{NaBH}_4$  concentrations, but higher peak power densities were achieved (Table 3) [72].

Table 3. Effect of  $\text{NaBH}_4$  concentration on peak power density and fuel utilization. Anode: 10 wt% Pd/ C,  $0.30 \text{ mg cm}^{-2}$ , cathode: 10 wt% Pt/ C,  $0.30 \text{ mg cm}^{-2}$ , membrane: Nafion<sup>®</sup> 117, Temperature: 298 K, humidified air (RH: 65%) flow rate: 0.15 SLPM,  $P_{\text{air}}$ : 1 atm (abs), fuel flow rate:  $2 \text{ ml min}^{-1}$ . Modified with permission from [72], Copyright 2010, Elsevier.

NaBH <sub>4</sub> Concentration (mol L <sup>-1</sup> )	Peak Power Density (mW cm <sup>-2</sup> )	Fuel Utilization Ratio (%)
0.5	7	30
1	10	22
1.5	12	20

High  $\text{BH}_4^-$  concentrations not only affect the reaction mechanism of  $\text{BH}_4^-$  electro-oxidation, but also cause some practical issues in a DBFC system. Jamard et al. [73]

tested a passive  $\text{BH}_4^-$  system at ambient conditions using two different anolyte compositions. They found that a DBFC system using an anolyte composition of 5 M  $\text{NaBH}_4$  – 1 M  $\text{NaOH}$  could only last half as long as a system employing 2 M  $\text{NaBH}_4$  – 1 M  $\text{NaOH}$  (250 hours of continuous operation versus 450 hours, respectively). The performance drop was proposed to be partially attributed to borate crossover to the cathode, impeding the mass transport of oxygen to the cathode catalysts. Carbonate formation was also a factor in the performance drop (Figure 7). Jamard et al. also found that an increased  $\text{BH}_4^-$  concentration led to a decrease in performance observed in their polarization curves. The negative effect of increased  $\text{BH}_4^-$  concentration on DBFC performance is contrary to the findings by Celik et al. [72]. It should be noted that a Morgane<sup>®</sup> ADP anion exchange membrane was used in their study versus a Nafion<sup>®</sup> 117 membrane in Celik et al.'s investigation. As discussed earlier, anion exchange membranes are more prone to  $\text{BH}_4^-$  crossover than cation exchange membranes. In addition, a Pt/ C anode was used by Jamard et al., which may lead to a greater hydrolysis rate than the Pd/ C anode used in the study by Celik et al. (a more detailed discussion on the characteristics of these catalysts can be found in section 1.3).

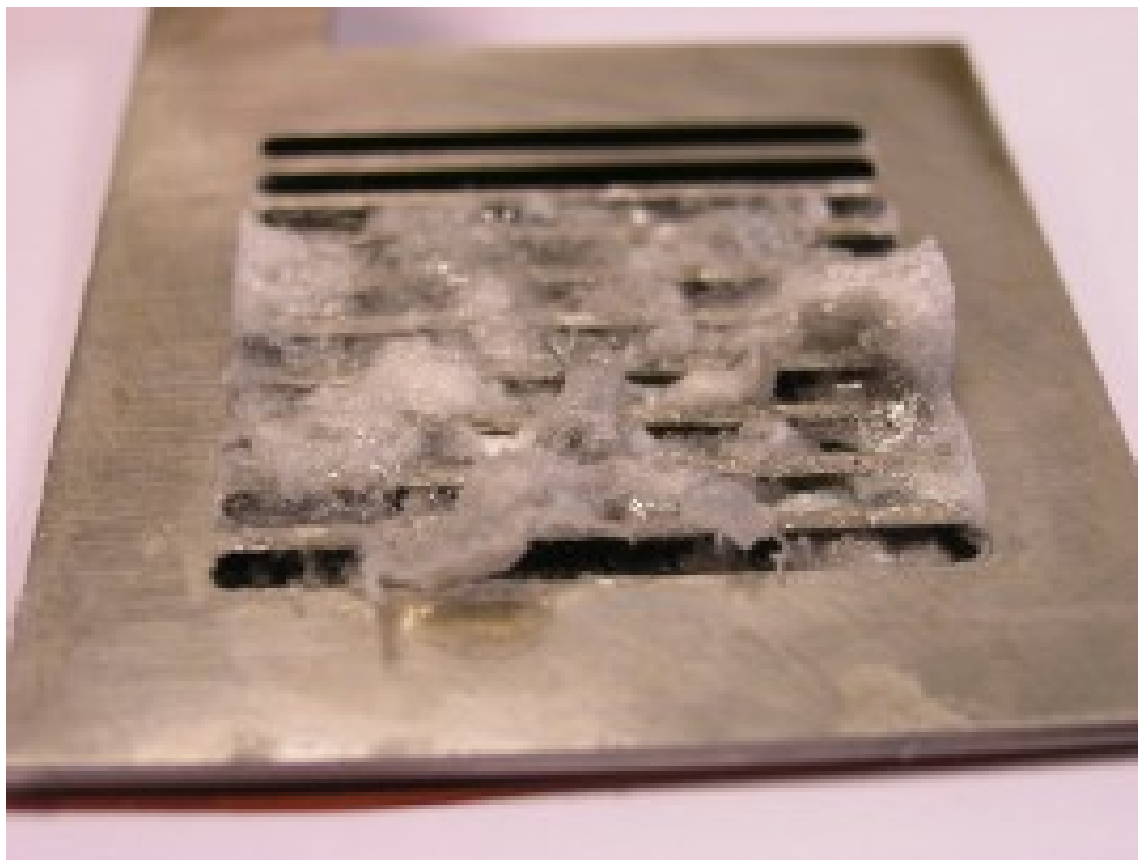


Figure 7. A picture of carbonate precipitation on the cathode current collector after up to 475 hours of operation in 1 M NaOH electrolyte. Reprinted with permission from [73], Copyright 2009, Elsevier.

The Faradaic efficiency of the DBFC system can also be increased through the suppression of  $\text{BH}_4^-$  hydrolysis with an additive such as thiourea (TU) in the anolyte. Gyenge [9] was the first to investigate TU and its effect on  $\text{NaBH}_4$  hydrolysis, based on its proven ability to impede the combination of  $\text{H}_{\text{ad}}$  to form  $\text{H}_2$  during the cathodic evolution of  $\text{H}_{2(\text{g})}$  on Pd [74]. Figure 8 shows a cyclic voltammogram of  $\text{BH}_4^-$  electro-oxidation on Pt disk without TU, and Figure 9 shows the effect on the cyclic voltammogram when adding  $1.5 \times 10^{-3}$  M TU. Gyenge found that the addition of TU simplified the  $\text{BH}_4^-$  cyclic voltammogram (Figure 8), leaving essentially one oxidation peak labeled as “a2” (0 to 0.2 V). The “a2” peak was interpreted to be the direct electro-

oxidation of  $\text{BH}_4^-$ , where the number of electrons exchanged was calculated to be four [9].

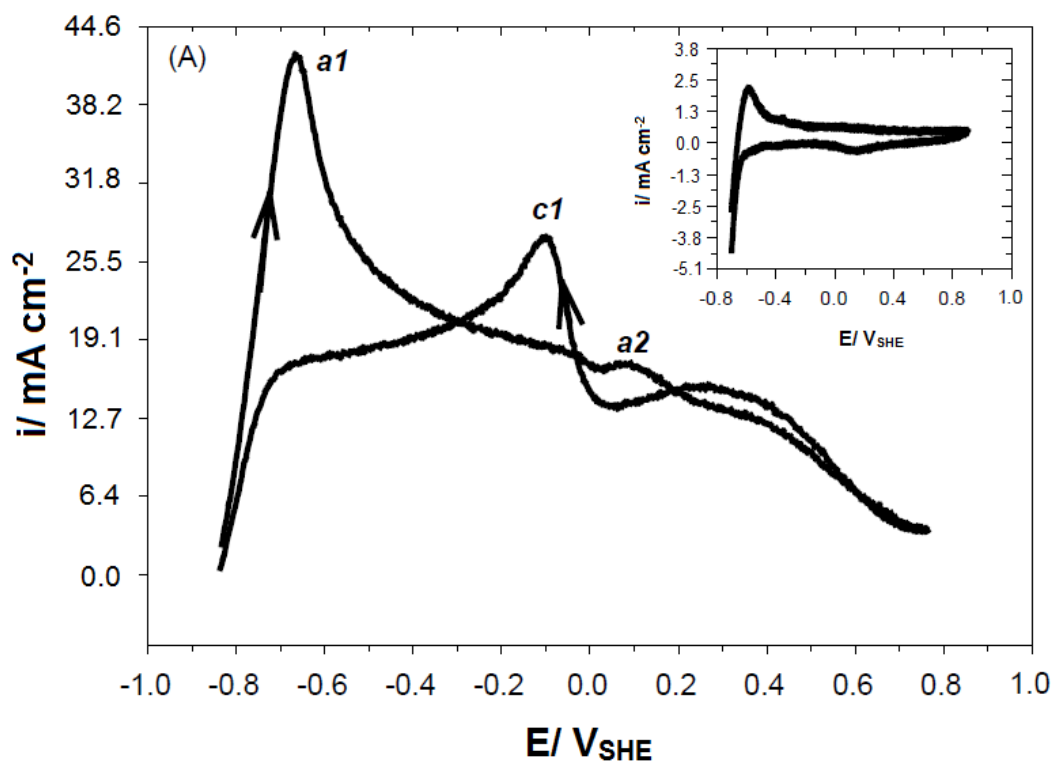


Figure 8. Borohydride electro-oxidation on 1 mm diameter Pt disk. Electrolyte: 0.03 M  $\text{NaBH}_4$  – 2 M  $\text{NaOH}$ , T: 295 K, scan rate:  $25 \text{ mV s}^{-1}$ . Inset: 2 M  $\text{NaOH}$  blank scan on 1 mm diameter Pt disk. Modified with permission from [9], Copyright 2004, Elsevier.

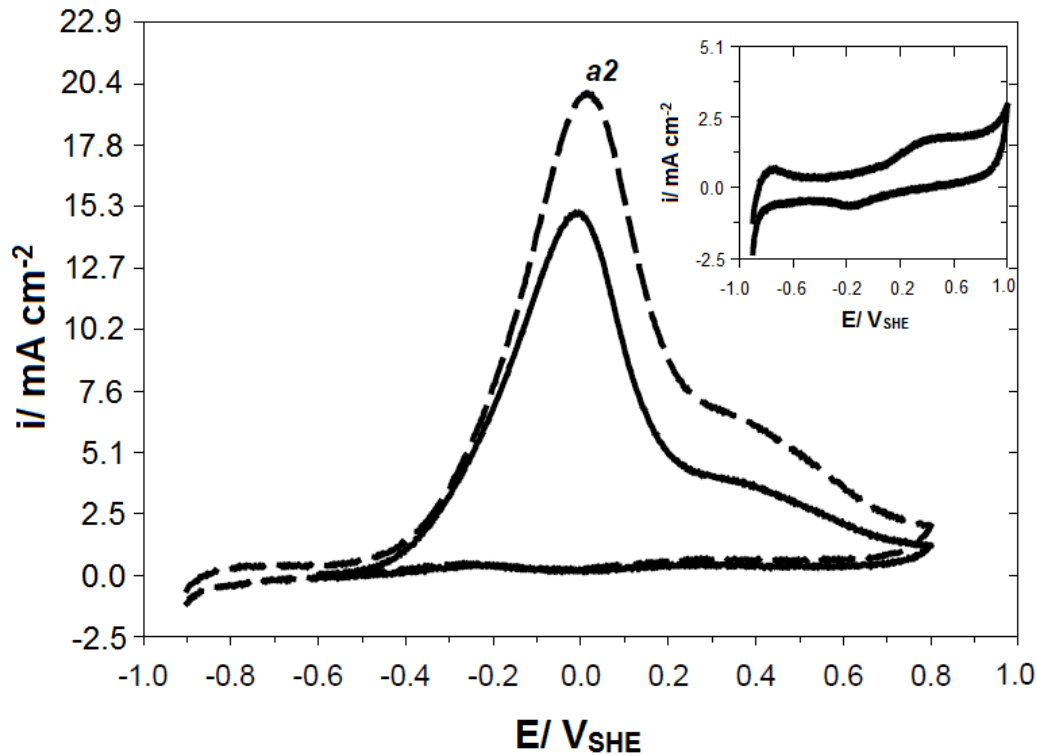


Figure 9. Borohydride electro-oxidation on 1 mm diameter Pt disk with TU. Electrolyte: 0.03 M NaBH<sub>4</sub> – 2 M NaOH – 1.5 × 10<sup>-3</sup> M TU, T: 295 K, scan rate: 50 mV s<sup>-1</sup> (—), 100 mV s<sup>-1</sup> (- - -). Inset: 2 M NaOH – 1.5 × 10<sup>-3</sup> M TU blank scan on 1 mm diameter Pt disk. Modified with permission from [9], Copyright 2004, Elsevier.

Celik et al. observed a modest increase in their DBFC system performance employing a Pd anode catalyst, when adding 1.6 × 10<sup>-3</sup> M TU. The peak power of their DBFC system increased from 144 to 151 W m<sup>-2</sup> and the fuel utilization increased from 22% to 23% at 298 K. The performance increase was explained by the inhibiting effect of TU on the recombination of surface adsorbed hydrogen radicals to form H<sub>2(g)</sub> [75]. The change in performance however, may not be considered statistically significant when considering the variance that is likely to occur in repeat experiments.

Jamard et al. [76] observed a more drastic increase in fuel utilization with 1 × 10<sup>-4</sup> M TU employing a Pt anode catalyst at room temperature. The measured discharge

capacity for their system without TU was 15 Ah of a theoretically possible 85 Ah, where 58% was lost to hydrogen production via hydrolysis, and 24% was lost to unreacted fuel. The measured anode capacity for their system with the addition of TU was 55 Ah; an increase from 18% to 64% fuel utilization efficiency. It should be noted however, that the overpotential of the DBFC for the current step was also increased significantly ( $\sim 0.48$  V) in the presence of TU.

Employing a hydrogen storage alloy anode and a Pt/ C cathode in a  $\text{NaBH}_4 - \text{H}_2\text{O}_2$  oxidant system, Towne et al. [77] found that the measured hydrogen evolution was drastically reduced in the presence of 0.015 M TU. At open circuit conditions at 353 K, the hydrogen evolution was decreased by  $\sim 78\%$ . Similar reductions in hydrogen evolution were observed when high current densities were drawn as well. In addition, a particle size effect was observed on hydrogen evolution. An increased anode catalyst particle size from 0.5  $\mu\text{m}$  to 60  $\mu\text{m}$  resulted in an  $\sim 80\%$  decrease in hydrogen evolution at open circuit conditions. It was postulated that an increased anode particle size would suppress hydrogen evolution, while having little effect on DBFC performance due to the extended triple phase boundary attributed to the high ionic conductivity of the anolyte. No polarization curves were shown by Towne et al. to corroborate their statement with respect to the proposed effect of increased particle size.

From the aforementioned investigations on the effect of TU on the DBFC system, it is evident that the extent to which TU is able to suppress the evolution of  $\text{H}_{2(\text{g})}$  is highly dependent upon the material of anode catalyst in the DBFC system. Also, one should consider the operating conditions of the DBFC system, in particular conditions in which  $\text{BH}_4^-$  hydrolysis is favourable such as temperature and potential.

### 1.2.3 Crossover

The crossover phenomena in fuel cells refer to the mass transfer of the reductant (and/ or oxidant) such that the oxidant and reductant are mixed at the anode and/ or the cathode of a fuel cell. This results in a mixed potential at the electrode, and ultimately reduces the potential difference between the anode and cathode of a fuel cell. Typically, crossover is induced by a concentration gradient of the reagent from one electrode to the other. In the case of DBFC, crossover normally refers to the migration of the reductant ( $\text{BH}_4^-$ ) to the cathode compartment. An investigation into the effect of crossover on DBFC performance by Liu and Suda suggests that the effect of fuel crossover is more critical during open circuit conditions or low current operations than during high current operations, due to the higher  $\text{BH}_4^-$  concentration gradient across the membrane [78]. This was also confirmed by Cheng and Scott who tested the effect of  $\text{BH}_4^-$  concentration on cathodic polarization curves and found that, low  $\text{BH}_4^-$  concentrations yielded a better performance at the cathode [6]. For a 25 wt%  $\text{NaBH}_4$  – 6 M  $\text{NaOH}$  solution, the  $\text{BH}_4^-$  crossover rate across a Nafion<sup>®</sup> 117 membrane was found to be  $4.01 \times 10^{-3} \text{ mol m}^{-2} \text{ s}^{-1}$  at an assumed temperature of 298 K (not specified) [14].

Borohydride crossover can be lessened in a DBFC system by employing thicker membranes and/or using cation exchange membranes over anion exchange membranes. The effect of crossover on the DBFC system can be further mitigated by the use of  $\text{BH}_4^-$  tolerant cathode catalysts. Examples of some  $\text{BH}_4^-$  tolerant air/  $\text{O}_2$  cathode catalysts are  $\text{MnO}_2$  [22],  $\text{LaNiO}_3$  [23],  $\text{La}_{1-x}\text{Sr}_x\text{CoO}_3$  [24],  $\text{LaCoO}_3$  [25],  $\text{Eu}_2\text{O}_3$  [26], and  $\text{CoPc}$  [27].

### 1.2.4 Oxidant Pressure

The effect of the oxidant pressure on the equilibrium cathode potential in an alkaline environment can be realized by equation (35), where the  $O_{2(g)}$  activity is expressed in terms of  $O_{2(g)}$  partial pressure in atm assuming ideal gas behaviour.

$$E_e = E_{O_2}^o - \frac{RT}{4F} \ln \frac{a_{OH^-}^4}{a_{O_2} a_{H_2O}^2} \quad (35)$$

$$a_{O_2} = p_{O_2} = X_{O_2} P_{Total} \quad (36)$$

where  $p_{O_2}$  is the partial pressure of  $O_{2(g)}$ ,  $X_{O_2}$  is the molar fraction of  $O_2$  in the gas, and  $P_{Total}$  is the total absolute pressure of the gas in the cathode compartment.

The effect of oxidant pressure and composition were explored by Cheng and Scott; their results are summarized in Table 4 [6]. The peak power density and current density of the fuel cell increased with increasing  $O_2$  content, and increasing oxidant pressure. These peak power densities also relate to higher exchange current densities on the cathode, due to higher  $O_2$  concentration. The overall improvement in performance from using air to using pure oxygen was approximately 15%.

Table 4. Effect of oxidant composition and pressure. T: 358 K, anode: Au/ C, 2 mg cm<sup>-2</sup>, cathode: Pt/ C, 2 mg cm<sup>-2</sup>, membrane: Nafion<sup>®</sup> 117, anolyte: 5 wt% NaBH<sub>4</sub> - 10 wt% NaOH, anolyte flow rate: 10 ml min<sup>-1</sup>, O<sub>2</sub> pressure: 1 atm (abs), O<sub>2</sub> flow rate: 0.2 SLPM. Modified with permission from [6], Copyright 2006, Elsevier.

Absolute Oxidant Pressure (bar)	OCV (V)	P <sub>peak</sub> (mW cm <sup>-2</sup> )	i <sub>peak</sub> (mA cm <sup>-2</sup> )
1 (O <sub>2</sub> )	0.99	72	350
2 (O <sub>2</sub> )	1.04	77	365
1 (air)	0.94	65	310
2 (air)	0.96	68	315

### 1.2.5 Anolyte Flow Rate

Few studies have been conducted on the effect of anolyte flow rates. In general it was found that DBFC performance improved with increased fuel flow rates due to the improved mass transport [6,15]. Other than the anode and flowfield designs, mass transport at the anode can also be influenced by H<sub>2(g)</sub> evolution from BH<sub>4</sub><sup>-</sup> hydrolysis or incomplete oxidation, which is in return affected by the anode catalyst material and operating conditions. In a situation where the anode catalyst is catalytically active towards BH<sub>4</sub><sup>-</sup> hydrolysis, and the catalyst is not able to oxidize the evolved H<sub>2(g)</sub> efficiently, an anolyte flow rate that is capable of removing the H<sub>2(g)</sub> effectively should be considered. If the rate of H<sub>2(g)</sub> evolution through BH<sub>4</sub><sup>-</sup> hydrolysis is low under the employed conditions, it may be sufficient to use lower anolyte flow rates, with subsequently lower parasitic load on the DBFC system.

From Figure 10 it is observed that when using an Au anode catalyst, which is catalytically slow for BH<sub>4</sub><sup>-</sup> hydrolysis [9], the effect of anolyte flow rate on the DBFC polarization curves was small, even at 333 K where the homogeneous hydrolysis reaction

is more kinetically favourable than at 298 K as modeled by equation (14). Figure 11 shows the effect of temperature and anolyte flow rate on DBFC polarization curves when using Au-Pt catalysts. It should be noted that Pt is well known to catalyze  $\text{BH}_4^-$  hydrolysis [9]. The anolyte flow rate did not have an effect on the system at 298 K, however at 333 K, the anolyte flow rate clearly had a noticeable effect on DBFC performance; particularly when changing the anolyte flow rate from  $20 \text{ mL min}^{-1}$  to  $50 \text{ mL min}^{-1}$ . At 333 K, the kinetics for heterogeneous  $\text{BH}_4^-$  hydrolysis on Pt is faster than at 298 K, however the evolved  $\text{H}_{2(\text{g})}$  was likely not efficiently oxidized on the catalyst. Keeping this in mind, the effect of the anolyte flow rate on DBFC performance in Figure 11 is explained by the ability of the higher anolyte flow rates ( $> 20 \text{ mL min}^{-1}$ ) to remove evolved  $\text{H}_{2(\text{g})}$ , thus preventing the  $\text{H}_{2(\text{g})}$  from creating mass transport issues at the active catalyst sites and improving the DBFC performance.

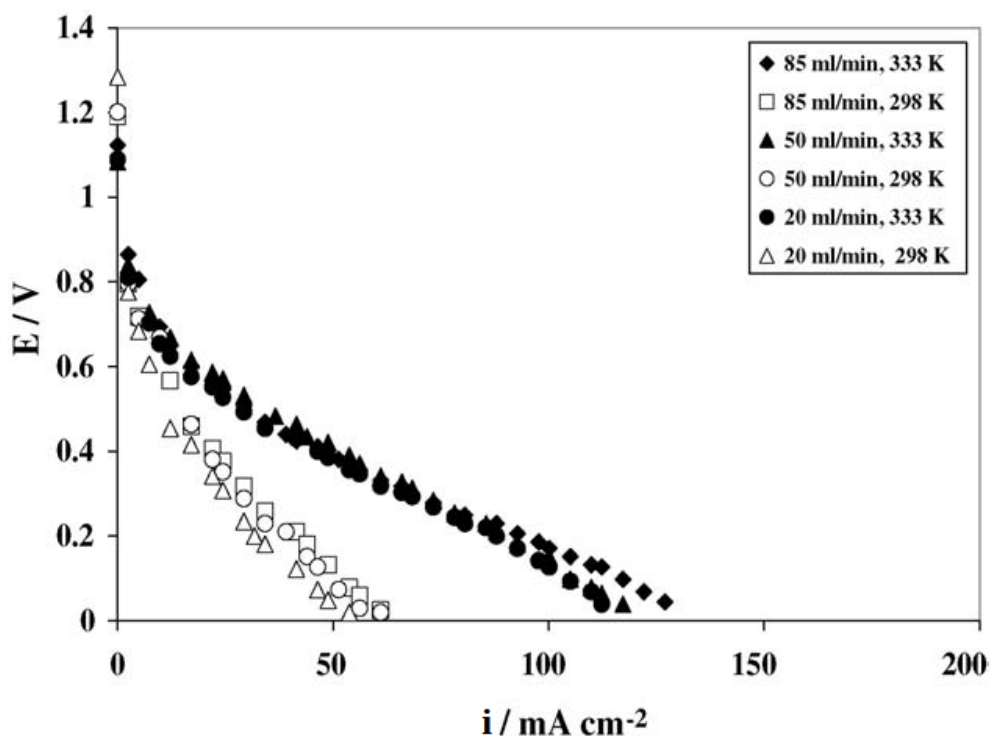


Figure 10. DBFC polarization curves. Anode:  $5 \text{ mg cm}^{-2} \text{ Au/ C}$ , anolyte:  $2 \text{ M NaBH}_4 - 2 \text{ M NaOH}$ , cathode:  $4 \text{ mg cm}^{-2} \text{ Pt/ C}$ ,  $\text{O}_2$  flow rate:  $0.2 \text{ SLPM}$ ,  $\text{O}_2$  pressure:  $2.7 \text{ atm (abs)}$ . Modified with permission from [15], Copyright 2006, Elsevier.

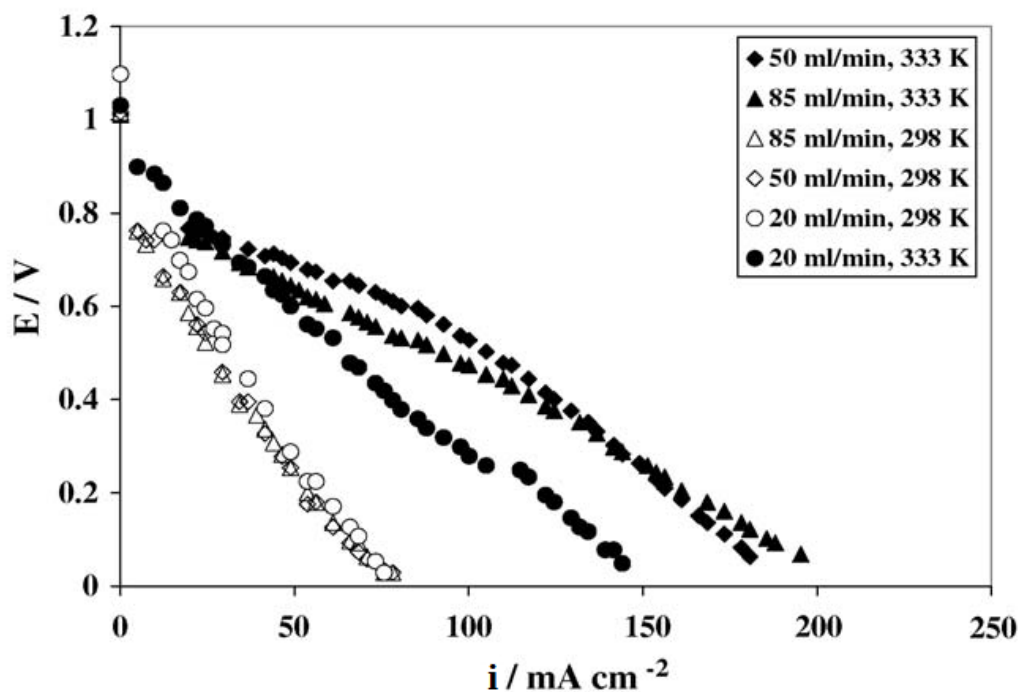


Figure 11. DBFC polarization curves. Anode:  $5 \text{ mg cm}^{-2}$  Au-Pt/ C, anolyte:  $2 \text{ M NaBH}_4 - 2 \text{ M NaOH}$ , cathode:  $4 \text{ mg cm}^{-2}$  Pt/ C,  $\text{O}_2$  flow rate:  $0.2 \text{ SLPM}$ ,  $\text{O}_2$  pressure:  $2.7 \text{ atm}$  (abs). Modified with permission from [15], Copyright 2006, Elsevier.

### 1.2.6 Direct Borohydride Fuel Cell Design Characteristics

There are a number of fuel cell system designs that have been developed specifically for DBFC in recent years. The following section will discuss a few of these designs.

Wang et al. designed an MEA which utilizes the hydrogen evolved during  $\text{BH}_4^-$  hydrolysis in a DBFC batch system (schematic design shown in Figure 12). They claim a Coulombic efficiency for their fuel cell system of up to 100% [79]. This is achieved through sectioned catalyst layers on both the anode and cathode. In the most Coulombic efficient configuration (MEA-B Figure 12B), the anode catalyst layer is divided into two sections. Each section contains a catalyst specifically for either hydrogen electro-

oxidation or  $\text{BH}_4^-$  electro-oxidation. The section for hydrogen electro-oxidation, containing 40% Pt/ C anode catalysts was hydrophobic, and the section for  $\text{BH}_4^-$  electro-oxidation containing 40%  $\text{Pt}_7\text{Ni}_3$ / C anode catalysts was hydrophilic. The hydrophilicity of the  $\text{BH}_4^-$  electro-oxidation section was facilitated by the addition of Nafion<sup>®</sup> ionomer in the catalyst layer. The hydrophobicity of the hydrogen electro-oxidation section is assumed to be facilitated by the addition of PTFE in the catalyst layer, however this was not specifically mentioned. The anode metal loadings were also not specified. The MEA-A (Figure 12A) did not contain any catalysts in the hydrophobic section, and was used as a basis of comparison for MEA-B (Figure 12B).

The cathode catalyst layer in both MEA-A and MEA-B was also sectioned into two halves where the bottom half directly facing the hydrophilic anode catalyst layer was composed of a  $1 \text{ mg cm}^{-2}$  loading of 40% Pt/ C. The upper half of the hydrophobic cathode was composed of carbon powder. It is surmised, that the uncatalyzed cathode section was introduced to lower the mixed potential on the cathode.

During operation of the DBFC system the anode compartment was half filled, where only the hydrophilic anode catalyst layer was submerged in the  $\text{NaBH}_4 - \text{NaOH}$  anolyte, and the cathode compartment was filled with  $\text{O}_{2(\text{g})}$ .

Maximum power outputs achieved were 33 mW and 42 mW for the MEA-A and MEA-B configurations respectively with a 1 M  $\text{NaBH}_4 - 6 \text{ M NaOH}$  anolyte at 333 K and an assumed  $\text{O}_2$  pressure of 1 atm (abs) (not specified). The increased power output (~28%) of MEA-B in reference to MEA-A was attributed by Wang et al. to the increased Coulombic efficiency of MEA-B due to its ability to oxidize the evolved hydrogen from  $\text{BH}_4^-$  hydrolysis.

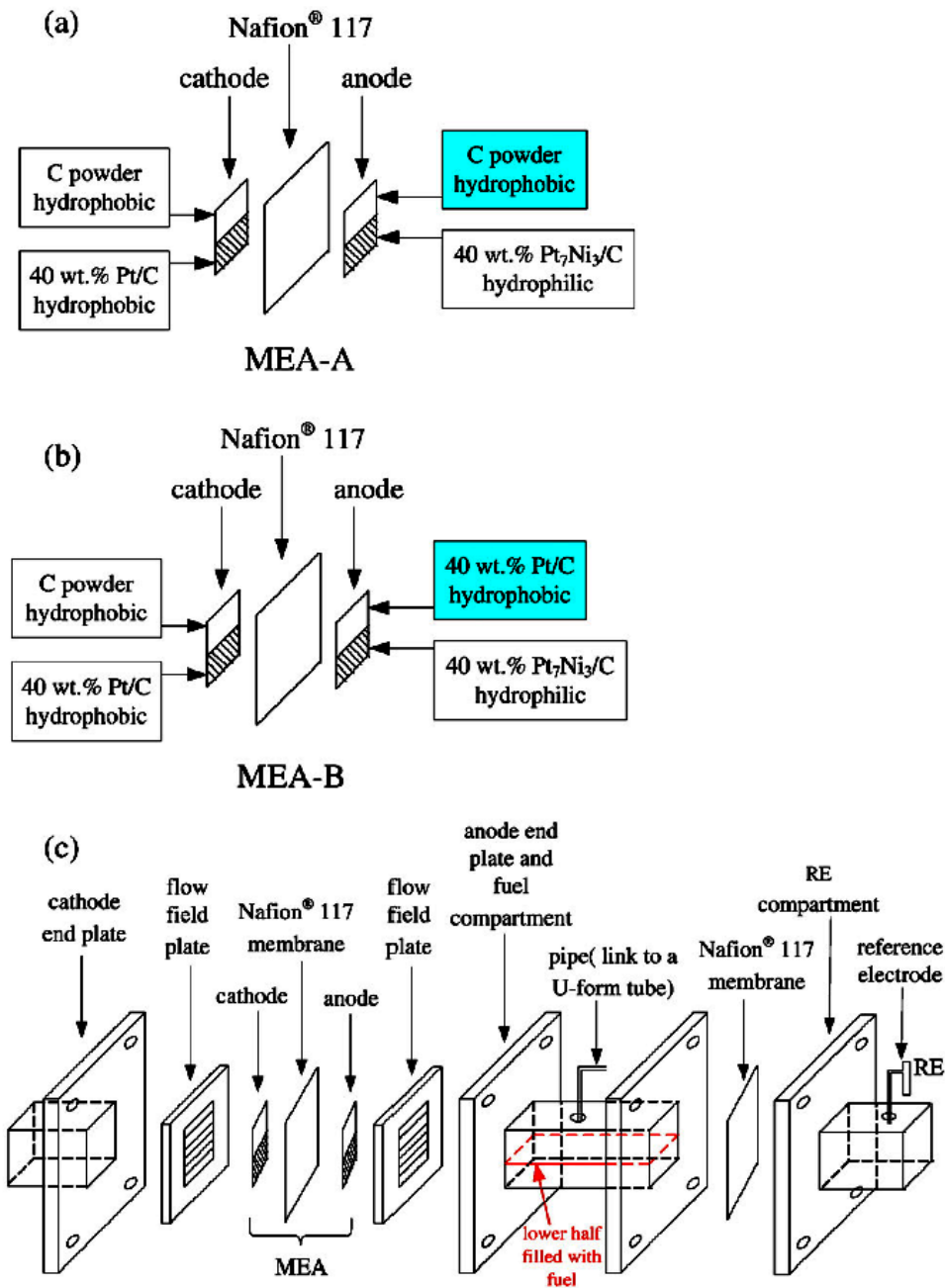


Figure 12. Diagram of MEA configurations by Wang et al.. A) MEA configuration MEA-A where both the anode and cathode active layers are sectioned into two halves but only one half of each side contains catalysts. B) MEA configuration MEA-B where both the anode and cathode active layers are sectioned into two halves, and one half of the anode active layer is hydrophobic with 40% Pt/ C for H<sub>2</sub> electro-oxidation. C) Experimental cell setup. Reprinted with permission from [79], Copyright 2010, Elsevier.

The Qineti Q tubular cell can achieve a maximum power density of  $28 \text{ mW cm}^{-2}$  under ambient conditions with a  $5\% \text{ NaBH}_4 - 6 \text{ M NaOH}$  anolyte [22]. The system employs a commercial  $\text{MnO}_2$  cathode, a  $0.8 \text{ mg cm}^{-2}$  nano-particulate Au anode, and an undisclosed anion exchange membrane. The nano-particulate Au anode was formed by electrodeposition of Au using a  $\text{HAuCl}_6$  precursor onto a Ni grid in an unspecified deposition bath. A picture of the system is shown below:

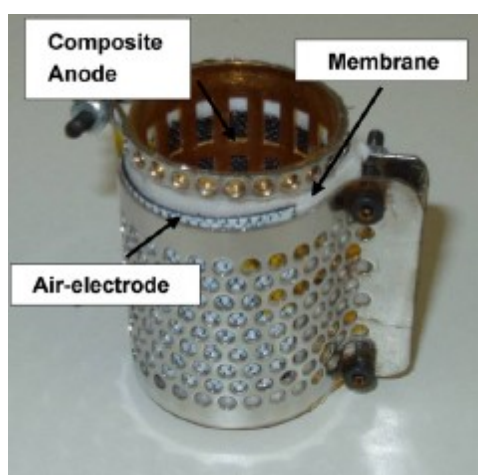


Figure 13. Qineti Q tubular cell with a  $0.8 \text{ mg cm}^{-2}$  Au/ Ni grid anode and an  $\text{MnO}_2$  cathode. Reprinted with permission from [22], Copyright 2008, Elsevier.

An important test for  $\text{NaBH}_4$  - Air DBFC's is their capability of operating under passive and ambient conditions. Using a parallel plate configuration DBFC system, Liu et al. [80] were able to achieve a single cell peak power density of  $80 \text{ mW cm}^{-2}$  under passive and near ambient conditions ( $T = 298 \text{ K}$ ), using a Pd/ C and Ni powder applied to a nickel foam substrate (Ni powder to Pd/ C to Nafion<sup>®</sup> ratio: 0.75:0.3:0.1 and metal loading:  $20 \text{ mg cm}^{-2}$ ), and a  $5\% \text{ NaBH}_4 - 20\% \text{ NaOH}$  anolyte composition. The cathode consisted of a  $1 \text{ mg cm}^{-2}$  loading of 30 wt% Pt/ C. In an 8-cell configuration, where the

effective area of each cell was  $6 \text{ cm}^2$ , Liu et al. achieved a power output of 2.5 W or  $52.1 \text{ mW cm}^{-2}$  from their fuel cell stack. A picture of their stack is depicted in Figure 14.



Figure 14. DBFC stack operating under passive and ambient conditions powering a small television. The anolyte composition was 5 wt%  $\text{NaBH}_4$  – 20 wt%  $\text{NaOH}$ , and the Ni powder to Pd/ C to Nafion<sup>®</sup> anode ratio was 0.75:0.3:0.1 with a  $20 \text{ mg cm}^{-2}$  metal loading. Reprinted with permission from [80], Copyright 2008, Elsevier.

Jamard et al. [73] also achieved a high performance in a passive parallel plate configuration DBFC stack operated at ambient conditions. A power output of  $200 \text{ mW cm}^{-2}$  (close to peak power) at  $400 \text{ mA cm}^{-2}$  was achieved using 80% Pt/ C anode catalysts with a loading of  $1.3 \text{ mg cm}^{-2}$ , a 2 M  $\text{NaBH}_4$  – 1 M  $\text{NaOH}$  anolyte composition, a Morgane<sup>®</sup> ADP anion exchange membrane, and an air-breathing O'CAT<sup>®</sup> non-platinum cathode supported on a nickel mesh. The superficial active area of one electrode was  $9 \text{ cm}^2$ . It should be noted that the polarization curves were measured at a current draw rate of  $0.22 \text{ mA cm}^{-2} \text{ s}^{-1}$ , therefore the power output of  $200 \text{ mW cm}^{-2}$  may not necessarily be stable.

### 1.3 Anode Catalysts

An ongoing challenge for fuel cells is to reduce the Pt catalyst loadings and/ or to find cheaper alternatives. Specifically for direct fuel cells, higher anode catalyst loadings are needed in comparison to the hydrogen PEMFC due to slower oxidation kinetics. A major hurdle specific to DBFC's is that many electrode material candidates catalyze the thermochemical (non-Faradaic) hydrogen generation from  $\text{BH}_4^-$  hydrolysis, leading to low faradaic efficiencies (Figure 2).

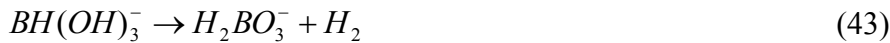
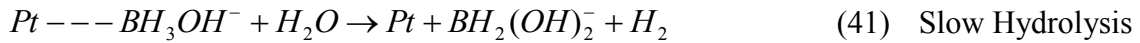
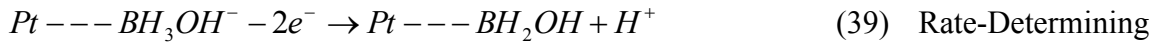
Investigations have been conducted using alternative, non-platinum, catalysts such as Ir, Os, Au, Ni, Fe, and Cu [9,15--21]. Playing a key role in determining the operating conditions of the DBFC system, and governing both the performance and cost of DBFC's, it is important to understand the kinetics, and reaction mechanisms of  $\text{NaBH}_4$  electro-oxidation on these catalysts. Studies of  $\text{BH}_4^-$  electro-oxidation kinetics have been carried out on many catalysts such as Au [9,15,17,81--83], Pt [9,17,18,84--86], Ag [87--89], Ni [11,17,19,20,90,91], Ni-Pd [80], Zr-Ni Lave phase alloy [69] and  $\text{LmNi}_{4.78}\text{Mn}_{0.22}$  alloy [92] (where Lm – La rich mischmetal; an alloy of rare earth metals). The oxidation of  $\text{BH}_4^-$  most commonly occurs on many of the listed catalysts according to a total four-electron transfer. Some studies have found evidence that Au and Ag can electro-oxidize  $\text{BH}_4^-$  with an up to 8 electron transfer [81]. This section will review some of the commonly researched anode catalysts.

#### 1.3.1 Platinum

The oxidation of  $\text{BH}_4^-$  on Pt is complex and not fully understood. Hydrogen generators based on  $\text{BH}_4^-$  hydrolysis using various high-surface area carbon black

supported Pt and Pt-alloy catalysts have been proposed for fuelling H<sub>2</sub>-O<sub>2</sub> fuel cells [93--96]. The kinetic rate law for the thermochemical hydrolysis reaction on 5%wt Pt/ C for BH<sub>4</sub><sup>-</sup> / Pt molar ratios between 200 and 1500 is zero-order with respect to BH<sub>4</sub><sup>-</sup> and first-order with respect to H<sub>2</sub>O, the corresponding activation energy is 45 kJ mol<sup>-1</sup> and the rate constant is 8.8x10<sup>-5</sup> M s<sup>-1</sup>[97].

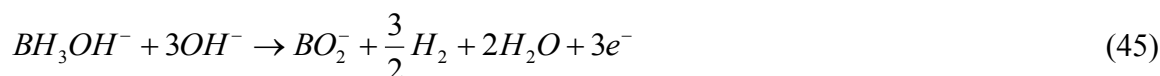
Below is the earliest reaction mechanism of BH<sub>4</sub><sup>-</sup> electro-oxidation on Pt proposed by Elder and Hickling in 1962 [84].



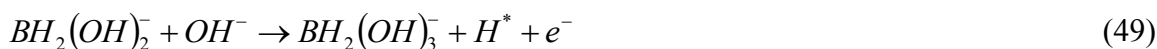
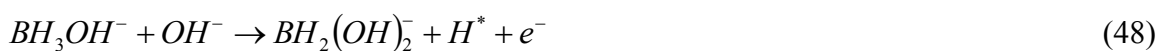
Initially the BH<sub>4</sub><sup>-</sup> undergoes partial hydrogen ionization leaving adsorbed borine (BH<sub>3</sub>) on the Pt according to reaction (37). The BH<sub>3</sub> then irreversibly reacts with water or hydroxide to produce BH<sub>3</sub>OH<sup>-</sup> which is considered to be a more stable species and will eventually oxidize according to reaction (39). These reaction pathways are considered to be the direct electro-oxidation of BH<sub>4</sub><sup>-</sup> on Pt. Indirect BH<sub>4</sub><sup>-</sup> electro-oxidation involves the formation of hydrogen gas through hydrolysis according to reaction (41), in which the formed hydrogen then proceeds to be oxidized.

Through polarography studies coupled with  $^{11}\text{B}$ -NRM, Gardiner and Collat identified the hydrolysis reaction intermediate  $\text{BH}_3\text{OH}^-$  formed in reaction (37), [98,99].

They proposed the following reactions:



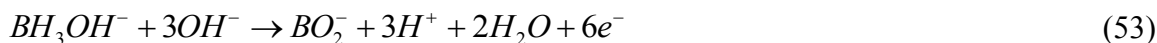
More recently in 2007, Martins et al. [86] have alternately proposed the following reaction mechanisms for  $\text{BH}_4^-$  electro-oxidation on Pt based on their own interpretation of the literature on this subject.



Thus, the four electron oxidation of  $\text{BH}_4^-$  with  $\text{H}_{2(\text{g})}$  evolution is :



Martins et al. also proposed an alternate reaction to (47), for the electro-oxidation of borane hydroxide via:



It is important to emphasize that many steps of the proposed mechanisms by Elder and Hickling, Gardiner and Collat, and Martins et al., have not been experimentally confirmed. Part of the problem being, that many of the reaction intermediates are likely short-lived, as in the case of  $BH_4^-$  hydrolysis [55]. Elder and Hickling proposed a stepwise mechanism where the initial step is the dissociation of the  $BH_4^-$  resulting in the formation of  $BH_3$ ,<sub>ad</sub> then  $BH_3OH^-$  and then finally boric acid. Only one hydrogen atom is exchanged in each step. Similar to Elder and Hickling, Martins et al. also proposed a mechanism in which only 4 electrons were exchanged. Up to 2009 the notion that  $BH_4^-$  electro-oxidation on Pt proceeded via a 4 electron process was widely accepted in the literature [100]. Differing from the mechanism proposed by Elder and Hickling, Martins et al. proposed a “two-pronged” approach in which  $BH_4^-$  proceeds to the formation of  $BH_3OH^-$  via two pathways (reactions (46) and (47)). In addition, Martins et al. recognized that the role of  $OH^-$  for  $BH_4^-$  electro-oxidation (reactions (47) to (50)) was more significant compared to the mechanism proposed by Elder and Hickling, where  $OH^-$  was only consumed in one step of the mechanism (reaction (38)). Finally, instead of boric acid being the final product in their mechanism, Martins et al. proposed an additional step in which the boric acid would become borate. In all three proposed mechanisms, the common theme is the formation of  $BH_3OH^-$  which was experimentally confirmed by Gardiner and Collat.

### 1.3.2 Gold

Au is perhaps one of the most well studied anode catalysts for the DBFC system; particularly because it has customarily been considered non-catalytic toward the  $\text{BH}_4^-$  hydrolysis reaction (equation (6)) [81,101]. Out of the possible 8 electrons,  $\text{BH}_4^-$  electro-oxidation on Au has been reported to yield approximately 7 to 8 electrons [4,9,17,81,102]. A cyclic voltammogram of the electro-oxidation of  $\text{NaBH}_4$  on Au is shown in Figure 15. In this Figure, three peaks were identified and were labeled as “a2,” “a3,” and “c1”. Peak “a2” is the direct electro-oxidation of  $\text{BH}_4^-$  through an eight electron process [81]. Peaks “a3” and “c1” are unidentified reaction intermediates from  $\text{BH}_4^-$  electro-oxidation, although it has been proposed that the “c1” peak can be attributed to the electro-oxidation of  $\text{BH}_3\text{OH}^-$  [103]. This sharp oxidation peak on the return scan has also been observed in Pt cyclic voltammograms for  $\text{BH}_4^-$  electro-oxidation, where it has been recently proposed to be the electro-oxidation of re-adsorbed  $\text{BH}_4^-$  [104].

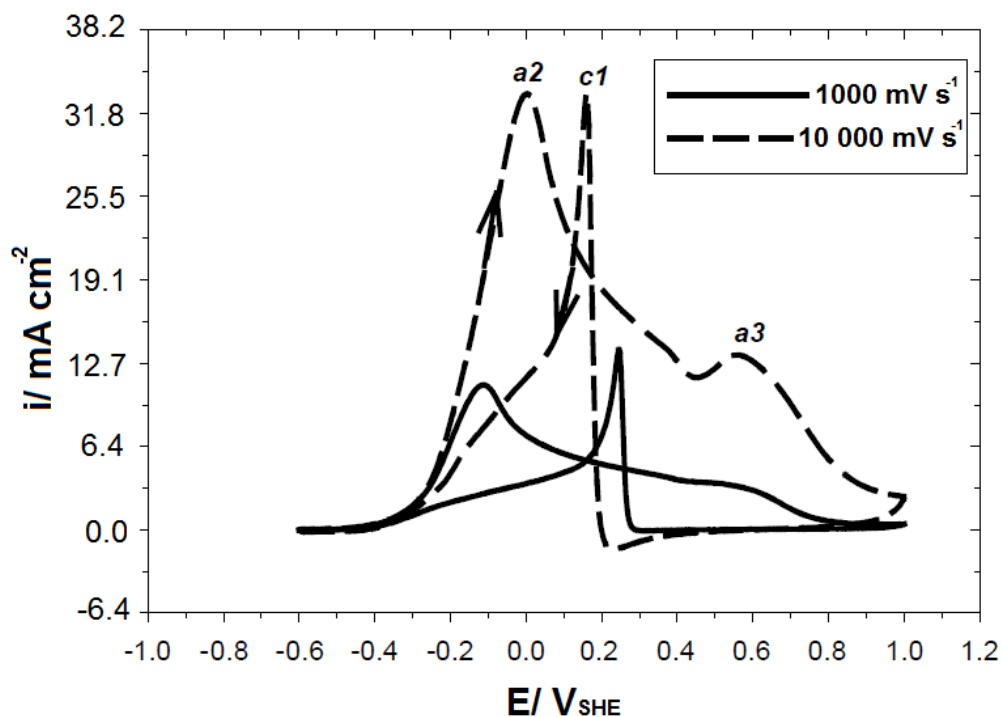


Figure 15. Cyclic voltammogram on 1 mm diameter Au disk electrode. Electrolyte: 0.03 M  $\text{NaBH}_4$  – 2 M  $\text{NaOH}$ , T: 295 K. Modified with permission from [9], Copyright 2004, Elsevier.

Recent experimental evidence including identification of the surface adsorbed species during  $\text{BH}_4^-$  oxidation on Au by in situ Fourier Transformed Infrared Spectroscopy (FTIR) and online electrochemical mass spectrometry (OLEMS) point to some degree of non-Faradaic hydrolysis of  $\text{BH}_4^-$  at open circuit and low anodic overpotentials forming  $\text{H}_2$  and  $\text{BH}_3\text{OH}^-$  as the first step of the overall oxidation process (equation(34)) [100,105,106].

The total number of electrons involved in  $\text{BH}_4^-$  oxidation on Au, as determined by applying either the Levich or Koutecky-Levich analysis to rotating disk electrode (RDE) voltammetry data, can reach virtually the maximum of 8 electrons at high anodic overpotentials, whilst at low anodic overpotentials, only 4-5 electrons were recovered per  $\text{BH}_4^-$  molecule [82,100]. When  $\text{BH}_4^-$ -air cells were discharged at low current

densities of 1 and 2.5 mA cm<sup>-2</sup>, thereby, imposing a small anodic overpotential, the number of electrons calculated based on the discharge capacity was 7.5 and 7, respectively [17]. The latter numbers agree very well with earlier measurements using the diffusion controlled peak current density in static electrode voltammetry [9,81].

This discrepancy among measurements is most likely due to the time scale of the experiments and the residence time of the BH<sub>4-y</sub>(OH)<sub>y</sub><sup>-</sup> species (especially BH<sub>3</sub>OH<sup>-</sup>) near the electrode surface, which in turn is dependent on the electrode design and hydrodynamic conditions. Slower measurements and hydrodynamic conditions that favour the accumulation of the reaction intermediates in the vicinity of the electrode surface, increasing the probability for their further oxidation, will inherently yield a higher apparent number of electrons exchanged per BH<sub>4</sub><sup>-</sup> molecule. Thus, the Faradaic efficiency is determined synergistically by a large number of factors including catalyst surface, electrode potential, BH<sub>4</sub><sup>-</sup>/OH<sup>-</sup> concentration ratio, temperature, electrode design and hydrodynamic conditions.

Despite its high Faradaic efficiency, the performance of Au catalysts in DBFC's is impeded by many other factors. Gyenge found that the surface coverage of BH<sub>4</sub><sup>-</sup> adsorbed on Au,  $\theta = 10^{-4}$  reported by Bard et al., was much lower than the surface coverage of BH<sub>4</sub><sup>-</sup> adsorbed on Pt in the presence of the hydrolysis inhibiting agent, thiourea (TU);  $\theta = 0.3$  [9,81]. This indicates a high concentration of vacant catalytic sites on Au and subsequently low catalyst utilization efficiency. Chronopotentiometry reveals that the operating potential of Pt in the presence of TU was more negative than that of Au by 0.15V [9]. Figure 16 shows Gyenge's chronoamperometry results, where the current produced on Pt/ TU is initially higher than on Au, but then decreases below the current

produced on Au [9]. The evidence indicates that in spite of the lower power output, Au may have superior long-term electrochemical performance than Pt/ TU.

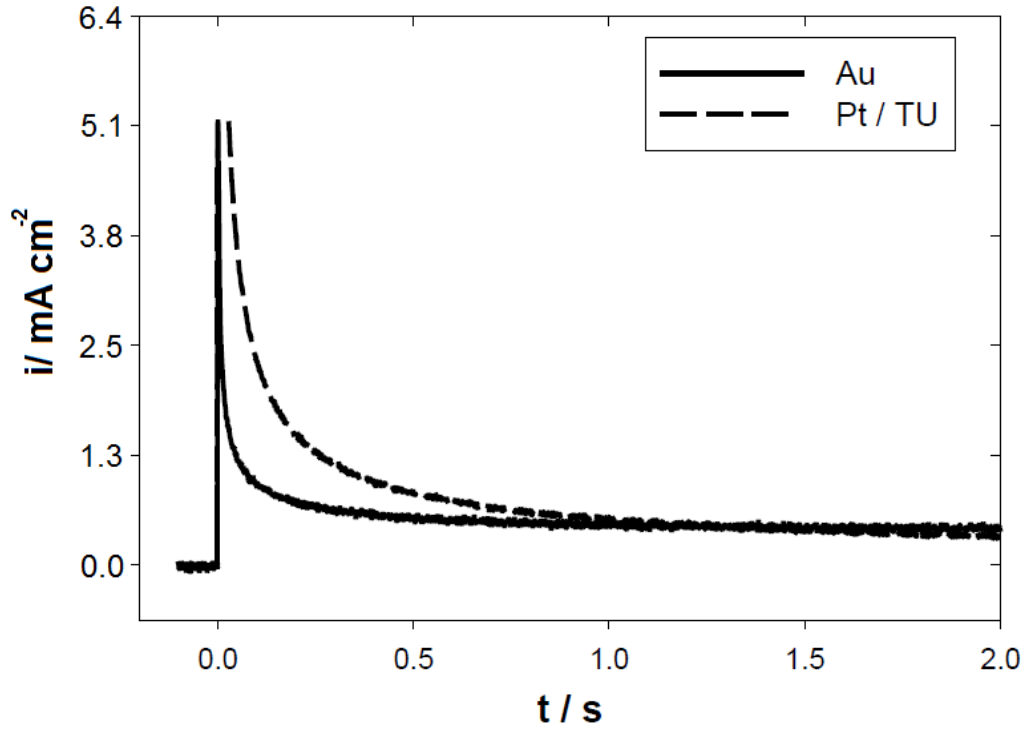


Figure 16. Chronoamperometry on Au and Pt/TU at 293 K. Electrolyte: NaBH<sub>4</sub> – 2 M NaOH, TU concentration:  $1.5 \times 10^{-3}$  M, potential step: -0.6 V to 0.2 V. Modified with permission from [9], Copyright 2004, Elsevier.

In an attempt to take advantage of the beneficial properties of both metals Au has been alloyed with Pt or combined with Pt as a binary catalyst. The earliest investigation into the performance of Pt-Au for DBFC's to the author's knowledge is the work of Amendola et al.. Amendola et al. constructed a catalyst layer of uniformly dispersed 97 wt% Au and 3 wt% Pt particles. They achieved a relatively high peak power density of 63 mW/ cm<sup>2</sup> at 343 K using an air cathode [4]. A comparative study conducted by Atwan et al. showed that 1:1 atomic ratio Pt-Au catalyst performance is indeed

favourable over Pt by cyclic voltammetry [18]. The higher peak current densities and the slightly more negative potentials of the peak on the Pt-Au catalyst versus the Pt catalyst are most likely a result of differing  $\text{BH}_4^-$  electro-oxidation mechanisms. Further analysis of the results by Atwan et al. showed that the electro-oxidation of  $\text{BH}_4^-$  on the Pt-Au catalyst occurred via an 8 electron process [18]. It was demonstrated by chronopotentiometry that 1:1 Pt-Au has superior long-term electrochemical performance compared to pure Pt (Figure 17) [18]. Despite the improved anode durability by alloying Au with Pt, fuel cell tests performed by Atwan et al. show that higher DBFC power densities are achieved with Pt alone (Figure 18) [18].

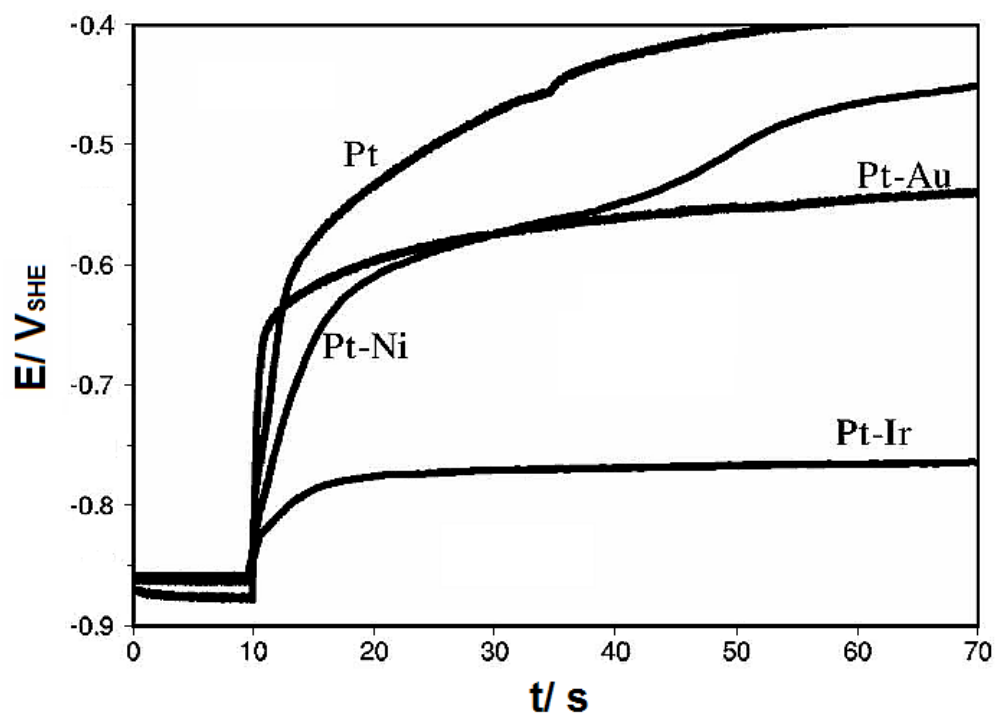


Figure 17. Chronopotentiometry on Pt and various 1:1 atomic ratio binary catalysts. electrolyte: 0.5 M  $\text{NaBH}_4$  – 2 M  $\text{NaOH}$ , T: 298 K. Current step from 0 to 10  $\text{mA}/\text{cm}^2$ . Modified with permission from [18], Copyright 2006, The Electrochemical Society.

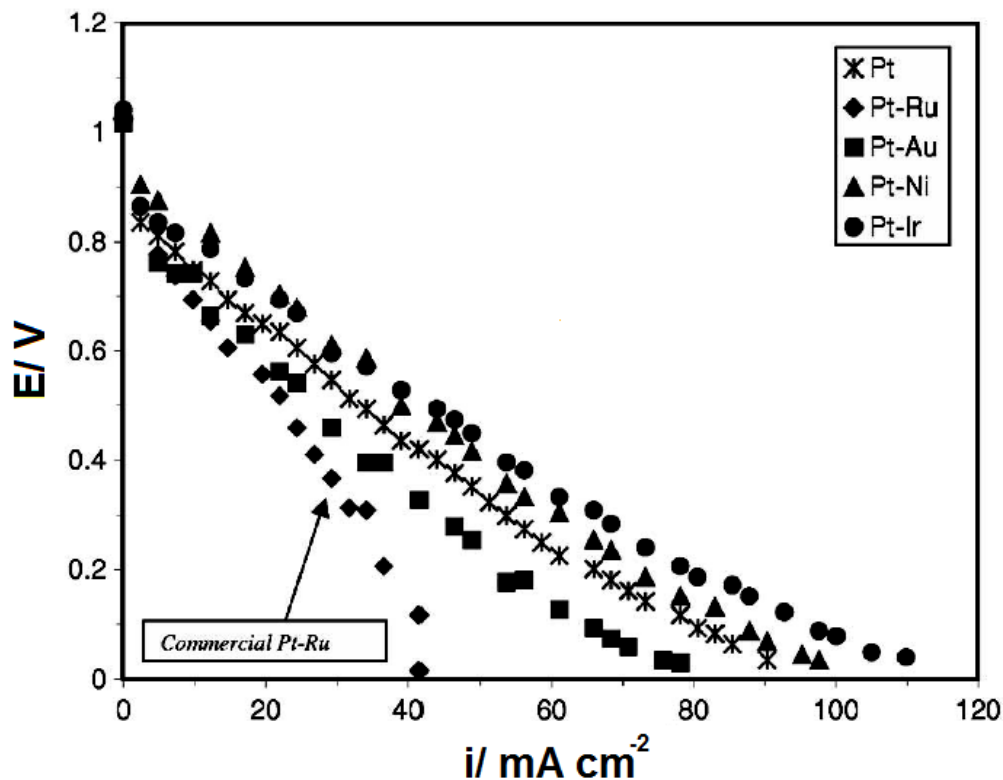
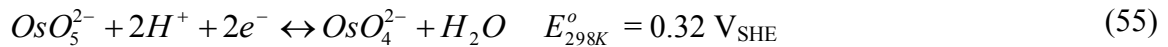
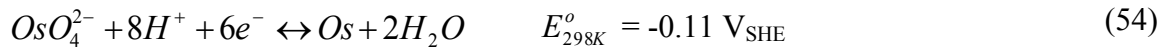


Figure 18. DBFC polarization curves of Pt and various 1:1 atomic ratio  $5 \text{ mg cm}^{-2}$  binary catalysts. Anolyte:  $2 \text{ M NaBH}_4 - 2 \text{ M NaOH}$ , anolyte flow rate:  $50 \text{ ml min}^{-1}$  at STP,  $\text{O}_2$  flow rate:  $0.2 \text{ SLPM}$ ,  $\text{O}_2$  pressure =  $2.7 \text{ atm (abs)}$ ,  $T: 298\text{K}$ , cathode:  $4 \text{ mg cm}^{-2} \text{ Pt/ C}$ . Modified with permission from [18], Copyright 2006, The Electrochemical Society.

### 1.3.3 Osmium

Osmium is an attractive electrocatalyst for DBFC due to its low price of  $\$11.25 \text{ g}^{-1}$  to  $\$14.47 \text{ g}^{-1}$  [107] relative to the price of Pt at  $\$52.47 \text{ g}^{-1}$  [108]. To date there are few investigations on Os as a potential catalyst for DBFC's. Atwan et al. have evaluated colloidal Os and Os alloys (Os-Sn, Os-Mo, and Os-V), prepared by a modified Bönnerman method for the electro-oxidation of  $\text{BH}_4^-$  by cyclic voltammetry, chronopotentiometry and chronoamperometry [109].

Figure 19 shows the oxidation and reduction peaks obtained by cyclic voltammetry of 20 wt% Os/ C catalyst in 2 M NaOH with and without 0.03 M NaBH<sub>4</sub>. In the blank scan, the following peaks were observed at: -0.05 V, -0.24 V, 0.36 V, and 0.27 V [109]. Atwan et al. suggested that the oxidation and reduction peaks at -0.05 V and -0.24 V respectively, are attributed to the formation and reduction of the osmate ion according to reaction (54) and that the oxidation and reduction peaks at 0.36 V and 0.27 V are attributed to the formation and reduction of the hyperosmate ion (OsO<sub>5</sub><sup>2-</sup>) according to reaction (55) [109]. With the addition of 0.03M NaBH<sub>4</sub>, it appeared that the peaks obtained from the blank scan increased and became more defined. It was proposed that the peak obtained at 0 V involves the direct oxidation of BH<sub>4</sub><sup>-</sup> concurrently with the formation of the osmate ion by reaction (54) [109]. Similarly the increased peaks at 0.36 V and 0.27 V are also attributed to the direct oxidation of BH<sub>4</sub><sup>-</sup> by the formed hyperosmate thus regenerating the osmate ion in situ according to reaction (55) [109].



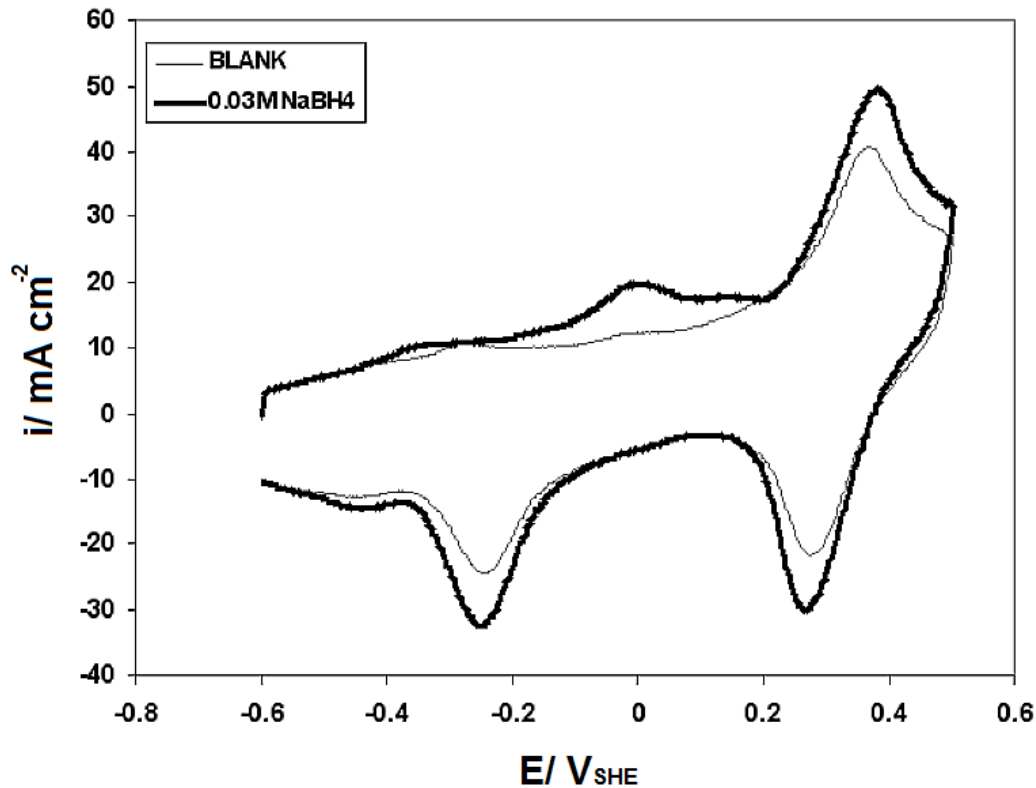


Figure 19. Cyclic voltammogram of freshly prepared 20% Os/ C by modified Bönnehan method. Load:  $30 \mu\text{g cm}^{-2}$ , electrolyte: 0.03 M  $\text{NaBH}_4 - 2 \text{ M NaOH}$ , blank scan electrolyte: 2 M  $\text{NaOH}$ , T: 295 K, scan rate:  $100 \text{ mV s}^{-1}$ . Modified with permission from [109], Copyright 2005, The Laboratory of New Materials for Energy and Electrochemistry Systems.

Os and Os alloys (Os-Sn, Os-Mo, and Os-V) showed some promising long-term electrochemical performance due to their relatively constant potential in chronopotentiometry and constant current density in chronoamperometry. However, these effects were not fully investigated [109]. Atwan et al. also found some evidence that the rate of  $\text{BH}_4^-$  hydrolysis on Os is very low comparatively to Pt and Ru, hence suggesting high faradaic efficiency for  $\text{BH}_4^-$  electro-oxidation on Os, similarly to Au.

No electrode poisoning was evident from chronoamperometry when increasing the  $\text{BH}_4^-$  concentration by tenfold (Figure 20) [109]. A more recent investigation into the

feasibility and performance of Os as an anode catalyst candidate for DBFC's have been completed, and is presented in Chapter 3.0.

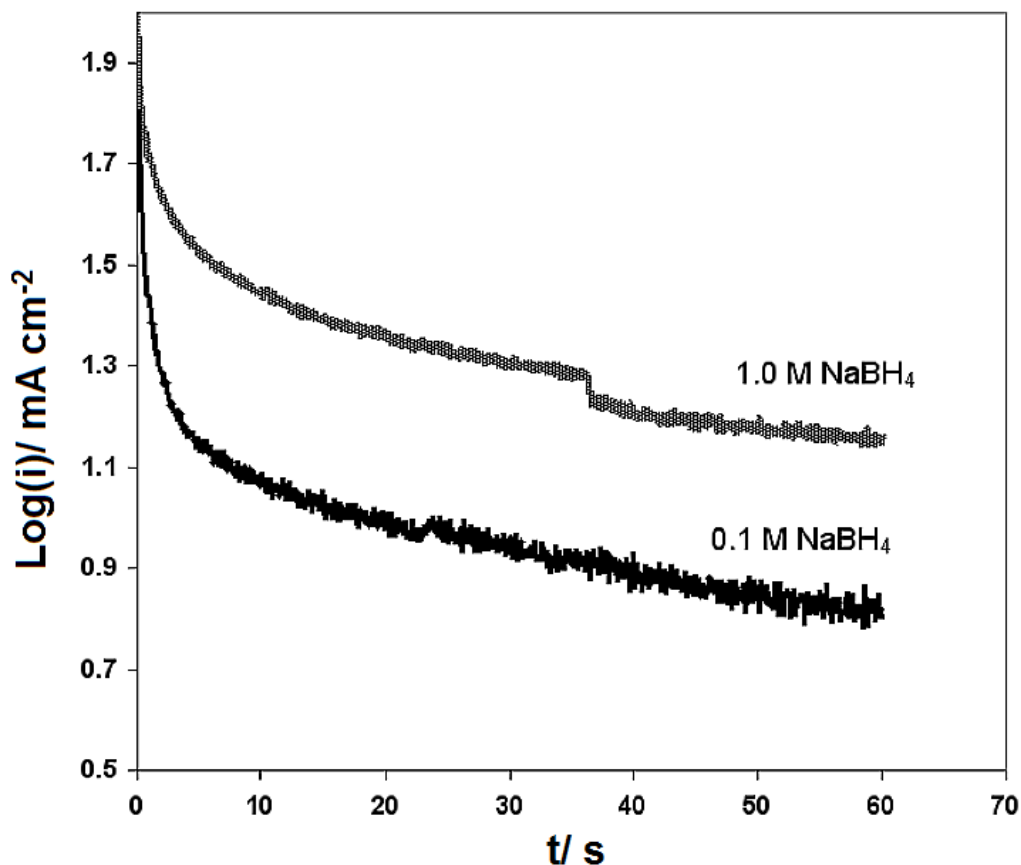
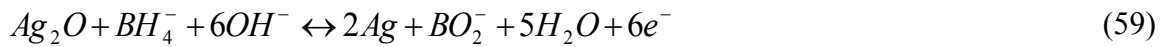


Figure 20. Chronoamperometry of freshly prepared 20% Os/ C by modified Bönnmeman method. Load:  $30 \mu\text{g cm}^{-2}$ , electrolyte:  $\text{NaBH}_4 - 2 \text{ M NaOH}$ , T: 295 K. Potential step from -0.6 V to 0.5 V. Modified with permission from [109], Copyright 2005, The Laboratory of New Materials for Energy and Electrochemistry Systems.

### 1.3.4 Silver

Ag has been studied both as a cathode catalyst and as an anode catalyst for the DBFC system [87,110--117]. Coulometry studies reveal that the  $\text{BH}_4^-$  electro-oxidation on Ag occurs via a 6 to 7 electron process, which also suggests low catalytic activity for

BH<sub>4</sub><sup>-</sup> hydrolysis [21,116]. Suda et al. reported the mitigation of BH<sub>4</sub><sup>-</sup> hydrolysis using Ag electrodes [90]. The onset potential of BH<sub>4</sub><sup>-</sup> electro-oxidation on Ag particles has been found to occur close to the potential of zero charge for Ag at -0.4 V<sub>NHE</sub> in 0.1 M NaOH and 1 mM NaBH<sub>4</sub> [112,113]. Based on the effect of the supporting electrolyte (NaOH) concentration on the cyclic voltammetry of BH<sub>4</sub><sup>-</sup> on Ag, Sanli et al. proposed that the surface oxides formed on the Ag surface, influence the electro-oxidation of BH<sub>4</sub><sup>-</sup>, with Ag<sub>2</sub>O being the most active [21,115]. Increased Ag surface oxidation lead to more negative open circuit potentials of Ag in NaBH<sub>4</sub> – NaOH solutions [115]. A multi-layered structure of Ag<sub>2</sub>O was shown to form due to high NaOH concentrations and the following electro-oxidation mechanism was proposed by Sanli et al. [21,115]:



The adsorption of OH<sup>-</sup> on Ag(111) occurs at -0.56 V [118]. At high NaOH concentrations (≥ 3 M) the Ag metal re-oxidizes to reform Ag<sub>2</sub>O, but at low NaOH concentrations (≤ 0.1 M) the formation of Ag<sub>2</sub>O (57) is hindered and the homogeneous hydrolysis of NaBH<sub>4</sub> is also more likely to occur. Concha and Chatenet also found that the Faradaic efficiency of BH<sub>4</sub><sup>-</sup> electro-oxidation on Ag was strongly dependant on pH. Higher pH (pH 14 versus pH 13) yielded higher Faradaic efficiencies, possibly due to the aforementioned mechanisms and activity of oxidized Ag surfaces [113]. The calculated

number of electrons rose from 1.6 to 5.6 when increasing the NaOH concentration from 0.1 M to 1 M NaOH with a  $\text{NaBH}_4$  concentration of  $1 \times 10^{-2}$  M in both cases.

Bimetallic Ag based colloidal catalysts have been investigated by Atwan et al. [87] including 1:1 atomic ratio Ag-Pt, Ag-Au, Ag-Ir, and Ag-Pd. Through evaluation of electrode kinetic parameters, it was determined that Ag-Pd exhibited the highest exchange current density, however it also exhibited the highest Tafel slope and the lowest yield of electrons ( $n = 2.1$ ). Ag-Au had the highest electron yield of  $n = 4.6$ . Overall, Ag-Ir exhibited the best performance [87].

Concha and Chatenet found that the calculated number of electrons for  $\text{BH}_4^-$  electro-oxidation on  $\text{Pt}_{95}\text{Ag}_5$  alloy increased with increasing  $\text{BH}_4^-$  concentration [113]. For example from  $1 \times 10^{-3}$  M  $\text{NaBH}_4 - 0.1$  M NaOH to  $1 \times 10^{-2}$  M  $\text{NaBH}_4 - 0.1$  M NaOH, the calculated number of electrons for  $\text{BH}_4^-$  electro-oxidation rose from 4.8 to 6.1 at 298 K. From their studies, there is an obvious effect of  $\text{NaBH}_4$  and NaOH concentration on the number of electrons generated from  $\text{BH}_4^-$  electro-oxidation on Ag and Ag alloys. For this reason, it is difficult to directly compare the kinetic parameters obtained for Ag and Ag alloys from different sources in the literature.

### 1.3.5 Zinc

Zinc is not a well known anodic catalyst for DBFC's. Initial experiments by Santos and Sequeira [101] have found that the open circuit potential of Zn in  $\text{BH}_4^-$  solutions supported in NaOH was very negative  $\sim -1.3$  V at 298 K in 4 M NaOH, which is very close to the calculated redox potential of  $-1.27$   $\text{V}_{\text{SHE}}$  for Zn in a solution with a pH of 14 according to reaction (60) [101].



Investigations of Zn anodes for the DBFC system by Santos and Sequeira revealed that Zn is active for  $\text{BH}_4^-$  electro-oxidation [119,120]. Figure 21 shows a cyclic voltammogram of Zn in 1 M  $\text{NaBH}_4$ . In the forward scan,  $\text{BH}_4^-$  electro-oxidizes until the Zn surface passivates. On the return scan, the surface of the electrode is reduced, and  $\text{BH}_4^-$  re-adsorbs onto the surface and oxidizes. Hong et al. [121] employed Zn as an anode catalyst in a fuel cell/ battery hybrid. They found that the addition of  $\text{BH}_4^-$  to the Zn –  $\text{MnO}_2$  or MH –  $\text{MnO}_2$  (MH =  $\text{LaNi}_{4.7}\text{Al}_{0.3}$ ) air battery significantly increased the capacity of the fuel cell/ battery hybrid. For example the MH- $\text{MnO}_2$  battery capacity increased from 30 mAhr  $\text{cm}^{-2}$  to 90 mAhr  $\text{cm}^{-2}$  with the addition of ~0.4 M  $\text{NaBH}_4$  in 7 M NaOH assumingly at room temperature.

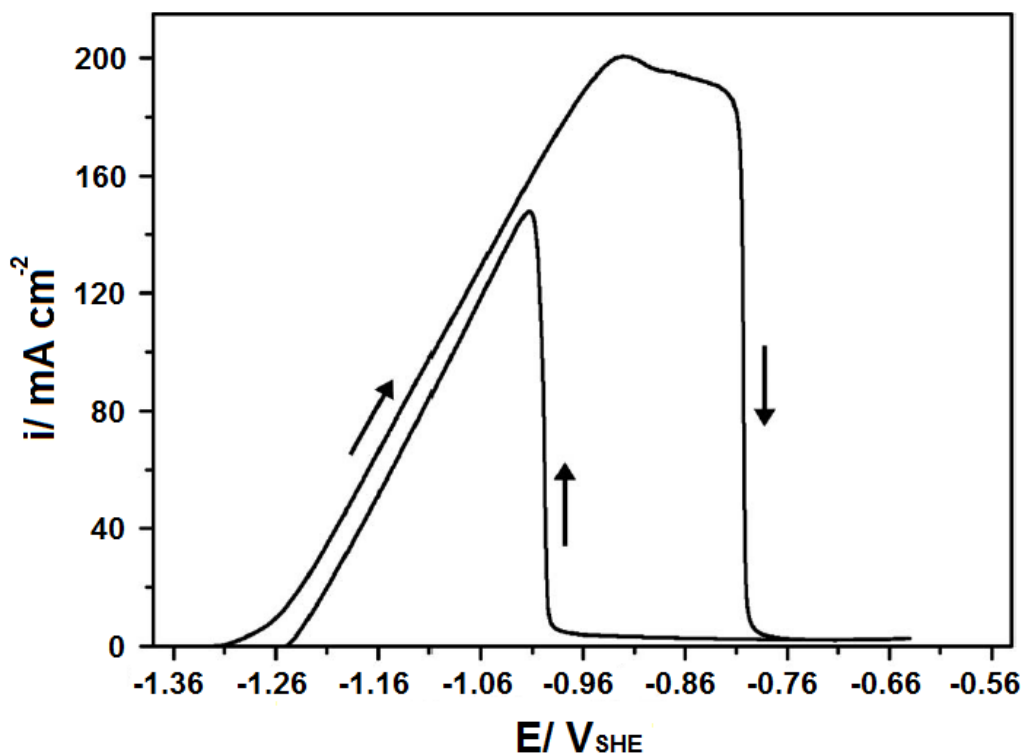


Figure 21. Zinc cyclic voltammogram. Electrolyte: 1 M NaBH<sub>4</sub> – 4 M NaOH, scan rate: 0.05 V s<sup>-1</sup>, T: 295 K. Modified with permission from [120], Copyright 2010, The Electrochemical Society.

A two step, four electron mechanism was proposed for the electrooxidation of NaBH<sub>4</sub> on the Zn anode shown by reactions (60) and (61) [101].



Santos and Sequeira employed Zn as an anode catalyst in their NaBH<sub>4</sub> – H<sub>2</sub>O<sub>2</sub> cell with a Pt cathode. They were able to achieve a peak power density of 470 mW cm<sup>-2</sup> with an open circuit potential of 2.14 V, of a possible 3.01 V, at 295 K, and an anolyte composition of 1 M NaBH<sub>4</sub> – 4 M NaOH (pH: 14.6). Their cell was not stable, being limited by the performance of the low anode activity at short operation times, eventual

degradation of the cathode performance at long operation times due to  $\text{BH}_4^-$  and  $\text{ZnO}_2^{2-}$  crossover to the cathode compartment, and possibly dissolution of the Zn. Operation stability of the cell was limited to 6 hours. The cell was also not stable under open circuit conditions for that matter.

### 1.3.6 Nickel

One of the attractive features of the DBFC is the possibility of using much cheaper electrocatalysts than Pt for both the cathode and the anode. Nickel is one of the cheapest metals ( $\sim \$22.6 \text{ USD kg}^{-1}$  as quoted from the LME on November 25, 2010 [122]) which is active as an anode electrocatalyst for  $\text{BH}_4^-$  electro-oxidation compared to Pt. However, Ni is also electroactive for the hydrolysis of  $\text{BH}_4^-$  [52], which can be problematic for the DBFC system. Poly(N-vinyl-2-pyrrolidone)-stabilized Ni(0) nanoclusters were synthesized by Metin and Özkar, having a  $\text{NaBH}_4$  hydrolysis activity, expressed as  $\text{H}_{2(\text{g})}$  evolution rate, of  $4.25 \text{ L}_{\text{H}_2} \text{ min}^{-1} \text{ g}^{-1}$  at STP [63,123]; the reaction temperature was not specified. Borohydride has been found to electro-oxidize on Ni via a 4 electron process [9,20,91,124]. However Ni is not as active as Pt for  $\text{BH}_4^-$  electro-oxidation. Compared to carbon supported Au, Pt, or Pd catalysts with the same loading, carbon supported Ni catalysts exhibited the lowest performance during fuel cell tests. For example, a peak power density of  $\sim 41 \text{ mW cm}^{-2}$  was achieved for a  $2 \text{ mg cm}^{-2}$  loading of Ni/ C in comparison to  $\sim 90 \text{ mW cm}^{-2}$  for Pd/ C under the same operating conditions (T: 358 K,  $\text{O}_2$  pressure: 1 atm (abs),  $\text{O}_2$  flow rate: 0.2 SLPM, anolyte: 5 wt%  $\text{NaBH}_4$  – 10 wt% NaOH, anolyte flow rate:  $10 \text{ mL min}^{-1}$ ) [88]. On the other hand, its stability has been found to exceed that of Ag, and Pd at high temperatures ( $\sim 343 \text{ K}$ ) [88]. It should be

noted that the electrochemical areas of the catalysts were not taken into account in this comparison. The results of Geng et al. [124] in Figure 22 appears to contradict the aforementioned fuel cell performances of Pt/ C and Ni/ C. It is unclear why the Ni/ C single cell test was much better than the Pt/ C single cell test in terms of power density. Geng et al. measured the mean Ni particle size to be 100 nm but did not measure the Pt particle size. If the Pt particle size was much smaller than the Ni, it is possible that the  $\text{BH}_4^-$  hydrolysis reaction rate was much higher on the Pt/ C than the Ni/ C catalysts during the fuel cell tests shown in Figure 22; leading to mass transport issues and subsequent poor fuel cell performance. This proposition is an example of the aforementioned particle size effect observed by Towne et al. [77] on  $\text{BH}_4^-$  hydrolysis in section 1.2.2. The assumption of a higher hydrolysis rate on the Pt/ C catalyst is supported by the much higher OCV of 1.25 V Geng et al. were able to achieve when using the Ni/ C anode catalysts in their DBFC system versus 1.08 V when using Pt/ C. Assuming the  $\text{BH}_4^-$  crossover rate was the same in the DBFC when testing the Pt/ C versus Ni/ C anode catalysts, a higher OCV may indicate an anode equilibrium potential closer to -1.24 V for the direct  $\text{BH}_4^-$  electro-oxidation versus an anode equilibrium potential of -0.83 V for the electro-oxidation of hydrogen at a pH of 14.

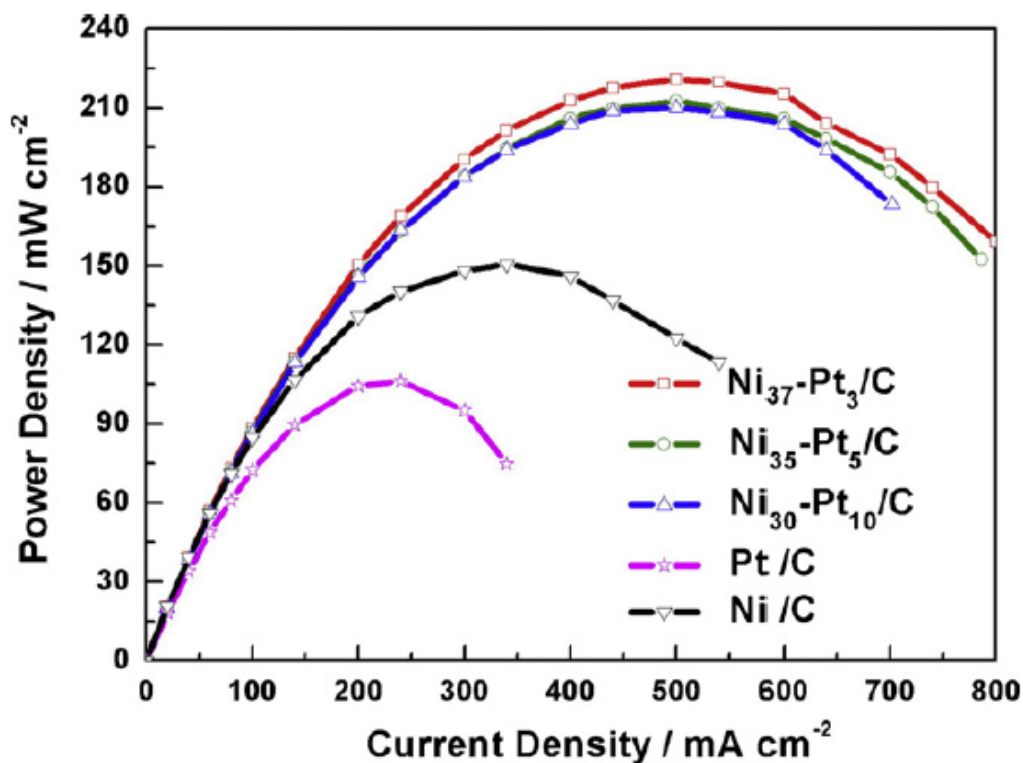


Figure 22. Power density curves of supported Pt, Ni, and Pt-Ni alloys. Anode loading: 1 mg cm<sup>-2</sup> metal, anolyte: 5 wt% NaBH<sub>4</sub> – 10 wt% NaOH, anolyte flow rate: 1 mL min<sup>-1</sup>, T: 333 K, cathode loading: 1 mg cm<sup>-2</sup> Pt/ C, oxidant: O<sub>2</sub>, P<sub>O<sub>2</sub></sub>: 2atm (abs), oxidant flow rate: 0.1 SLPM. Modified with permission from [124], Copyright 2008, Elsevier.

Recent findings have revealed that bimetallic Pt-Ni catalysts of various atomic ratios (1:41 [124], 1:1 [18], 7:3 [125], 1:25 [126]) exhibit much higher performance than the respective individual catalyst components alone (Figure 22). There is also evidence that the Coulombic efficiency of BH<sub>4</sub><sup>-</sup> electro-oxidation on 1:1 atomic ratio Pt-Ni is much greater than the Coulombic efficiency of Pt, which was demonstrated via a comparison of DBFC discharge performances at room temperature [76]. Under the same experimental conditions, Jamard et al. measured a DBFC discharge capacity of 15 Ah (18% Coulombic efficiency) when using a 1.3 mg cm<sup>-2</sup> 80% Pt/ C anode catalyst versus 59 Ah (69% Coulombic efficiency) for a 1:1 atomic ratio 0.8 mg cm<sup>-2</sup> 20% Pt-Ni/ C anode catalyst.

Gyenge et al. [18] reported one of the earliest findings on the performance of Pt-Ni colloidal catalysts for the DBFC system. Comparing a Pt-Ni polarization curve against supported colloidal Pt and various Pt alloys, namely 1:1 atomic ratio Pt-Ir and Pt-Au, Pt-Ni was found to exhibit the highest performance. However, a comparison of the chronopotentiometry results demonstrate that Pt-Ir was a more active/ stable catalyst. No clear evidence was presented with regards to the degree of alloying. Wang et al. [125] demonstrated that alloyed 7:3 Pt-Ni/ C exhibited a similar onset potential ( $\sim -0.9$  V) and a similar but higher peak current density ( $\sim 240$  versus  $220$  mA cm<sup>-2</sup>) in comparison to Pt/ C with similar electrochemical surface areas, using cyclic voltammetry combined with RDE (T: 298 K, rotation rate: 3000 rpm, scan rate: 100 mV s<sup>-1</sup>, electrolyte: 0.1 M NaBH<sub>4</sub> – 6 M NaOH). Non-alloyed Pt-Ni catalysts have also been found to display synergistic effects on DBFC performance. Ma et al. [126] were able to achieve a peak power density of 270 mW cm<sup>-2</sup> using a 1 mg cm<sup>-2</sup> 25:1 Ni:noble metal mixtures of non-alloyed Ni powder mixed with Pt/ C anode catalysts, 1 mg cm<sup>-2</sup> Pt cathode, 5 wt% NaBH<sub>4</sub> – 10 wt% NaOH fuel, and O<sub>2</sub> oxidant at 333 K.

Regarding the catalytic durability, Ni/ C and 1:41 atomic ratio Pt-Ni/ C catalysts, prepared via a N<sub>2</sub>H<sub>2</sub> reduction method, were cycled up to 10 times in 0.2 M NaBH<sub>4</sub> – 2 M NaOH solution at 0.05 V s<sup>-1</sup> and 293 K [124]. While the Ni/ C catalyst activity deactivated substantially after 10 scans, the 1:41 Pt-Ni/ C catalyst activity remained strong (Figure 23).

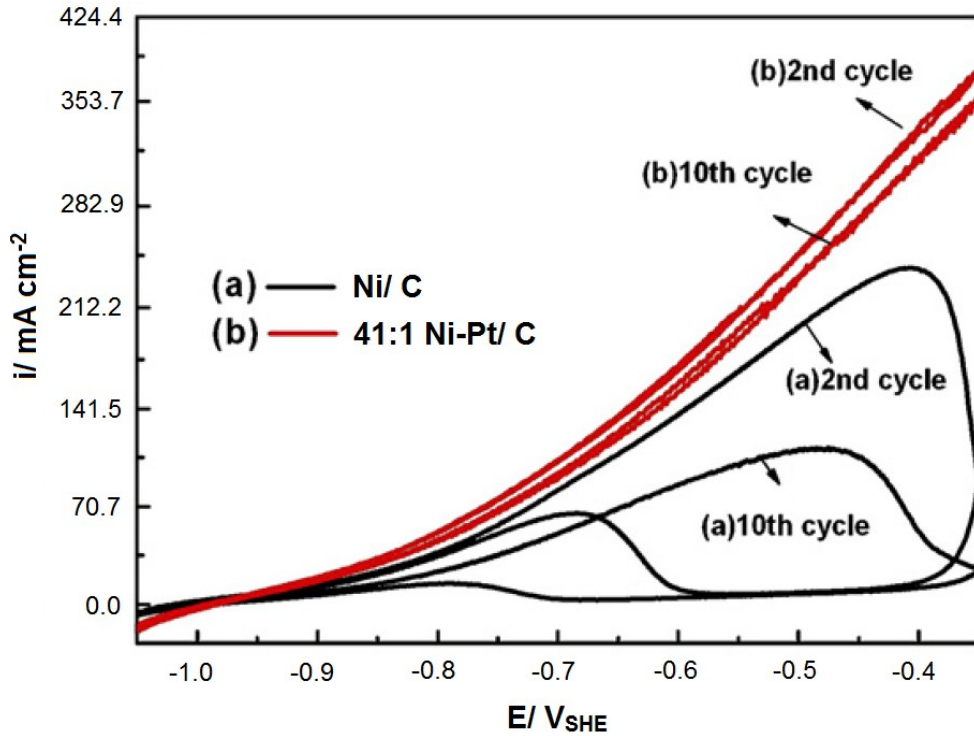


Figure 23. Cyclic voltammograms of (a) Ni/ C and (b) 41:1 Ni-Pt/ C. Anolyte: 0.2 M NaBH<sub>4</sub> – 2 M NaOH, scan rate: 50 mV s<sup>-1</sup>, rotation rate: 1600 rpm, T: 293 K. Modified with permission from [124], Copyright 2008, Elsevier.

### 1.3.7 Palladium

Cheng et al. [88] showed that a DBFC with 2 mg cm<sup>-2</sup> Pd/ C anode catalysts outperformed a DBFC using 2 mg cm<sup>-2</sup> Pt/ C anode catalysts in terms of peak power density. The respective peak power densities were ~90 mW cm<sup>-2</sup> and ~51 mW cm<sup>-2</sup> for Pd/ C and Pt/ C at 358 K. The DBFC longevity tests using Pd/ C were, however, very poor. Pd completely deactivated in less than 5 hours at 50 mA cm<sup>-2</sup> in comparison to Pt/ C where less than 25% of the cell voltage was lost after 50 hours under the same conditions. A stability test on a DBFC employing Pd-Ni anode catalysts showed that Pd-Ni was fairly

stable over 100 hours at  $50 \text{ mA cm}^{-2}$ , the cell voltage linearly decaying to only  $\sim 70\%$  of the starting cell voltage over time [126]

Borohydride electro-oxidation on Pd occurs via a 4 electron process on supported palladium catalysts [127]. The number of electrons for  $\text{BH}_4^-$  electro-oxidation on Pd/ C was calculated and compared to Au/ C and Pd-Au/ C alloys by Simões et al. (Figure 24) [128]. At low overpotentials, the Faradaic efficiency for  $\text{BH}_4^-$  electro-oxidation on Pd/ C is relatively low ( $< 5$  electrons), however, as the potential is increased to  $-0.3 \text{ V}$  to  $-0.2 \text{ V}$ , the faradaic efficiency reaches a maximum ( $6.5 < n < 7$ ).

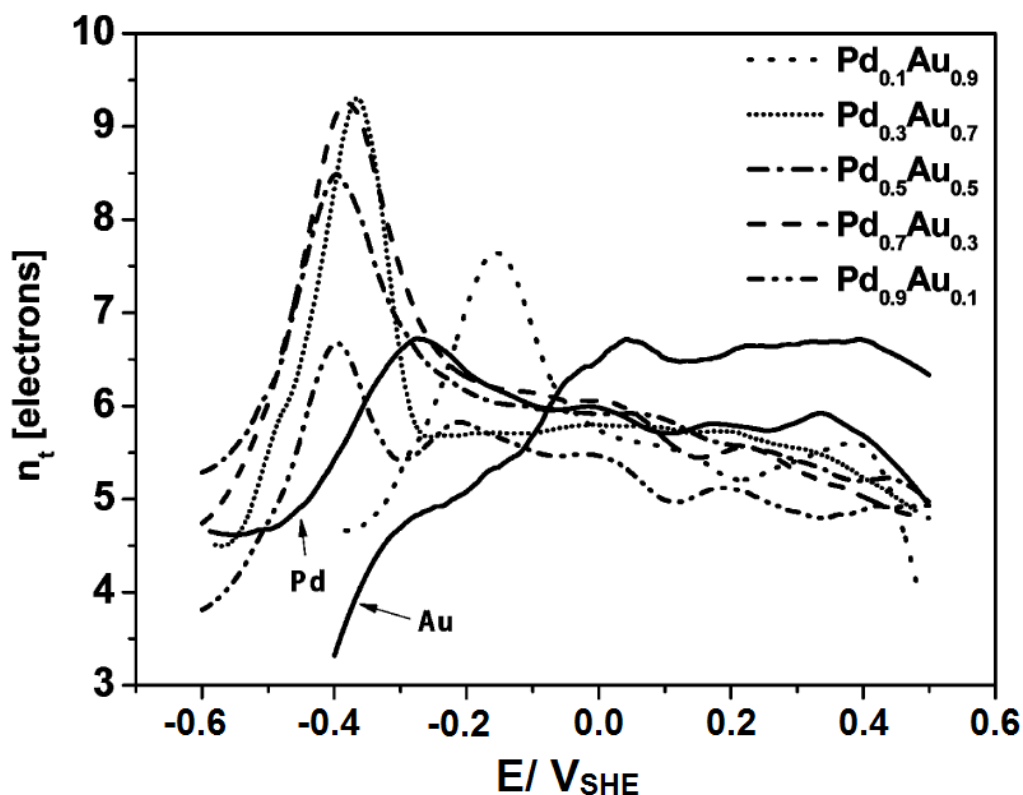


Figure 24. Calculated number of electrons exchanged on Pd/ C, Au/ C, and Pd-Au/ C alloys. Electrolyte:  $1 \times 10^{-2} \text{ M NaBH}_4 - 1 \text{ M NaOH} - \text{N}_2$  saturated, T: 293 K. Modified with permission from [128], Copyright 2009, American Chemical Society.

Alloying Pd with Au revealed some interesting insights into the mechanism of  $\text{BH}_4^-$  electro-oxidation. It was found that hydrogen evolution was more severe when using Pd-Au/ C alloy compared to Pd/ C (Figure 25) [128]. A possible explanation for the observed lower Faradaic efficiency of the Pd-Au catalyst is the lower activity of Au for hydrogen electro-oxidation produced by  $\text{BH}_4^-$  hydrolysis on Pd. The lower  $\text{H}_{2(\text{g})}$  evolution on Pd at  $E > -0.5$  V compared to Au demonstrates the greater activity of Pd for hydrogen electro-oxidation (Figure 25). In addition, Pd has also been found to suppress hydrogen evolution due to its' ability to absorb hydrogen [90,129].

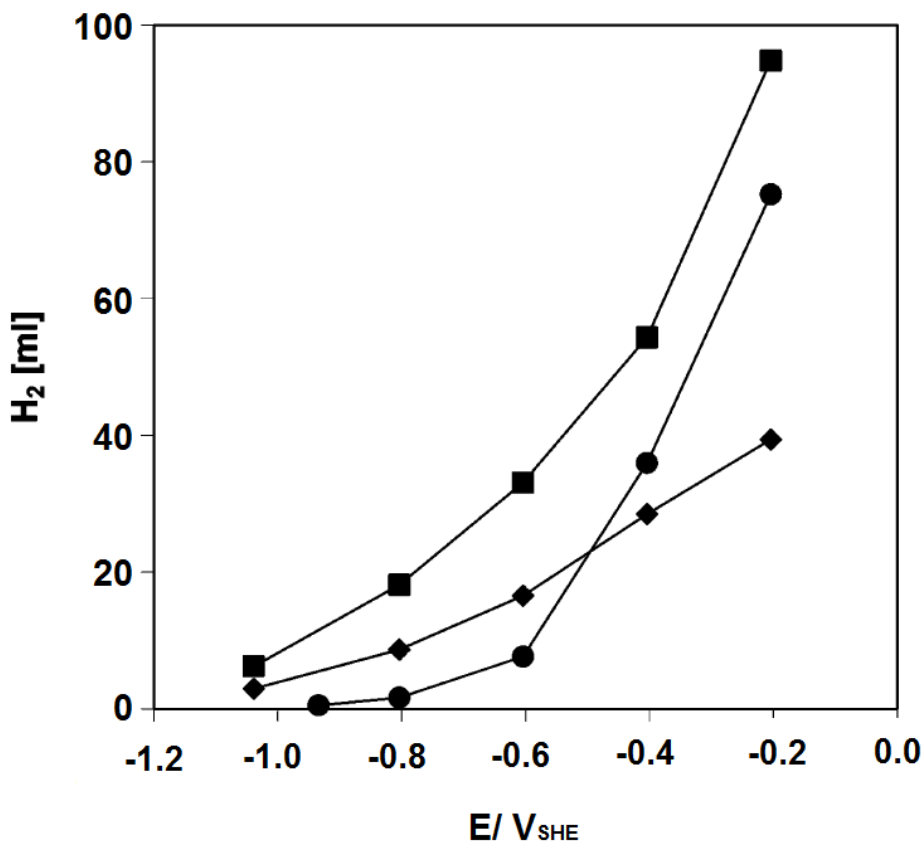


Figure 25. Hydrogen generation on  $\blacklozenge$  Pd/ C,  $\bullet$  Au/ C, and  $\blacksquare$  Pd<sub>0.7</sub>Au<sub>0.3</sub>/ C catalysts. Hydrogen was measured by water displacement in a column at ambient conditions. Electrolyte: 0.124 M NaOH – 0.136 M NaBH<sub>4</sub>, T: 293 K, P: 1 atm (abs), Metal loading: 0.4 mg cm<sup>-2</sup>, Electrode Area: 2.42 cm<sup>2</sup>. Modified with permission from [128], Copyright 2009, American Chemical Society.

### 1.3.8 Hydrogen Storage Alloys

The oxidation mechanism of BH<sub>4</sub><sup>-</sup> on hydrogen storage alloys differ in comparison to the catalysts previously discussed. Whereas DBFC catalysts are conventionally designed to avoid NaBH<sub>4</sub> hydrolysis, hydrogen storage alloys are designed to absorb hydrogen produced from NaBH<sub>4</sub> hydrolysis. “Chemical charging” of the hydrogen storage alloy occurs by simply immersing the electrode in NaBH<sub>4</sub> solution. Optimal “charging” or activation of the hydrogen storage alloy may require several hours

of immersion. Using  $MmNi_{4.03}Co_{0.42}Mn_{0.31}Al_{0.24}$ , Wang et al. found that increased “charging” times, up to 93 hours in 0.1 M  $NaBH_4$  at 293 K and 1 atm can increase the catalyst performance significantly, however the performance will gradually degrade over time as the absorbed hydrogen is consumed but not replaced at the same rate [130]. One gram of hydrogen storage alloy can absorb approximately 0.17 L of hydrogen at STP or an equivalent capacity of  $400 \text{ Ah kg}^{-1}$  [131]. During fuel cell operation, the absorbed hydrogen is oxidized via the following reaction:



High fuel utilization efficiencies, greater than 90% at  $50 \text{ mA cm}^{-2}$ , have been reported for this reaction on  $LaNi_{4.5}Al_{0.5}$  [131,132]. By contrast, fuel utilization efficiencies of a DBFC using a Ni anode catalyst have been shown to range from 18% to 50% depending on the current density [20,133]. Suda and co-workers achieved a power density of  $190 \text{ mW cm}^{-2}$  at 358 K using a  $Zr_{0.9}Ti_{0.1}Mn_{0.6}V_{0.2}Co_{0.1}Ni_{1.1}$  anode catalyst and a Pt cathode [69]. Arguably, the DBFC systems that employ hydrogen storage alloys as an anode catalyst are more similar to an insitu IBFC than a DBFC.

Liu and Suda found that at low  $BH_4^-$  concentrations ( $0.37 \text{ M } BH_4^-$ ), the evolution of hydrogen due to  $BH_4^-$  hydrolysis can be partially depressed due to its absorption in hydrogen storage alloys [131]. However, at higher  $BH_4^-$  concentrations ( $2.4 \text{ M } BH_4^-$ ) at 303 K, the rate of  $BH_4^-$  hydrolysis exceeds the rate and/ or capacity of hydrogen absorption and electro-oxidation [131,132]. The effect of  $BH_4^-$  hydrolysis in a DBFC system employing hydrogen storage alloy catalysts is especially noticeable when creating a stack [129]. A significant decrease in performance per cell was observed by Liu et al.

when stacking ten cells, using bipolar stainless steel plates, and employing hydrogen storage alloy catalysts, versus a single cell performance (Figure 26). The performance decrease was attributed to uneven fuel distribution caused by hydrogen evolution.

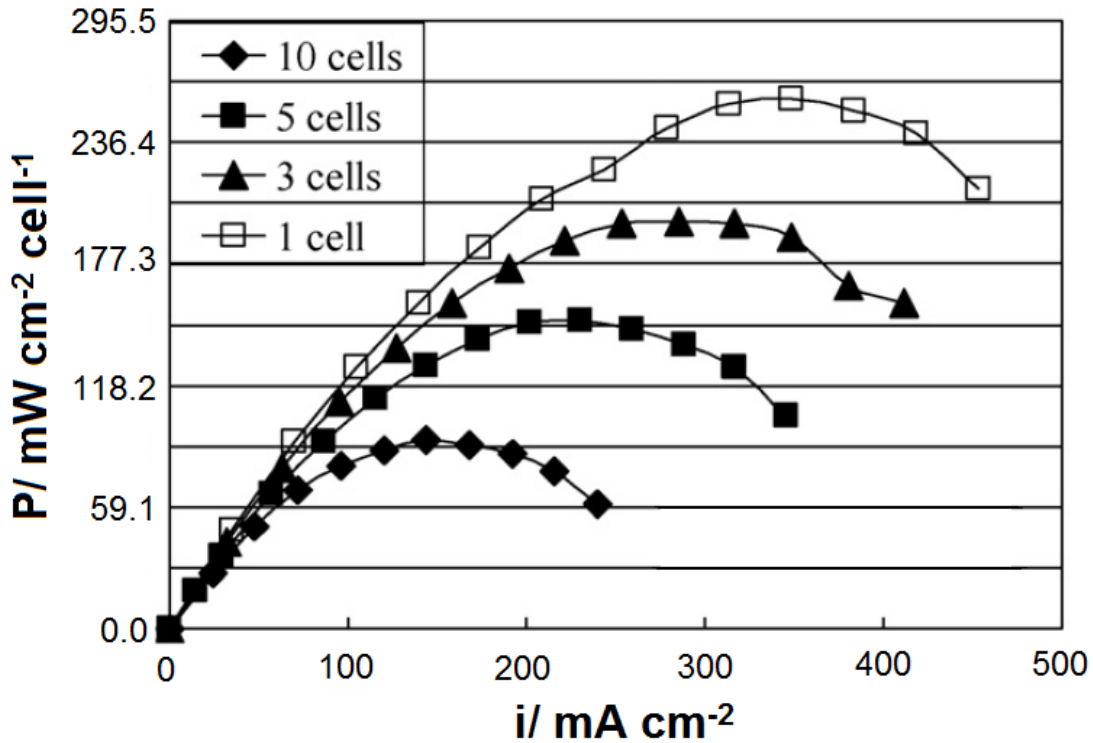


Figure 26. Single and multi-cell stack performance using bipolar stainless steel plates. Anode: 150 mg cm<sup>-2</sup> Zr-Ni alloy with Ni powder and PTFE binder, anolyte: 10 wt% NaBH<sub>4</sub> – 5 wt% NaOH, anolyte flow rate: cell number x 150 mL min<sup>-1</sup>, T: 333 K, cathode: 1 mg cm<sup>-2</sup> 50% Pt/ C, oxidant: air, oxidant flow rate: cell number x 5 SLPM, P<sub>air</sub>: not reported. Modified with permission from [129], Copyright 2008, Elsevier.

### 1.3.9 Rhodium and Rh-Ir Alloys

A peak power density of 270 mW cm<sup>-2</sup> at 290 mA cm<sup>-2</sup> was achieved by Kiran et al. [134] using a 2:1 atomic ratio Rh-Ir/ C alloyed anode catalysts at 353 K. The catalyst loadings were of 0.5 mg cm<sup>-2</sup> Rh-Ir/ C and 2 mg cm<sup>-2</sup> Pt/ C for the anode and cathode

respectively. The anolyte and catholyte of the system consisted of 2.64 M NaBH<sub>4</sub> – 2.5 M NaOH, and 2.2 M H<sub>2</sub>O<sub>2</sub> – 1.5 M H<sub>2</sub>SO<sub>4</sub>. With unalloyed Rh/ C and Ir/ C loadings under the same conditions 200 mW cm<sup>-2</sup> and 140 mW cm<sup>-2</sup> peak power densities were achieved, respectively. At a lower temperature, 298 K, Kiran et al. were only able to achieve 10.7 % of the theoretical discharge capacity when using Rh-Ir/ C and even poorer efficiencies were reported when using monometallic Rh/ C and Ir/ C catalysts; 8.1% and 7.9% respectively. The poor discharge capacity efficiency was attributed to a combination of BH<sub>4</sub><sup>-</sup> hydrolysis and crossover. Neutralization of the anolyte by catholyte crossover, and the high BH<sub>4</sub><sup>-</sup> concentration of 2.64 M likely enhanced both BH<sub>4</sub><sup>-</sup> hydrolysis and crossover in the system as well. The performance of the DBFC system employed by Kiran et al. was particularly hampered by the performance of the H<sub>2</sub>O<sub>2</sub> cathode (Figure 27). In addition to creating a mixed potential at the cathode, thus effectively lowering the cathode potential, BH<sub>4</sub><sup>-</sup> crossover may directly reduce the H<sub>2</sub>O<sub>2</sub> before it is consumed by the fuel cell. In summary, mixed potentials, Ohmic resistance due to electrolyte neutralization, and mass transport issues due to H<sub>2</sub>O<sub>2</sub> consumption all plague the performance of the cathode.

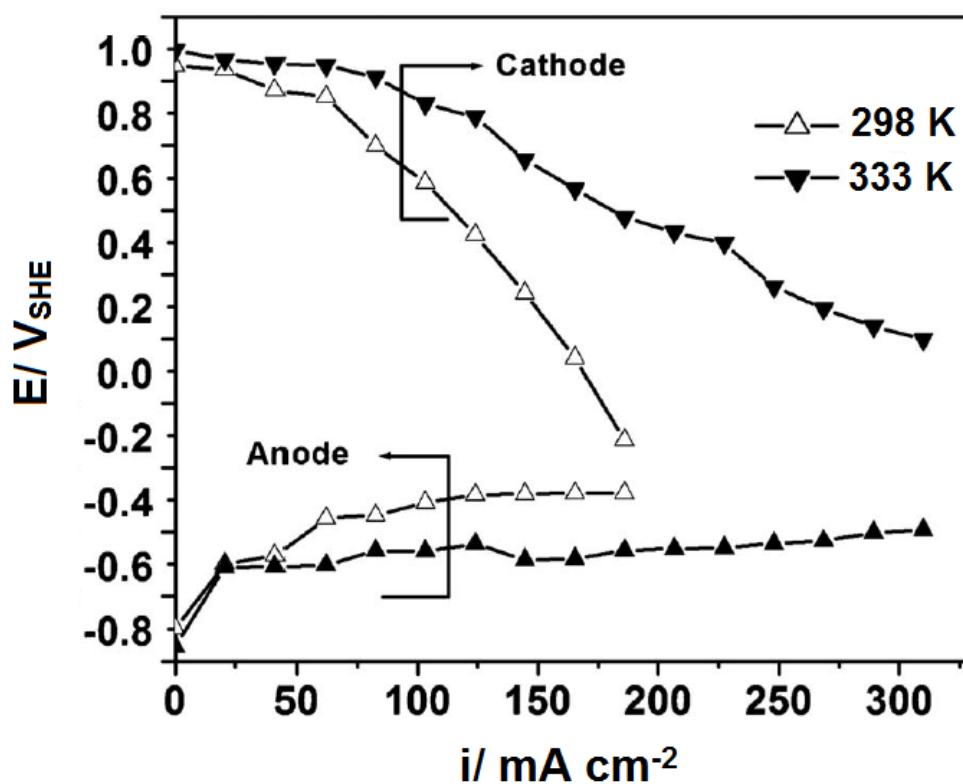


Figure 27. Rh-Ir/ C anode catalyst DBFC polarization curve at 298 K and 333 K. Anode:  $0.5 \text{ mg cm}^{-2}$  Rh-Ir/ C, anolyte:  $2.64 \text{ M NaBH}_4 - 2 \text{ M NaOH}$ , anolyte flowrate:  $1.5 \text{ L min}^{-1}$ , cathode:  $2 \text{ mg cm}^{-2}$  Pt/ C, catholyte:  $2.2 \text{ M H}_2\text{O}_2 - 1.5 \text{ M H}_2\text{SO}_4$ , catholyte flow rate:  $2.1 \text{ L min}^{-1}$ . Modified with permission from [134], Copyright 2010, The Electrochemical Society.

### 1.3.10 Catalyst Summary

Here, a brief summary is presented in the table below for the top five performing anode catalysts in terms of DBFC peak power density.

Table 5. Top five performing anode catalysts in DBFC using an Air or O<sub>2</sub> oxidant.

Anode catalyst and loading	T (K)	Anolyte	P (mW cm <sup>-2</sup> )	Cathode catalyst and loading	Oxidant (atm <sub>abs</sub> )	Ref.	Comments
25:1 Ni + Pt/ C 1 mg cm <sup>-2*</sup>	333	5 wt% NaBH <sub>4</sub> 10 wt% NaOH	270	Pt/ C 1 mg cm <sup>-2</sup>	O <sub>2</sub> (N/A)	[126]	Ni is relatively cheaper than Pt however Ni by itself is unstable. Some half-cell evidence of increased stability when alloyed with Pt, but no fuel cell data.
44:1 Ni + Pd/ C 15 mg cm <sup>-2*</sup>	333	10 wt% NaBH <sub>4</sub> 20 wt% NaOH	250	Pt/ C 1 mg cm <sup>-2</sup>	Air (N/A)	[90]	Both Ni and Pd are less stable than Pt. No evidence of increased stability when Ni and Pd are alloyed.
PtRu/ C 1 mg cm <sup>-2</sup>	333	2 M NaBH <sub>4</sub> 1 M NaOH	200	Pt/ C 1 mg cm <sup>-2</sup>	O <sub>2</sub> (1)	[135]	Ru increases BH <sub>4</sub> <sup>-</sup> hydrolysis resulting in low fuel utilization and two phase flow in the anode compartment.
Zr <sub>0.9</sub> Ti <sub>0.1</sub> Mn <sub>0.6</sub> V <sub>0.2</sub> Co <sub>0.1</sub> Ni <sub>1.1</sub> 200 mg cm <sup>-2</sup>	358	10 wt% NaBH <sub>4</sub> 20 wt% NaOH	190	Pt/ C 2 mg cm <sup>-2</sup>	O <sub>2</sub> (1)	[69]	BH <sub>4</sub> <sup>-</sup> hydrolysis rate on Ni can be high. Zr is expensive relative to non-precious metals. High catalyst loadings are typically required for DBFC operation.
Pt/ C 1 mg cm <sup>-2</sup>	333	5 wt% NaBH <sub>4</sub> 10 wt% NaOH	106	Pt/ C 1 mg cm <sup>-2</sup>	O <sub>2</sub> (2)	[124]	Pt has high durability in alkaline conditions but is expensive relative to most precious metals.

\* Total loading of unalloyed mixture

## 1.4 Objectives

The focus of the following work is to investigate the mechanism for  $\text{BH}_4^-$  electro-oxidation on Pt and to develop the DBFC anode.

The electro-oxidation of  $\text{BH}_4^-$  on Pt has been studied since the mid 20<sup>th</sup> century; however its exact mechanism has not yet been resolved. Here, for the first time, fundamental electrochemical methods in conjunction with the quartz crystal microbalance were used in an attempt to contribute to the understanding of the  $\text{BH}_4^-$  electro-oxidation on Pt.

Development of the DBFC anode was undertaken by investigating the effect of anode electrocatalysts and support or structure on DBFC performance. A novel DBFC anode electrocatalyst, Os, was tested in a DBFC for the first time and its performance relative to Pt and PtRu electrocatalysts was evaluated. Also, monolithic three-dimensional electrodes were compared against Vulcan<sup>®</sup> carbon supported and non-supported electrocatalysts and evaluated via fuel cell tests.

## 2 Sodium Borohydride Electro-oxidation Mechanism on Polycrystalline Platinum\*

The goal of the investigation presented in this chapter is to contribute to the understanding of the  $\text{BH}_4^-$  electro-oxidation on Pt through investigation of the  $\text{BH}_4^-$  concentration and thiourea adsorption effects. These aspects were less systematically investigated previously in the literature. Moreover, for the first time in the study of  $\text{BH}_4^-$  electro-oxidation, the voltammetry is coupled with electrochemical quartz crystal microbalance (EQCM) measurements (In Appendix B a general description of the EQCM technique is provided).

A study by Rostamikia and Janik on the reaction mechanism of  $\text{BH}_4^-$  electro-oxidation using density functional theory calculations showed that adsorption of  $\text{BH}_4^-$  on Pt (111) is dissociative in nature [136]. During the initial adsorption,  $\text{BH}_4^-$  breaks down into adsorbed  $\text{BH}^*$  and three  $\text{H}^*$  species. It was suggested that the excess of adsorbed  $\text{H}^*$  species may be responsible for the hydrogen evolution that has been observed to occur on Pt anodes [136].

Regarding the  $\text{BH}_4^-$  electro-oxidation mechanism on Pt the number of electrons determined by the Koutecky-Levich analysis of RDE data was close to 8 (i.e., between 7.1 and 7.7) at low anodic overpotentials (i.e. in the hydrogen adsorption/desorption

---

\* This chapter is based on the following published works:

V.W.S. Lam, D.C.W. Kannangara, A. Alfantazi, and E.L. Gyenge, *J. Phys. Chem. C* 115 (2011) 2727.

V.W.S. Lam, D.C.W. Kannangara, A. Alfantazi, and E.L. Gyenge, *J. Phys. Chem. C* 115 (2011) 10312.

V. W. S. Lam, D. Kannangara, A. Alfantazi, and E. L. Gyenge, *Borohydride Electrooxidation on Polycrystalline Pt Electrodes* (Regional Electrochemistry Meeting of South-East Asia, Thailand, November 17, 2010).

region of the Pt) and decreased to 5 – 6 electrons at high overpotentials (i.e. on the partially oxidized Pt surface) [100]. Employing the  $\text{BH}_4^-$ -air cell discharge experiment, however, only 4 and 5 electrons were calculated at discharge current densities of  $25 \text{ mA cm}^{-2}$  and  $50 \text{ mA cm}^{-2}$ , respectively [17].

Further discussion of the literature regarding the mechanism for  $\text{BH}_4^-$  electro-oxidation on Pt can be found in Section 1.3.1 and the effect of TU on  $\text{BH}_4^-$  electro-oxidation on Pt was presented in Section 1.2.2.

## **2.1 Experimental Procedure**

### **2.1.1 Rotating Disk Electrode (RDE) and Cyclic Voltammetry (CV)**

Rotating disk electrode and CV experiments were conducted with a 0.5 cm diameter ( $0.196 \text{ cm}^2$ ) Pt disk (Pine Inc.) electrode. The Pt disk was polished with a  $1 \mu\text{m}$  diamond paste for 2 minutes and sonicated in  $15 \text{ M}\Omega$  deionized water for 1 minute. The electrochemical area of the Pt disk electrode was determined to be  $0.276 \text{ cm}^2$  using the hydrogen underpotential adsorption/desorption method in  $0.5 \text{ M H}_2\text{SO}_4$  at  $20 \text{ mV s}^{-1}$  (see Appendix A for a description on determining the electrochemical area). Thus, the surface roughness factor was 1.4. The current densities on the Pt disk are reported per electrochemical area. After the area measurement, and prior to the CV/ RDE experiments the Pt disk electrode was subjected to electrochemical cleaning by carrying out 10 cyclic voltammograms between  $-0.9$  and  $0.6 \text{ V}$  in  $2 \text{ M NaOH}$  at  $10 \text{ mV s}^{-1}$ . Note the cleaning step was performed in  $2 \text{ M NaOH}$  and not in acid electrolyte (e.g.  $0.1\text{-}0.5 \text{ M}$

H<sub>2</sub>SO<sub>4</sub>) as in other publications [100], to maintain fidelity with the actual experimental conditions.

A typical three-electrode setup was used with a Hg/HgO, 0.1 M KOH reference electrode (Materials Mates) (0.0926 V versus SHE) and a platinum mesh counter electrode. NaBH<sub>4</sub> solutions of 150 ml were prepared from 98 wt% NaBH<sub>4</sub> (ACROS) at varied concentrations in 2 M NaOH (certified A.C.S. Fisher Scientific). For all solution preparations, 18 MΩ deionized water was used. Various TU concentrations in the working electrolyte were prepared from stock TU (Sigma Aldrich) solutions in 2 M NaOH. All solutions were purged with N<sub>2</sub> gas (Praxair) for two minutes then blanketed with N<sub>2</sub> gas during experiments. The temperature was controlled at 298 K by a borosilicate jacketed glass cell and a water bath.

### **2.1.2 Electrochemical Quartz Crystal Microbalance Experiments**

Microbalance studies were carried out with 0.196 cm<sup>2</sup> standard finished 9 MHz AT Cut platinum resonators (Princeton Applied Research) sputtered on quartz (refer to Appendix B for a general description of the EQCM technique and setup). The quartz crystal microbalance instrument QCA 922 (Seiko, Princeton Applied Research) was used in conjunction with a PARSTAT 2263 (Princeton Applied Research) potentiostat. Experiments were carried out in a three-electrode setup with a Hg/HgO reference electrode (Materials Mates) and a platinum mesh counter electrode. All experiments were conducted using 25 ml solution at room temperature. The Pt resonators were first soaked for 30 seconds in a solution composed of a 1:1 volume ratio of 95 wt% H<sub>2</sub>SO<sub>4</sub> (Fisher) and 30 wt% H<sub>2</sub>O<sub>2</sub> (Fisher) at 293 K. Afterwards, an electrochemical cleaning

was applied in 2 M NaOH identical to the procedure described in section 2.1.1. The electrochemical area of a representative Pt resonator electrode was 0.230 cm<sup>2</sup> as determined by the underpotential hydrogen adsorption/desorption method in 0.5 M H<sub>2</sub>SO<sub>4</sub> at 20 mV s<sup>-1</sup> (Appendix A), which corresponds to a surface roughness factor of 1.17. For voltammograms recorded on the Pt resonator electrode the current density is expressed per the aforementioned electrochemical area.

The quartz crystal microbalance (QCM) was operated simultaneously with cyclic voltammetry (see experimental setup in Appendix B). Thus, the mass changes of the Pt resonator/electrode, detected as differences in the resonant frequency, were recorded as a function of potential. The EQCM is capable of detecting frequency changes as low as 0.1 Hz. The mass changes are calculated based on the proportional relationship with the frequency change of the resonating piezoelectric material (i.e., quartz):

$$\Delta f = -C_f \Delta m \quad (63)$$

where  $\Delta f$  is the deviation from the fundamental resonant frequency of the piezoelectric material (Hz),  $C_f$  is the Sauerbrey constant (Hz cm<sup>2</sup>μg<sup>-1</sup>), and  $\Delta m$  is the mass change per unit area (μg cm<sup>-2</sup>).

The experimentally determined Sauerbrey constant for the 9 MHz Pt resonator using Cu underpotential deposition (Cu-UPD) was 168.2 Hz cm<sup>2</sup>μg<sup>-1</sup> (Appendix C). The theoretical values reported in the literature for  $C_f$  in vacuum are between 179 Hz cm<sup>2</sup>μg<sup>-1</sup> [137] and 183 Hz cm<sup>2</sup>μg<sup>-1</sup> [138]. The approximately 6-8% difference between the experimental and theoretical values is acceptable and it can be caused by a number of

factors such as the method used for experimental determination of  $C_f$ , the scan rate applied for the stripping voltammetry, surface roughness and thickness of the deposited film. The experimental value of the Sauerbrey constant decreases with decreasing film thickness, from  $238 \text{ Hz cm}^2 \mu\text{g}^{-1}$  (for films thicker than 7 monolayers) to  $167 \text{ Hz cm}^2 \mu\text{g}^{-1}$  [137]. Thus, the thin Cu-UPD layer (about one monolayer) generates a  $C_f$  value closer to the lower limit.

## 2.2 Pt Rotating Disk Electrode Studies

Typical cyclic voltammograms of  $\text{BH}_4^-$  on Pt show four characteristic peaks corresponding to the peaks annotated as *a1*, *a2*, and *c1*, and *c2* in Figure 28. The *a1* peak was believed to be largely attributed to the oxidation of evolved hydrogen, *a2* was believed to be the direct 4 electron electro-oxidation of  $\text{BH}_4^-$ , and *c1* was proposed to be due to the electro-oxidation of  $\text{BH}_3\text{OH}^-$  [9].

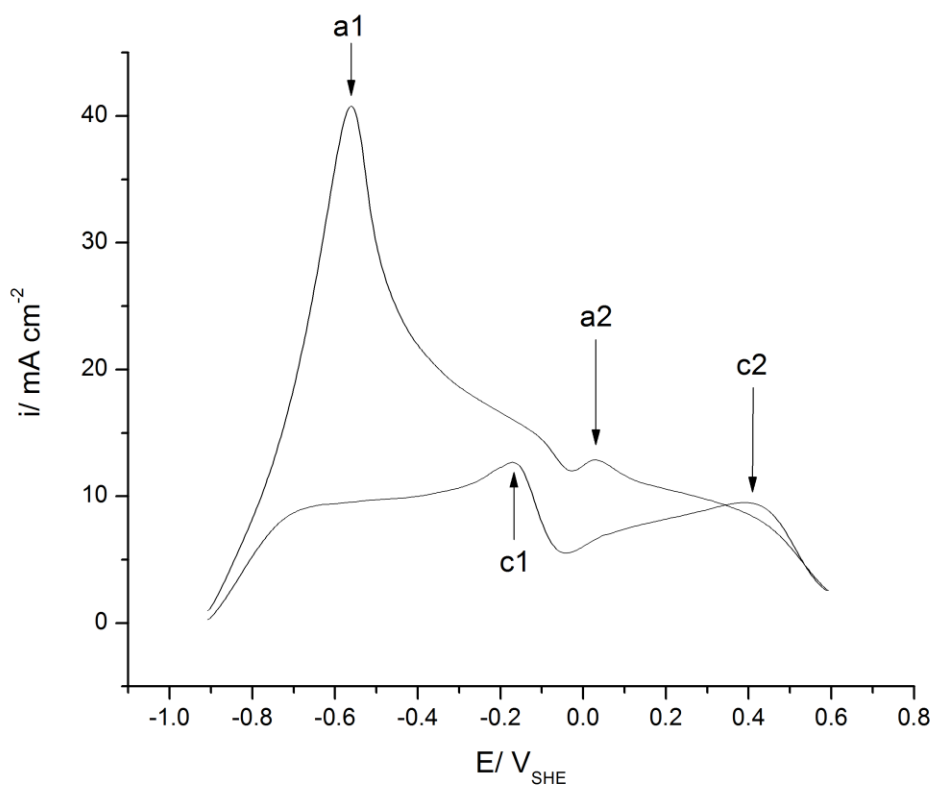


Figure 28. Cyclic voltammogram of 0.5 mM NaBH<sub>4</sub> – 2 M NaOH on Pt at 0 rpm and 298 K. Scan rate: 10 mV s<sup>-1</sup>.

It was observed that the behaviour of the limiting current densities varied with rotation rates according to the Levich equation, at low concentrations of NaBH<sub>4</sub> (Figure 29).

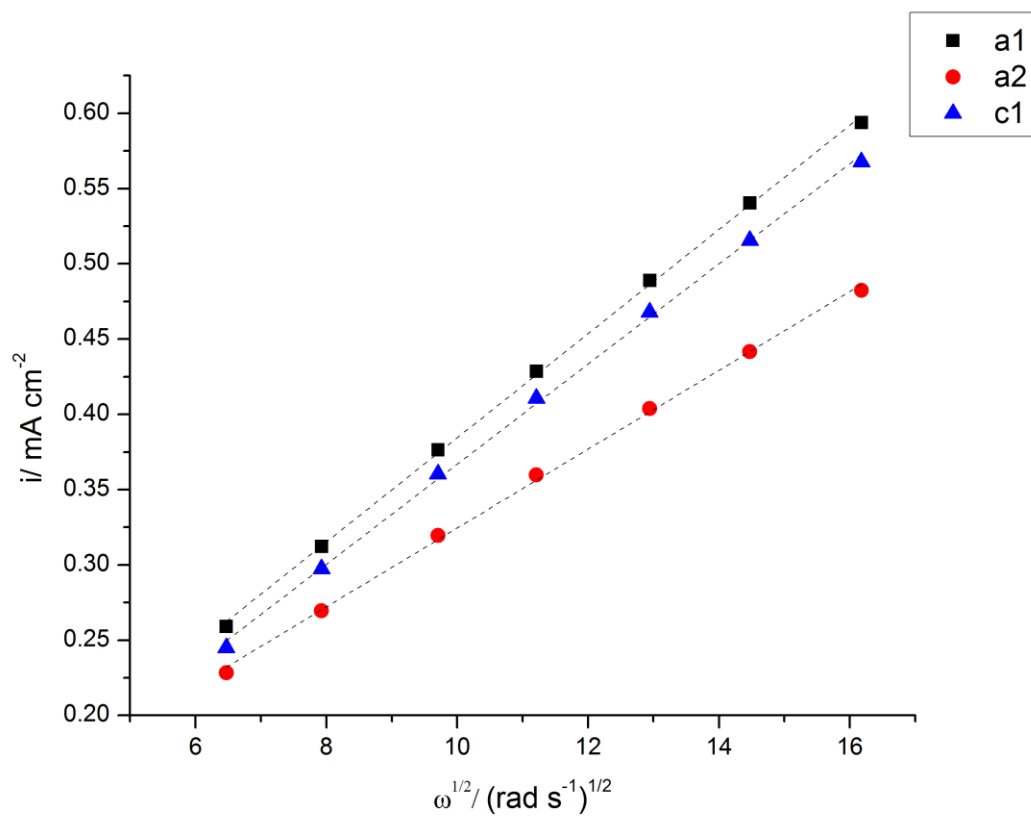


Figure 29. Levich plot of 0.1 mM  $\text{NaBH}_4$  – 2 M  $\text{NaOH}$  electro-oxidation on Pt at 298 K. Scan rate:  $10 \text{ mV s}^{-1}$ .

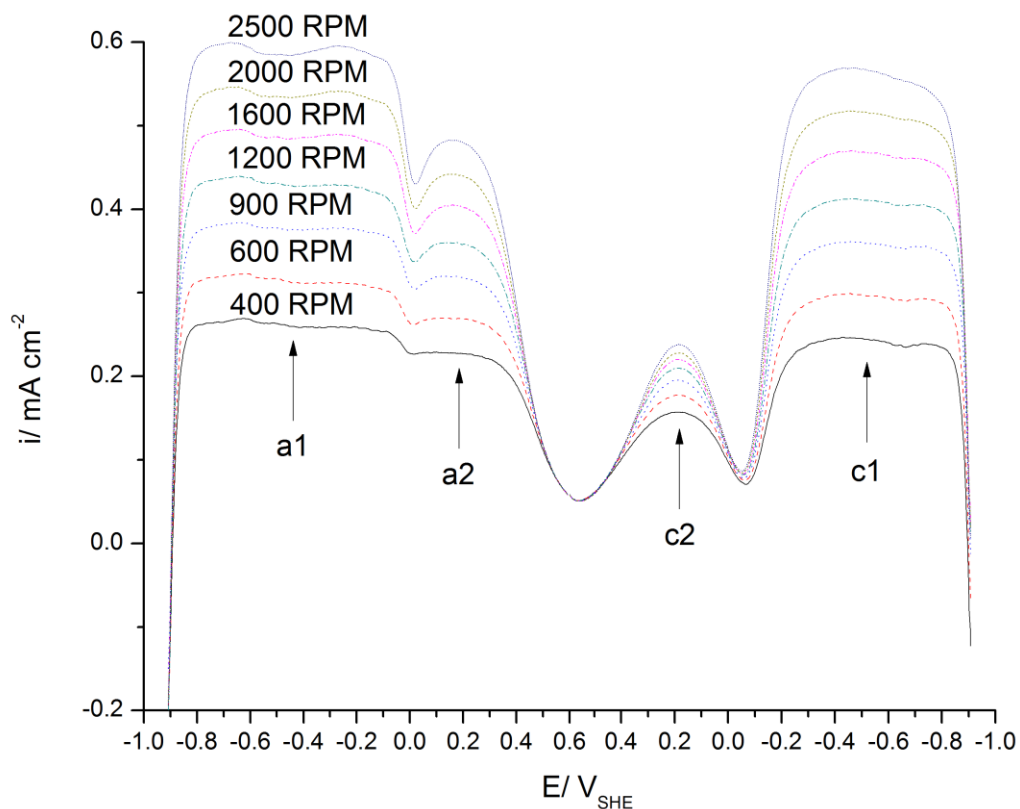


Figure 30. Effect of rotation rate for 0.1 mM NaBH<sub>4</sub> – 2 M NaOH at 298 K. Scan rate: 10 mV s<sup>-1</sup>.

Using the Levich equation (64), the number of electrons for the electro-oxidation of BH<sub>4</sub><sup>-</sup> species responsible for the presence of the a1, a2, and c1 peaks were calculated for varied BH<sub>4</sub><sup>-</sup> concentrations and are shown in Figure 31.

$$i_l = 0.62nFD_o^{\frac{2}{3}}\omega^{\frac{1}{2}}\nu^{\frac{-1}{6}}C_o \quad (64)$$

$i_l$  is the limiting current density,  $n$  is the number of electrons,  $F$  is Faraday's constant,  $D_o$  is the diffusion coefficient of BH<sub>4</sub><sup>-</sup> ( $1.25 \times 10^{-5}$  cm<sup>2</sup> s<sup>-1</sup> at 298 K [139]),  $\omega$  is the angular

rotation rate in  $\text{rad s}^{-1}$ ,  $\nu$  is the kinematic viscosity ( $0.0126 \text{ cm}^2 \text{ s}^{-1}$  at 298 K [82]),  $C_o$  is the bulk  $\text{BH}_4^-$  concentration.

Interestingly, the number of electrons for the a1 peak at 0.5 mM  $\text{NaBH}_4$  was calculated to be approximately 5.8 electrons; indicating that the direct  $\text{BH}_4^-$  electro-oxidation occurs at much lower overpotentials than previously thought [9,17,84,86]. Undoubtedly, hydrogen oxidative desorption also occurs within the potential range of the a1 peak. The measured current from the a1 peak is most likely a composition of the contribution of direct  $\text{BH}_4^-$  electro-oxidation and hydrogen electro-oxidation. It is possible that the increased convection of evolved hydrogen away from the electrode surface with increased rotation rates decreases the contribution of hydrogen electro-oxidation to the measured current; resulting in the high number of electrons calculated for the a1 peak.

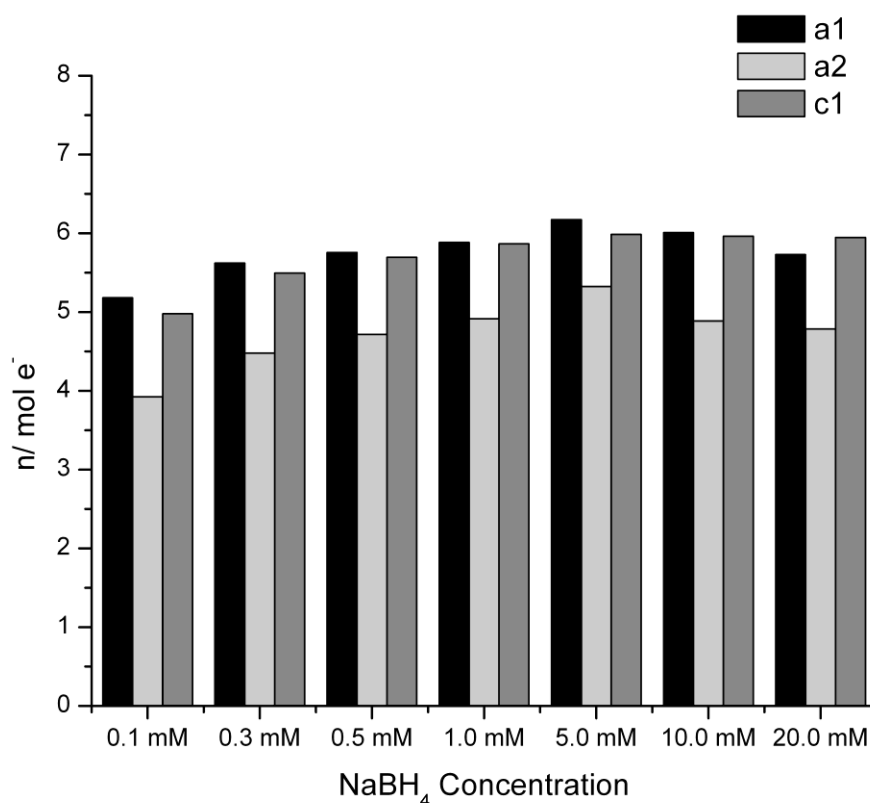


Figure 31. Effect of NaBH<sub>4</sub> concentration on calculated number of electrons from Pt RDE studies. T: 298 K, electrolyte: NaBH<sub>4</sub> – 2 M NaOH.

The a2 peak which was previously identified as the direct BH<sub>4</sub><sup>-</sup> electro-oxidation was calculated to be a 4.7 electron process at 0.5 mM NaBH<sub>4</sub> (Figure 30), which is comparable to the 4 electrons calculated by Gyenge in his cyclic voltammetry experiments on BH<sub>4</sub><sup>-</sup> electro-oxidation with thiourea as an additive [9]. The c1 peak which was believed to be attributed to the oxidation of BH<sub>3</sub>OH<sup>-</sup>, identified by Gardiner and Collat as a 3 electron process [98,99], was calculated to be close to a 5.7 electron process.

As the ratio of BH<sub>4</sub><sup>-</sup> to OH<sup>-</sup> in solution increases, the number of electrons for the oxidation at a1, a2, and c1 also increased in Figure 31. The highest number of electron

counts were obtained at a  $\text{BH}_4^-$  concentration of 5 mM; while at concentrations above 5 mM a decline to 4 electrons is observed for the a2 peak. The lower number of electrons for  $\text{BH}_4^-$  electro-oxidation on Pt at high  $\text{BH}_4^-$  concentrations appears to be in agreement with the literature [9,17,84,86]. Martins et al. calculated 5.7 electrons for 26.5 mM  $\text{NaBH}_4$  and 4.3 electrons for 39.7 mM  $\text{NaBH}_4$ , Gyenge calculated 4 electrons for 30 mM  $\text{NaBH}_4$ , and Elder and Hickling calculated 2 to 4 electrons for 100 mM  $\text{KBH}_4$  [9,17,84,86].

An effect of  $\text{BH}_4^-$  concentration on the number of electrons was also observed by Martins et al. through analysis of  $\text{BH}_4^-$  oxidation discharge curves in 3 M NaOH supporting electrolyte [140]. They found that the number of electrons initially increased with increased  $\text{BH}_4^-$  concentration, then decreased upon further increase of  $\text{BH}_4^-$  concentration (Table 6) [140]. The change in the number of electrons with  $\text{BH}_4^-$  concentration is indicative of a change of  $\text{BH}_4^-$  reaction intermediate species occupying the active surface sites on the Pt electrode and the relative rates of electro-oxidation versus hydrolysis.

Table 6. Calculated number of electrons for  $\text{BH}_4^-$  electro-oxidation on Pt/ C in 3 M NaOH at 298 K [140].

Number of Electrons	$\text{BH}_4^-$ Concentration (mM)
5.3	13.2
5.7	26.5
4.3	39.7

### 2.3 Electrochemical Quartz Crystal Microbalance Study of Pt in 2 M NaOH

Firstly the EQCM response of the bare Pt in 2 M NaOH was evaluated in the absence of  $\text{BH}_4^-$  as a baseline study. Concentrated alkaline solutions (e.g. between 2 to 6 M NaOH) are typically used in DBFC systems to suppress the homogeneous pH-dependent decomposition of  $\text{BH}_4^-$  and to increase the ionic conductivity on the anode side.

Figure 32 shows the EQCM response of the Pt resonator electrode in 2 M NaOH after eleven cycles. The cyclic voltammogram of Pt is characterized by the following four regions (Figure 32): cathodic  $\text{H}_{2(\text{g})}$  evolution and its oxidation (between -0.9 V and -0.75 V), hydrogen underpotential deposition (H- UPD) on the cathodic scan (-0.72 V to -0.55 V), the double layer region (-0.55 V to -0.35 V) and the hydroxide-oxide (-0.35 V to +0.50 V) region.

The cathodic H- UPD peak was at -0.68 V, but, the associated adsorbed hydrogen oxidation on the anodic scan was not distinguishable from the large oxidation current given by the, overpotentially evolved, bulk  $\text{H}_{2(\text{g})}$  (Figure 32). The adsorbed hydrogen can be engaged in a network of hydrogen-bonded  $\text{H}_2\text{O}$  dipoles and  $\text{OH}^-$  ions close to the surface [141,142]. This explains the weakening of the Pt-H bond resulting in the inability for the EQCM to appreciably detect hydrogen adsorption/ desorption. It must be noted that in alkaline solutions, the adsorption of  $\text{H}_2\text{O}$  also does not influence the frequency response, hence no mass change due to  $\text{H}_2\text{O}$  adsorption or desorption can be measured [143].

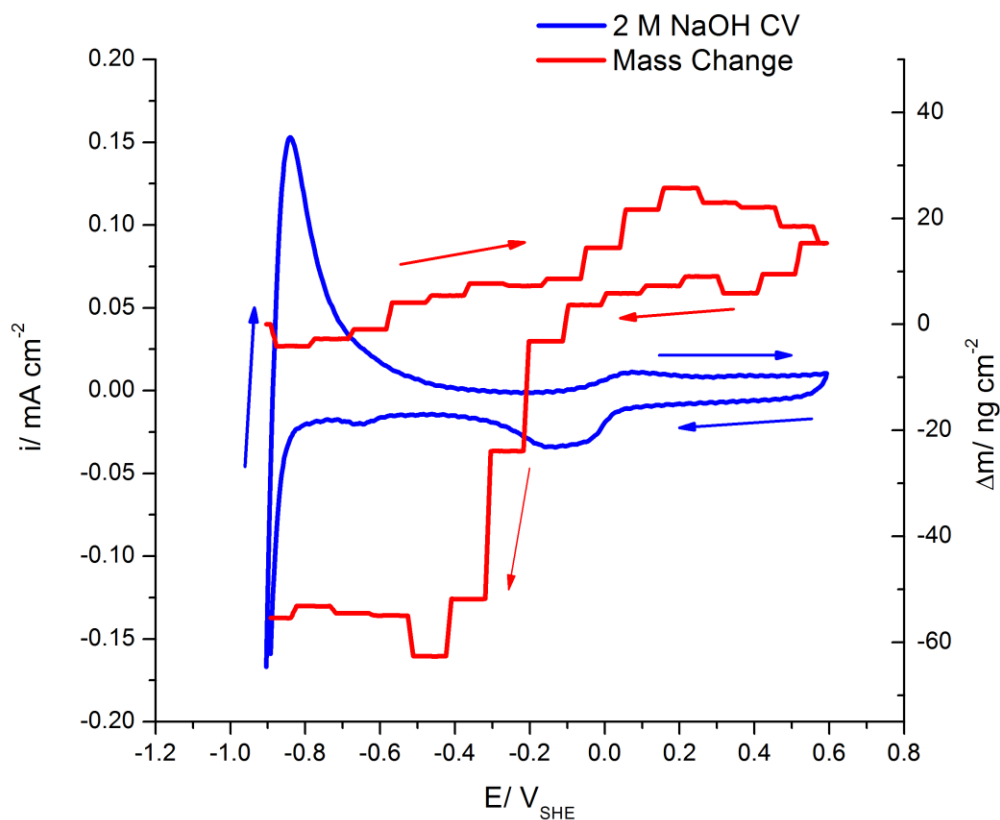
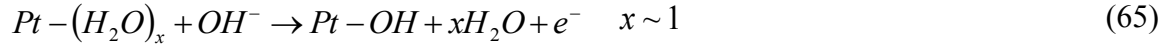


Figure 32. Surface mass changes of the Pt resonator electrode during cyclic voltammetry in 2 M NaOH after 11 scans. T: 293 K; scan rate:  $10 \text{ mV s}^{-1}$ . Reproduced with permission from [104], Copyright 2011, American Chemical Society.

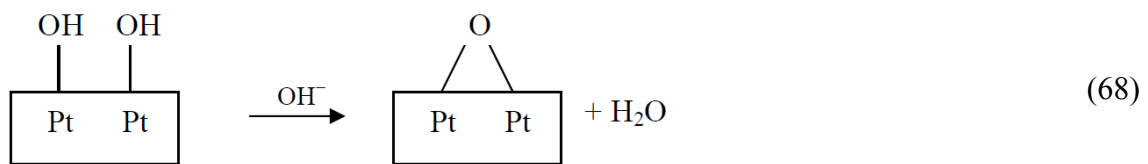
As the potential is scanned beyond the hydrogen region in the anodic direction (forward scan in Figure 32), there is a slight but gradual mass increase in the double layer region, followed by a rapid increase starting at  $-0.06 \text{ V}$  and extending up to  $0.2 \text{ V}$  which is associated with the development of an oxidation peak. In this potential region  $\text{OH}^-$  electrosorption (equation (65)) occurs from approximately  $-0.21 \text{ V}$  to  $0.093 \text{ V}$  for a Pt (111) surface [144].



Since as mentioned earlier in alkaline solutions the adsorption of H<sub>2</sub>O does not influence the frequency response [143], the mass gain between -0.06 V and +0.20 V is due to the formation of surface hydroxide OH<sub>ad</sub> and equation (65) can be written from the point of view of EQCM simply as:



The Pt-OH could be partially converted to surface oxide species either by a non-electrochemical reaction (equations (67) and/ or (68)) or electro-oxidation at potentials higher than 0.2 V (equation (69)). The rate of reaction (68) is strongly dependent on the OH<sub>ad</sub> surface coverage and it is catalyzed by OH<sup>-</sup> which is plentiful in the vicinity of the surface. The formation of surface oxide is reflected by the slight mass decrease on the anodic scan immediately following the surface hydroxide region (Figure 32).



A distinctive second oxidation peak following the one at 0.05 V was not observed (Figure 32) casting doubt therefore on the occurrence of equation (69) in the potential

domain explored here. However, the oxidation wave is fairly broad suggesting that at the employed scan rate of  $10 \text{ mV s}^{-1}$  a distinct second wave might not have been detectable.

The only available literature for comparison is on Pt in 0.1 M NaOH, in which case a second oxidation peak current of fairly similar magnitude with the first one was recorded on Pt(111) with peak potential separation between 0.2 and 0.3 V depending on the state of the surface [145,146]. However, on Pt(110) and Pt(100) the potential separation between the two oxidation waves was smaller. The oxidation at higher potentials on the Pt(100) surface especially [146], bears resemblance to the case shown by Figure 32. The oxidation waves on the Pt surface between -0.06 and +0.3 V were attributed in the literature to the electrochemical generation of both weakly and strongly adsorbed  $\text{OH}_{\text{ad}}$  species (equation (66)) [145].

On the cathodic scan (Figure 32), the first reduction wave after potential switching is very broad, between +0.05 V and -0.35 V, and is coupled with a large mass loss. It is plausible to assume that more than one type of surface adsorbed species were involved in this reduction reaction, such as Pt-OH and Pt oxide species and/ or other types of Pt-OH (e.g. adsorbed on step sites and terrace sites). Furthermore, some of the surface hydroxide/ oxide species originally present on the surface at the start of the scan, were also reduced because the mass loss in the cathodic direction exceeded the mass gain on the anodic scan.

The successive potential cycling of the Pt resonator electrode in 2 M NaOH with associated mass change measurements (Figure 33 A and B) revealed significant surface modifications during the first ten or eleven scans, afterwards the mass profile stabilized. The quartz crystal microbalance measures mass changes relative to the mass of the

surface at the start of the scan. Therefore, the time-dependent evolution of the Pt EQCM in 2 M NaOH in Figure 33A for the first 11 cycles should be looked upon as follows: the start of scan (N + 1) with  $\Delta m = 0$  corresponds to the mass of the Pt surface at the end of scan N, plus any measurable adsorption that occurred on the electrode exposed to the electrolyte at open-circuit during the time between the two scans. Stated briefly, Figure 33A shows that carrying out a mass balance between the anodic and cathodic scans for all the scans 1 to 11, the mass gains virtually equal the mass losses. Thus, as mentioned before, after the 11th scan the surface became voltammetrically stable, and we confirmed this separately by carrying out 200 scans. Figure 34 confirms a similar mass profile for the Pt resonator in 2 M NaOH after 100 scans as Figure 32\*. After 200 scans (Figure 34B) the observed trends of the mass changes on the Pt surface in Figure 32 remain, however the mass changes converge back to the starting point. This convergence and divergence from the starting point of the mass profile was observed throughout the 200 scans performed on the Pt resonator in 2 M NaOH at 293 K.

---

\* The mass profile data resolution of the scans presented in Figure 34 was much higher than Figure 32 and Figure 33 due to the shortened sampling time of the EQCM data, also known as the gate time. The gate time for Figure 34 was 1 s compared to 10 s for the remaining mass profiles presented in this chapter. It was necessary to run the EQCM at a 10 s gate time when studying  $\text{BH}_4^-$  electro-oxidation on Pt due to the signal noise created from the complicated reaction mechanism. Therefore the blank scans for Pt in 2 M NaOH were also run using 10 s gate times in the EQCM to serve as a reference for the  $\text{NaBH}_4$  electro-oxidation EQCM data on Pt.

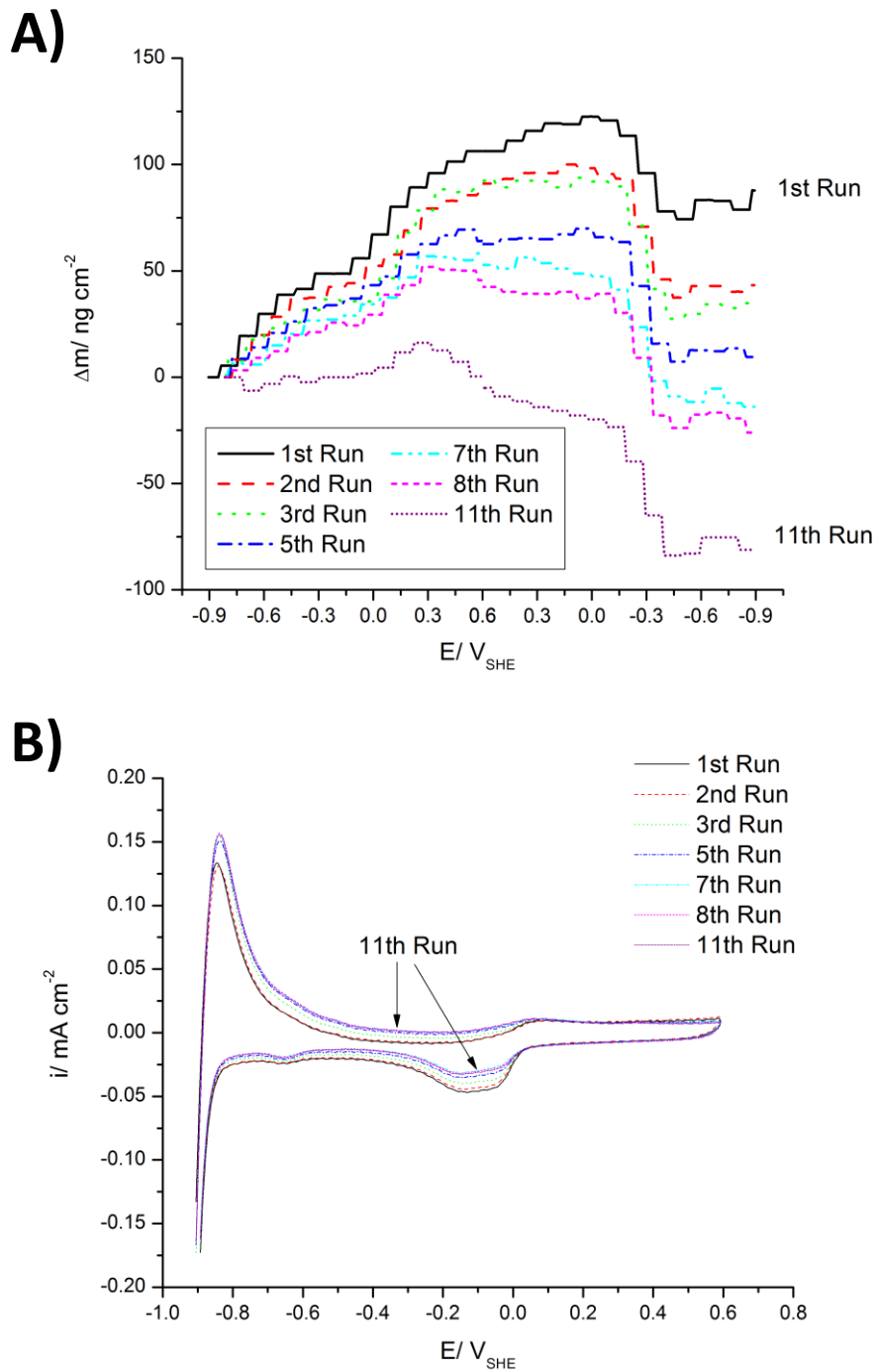


Figure 33. Surface mass changes (a) of the Pt resonator electrode during consecutive cyclic voltammetry scans in 2 M NaOH (b). Consecutive Pt cyclic voltammograms in 2 M NaOH. T: 293 K; scan rate:  $10 \text{ mV s}^{-1}$ . Reproduced with permission from [104], Copyright 2011, American Chemical Society.

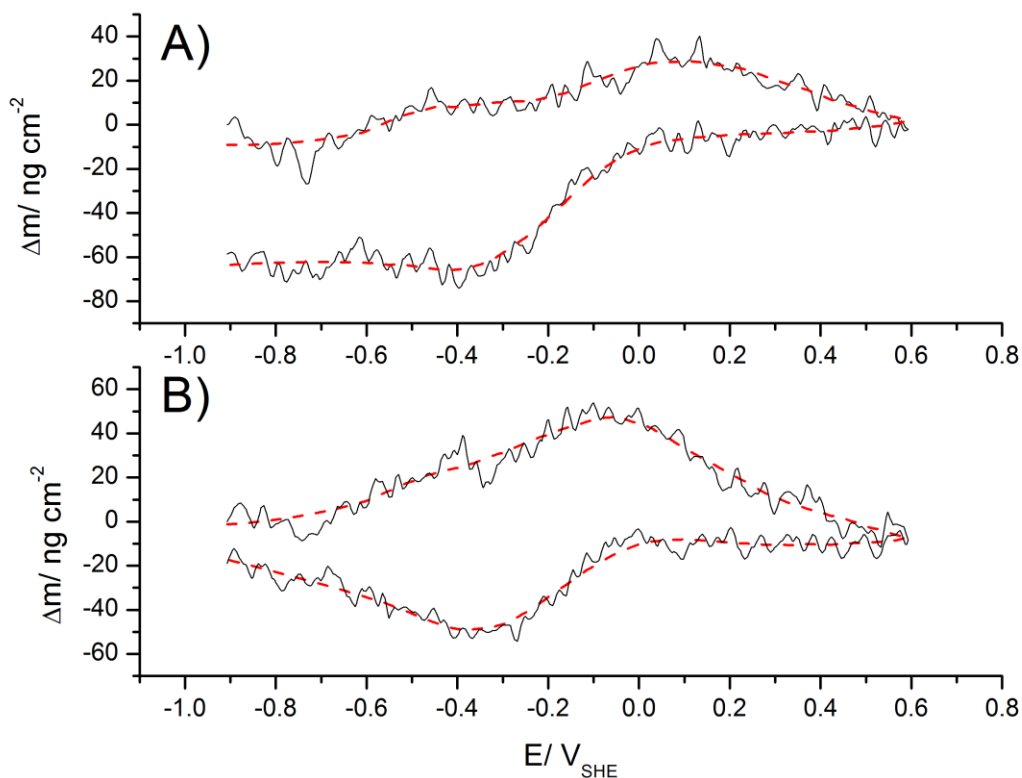


Figure 34. Surface mass changes of the Pt resonator electrode during cyclic voltammetry in 2 M NaOH after A) 100 scans and B) 200 scans. T: 293 K; scan rate: 10  $\text{mV s}^{-1}$ .

Figure 33A, shows that during the first scan, the fresh Pt surface experienced a continuous, almost linear, mass increase over the entire anodic scan (up to 0.6 V), but with each subsequent scan, the mass gain on Pt during the anodic scan diminished (Figure 33A). The observed mass profile in Figure 33A indicates that on the pristine Pt surface an adsorbed  $\text{OH}^-$  and/ or OH layer builds up over the entire potential range, starting from the hydrogen region. This explanation is supported by the electroreflectance spectrum of a Pt(111) electrode in 0.1 M NaOH [141]. In the potential region corresponding to the oxidation wave between -0.06 to +0.20 V (Figure 33B), electrosorption of  $\text{OH}^-$  takes place involving charge transfer (reaction(66)) and forming

Pt-OH. As the surface coverage of  $\text{OH}_{\text{ad}}$  is increasing, i.e. after the first 5 cycles, a significant anodic mass loss develops in the potential range immediately following  $\text{OH}_{\text{ad}}$  formation (between 0.2 and 0.6 V). The observed mass loss is likely due to reactions converting Pt-OH into Pt oxide species such as:  $\text{Pt-O}^-$ ,  $\text{Pt=O}$ , or  $\text{Pt}_2\text{=O}$  (reaction (68)).

The exact stoichiometry of the Pt surface hydroxide cannot be easily established as discussed extensively in the case of acidic media by Angertstein-Kozłowska et al. [147]. A number of researchers, including Appleby [148], Drazic et al. [144], Tripkovic et al. [145], and others proposed the formation of two types of  $\text{OH}_{\text{ad}}$  species on Pt in alkaline media, namely, “weakly” (or reversibly) adsorbed and “strongly” (or irreversibly) adsorbed. Conway in his review of Pt electrochemistry [149] referring to his original work with Angertstein-Kozłowska [147], attributed the overlapping anodic peaks in the hydroxide region to different Pt - OH stoichiometries such as  $\text{PtOH}$ ,  $\text{Pt}_2\text{OH}$ , and  $\text{Pt}_5\text{OH}$ .

During cycling, the bulk  $\text{H}_{2(\text{g})}$  oxidation peak increased, as well as the double layer region, while the oxidation of the surface according to equation (66) (i.e.  $\text{OH}^-$  electrosorption) decreased (Figure 33B), as shown also by the corresponding decrease of the anodic mass gain with each scan (Figure 33A). These results suggest that the electrosorption leads partly to the formation of strongly adsorbed OH on the Pt surface, which cannot be completely removed on the cathodic scan therefore inhibiting the specific adsorption of fresh  $\text{OH}^-$  on subsequent scans. The surface coverage of strongly adsorbed OH increases with cycling.

The steep mass decrease on the anodic scan between 0.2 V and 0.6 V for cycle number 11 suggests the possibility of reaction (68) occurring preferentially as opposed to

either reactions(67) or (69) that would have generated lower mass losses (only one H atom eliminated per Pt-OH site).

## **2.4 Electrochemical Quartz Crystal Microbalance Study of $\text{BH}_4^-$ on Pt in 2 M NaOH**

Figure 35 shows the effect of the  $\text{BH}_4^-$  concentration on the cyclic voltammograms at a scan rate of  $100 \text{ mV s}^{-1}$ . The four characteristic oxidation peaks: *a1*, *a2*, *c2* and *c1* previously mentioned, are shown (Figure 28). The most significant concentration effect was observed in case of oxidation wave *a1* where the peak potential shifted toward more positive values with increasing  $\text{BH}_4^-$  concentration. A non-linear increase of the peak current density was observed at low  $\text{BH}_4^-$  concentrations from 0.5 to 5 mM  $\text{NaBH}_4$  (Figure 35 inset). Wave *a1* can be broadly defined between -0.9 and -0.1 V, wave *a2*: between -0.05 and +0.6 V, followed by other two oxidation waves on the cathodic scan, *c2*: between +0.6 and 0 V, and lastly *c1*: between -0.05 and -0.8 V. From the point of view of fuel cell application only the potential range between the open-circuit value and -0.6 V is relevant.

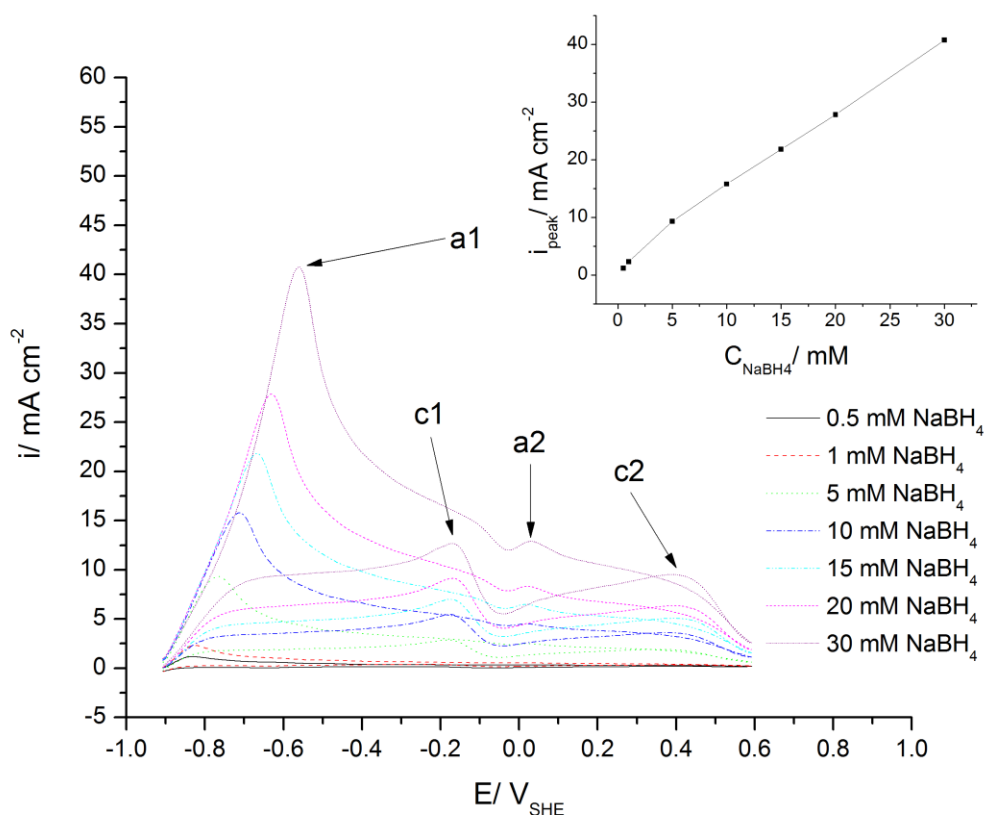


Figure 35. Effect of  $\text{BH}_4^-$  concentration on the stationary cyclic voltammograms on Pt disk. All the scans started in the anodic direction. Inset:  $\text{BH}_4^-$  electro-oxidation peak current density versus  $\text{BH}_4^-$  concentration. Supporting Electrolyte: 2 M NaOH; T: 298 K; scan rate: 100 mV s<sup>-1</sup>. Reproduced with permission from [104], Copyright 2011, American Chemical Society.

The mechanisms responsible for the four oxidation peaks are discussed based on the EQCM experiments (Figure 36 and Figure 37). In selecting the NaBH<sub>4</sub> concentration for EQCM experiments the goal was to use higher concentrations (10 and 60 mM, respectively) such that the fundamental studies to be more relevant to practical fuel cell applications. Furthermore, the scan rate employed for EQCM was lower (10 mV s<sup>-1</sup>) for synchronization between the electrode polarization and resonator frequency change.

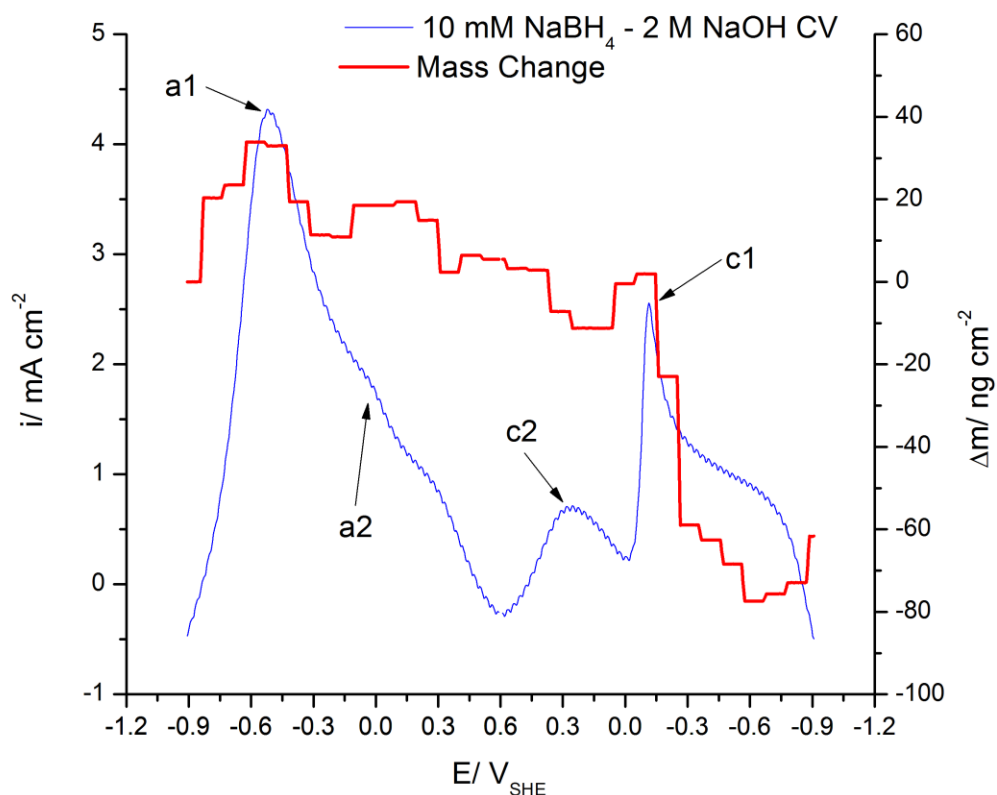


Figure 36. Cyclic voltammetry and surface mass changes of a Pt resonator electrode in 10 mM  $\text{NaBH}_4$  - 2 M NaOH. T: 293 K; scan rate:  $10 \text{ mV s}^{-1}$ . Reproduced with permission from [104], Copyright 2011, American Chemical Society.

Figure 36 shows the cyclic voltammogram of 10 mM  $\text{NaBH}_4$  in 2 M NaOH at a scan rate of  $10 \text{ mV s}^{-1}$ . Starting at  $-0.9 \text{ V}$ ,  $\text{BH}_4^-$  adsorbs onto the surface as shown by the sudden mass increase between  $-0.9$  and  $-0.75 \text{ V}$ . This mass increase is above the level what would be expected based only on  $\text{OH}^-$  adsorption (compare Figure 32 and Figure 36). Thus, a competitive adsorption on Pt between  $\text{BH}_4^-$  and  $\text{OH}^-$  takes place with the former prevailing starting at and immediately after the *a1* peak potential (Figure 36). The electrode mass decreased significantly due to oxidation of surface adsorbed species.

When the  $\text{BH}_4^-$  concentration was increased (i.e., 60 mM, Figure 37), the *a1* peak potential shifted to a more positive value ( $-0.2 \text{ V}$ ), and similarly at  $E > E_p$  (*a1*), a mass

decrease was observed, albeit the decrease was not as steep as in the case of 10 mM  $\text{BH}_4^-$  concentration (compare Figure 36 and Figure 37).

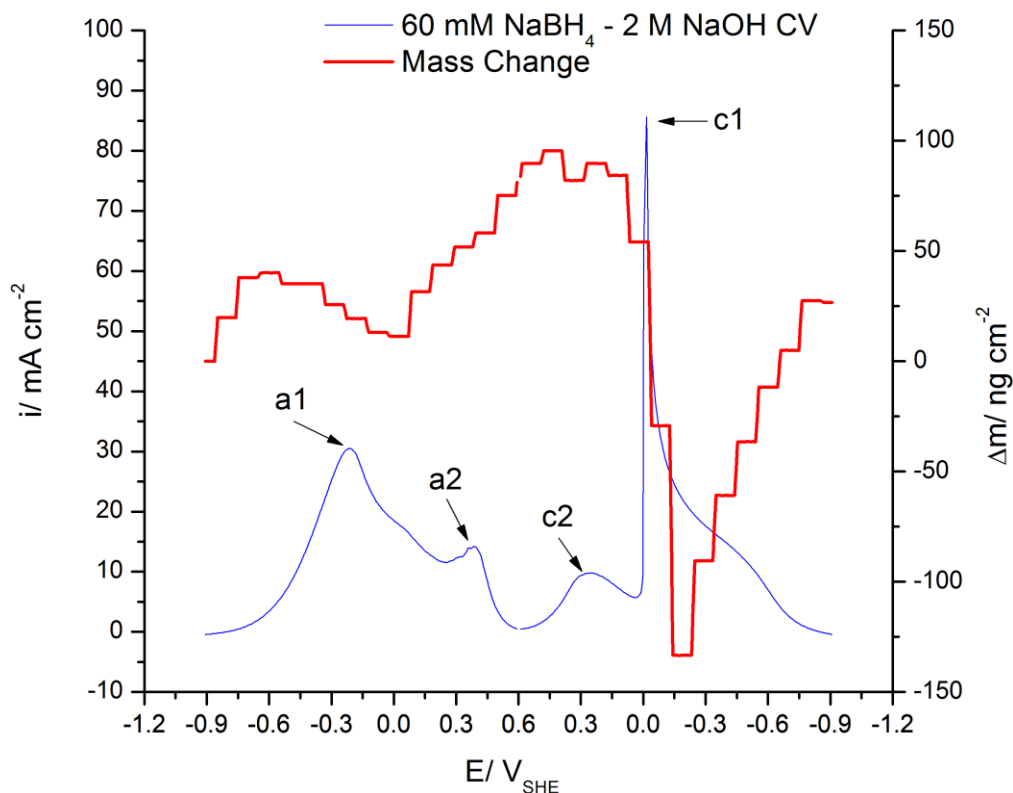


Figure 37. Cyclic voltammetry and surface mass changes of a Pt resonator electrode in 60 mM  $\text{NaBH}_4$  - 2 M  $\text{NaOH}$ ; T: 293 K; scan rate:  $10 \text{ mV s}^{-1}$ . Reproduced with permission from [104], Copyright 2011, American Chemical Society.

The decrease in mass associated with the oxidation wave *a1* at both 10 mM and 60 mM  $\text{BH}_4^-$  concentrations suggests the consumption of the adsorbed reactant species that caused initially the mass increase and formation of reaction products that are easily desorbed from the surface. The processes responsible for the first oxidation wave *a1* have been recently debated in the literature [9,17,100,113]. Essentially, two “schools of thought” have emerged. One of them proposes an almost complete oxidation of  $\text{BH}_4^-$  (7-

electron) between -0.6 V and -0.05 V involving surface hydrides and forming oxidized species that poison the surface [17,100]. The other explanation is based on catalytic hydrolysis of  $\text{BH}_4^-$  and oxidation of the evolved hydrogen [9,113].

To interpret the oxidation wave *a1* based on the EQCM results (Figure 36 and Figure 37) one must consider that the  $\text{BH}_4^-$  chemisorption on Pt is thermodynamically favourable over the entire potential range including open-circuit. Density functional theory (DFT) modelling on Pt(111) showed the energetically most favourable pathway when there are sufficient free surface sites available, is the dissociative adsorption of  $\text{BH}_4^-$  generating  $\text{BH}_{\text{ad}} + 3\text{H}_{\text{ad}}$  [150]. Thus, for wave *a1* the following electrochemical-chemical (EC) sequence of steps is proposed:



The change in surface coverage associated with the rising portion of wave *a1* was estimated with reference to the coverage at the start of the scan (at -0.9 V, Figure 36 and Figure 37). Adsorption can occur already under open circuit conditions leading to hydrolysis according to reaction (34).

However,  $\text{BH}_3\text{OH}^-$  is not expected to accumulate on the surface, DFT modelling showed it is weakly adsorbed [150]. Using the calculation procedure presented in Appendix D, at 10 mM  $\text{BH}_4^-$  the surface coverage increase corresponding to the *a1* mass gain (Figure 36), was equivalent to about 1.6 monolayers (ML) of  $\text{BH}_{4,\text{ad}}$ . A similar calculation for 60 mM  $\text{BH}_4^-$  concentration (Figure 37), revealed that the surface coverage

increase with respect to the reference surface at -0.9 V, was only slightly different, namely 1.7 ML, in spite of about six times higher anodic current. Thus, it can be argued that in both cases the surface was saturated with  $\text{BH}_{4,\text{ad}}$  near the peak *a1* potential. As the potential was scanned more positive with respect to the peak *a1* potential,  $\text{BH}_{4,\text{ad}}$  was rapidly transformed into products that easily desorbed from the surface as shown by the Pt resonator mass decrease (Figure 36 and Figure 37).

Therefore, with respect to wave *a1* in addition to reaction (71) three surface processes can occur: a)  $\text{H}_{2(\text{g})}$  evolution by thermocatalytic recombination of  $\text{H}_{\text{ad}}$  (Tafel step), b)  $\text{H}_{\text{ad}}$  oxidation ( $\text{H}_{\text{ad}} + \text{OH}^- \rightarrow \text{H}_2\text{O} + 1\text{e}^-$ ; referred to as the Volmer step) and c) either thermocatalytic or electrocatalytic oxidation of  $\text{BH}_{\text{ad}}$ . The relative rates of  $\text{H}_2$  evolution and  $\text{H}_{\text{ad}}$  oxidation depend synergistically on  $\text{H}_{\text{ad}}$  surface coverage, electrode potential, and temperature.

The question is what is happening to the  $\text{BH}_{\text{ad}}$  species? There are a number of theoretically feasible pathways [150], but without identification of surface adsorbed species it is difficult to draw unequivocal conclusion. As it may be recalled, for peak *a1*, the number of electrons was between 5 and 6 per  $\text{BH}_4^-$  molecule (Figure 31). Considering a maximum of only 3 electrons could be generated by  $3\text{H}_{\text{ad}}$  oxidation, it is proposed that wave *a1* (Figure 36 and Figure 37) incorporates also the step-wise oxidation of  $\text{BH}_{\text{ad}}$  following the energetically favourable pathways revealed by DFT calculation generating  $\text{B}(\text{OH})_3$  which is weakly adsorbed on the surface:





Reactions (72) - (75) are electrochemical variants of Eley-Rideal type mechanism. Out of the total 8 electrons from reactions (70) - (76), including the theoretical 3 electrons from  $3H_{ad}$  oxidation, in practice 6 electrons were determined, which indicates the contribution of the thermocatalytic  $H_{2(g)}$  evolution ( $2H_{ad} \rightarrow H_{2(g)}$ ).

The thermocatalytic  $H_{2(g)}$  evolution and electrocatalytic  $H_{ad}$  oxidation in conjunction with the facile desorption of boric acid (reaction (76)) could explain the decrease of the Pt electrode mass at  $E > E_p$  (a1). However, at the completion of wave a1, the Pt mass is somewhat higher than at the beginning of the scan, indicating that some of the boron hydroxide intermediates formed in reactions (72) - (75) remain adsorbed.

Continuing the scan in the anodic direction, between 0 V and 0.6 V new oxidation waves develop (Figure 35 - Figure 37). Depending on the scan rate and  $BH_4^{-}$  concentration these waves can be more or less resolved into distinctive peaks. Higher  $BH_4^{-}$  concentration favoured the peak behaviour (compare Figure 36 and Figure 37), referred to as peak a2 (Figure 35). The QCM measurements in the range of 0 to 0.6 V differed between the 10 and 60 mM  $BH_4^{-}$  bulk concentrations (compare Figure 36 and Figure 37). In case of the higher  $BH_4^{-}$  concentration, the mass increased continuously with potential scanning, extending into the early part of the reverse cathodic scan, generating a mass gain of up to  $90 \text{ ng cm}^{-2}$  (Figure 37). For the lower concentration on the other hand, the mass of the Pt electrode resonator increased with potential only up to

0.2 V reaching a value of  $20 \text{ ng cm}^{-2}$ , which was followed by a mass decrease and stabilization at a level almost identical to the start of the scan lasting up to the switching potential of 0.6 V (Figure 36).

This potential region between 0 V and 0.6 V corresponds to the electroadsorption of  $\text{OH}^-$  and formation of  $\text{OH}_{\text{ad}}$  on Pt, as previously discussed. For the hydroxide region of Pt in the absence of  $\text{BH}_4^-$  the mass gain was as high as  $110 \text{ ng cm}^{-2}$  on the very first scan at 0.6 V but it dropped with subsequent scans stabilizing around  $20 \text{ ng cm}^{-2}$  at 0.2 V (Figure 33A, scan 11). The latter mass gain can be considered representative for the intrinsic state of the Pt surface in the hydroxide region and it corresponds to an additional  $\text{OH}_{\text{ad}}$  surface coverage increase of 0.5 ML with respect to the beginning of the scan (Appendix D).

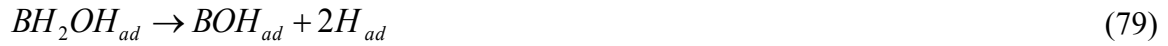
In the potential domain of wave *a2*, corresponding to the hydroxide/ oxide region of Pt, due to the adsorption of a number of species  $\text{OH}_{\text{ad}}$ ,  $\text{BH}_4^-_{\text{ad}}$  and possibly some oxidized intermediates, the surface is crowded hence, the minimum 9 free adjacent Pt atoms necessary for the dissociative adsorption of one  $\text{BH}_4^-$  according to equation (71) is likely not available [150]. Instead, it is proposed that  $\text{BH}_4^-$  engages in another type of dissociative adsorption that requires only 1-3 free Pt atoms, generating borane ( $\text{BH}_{3,\text{ad}}$ ) and  $\text{H}_{\text{ad}}$  [150]:



The borane (BH<sub>3</sub>) is unstable in aqueous solution and forms either BH<sub>3</sub>OH<sup>-</sup><sub>aq</sub> or B<sub>2</sub>H<sub>6(g)</sub>. On the Pt surface BH<sub>3,ad</sub> can readily react with OH<sub>ad</sub> in the potential domain of oxidation wave *a2* according to the Langmuir-Hinshelwood mechanism:



Followed by the dissociation of BH<sub>2</sub>OH<sub>ad</sub> (equation (79)), provided that there are sufficient surface sites available:



Once BOH<sub>ad</sub> has been formed, it follows the same oxidative pathway as described previously by equations (74) -(76) forming B(OH)<sub>3,aq</sub> and H<sub>2(g)</sub>. Thus, it is proposed the oxidation wave *a2* is composed of reactions (66), (74) - (76) and (77) - (79) with a total of 4 electron transfer corresponding to the overall stoichiometry expressed by equations (80) and (81). This is supported by experimental determination of the total number of electrons of 4.7 on average by RDE in the previous section. The slightly higher electron number may indicate some additional contributions by high potential oxidation of adsorbed species formed in wave *a1*.



For the 10 mM  $\text{BH}_4^-$  concentration at the switching potential of 0.6 V, the electrode mass returned to a level only slightly higher than at the start of the scan (Figure 36). This indicates near complete consumption of all the adsorbed species including  $\text{OH}_{\text{ad}}$ . In the case of high  $\text{BH}_4^-$  concentrations (e.g., 60 mM) there is a build-up of adsorbed species up to and beyond 0.6 V (Figure 37). The availability of  $\text{OH}_{\text{ad}}$  could become rate limiting and there might not be enough free surface sites for complete dissociation of  $\text{BH}_2\text{OH}_{\text{ad}}$  according to eq. (79) leading to the accumulation of the latter on the surface.

Furthermore, if  $\text{OH}_{\text{ad}}$  is unavailable,  $\text{BH}_{3,\text{ad}}$  could react with  $\text{OH}^-$  from the solution based on an Eley-Rideal type of mechanism:



Hence,  $\text{BH}_2\text{OH}_{\text{ad}}$  (or  $\text{BH}_2\text{OH}_{\text{ad}}^-$ ) and  $\text{BOH}_{\text{ad}}$  accumulate on the surface and are responsible for the increased Pt mass over the entire region starting from 0.1 V up to 0.6 V (Figure 37). Therefore, these species will play an important role on the reverse cathodic scan.

In addition to  $\text{BH}_2\text{OH}_{\text{ad}}$  generated on the surface by reactions (77) - (78) another source for this species could be the oxidative dissociative adsorption or electrosorption of  $\text{BH}_3\text{OH}^-$  formed by the pH-dependent thermocatalytic hydrolysis of  $\text{BH}_4^-$  (reaction (34)) according to reactions (83) or (84).



In the literature it was shown the oxidation of  $\text{BH}_3\text{OH}^-$  takes place exactly in the potential domain of wave *a2* and it is a 3 to 6 electron oxidation [100]. The lower the pH and the higher the temperature the more significant will be the contribution of reaction (34) and  $\text{BH}_3\text{OH}^-$ .

Subtracting from the total mass gain at 0.6 V (Figure 37), the estimated contribution of  $\text{OH}_{\text{ad}}$  from Figure 33A (scan 11) leads to approximately 0.6 ML coverage increase due to  $\text{BH}_2\text{OH}_{\text{ad}}$  at 0.6 V in case of 60 mM  $\text{BH}_4^-$  concentration.

On the reverse cathodic scan again two oxidation waves, *c2* and *c1* can be identified, with peak potentials of 0.3 V (*c2*) and -0.05 to -0.15 V (*c1*), (Figure 36 and Figure 37). Peak *c1* potential was somewhat scan rate dependent, shifting toward a more positive value at a slower scan rates (compare Figure 35 with Figure 36). The cathodic oxidation waves have a ‘cleaning’ effect on the electrode surface, especially at high  $\text{BH}_4^-$  concentrations. This effect is nicely revealed by the influence of the positive switching potential in Figure 38. The more positive the switching potential at the end of the anodic scan, the more negative is  $E_p(a1)$  on the next anodic scan. When the switching potential was only +0.1 V on the subsequent (2<sup>nd</sup>) scan  $E_p(a1) = -0.25$  V, while switching at +0.5 V on the following (6<sup>th</sup>) scan  $E_p(a1) = -0.42$  V (Figure 38). Thus, the surface ‘cleaning’ at 0.5 V lowered the peak *a1* potential by almost 0.2 V. The efficient oxidative removal of adsorbed species is paramount to create the number of free sites necessary for the dissociative adsorption according to eq. (10) (e.g., nine per  $\text{BH}_{4,\text{ad}}$  [150]).

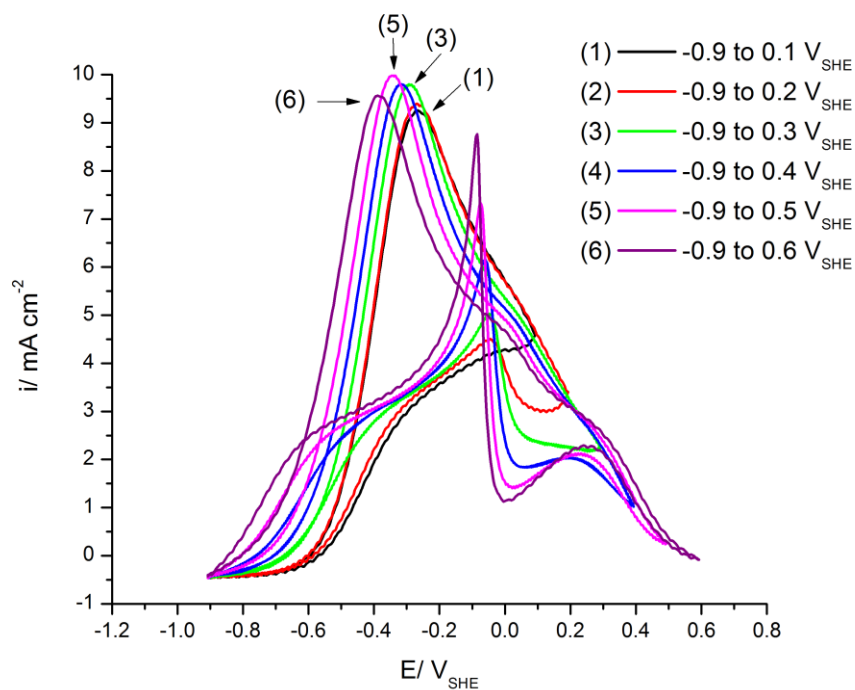


Figure 38. Effect of the switching potential on the cyclic voltammetry behaviour of  $\text{BH}_4^-$  on Pt disk electrode. All scans started in the anodic direction. Analyte: 20 mM  $\text{NaBH}_4$  – 2 M  $\text{NaOH}$ ; T: 293 K; scan rate:  $10 \text{ mV s}^{-1}$ . Reproduced with permission from [104], Copyright 2011, American Chemical Society.

Wave  $c2$  is in the potential region where Pt surface hydroxides and possibly some oxides, are present on the surface. The EQCM measurement showed that at a potential  $E \sim E_p(c2)$  the resonator mass decreased (Figure 36 and Figure 37).

RDE experiments revealed that wave  $c2$  became more independent of the rotation rate as the rotation rates increased from 400 RPM to 2500 RPM (Figure 30), which suggests surface reaction controlled peak. In case of 10 mM  $\text{BH}_4^-$  concentration at the end of the anodic scan there are very few adsorbed species left on the surface hence, the peak  $c2$  current density was very small, about  $0.7 \text{ mA cm}^{-2}$  compared to  $10 \text{ mA cm}^{-2}$  in case of 60 mM  $\text{BH}_4^-$  (Figure 36 and Figure 37, respectively). One possible option is the

removal of  $\text{BOH}_{\text{ad}}$  following the sequence of reactions (74) - (76). Alternatively, Langmuir-Hinshelwood type mechanism can be envisaged between  $\text{BOH}_{\text{ad}}$  and  $\text{OH}_{\text{ad}}$ .

Continuing further on the cathodic scan, the sharp oxidation peak *c1* between -0.05 V and -0.15 V is a characteristic feature of  $\text{BH}_4^-$  cyclic voltammograms (Figure 36 and Figure 37). Koper showed by theoretical modelling that generally sharp voltammetric peaks are caused by competitive adsorption between small and large adsorbates [151]. The peak *c1* current density is strongly dependent on bulk  $\text{BH}_4^-$  concentration and scan rate (compare Figure 35 and Figure 36). Increase of the peak *c1* current density is favored by slower scan rate and higher  $\text{BH}_4^-$  concentration. This indicates that *c1* is generated by a slow oxidation reaction, which requires time to develop. Furthermore, this peak is strongly dependent on the switching potential, namely the more positive the switching potential the more negative is the *c1* peak potential and the higher its current density (Figure 38).

In the literature peak *c1* has been related either to the oxidation of  $\text{BH}_3\text{OH}^-$  or adsorbed  $\text{BH}_2(\text{OH})_2^{2-}$  [9,100]. From the point of view of QCM, wave *c1* was associated with a large mass loss:  $-130 \text{ ng cm}^{-2}$  in case of 60 mM  $\text{BH}_4^-$  (Figure 37) and  $-79 \text{ ng cm}^{-2}$  for 10 mM  $\text{BH}_4^-$  (Figure 36). However, there is a difference in the QCM behaviour for the two concentrations. In the case of the lower concentration the sharp mass loss was preceded by a build-up (i.e., mass gain) on the surface (Figure 36) while for the higher  $\text{BH}_4^-$  concentration the mass of the electrode decreased directly from the high level it was preceding peak *c1* (Figure 37). This means for 10 mM  $\text{BH}_4^-$  the oxidation wave *c1* involves also a freshly adsorbed species, while for 60 mM  $\text{BH}_4^-$  the already existent surface species are consumed. Furthermore, in the absence of  $\text{BH}_4^-$  in the same potential

window the Pt mass decreased due to the reductive removal of  $\text{OH}_{\text{ad}}$  (Figure 32), but there was no net reductive current measured with  $\text{BH}_4^-$  (Figure 36 and Figure 37).

The following scenarios are proposed for wave *c1* as a function of  $\text{BH}_4^-$  concentration. In case of 10 mM  $\text{BH}_4^-$  at potentials just preceding *c1*, around 0 V, there are some free surface sites that became available after the oxidation wave *c2*. It is proposed that in the first step  $\text{BH}_4^-$  re-adsorbs on the surface and reacts with  $\text{OH}_{\text{ad}}$  generating in the first step  $\text{BH}_2\text{OH}_{\text{ad}}$ . This reaction is responsible for the mass increase just preceding peak *c1* (Figure 36):



At  $E \sim E_p(c1)$  the overall reaction is:



Reaction (86) is responsible for the mass decrease on the Pt electrode and the sharpness of the peak is due to exchange on the same surface site of the large adsorbate  $\text{BH}_2\text{OH}_{\text{ad}}$  with a small one  $\text{H}_{\text{ad}}$ , (by analogy to the adsorption cases discussed by Koper [151]). RDE experiments revealed a total of 6 electrons for peak *c2*, which is indicated by eqns. (85) and (86), including 3 electrons from further electro-oxidation of  $3\text{H}_{\text{ad}}$  under the high anodic overpotential existent at  $E_p(c1)$ .

For 60 mM  $\text{BH}_4^-$  concentration the main difference is that there is no newly formed  $\text{BH}_2\text{OH}_{\text{ad}}$ . Hence, the already adsorbed species formed in the anodic scan in wave *a2* are engaged in the oxidative desorption. The Pt resonator electrode mass

decreased abruptly in the potential domain of peak *c2* (Figure 37). The oxidative removal of  $\text{BH}_2\text{OH}_{\text{ad}}$  is essential to regenerate the catalytic activity and create the surface sites necessary for specific adsorption of  $\text{BH}_4^-$ . The latter is reflected by the Pt mass increase in the cathodic direction immediately following wave *c2*, which is much more pronounced in case of high bulk  $\text{BH}_4^-$  concentration (compare Figure 37 with Figure 36).

## **2.5 Electrochemical Quartz Crystal Microbalance Study of Thiourea on Pt in 2 M NaOH**

Figure 39 presents the EQCM behaviour of 1.5 mM TU in 2 M NaOH. Between -0.9 and 0.09 V the resonator mass was virtually constant indicating that in this region the adsorption of TU was independent of potential. This finding is interesting when compared to the bare Pt in 2 M NaOH where typically some level of mass increase occurred in the same potential domain depending on the number of cycles (Figure 32 and Figure 33). It suggests that TU, which is adsorbed on the surface from the outset of the scan, hampers the specific adsorption of  $\text{OH}^-$ . Moreover, the hydrogen oxidation (either  $\text{H}_{2(\text{g})}$  or underpotentially deposited hydrogen) was completely inhibited by 1.5 mM TU, whereas the cathodic  $\text{H}_{2(\text{g})}$  evolution was suppressed (Figure 39).

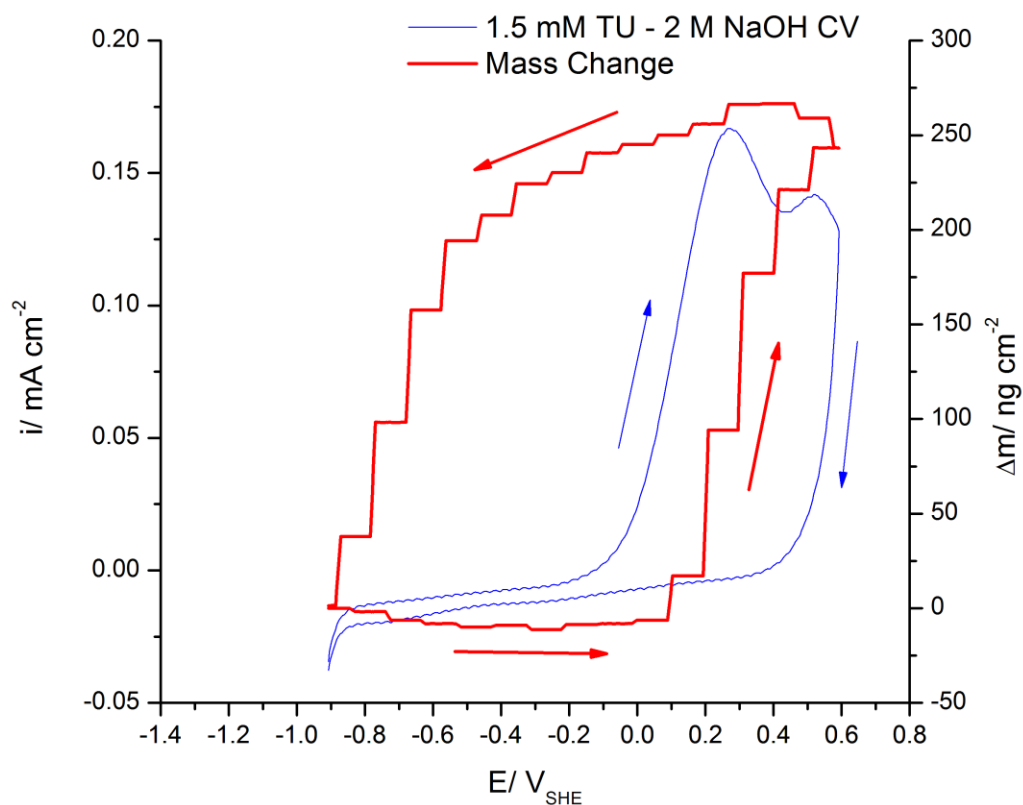
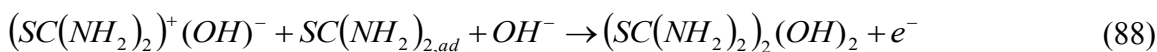
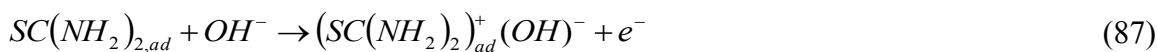


Figure 39. Effect of TU on the cyclic voltammogram and surface mass changes of a Pt resonator electrode in 2 M NaOH - 1.5 mM TU. 293 K, scan rate: 10 mV s<sup>-1</sup>. Reproduced with permission from [104], Copyright 2011, American Chemical Society.

Oxidation of TU commences at -0.2 V with two distinct irreversible peaks at 0.18 and 0.48 V, respectively (Figure 39). The oxidation is associated with a mass gain on the surface of almost ~250 ng cm<sup>-2</sup> starting from 0.1 V. The first TU oxidation peak at 0.18 V is due to reaction (87). At more positive potentials, with a peak at 0.48 V dithiodiformamidinium hydroxide (reaction (88)) is generated [152--154].



The fact that at the end of the voltammetric cycle the Pt mass recovered completely its original value without faradaic reduction on the reverse cathodic scan, hints toward electrode potential dependent adsorption-desorption hysteresis of TU and its oxidation products.

In the cathodic direction, two different slopes for the mass decrease can be observed (Figure 39): a) moderate mass loss between  $-0.4 \text{ V} < E \leq 0.25 \text{ V}$ ; and b) abrupt mass loss between  $-0.9 \text{ V} \leq E \leq -0.4 \text{ V}$ . The moderate mass loss can be attributed to desorption of the weakly adsorbed  $(SC(NH_2)_2)_2(OH)_{2,ad}$ , which is soluble in aqueous solutions [152--154]. An estimate shows this mass loss could correspond to the removal of 0.7 ML of  $(SC(NH_2)_2)_2(OH)_{2,ad}$  (Appendix D).

Further on the cathodic scan, extensive desorption started at  $-0.4 \text{ V}$  where the resonator mass decreased by about  $215 \text{ ng cm}^{-2}$  (Figure 39). If this entire mass change is attributed to desorption of TU, it would correspond to the removal of 3 ML with respect to the situation at the beginning of the scan (Appendix D).

The potential of zero charge of Pt ( $E_{PZC}$ ) in 2 M NaOH estimated with the Bockris-Argade-Gileadi equation [155] is  $-0.4 \text{ V}_{SHE}$ . It is accepted in the literature that at negative potentials the preferred adsorption mode of the zwitter-ionic TU [156] is with the sulphur oriented toward the surface [157]. Therefore, at  $E < E_{PZC} = -0.4 \text{ V}$ , the TU adsorption weakens due to the electrostatic repulsion between the negatively charged surface and the negatively charged sulphur atom pointing toward the surface. The weakened adsorption is reflected by the mass loss measured with EQCM.

At positive potentials on the other hand, the TU adsorption mode changes with the molecular plane now parallel to the surface [154]. This arrangement is favourable for

multi-layer adsorption of TU and electro-oxidative dimerization (reaction (88)). Moreover, the interaction between adsorbed TU and the molecular environment in the vicinity of the electrode surface such as hydrogen bonding with H<sub>2</sub>O and OH<sup>-</sup> plays a significant role in determining the various phases for the adsorbed layer and the associated electrochemical response [158].

## **2.6 Electrochemical Quartz Crystal Microbalance Study of the Thiourea effect on BH<sub>4</sub><sup>-</sup> on Pt in 2 M NaOH**

Figure 40 shows the effect of increasing TU concentrations on the BH<sub>4</sub><sup>-</sup> cyclic voltammograms. Figure 41 shows the corresponding EQCM response in the presence of TU. The BH<sub>4</sub><sup>-</sup> concentration was constant 30 mM.

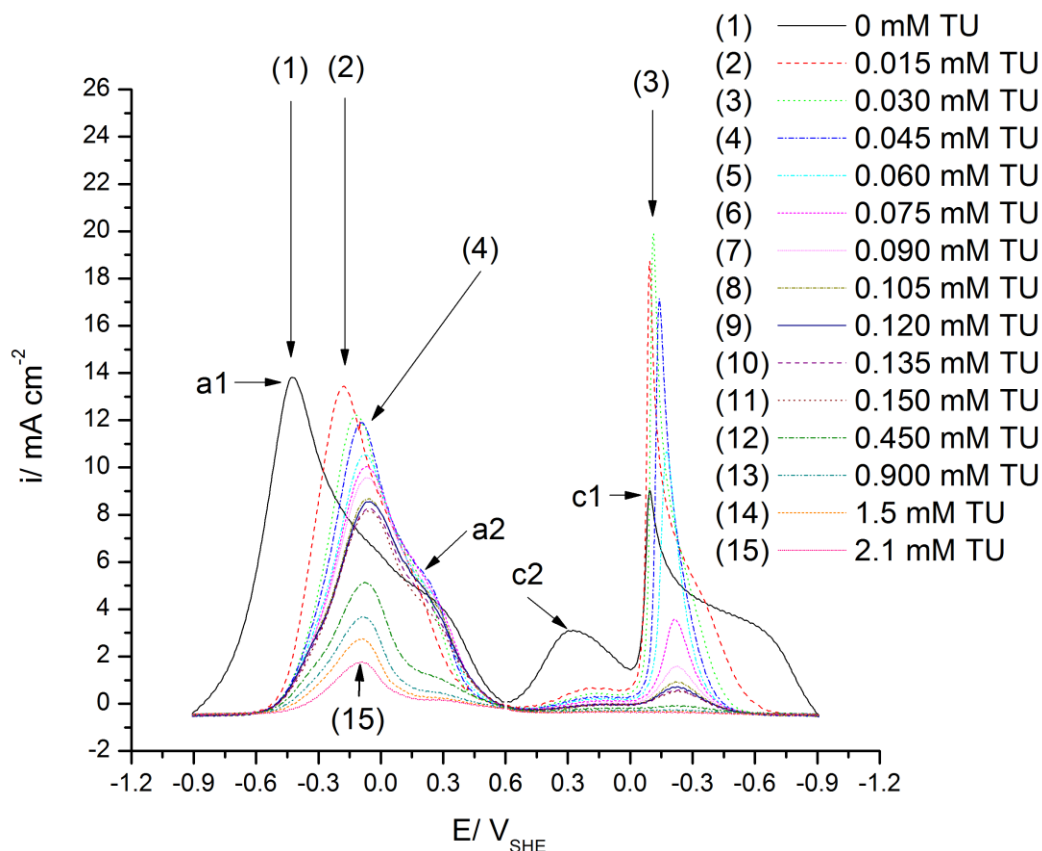


Figure 40. Effect of TU concentration on the cyclic voltammetry of  $\text{BH}_4^-$  on a Pt resonator electrode. Electrolyte: 30 mM  $\text{NaBH}_4$  - 2 M  $\text{NaOH}$ ; T: 293 K; scan rate:  $10 \text{ mV s}^{-1}$ . Reproduced with permission from [104], Copyright 2011, American Chemical Society.

Increasing the TU concentration from 0 to 0.1 mM shifted the first  $\text{BH}_4^-$  oxidation peak *a1* by +0.3 V. Further increase of the TU concentration had virtually no effect on the peak potential, which stabilized at -0.1 V, but the peak current density gradually decreased (Figure 40). Analyzing Figure 41, an interesting effect of the TU concentration is revealed with respect to the region of wave *a1* (between -0.9 and -0.1 V).

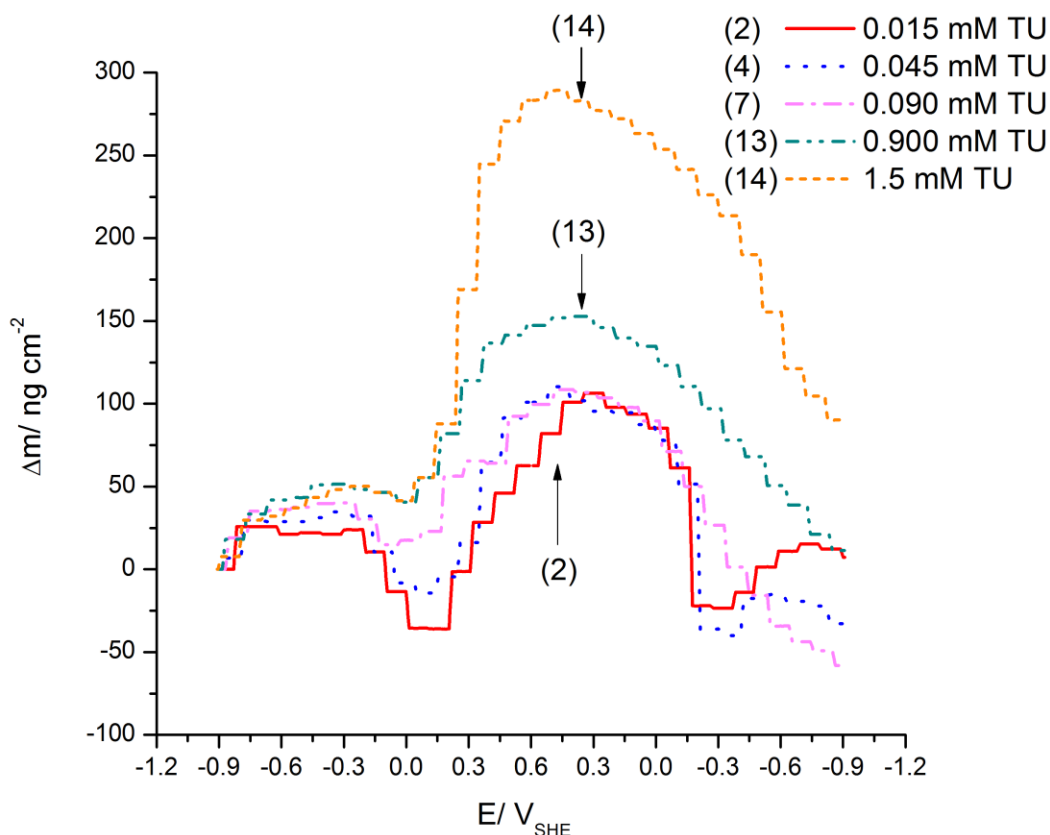


Figure 41. Effect of TU on surface mass changes of a Pt resonator electrode during cyclic voltammetry in  $\text{BH}_4^-$  solution. Electrolyte: 30 mM  $\text{NaBH}_4$  - 2 M  $\text{NaOH}$ ; T: 293 K; scan rate:  $10 \text{ mV s}^{-1}$ . Reproduced with permission from [104], Copyright 2011, American Chemical Society.

With increased TU concentration the surface mass increased as well in the potential region of wave *a1*, reaching an approximately constant maximum value of  $50 \text{ ng cm}^{-2}$  between 0.9 mM and 1.5 mM TU (Figure 41). The mass gain of  $50 \text{ ng cm}^{-2}$  in terms of  $\text{BH}_{4,\text{ad}}$  corresponds to 2 ML.

This seemingly counter intuitive fact can be explained by the fact that at higher TU concentrations, Lewis adduct type molecular associations between TU (weak Lewis acid) and  $\text{BH}_4^-$  (Lewis base) are possible, leading to a stable bi-layer build-up on the surface. The  $\text{BH}_4^-$  electro-oxidation process is hampered in such a layer, leading to

incomplete oxidation products that accumulated on the surface. Comparatively in the absence of TU, between -0.2 V to 0 V there was a significant mass decrease, as discussed previously.

Thus, it is proposed that the inhibited  $\text{BH}_4^-$  electro-oxidation is related to the stabilization of  $\text{BH}_{4,\text{ad}}^-$  and  $\text{BH}_{4,\text{ad}}$  in the TU intercalated bi-layer, which prevents the dissociation according to reaction (71). This argument was further validated by calculating the number of electrons exchanged using RDE experiments. It was found that increasing the TU concentration reduced the number of electrons involved in  $\text{BH}_4^-$  oxidation at peak *a1* from 6 to 5, providing further evidence for the proposed mechanism. The formation of the TU intercalated bi-layer can also offer an explanation for the inhibition of the thermocatalytic hydrolysis reaction (reaction (6)). Furthermore,  $\text{TU}_{\text{ad}}$  inhibited completely the  $\text{H}_{\text{ad}}$  oxidation as shown by Figure 39. This effect also contributed to the higher  $\text{BH}_4^-$  oxidation potentials encountered for wave *a1*, starting at very low concentration of TU such as 0.015 mM (Figure 40).

From 0.1 V and extending to the switching potential of 0.6 V the mass of the resonator electrode increased sharply with TU concentration (Figure 41). This is dominated by the TU oxidative adsorption (Figure 39) with contribution from  $\text{BH}_4^-$  oxidation wave *a2*.

On the reverse cathodic scan two features are evident: a) the virtual absence of peak *c2* (at 0.3 V) even in the presence of only 0.015 mM TU (Figure 40) and b) the unusual dependence of peak *c1* (at -0.1 V to -0.15 V) current density on TU concentration (Figure 40).

In the potential range of wave *c2* oxidized TU derivatives are heavily adsorbed on the surface (Figure 39) inhibiting virtually completely the electrochemical reactions involving  $\text{BH}_4^-$  species described in section 3.2.

Regarding wave *c1* with peak potential of -0.1 to -0.15 V, since the surface adsorbed intermediates generated from  $\text{BH}_4^-$  oxidation on the anodic scan such as  $\text{BH}_2\text{OH}_{\text{ad}}$  were not removed at high anodic potentials due to inhibition by TU, the oxidation current *c1* increases at low TU concentrations as these intermediates are being oxidized (Figure 40). This is reflected by the sharp decrease of the Pt mass between 0.3 and -0.2 V (Figure 41), which is more pronounced than in the case of TU alone (Figure 39). However, at TU concentrations close to and above 0.1 mM the oxidation wave *c1* is inhibited as well (Figure 40) and ultimately the removal of adsorbed  $\text{BH}_4^-$  species was no longer possible as evidenced by the higher final mass of the Pt electrode at the end of the cycle with 1.5 mM TU (Figure 41).

## 2.7 Summary for Chapter 2.0

The electro-oxidation mechanism of  $\text{BH}_4^-$  on Pt was discussed with respect to the four voltammetric oxidation waves *a1*, *a2*, *c2*, and *c1*, and their EQCM responses. The oxidation mechanisms were developed by correlating the rotating disk electrode and EQCM experimental results with predictions based on DFT calculations from the literature showing the energetically most favourable pathways [150].

It was proposed that on the anodic scan,  $\text{BH}_4^-$  electrosorption was followed by dissociation of  $\text{BH}_{4,\text{ad}}$  generating  $\text{BH}_{y,\text{ad}}$  and  $(4-y) \text{H}_{\text{ad}}$ , with *y* between 1 and 3, depending on the available surface sites.  $\text{BH}_{y,\text{ad}}$  is engaged, as a function of electrode potential, in

Eley-Rideal and Langmuir-Hinshelwood type electro-oxidation mechanisms involving  $\text{OH}^-$  and  $\text{OH}_{\text{ad}}$ , respectively.  $\text{OH}_{\text{ad}}$  is formed by electrosorption on the Pt surface between -0.05 V and +0.6 V.

The first  $\text{BH}_4^-$  oxidation wave *a1* occurs over a broad range of negative potentials (between -0.9 V and -0.2 V). This wave is a composite of both  $\text{H}_{\text{ad}}$  and  $\text{BH}_{\text{ad}}$  oxidations generating  $\text{H}_{2(\text{g})}$  and  $\text{B}(\text{OH})_{3,\text{aq}}$ . Thermocatalytic recombination of  $\text{H}_{\text{ad}}$  is also taking place, decreasing the number of electrons that could be obtained, from 8 to 6 electrons. The oxidative removal of key intermediates such as  $\text{BH}_2\text{OH}_{\text{ad}}$  and  $\text{BOH}_{\text{ad}}$  either at high constant anodic potential (0.5 V or 0.6 V) or during potential scanning in the reverse cathodic direction starting from 0.5 V or 0.6 V, is essential for recovery and regeneration of the electrocatalytic activity with respect to  $\text{BH}_4^-$  oxidation. On the cathodic scan, peak *c1* (-0.05 to -0.15 V) and *c2* (at 0.3 V) were attributed to the oxidation of  $\text{BH}_2\text{OH}_{\text{ad}}$  and  $\text{BOH}_{\text{ad}}$ , respectively.

The presence of TU produced interesting effects. It is proposed that at TU concentrations higher than about 0.045 mM (with reference to 30 mM  $\text{BH}_4^-$ ), Lewis adducts are formed between  $\text{BH}_4^-$  and TU, leading to the build-up and stabilization of a  $\text{BH}_4^-$  based bi-layer with intercalated TU. This adsorbed layer increases the  $\text{BH}_4^-$  oxidation overpotential, while decreasing the rate of the thermocatalytic hydrolysis of  $\text{BH}_4^-$ .

### 3 Anode Catalyst Investigation: Os/ C, Pt/ C, and PtRu/ C\*

In this chapter, a comprehensive comparative study of Os/ C, Pt/ C and PtRu/ C anode electrocatalysts employing a range techniques such as voltammetry, chronoamperometry, chronopotentiometry, surface analysis and fuel cell experiments, is presented. Previously, Atwan et al. investigated the electrochemical properties of Os/ C and showed preliminary half-cell results revealing electroactivity toward  $\text{BH}_4^-$  electro-oxidation [16,109]. The experimental work and results presented in this chapter are the first to demonstrate the performance of Os/ C anode catalysts in a DBFC system.

Among precious-metal catalysts, Os has found limited use thus far. Kua and Goddard carried out first principle quantum chemical calculations on Os, Pt, Ru (and other catalysts) for the reaction enthalpies associated with step-wise dissociation of  $\text{CH}_3\text{OH}$  and  $\text{H}_2\text{O}$  [159]. These authors concluded that in terms of the bifunctional mechanism Os could provide the same activity as PtRu, since it could catalyze both  $\text{CH}_3\text{OH}$  and  $\text{H}_2\text{O}$  dissociation. However, experimental evidence did not support this observation, since pure Os was inactive toward  $\text{CH}_3\text{OH}$  oxidation as determined by cyclic voltammetry [16]. Binary PtOs alloys showed in some cases enhanced activity toward methanol oxidation compared to pure Pt depending on the catalyst preparation method, osmium surface oxidation and Pt/Os atomic ratio [160,161].

The cyclic voltammogram of Os nanoparticles (prepared by a colloidal organosol method) showed redox features in 2 M NaOH consistent with Os oxidation [109] such as:  $\text{Os}/\text{OsO}_4^{2-}$  at -0.05 V and  $\text{OsO}_4^{2-}/\text{OsO}_5^{2-}$  at +0.36 V (Figure 19). Interestingly,  $\text{BH}_4^-$  electro-oxidation on Os has been detected over a wide potential range between -0.6 V and

---

\* This chapter is based on the following published work:  
V.W.S. Lam, E.L. Gyenge, J. Electrochem. Soc.155 (2008) B1155.

+0.4 V, indicating that both elemental Os and various osmium oxides are active. At high potentials, the surface redox mediation of  $\text{BH}_4^-$  oxidation by  $\text{OsO}_5^{2-}/\text{OsO}_4^{2-}$  has been proposed [109].

### 3.1 Experimental Procedure

In the present work we employed the same Os/ C (20 %wt metal) catalyst as described in detail by our group in reference [109]. The nanoparticle preparation was based on a variant of the Bönneiman organosol method [162,163], where tetrabutylammonium-triethylhydroborate  $(\text{C}_4\text{H}_9)_4\text{N}[\text{BH}(\text{C}_2\text{H}_5)_3]$  acted as both reductant and colloidal particle stabilizer. The Os colloid was adsorbed on Vulcan<sup>®</sup> XC-72 and the surfactant was removed by successive washing and heat treatment procedures [109]. It is important to note that the Os/ C catalysts prepared by the Bönneiman method had excellent shelf-life, as determined by retesting it after a couple of years of storage. Comparative experiments were performed using commercial Pt/ C and PtRu (1:1 at. ratio)/ C (both 20 %wt metal) supplied by ETEK Inc. The mean particle sizes were 2-3 nm, the same as for Os with a mean particle size of 2.4 nm as determined by a 100 particle count of the Os/ C catalyst using TEM (Figure 42 and Figure 43). TEM imaging was performed with a Hitachi H7600 microscope using an accelerating voltage of 100 kV. Therefore, the structural sensitivity can be neglected as a possible cause for different behaviour on the three catalysts under investigation.

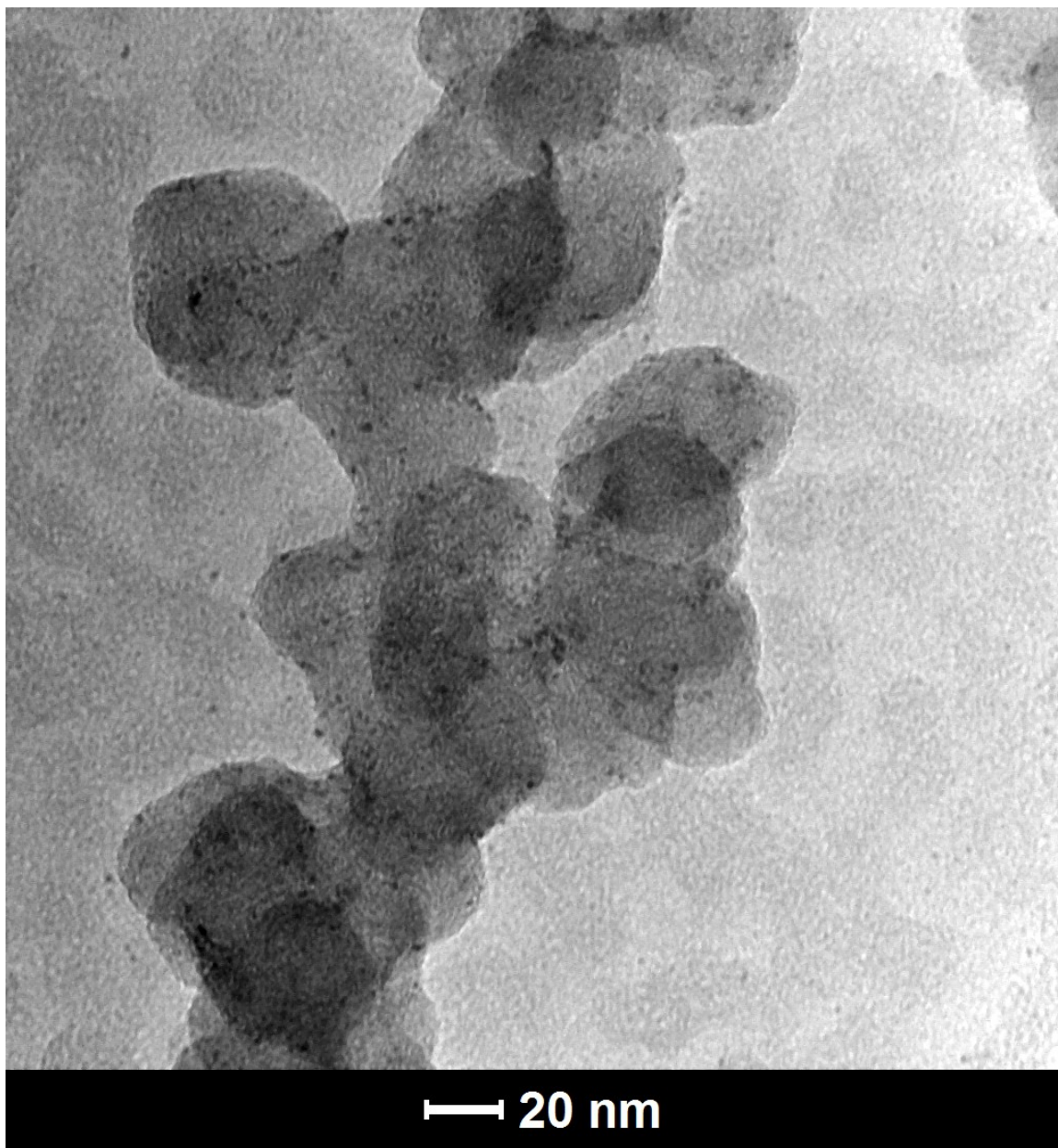


Figure 42. TEM image of Os/ C prepared by a modified Bönnerman method.

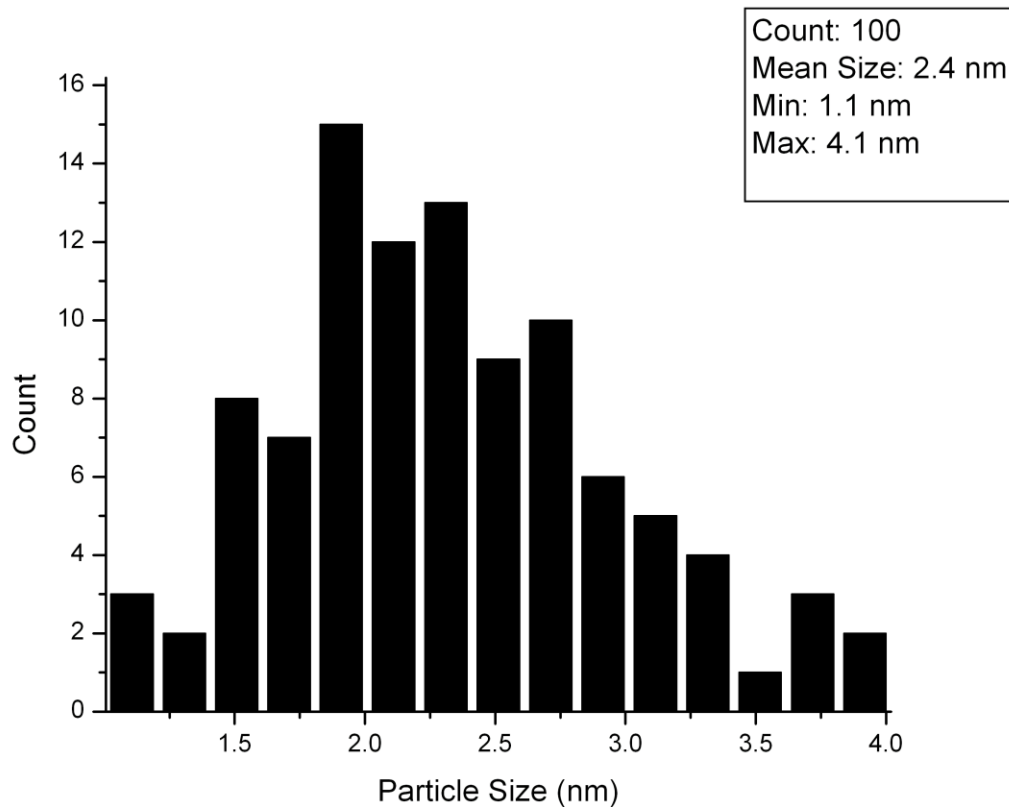


Figure 43. Distribution of Os/ C particle sizes as observed by TEM.

Figure 44 shows the XPS spectrum of the supported Os nanoparticles. The XPS spectrum indicates based on the 4f energy levels the presence of OsO<sub>2</sub> [164] and likely the presence of Os (VIII) in the form of OsO<sub>4</sub>. This is supported by the high binding energy of the proposed OsO<sub>4</sub> doublet (56.7.eV and 52.5 eV).

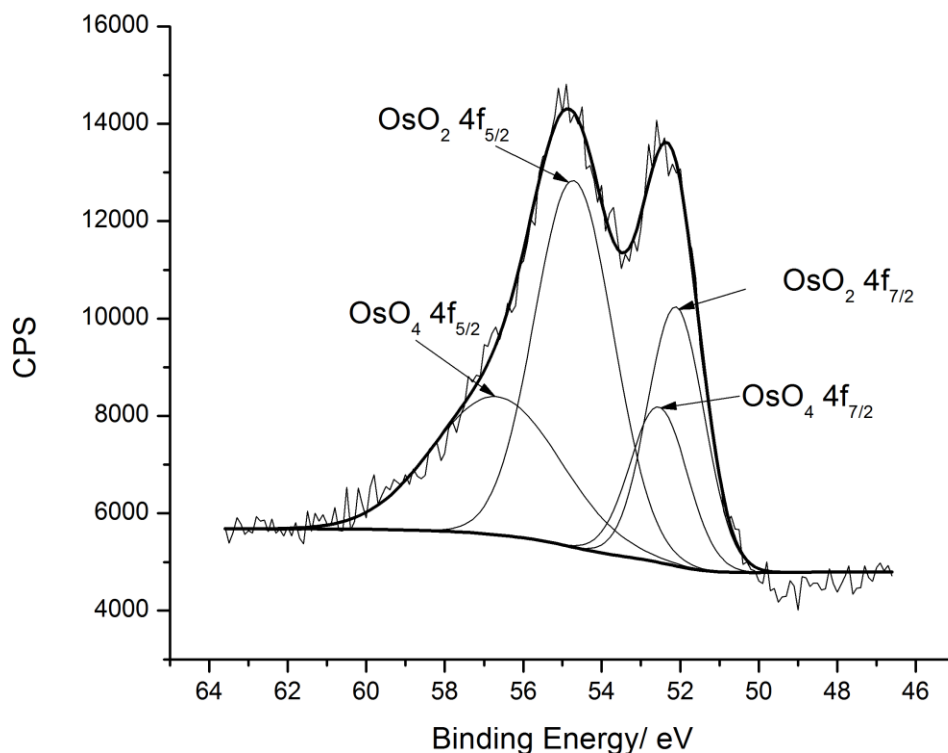


Figure 44. XPS spectra of Os/ C prepared by the modified Bönneinan method. Reproduced with permission from [165], Copyright 2008, The Electrochemical Society.

In fundamental electrochemical studies the conventional three-electrode set-up was used. The working electrode consisted of 1 cm<sup>2</sup> area Toray carbon paper (E-TEK) sprayed with supported catalyst ink containing 1 mg metal. The catalyst ink used in both half-cell electrochemical experiments and fuel cells consisted of a 1.5:1 weight ratio between supported catalyst (Os/ C, Pt/ C and PtRu/ C) and Nafion<sup>®</sup> (prepared using 5 wt% Nafion<sup>®</sup> solution (Alfa Aesar Inc.)). The supported catalyst-Nafion mixture was dispersed in 15 MΩ deionized water and 2-propanol (Fisher) in a 1:0.5:2 mass ratio. The catalyst ink was stirred for 5 minutes then sonicated for three hours prior to spraying.

In half-cell experiments two graphite rod counter electrodes (Princeton Applied Research) were placed on either side of the working electrode and the Hg/HgO, 0.1 M KOH reference electrode was placed close to the working electrode using a Luggin capillary.

The fuel cell membrane electrode assemblies (MEA) were assembled by spraying the anode catalyst ink (load  $1 \text{ mg cm}^{-2}$ ) on the membrane (Nafion<sup>®</sup> 117, 183  $\mu\text{m}$  dry thickness) of a half-MEA with  $4 \text{ mg cm}^{-2}$  Pt black on the cathode side. The half-MEA with geometric working area of  $5 \text{ cm}^2$  were supplied by Lynntech Inc. Untreated carbon cloth and ELAT<sup>®</sup> gas diffusion layers were positioned between the MEA and the serpentine flow-field plates on the anode and cathode sides, respectively. Additional information regarding the fuel cell setup can be found in Appendix H.

### 3.1 Half-Cell Studies

Figure 45 shows the cyclic voltammograms obtained in 0.05 M NaBH<sub>4</sub> – 2 M NaOH using Pt/ C, PtRu/ C and Os/ C. In the absence of BH<sub>4</sub><sup>-</sup> for both Pt/ C and PtRu/ C the anodic scans between -0.8 V and -0.3 V exhibit the typical H-UPD oxidation peaks as a function of Pt crystallographic features (Figure 45B and Figure 45D). This is an important indication for the absence of Nafion<sup>®</sup> adsorption interference in the catalyst layer, thus, the intrinsic kinetic effects can be revealed.

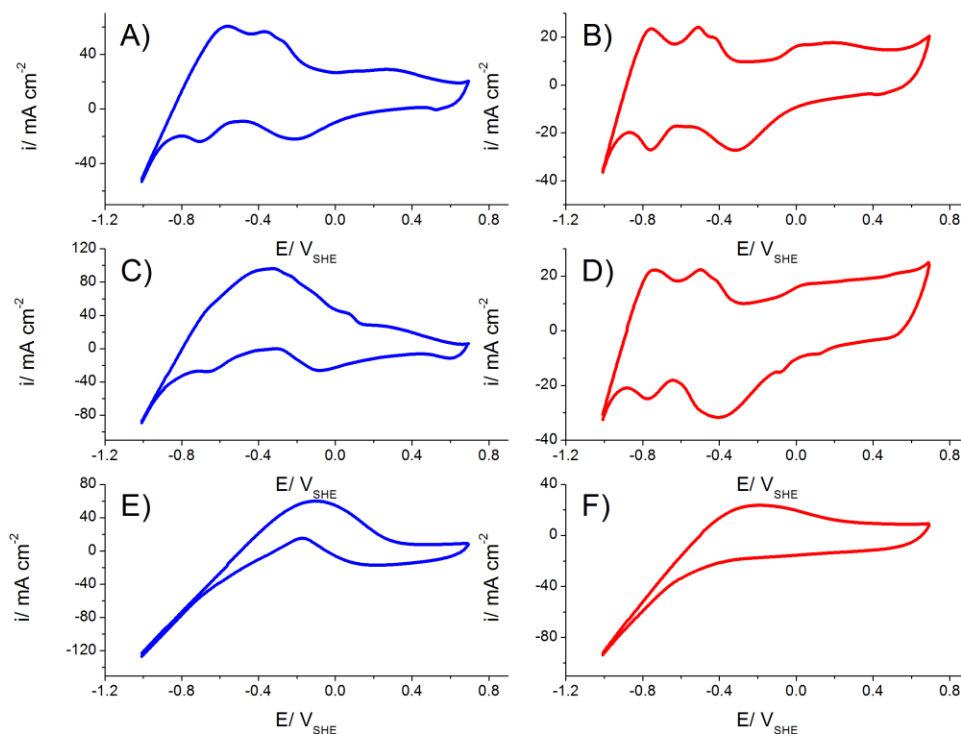


Figure 45. Cyclic voltammograms of A) Pt/ C, C) PtRu/ C, and E) Os/ C in 0.05 M NaBH<sub>4</sub> – 2 M NaOH, and B) Pt/ C, D) PtRu/ C, and F) Os/ C in 2 M NaOH. T: 293 K, scan rate: 50 mV s<sup>-1</sup>. Reproduced with permission from [165], Copyright 2008, The Electrochemical Society.

With BH<sub>4</sub><sup>-</sup> present in the electrolyte, on Pt/ C (Figure 45A) oxidation of BH<sub>4</sub><sup>-</sup> is observed in the entire potential domain, including the hydrogen and oxide-regions (the latter starting at 0 V). Hence, corroborating our findings in Chapter 2.0 both H<sub>ad</sub> and BH<sub>4</sub><sup>-</sup><sub>ad</sub> participate in the anodic process. It is interesting to note that on the cathodic scan in the presence of BH<sub>4</sub><sup>-</sup> (Figure 45A) the underpotential deposition hydrogen peak originally at -0.84 V generated from H<sub>2</sub>O<sub>ad</sub> (reaction (89)) is shifted to -0.76 V, suggesting that BH<sub>4</sub><sup>-</sup><sub>ad</sub> competes with H<sub>2</sub>O<sub>ad</sub> for the same active sites.



In the case of PtRu (Figure 45D) while some of the features observed on Pt are retained, the role of Ru as an effective catalyst of the non-Faradaic  $BH_4^-$  hydrolysis accompanied by hydrogen evolution [166], can be clearly identified. The anodic current in the hydrogen region is significantly enhanced with  $BH_4^-$  present, generating one broad current response over a wide potential range (compare Figure 45A and Figure 45C). The behaviour of Os/ C on the other hand (Figure 45E), contrasts to a large extent to that of Pt/ C and PtRu/ C. It should be noted that the switching potential was less positive (i.e., -0.3V) than in the case of Pt/ C and PtRu/ C, to avoid the possibly irreversible oxidative changes of the Os surface [109]. In the absence of  $BH_4^-$ , on Os/ C there are no peaks associated with the H-UPD, indicating a different surface chemistry compared to Pt or PtRu (compare Figure 45B, D, and F). With  $BH_4^-$  present on Os/ C (Figure 45C) one single broad oxidation wave is observed with a peak potential at -0.7 V. This peak is characteristic for the direct  $BH_4^-$  oxidation. Furthermore, on the cathodic scan, one oxidation wave is apparent at -0.76 V related to  $BH_4^-$  species.

To further understand the voltammetric behaviour, experiments were carried out at scan rates of 5, 10, 20, and 25  $mV s^{-1}$  (Figure 46). For Os/ C the cyclic voltammetry modeling equations assuming mixed control (activation-diffusion) were applicable and the  $E_p$  vs.  $\log(v)$  (Figure 46 inset) and  $i_p$  vs.  $v^{1/2}$  functions were employed according to equations (91) to (93) to calculate the apparent Tafel slope and the number of electrons exchanged [70,167].

It must be noted that the differences between the peak current densities (per geometric area) were used for the runs with and without  $BH_4^-$  (Figure 45E and Figure

45F) to separate the direct  $\text{BH}_4^-$  oxidation from hydrogen. Using the  $\text{BH}_4^-$  bulk diffusion coefficient of  $1.09 \times 10^{-5} \text{ cm}^2 \text{ s}^{-1}$  [168] and the Bruggeman type equation (90) [169], to calculate the effective diffusion coefficient in the catalyst layer assuming a porosity  $\varepsilon$  of 0.85, we found the total number of electrons exchanged  $n = 7.1$  and the apparent Tafel slope  $b = 0.23 \text{ V dec}^{-1}$ . The origin of the high apparent Tafel slope relates to the ohmic effects in the porous electrode containing the polymer electrolyte (Nafion<sup>®</sup>). It is well-known that a significant ohmic drop across the porous electrode brings about the doubling of the Tafel slope [169]. Hence, it could be assumed that the intrinsic kinetic Tafel slope (i.e. in the absence of ohmic drop across the catalyst layer) is  $b = 0.11 \text{ V dec}^{-1}$ .

$$D = D_o (\varepsilon)^{\frac{3}{2}} \quad (90)$$

$$E_p = E^{o'} + b \left[ 0.52 - \frac{1}{2} \log \left( \frac{b}{D} \right) - \log(k^o) + \frac{1}{2} \log(v') \right] \quad (91)$$

$$b = \frac{2.3RT}{(1-\alpha)n_a F} \quad (92)$$

$$I_p = (3 \times 10^5) n \left( \frac{2.3RT}{bF} \right)^{\frac{1}{2}} A C_o D^{\frac{1}{2}} v'^{\frac{1}{2}} \quad (93)$$

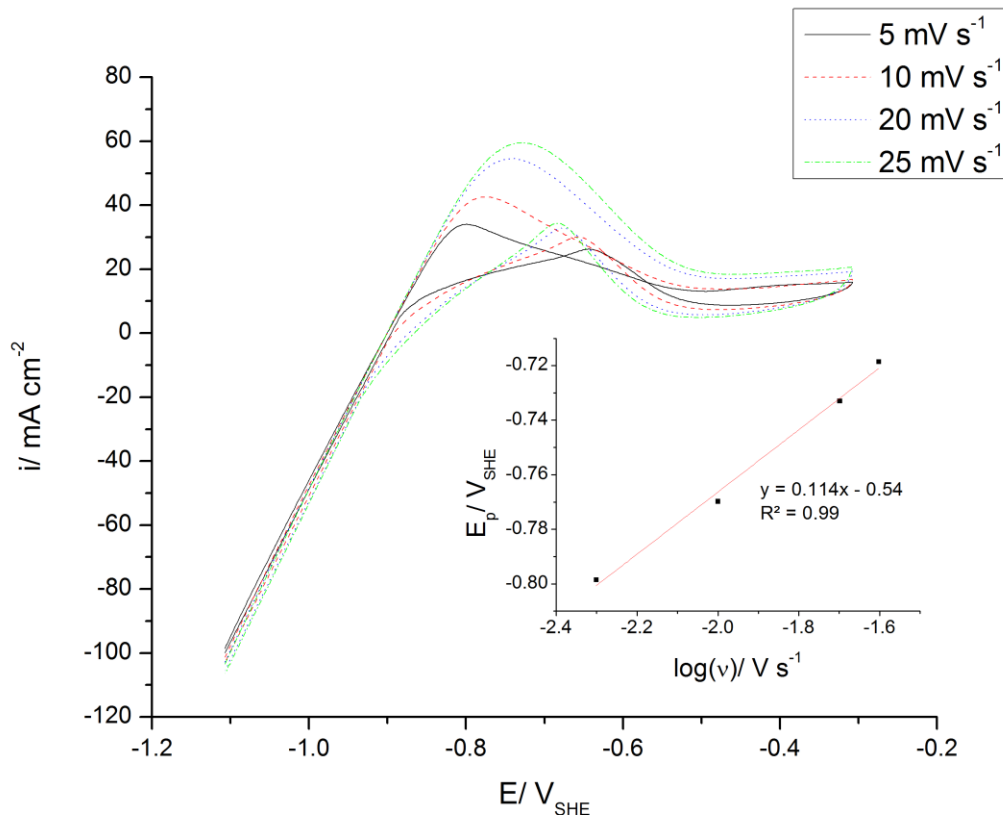


Figure 46. 20% Os/ C cyclic voltammograms at varied scan rates. Inset: Potential at peak current density ( $E_p$ ) versus logarithm of scan rate. Electrolyte: 0.05 M  $\text{NaBH}_4$  – 2 M NaOH, T: 293 K.

where  $E_p$  is the peak potential in V,  $E^{0'}$  is the formal potential in V,  $b$  is the Tafel slope in  $\text{V dec}^{-1}$ ,  $D$  is the diffusion coefficient according to (90) in  $\text{cm}^2 \text{ s}^{-1}$ ,  $k^0$  is the standard heterogeneous rate constant in  $\text{cm s}^{-1}$ ,  $v'$  is the scan rate in  $\text{V s}^{-1}$ ,  $R$  is the universal gas constant in  $\text{J mol}^{-1} \text{ K}^{-1}$ ,  $T$  is the temperature in K,  $\alpha$  is the transfer coefficient (assumed to be 0.5),  $n$  is the number of electrons,  $F$  is Faraday's constant in  $\text{C (mol e}^{-})^{-1}$ ,  $C_0$  is the bulk concentration in  $\text{mol cm}^{-3}$ ,  $A$  is the electrochemical area assumed to be equal to the geometric area of  $1 \text{ cm}^2$ , and  $n_a$  is the number of electrons transferred in the anodic rate determining reaction.

The Coulombic efficiency of Os/ C is therefore, among the very few electrocatalysts where close to eight-electron transfer is possible (the others being Au [81] and Hg [98] as a function of electrode potential and  $[\text{OH}^-]/[\text{BH}_4^-]$  ratio). This is the first time when an almost eight electron transfer of  $\text{BH}_4^-$  oxidation on Os has been described.

Chronoamperometry revealed additional subtle differences and insights regarding the mechanisms of  $\text{BH}_4^-$  oxidation on the three catalysts under consideration (Figure 47). In these experiments the electrode potential was stepped from the open circuit values ( $\sim$ -0.9 V for 20% Pt, PtRu, and Os) for each electrode to -0.6, -0.5 and -0.4 V respectively. Figure 47 presents the corresponding  $I$  vs.  $1/t^{1/2}$  curves as a function of potential.

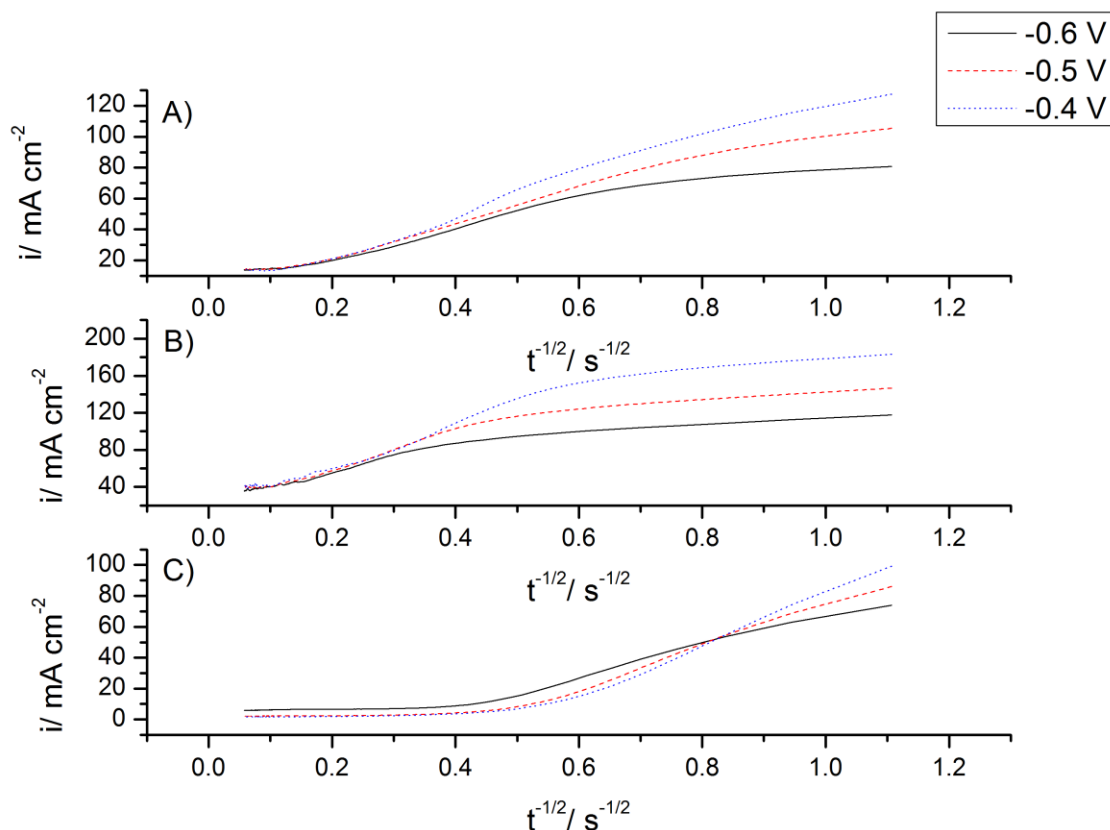


Figure 47. Chronoamperometry curves for  $\text{BH}_4^-$  oxidation on a) Pt/ C, b) PtRu/ C and c) Os/ C catalysts. Potential step from open circuit to -0.6 V, -0.5 V, and -0.4 V, respectively. Electrolyte: 0.05 M  $\text{NaBH}_4$  – 2 M NaOH, T: 293 K. Reproduced with permission from [165], Copyright 2008, The Electrochemical Society.

Pt/ C, PtRu/ C, and Os/ C differed markedly in their chronoamperometric responses. In the case PtRu/ C, for each potential step two distinct linear portions can be identified (Figure 47B). The change in slope between the two sections occurred at about 2.8 s when the anode potential was -0.4 V and at 6.25 s when the potential was -0.6 V (Figure 47B). The two different slopes for the same potential step, can be attributed to a change in the total number of electrons exchanged as a function of time due to the competing  $\text{H}_2$  and  $\text{BH}_4^-$  oxidation reactions. Fitting the Cottrell equation (equation (94))

to the two linear regions, it was found that the ratio of the slopes of the two linear portions was approximately equal to 4.

$$i = \frac{nFD_o^2 C_o}{\pi^2 t^2} \quad (94)$$

It was surmised in the case of PtRu, early on, the oxidation of H<sub>2</sub> generated *in-situ* from the catalytic BH<sub>4</sub><sup>-</sup> hydrolysis takes place (n = 2) due to the severe autocatalytic BH<sub>4</sub><sup>-</sup> hydrolysis, while after about 2.8 to 6.25 s (depending on the applied potential) the apparent number of electrons exchanged is close to n = 8. A total of eight electrons can be generated either by direct BH<sub>4</sub><sup>-</sup> oxidation or complete hydrolytic decomposition of BH<sub>4</sub><sup>-</sup> followed by oxidation of the resulting H<sub>2</sub> with 100% efficiency. It is possible to associate a bifunctional role to PtRu, where Ru serves mainly as the non-faradaic BH<sub>4</sub><sup>-</sup> hydrolysis catalyst, while Pt acts as the electrocatalyst for both H<sub>2</sub> and BH<sub>4</sub><sup>-</sup> oxidation.

The chronoamperometry response for Pt was similar to PtRu (Figure 47A). As discussed in Chapter 2.0, the number of electrons for BH<sub>4</sub><sup>-</sup> electro-oxidation on Pt may change depending on the adsorption of reaction intermediates and the number of available Pt sites to facilitate the reaction.

In practice, the relative rate of hydrogen oxidation versus the rate of its generation depends on a number of factors such as: anode potential, electrocatalyst, anode design, mass transport effects (e.g., two-phase gas-liquid mass transport), temperature, pressure, and time. In liquid-flooded porous electrodes, such as those employed in the chronoamperometry studies, due mostly to mass transfer related effects, the oxidation of

hydrogen is less efficient than what would be expected based purely on kinetic considerations, hence, gas accumulation and evolution has been observed.

The chronoamperometry curves for Os (Figure 47C) on the other hand, show that there was virtually no change in the slope of the  $I$  vs.  $1/t^{1/2}$  curves up to 4 s, a behavior which is consistent with direct  $\text{BH}_4^-$  oxidation as the only electrochemical reaction. The leveling off observed for  $t > 4$  s is related to the depletion of the boundary  $\text{BH}_4^-$  concentration due to the enhanced oxidation on the high-surface area electrode.

To study the longer-term performance of the catalysts, chronopotentiometry was conducted applying a constant current step of  $10 \text{ mA cm}^{-2}$  for 3 hrs. (Figure 48). Os/ C operated at the most negative anode potential among the catalysts under investigation. Furthermore, Os/ C showed minor deactivation, its potential drifted by only  $+3 \text{ mV h}^{-1}$  which could have been due solely to the consumption of  $\text{BH}_4^-$  in the batch experiment. It is interesting to note that the open circuit anode potentials were more positive than the  $\text{BO}_2^-/\text{BH}_4^-$  equilibrium potential of  $-1.24 \text{ V}$ . In fact the open circuit potentials (between  $-0.89$  and  $-0.91 \text{ V}$ ) are close to the equilibrium potential of the  $\text{H}_2$  electrode in  $2 \text{ M NaOH}$ . This shows that the  $\text{BO}_2^-/\text{BH}_4^-$  redox couple is highly irreversible on each of the three electrodes with the equilibrium strongly shifted in the anodic direction (i.e., toward  $\text{BO}_2^-$  formation). In the case of PtRu and Pt, non-faradaic  $\text{H}_2$  evolution takes place under open circuit conditions, affecting as well the measured potential.

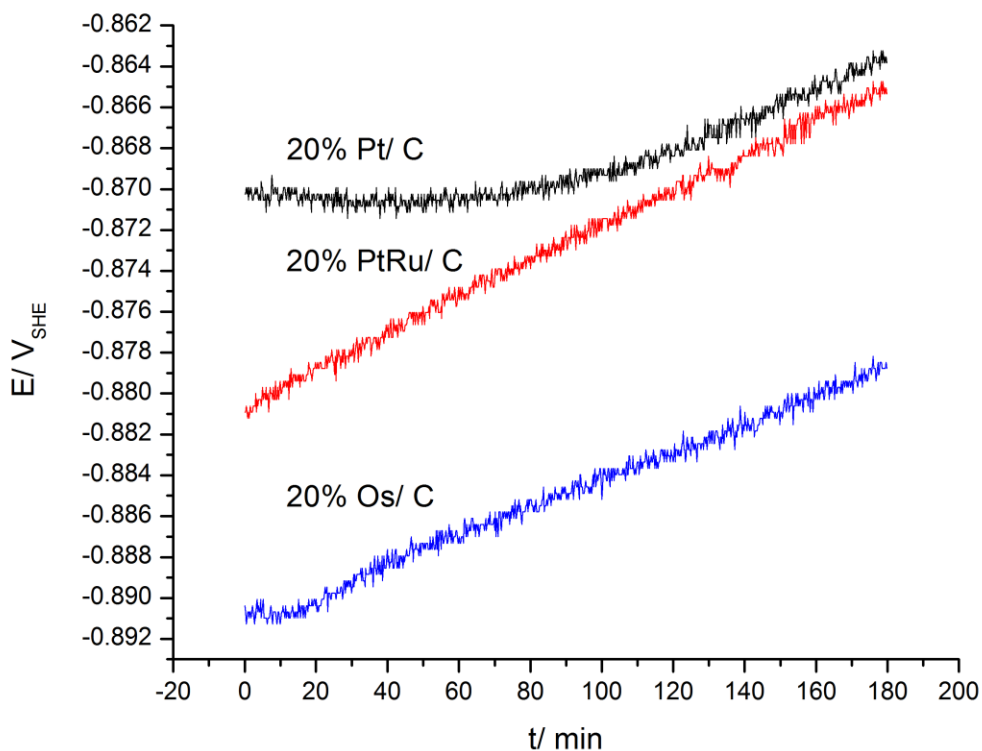


Figure 48. Chronopotentiometry profiles for  $BH_4^-$  oxidation on 20% Pt/ C, PtRu/ C and Os/ C catalysts. Anolyte: 0.05 M  $NaBH_4$  – 2 M NaOH, T: 293 K, P: 1 atm (abs), i: 10  $mA\ cm^{-2}$ . Reproduced with permission from [165], Copyright 2008, The Electrochemical Society.

### 3.2 Fuel Cell Experiments

The fundamental electrochemical studies were followed up by fuel cell experiments using polymer electrolyte membrane (Nafion 117<sup>®</sup>) electrode assemblies coated on the anode side with the supported catalysts (20 % metal/ C) having 1  $mg\ cm^{-2}$  metal load. Figure 49 compares the fuel cell polarization behaviour for the three catalysts at 298 K and 333 K, respectively.

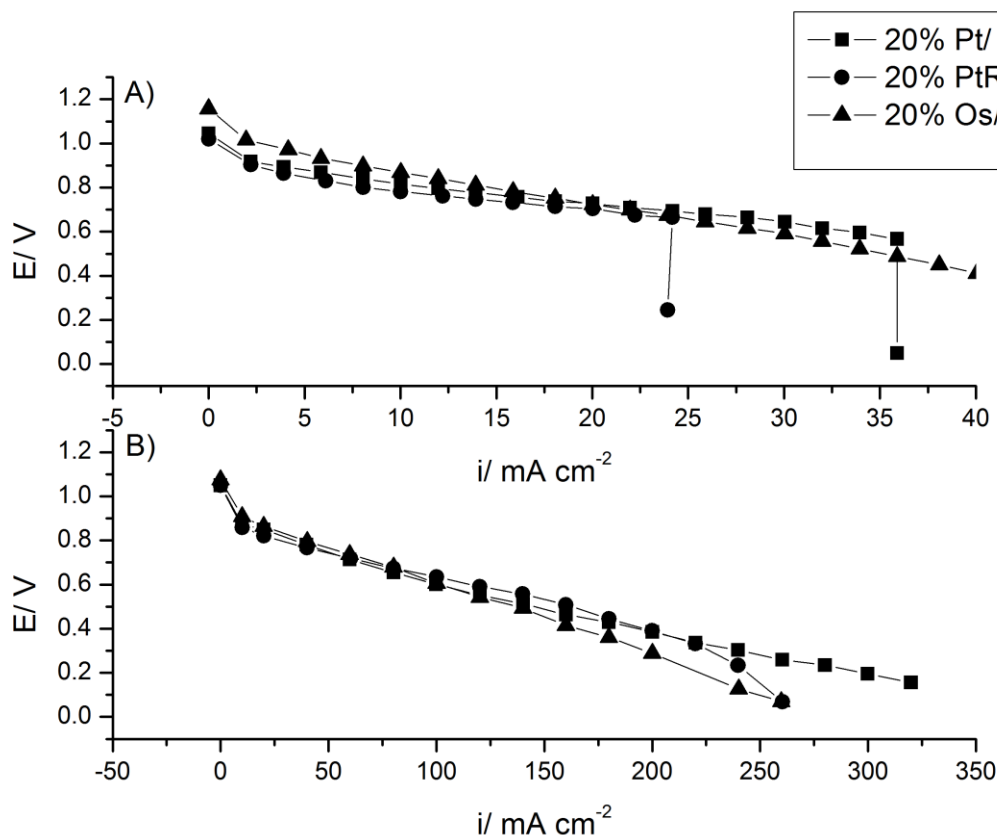


Figure 49. Direct borohydride fuel cell polarization curves using 20% Pt/ C, 20% PtRu/ C and 20% Os/ C anode catalysts with a load of  $1 \text{ mg cm}^{-2}$ . Cathode catalyst Pt black  $4 \text{ mg cm}^{-2}$ . a) T: 298 K, b) T: 333 K. Anolyte:  $0.5 \text{ M NaBH}_4 - 2 \text{ M NaOH}$ , anolyte flow rate:  $10 \text{ ml min}^{-1}$ , oxidant:  $\text{O}_2$ , oxidant flowrate:  $1.25 \text{ SLPM}$ , oxidant pressure:  $4.4 \text{ atm (abs)}$ . Reproduced with permission from [165], Copyright 2008, The Electrochemical Society.

At 298 K (Figure 49A) Os/ C gave the highest open circuit and operating cell voltages in the kinetic region (i.e.,  $E_{\text{cell}} \geq 0.9 \text{ V}$ ). Furthermore, in the polarization region where mass transfer effects could become prevalent (i.e.,  $E_{\text{cell}} < 0.7 \text{ V}$ ), the performance of the PtRu/ C and Pt/ C electrodes decayed abruptly, while the Os/ C decayed more gradually (Figure 49A). The anode mass transfer limiting current densities (Figure 49A) at 298 K were  $24 \text{ mA cm}^{-2}$  for PtRu/ C at  $0.23 \text{ V}$ ,  $36 \text{ mA cm}^{-2}$  for Pt/ C at  $0.05 \text{ V}$  while with Os/ C  $40 \text{ mA cm}^{-2}$  was achieved at  $0.41 \text{ V}$ . In the case of PtRu/ C and Pt/ C the

accumulation of H<sub>2</sub> gas in the anode catalyst layer due to the incomplete oxidation, blocked the active sites and impeded the liquid BH<sub>4</sub><sup>-</sup> mass transfer.

Operating at 333 K improved the power output with both PtRu/ C and Pt/ C catalysts, by enhancing the catalytic H<sub>2</sub> generation and oxidation rates (Figure 49B). In 3 hr DBFC experiments at 333 K, and a constant current density of 120 mA cm<sup>-2</sup> (Figure 50), the DBFC equipped with Os/ C anode catalysts exhibited similar stability to when using Pt/ C and PtRu/ C anode catalysts. The rate of voltage decay when using Os/ C anode catalysts was approximately 2.9 mV h<sup>-1</sup>. Pt/ C and PtRu/ C showed cell voltage losses of 6 and 4.2 mV h<sup>-1</sup>, respectively. The maximum power densities with Os/ C were 18 mW cm<sup>-2</sup> at 298 K and 69 mW cm<sup>-2</sup> at 333 K (Figure 49A and B).

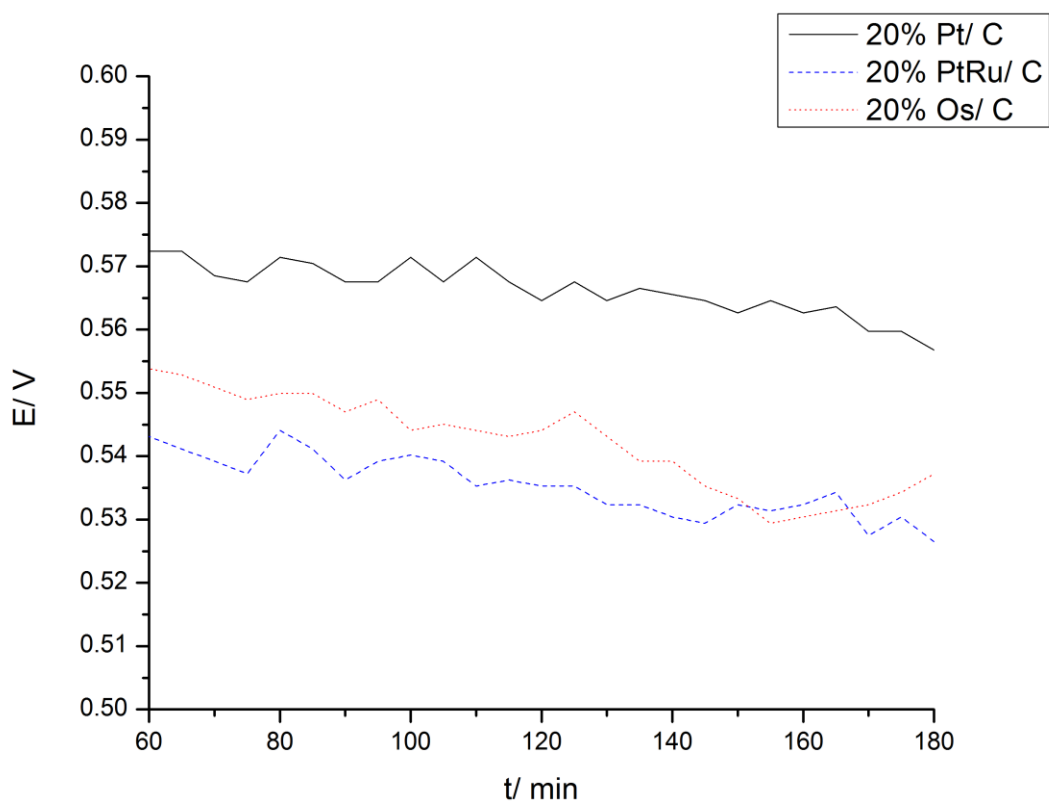


Figure 50. 20% Pt/ C, PtRu/ C, and Os/ C direct fuel cell longevity tests over 3 hours at a constant current of  $120 \text{ mA cm}^{-2}$ . Anode catalysts with a load of  $1 \text{ mg cm}^{-2}$ . Cathode catalyst Pt black  $4 \text{ mg cm}^{-2}$ . T: 333 K, anolyte:  $0.5 \text{ M NaBH}_4 - 2 \text{ M NaOH}$ , anolyte flow rate:  $10 \text{ mL min}^{-1}$ , oxidant:  $\text{O}_2$ , oxidant flow rate: 1.25 SLPM, oxidant pressure: 4.4 atm (abs).

With regard to Os, the effect of metal dispersion on the carbon support (Os: 10 wt%, 20 wt% and 30 wt% / C) was also investigated. Figure 51 shows the DBFC fuel cell polarization curves at 333 K as a function of Os dispersion for a constant metal load of  $1 \text{ mg cm}^{-2}$ . It was found that increasing the metal dispersion from 10 wt% to 20 wt% on carbon brings about a very significant improvement throughout the polarization curve. Further increase of the Os dispersion from 20 wt% to 30 wt%, while it provides some

benefits in the kinetic region of the curve ( $E_{\text{cell}} \geq 0.9$  V), is less advantageous at higher current densities where Ohmic and mass transfer effects also play a role (Figure 51).

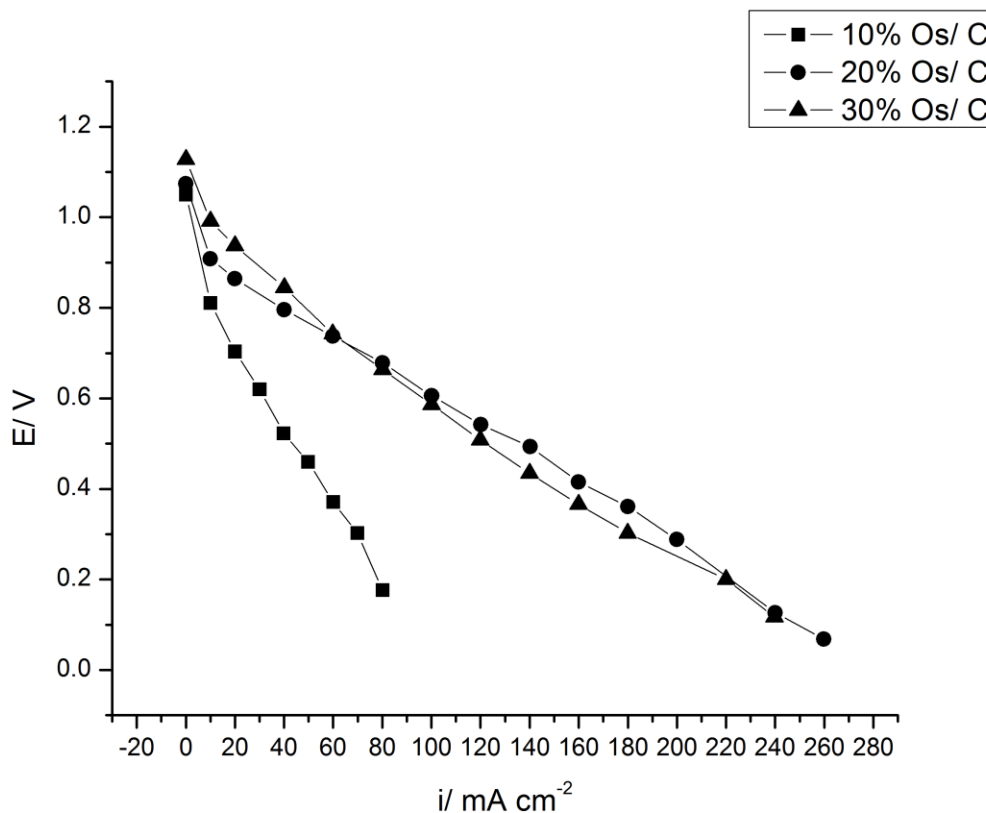


Figure 51. Effect of Os dispersion on the carbon support on the DBFC polarization curves. Anode catalysts with a load of  $1 \text{ mg cm}^{-2}$ . Cathode catalyst Pt black  $4 \text{ mg cm}^{-2}$ . T: 333 K, anolyte:  $0.5 \text{ M NaBH}_4 - 2 \text{ M NaOH}$ , anolyte flow rate:  $10 \text{ mL min}^{-1}$ , oxidant:  $\text{O}_2$ , oxidant flow rate: 1.25 SLPM, oxidant pressure: 4.4 atm (abs). Reproduced with permission from [165], Copyright 2008, The Electrochemical Society.

### 3.3 Summary for Chapter 3.0

Osmium nanoparticles synthesized by the Bönnerman organosol method and supported on Vulcan XC-72 are electrochemically active for  $\text{BH}_4^-$  electro-oxidation, exhibit similar stability to Pt/ C and PtRu/ C catalysts, and are relatively cheaper than Pt at  $\$11.25 \text{ g}^{-1}$  to  $14.47 \text{ g}^{-1}$  [107] versus  $\$52.47 \text{ g}^{-1}$  [108]. Cyclic voltammetry of  $\text{BH}_4^-$

electro-oxidation on Os/ C shows a significant difference to that of Pt/ C and PtRu/ C. The most notable difference being the absence of H-UPD peaks, which are present during  $\text{BH}_4^-$  electro-oxidation on both Pt/ C and PtRu/ C. At the same metal loadings, the FC performance of 20% Os/ C was lower but comparable to 20% Pt/ C and 20% PtRu/ C at 333 K. Both half-cell and fuel cell experiments confirm the stability of Os/ C compared to Pt/ C and PtRu/ C catalysts. At 298 K,  $\text{BH}_4^-$  hydrolysis had significant influence on the performance of Pt/ C and PtRu/ C catalysts in a fuel cell setup, resulting in a sudden drop in the polarization curves at high current densities. This is attributed to mass transport issues induced by the two-phase flow of fuel. In contrast, the Os/ C catalysts did not appear to be affected by  $\text{BH}_4^-$  hydrolysis, thereby, supporting the Faradaic efficiency calculated for  $\text{BH}_4^-$  electro-oxidation on the Os/ C catalysts ( $n = 7.1$  of a total possible  $n = 8$ ). Comparison of three different metal dispersions of Os/ C show a significant improvement between 10% Os/ C and 20% Os/ C, but between 20% Os/ C and 30% Os/ C, the differences in fuel cell performances were minor.

## 4 The Effect of Catalyst Support on Direct Borohydride Fuel Cell Performance\*

In this chapter, the effect of catalyst support was studied and compared in fuel cell experiments. Unsupported PtRu black versus PtRu/ C versus graphite felt supported PtRu were analyzed. The graphite felt supported PtRu electrode, also referred to as a three-dimensional electrode, was synthesized via electrodeposition in the presence of a non-ionic surfactant and characterized using TEM, and XRD.

An investigation conducted by Özkar and Zahmakiran on Ru nanoclusters revealed that the activation energy for  $\text{BH}_4^-$  hydrolysis is much lower on Ru compared to other metal catalysts known to be active for  $\text{BH}_4^-$  hydrolysis;  $28.5 \text{ kJ mol}^{-1}$  for Ru versus  $75 \text{ kJ mol}^{-1}$  for Co, and  $71 \text{ kJ mol}^{-1}$  for Ni [65].

A patent by Tsang and Prasad addressed the potential of PtRu for DBFC anodes [170]. According to these authors, the basis for PtRu is to facilitate the hydrolysis of  $\text{BH}_4^-$  on Ru and oxidize the evolved hydrogen on Pt. It is likely that  $\text{BH}_4^-$  electro-oxidation also takes place directly on Pt. Duteanu et al. tested a PtRu/ C anode in a DBFC system and reported power densities of up to  $145 \text{ mW cm}^{-2}$  at 333 K with a  $1 \text{ mg cm}^{-2}$  PtRu/ C anode, a  $1 \text{ mg cm}^{-2}$  Pt/ C cathode, an anion exchange membrane, 1 M  $\text{NaBH}_4$  – 1 M NaOH anolyte composition, and  $\text{O}_2$  oxidant (oxidant pressure not specified) [135]. Tsang and Prasad also emphasized the importance of controlling the operating parameters and fuel composition such that the rate of hydrogen formation does not exceed the rate of  $\text{H}_2$  electro-oxidation [170]. A ratio of  $\text{H}_2$  evolution rate versus  $\text{H}_2$

---

<sup>4</sup> This chapter is based on the following published work:

V.W.S. Lam, A. Alfantazi, E.L. Gyenge, J. Appl. Electrochem. 39 (2009) 1763.

electro-oxidation rate greater than one would lead to the accumulation of hydrogen gas within the anode compartment, thus creating mass transport problems for the reactant to the catalytic sites.

The hydrogen evolution from  $\text{BH}_4^-$  hydrolysis creates a two phase (liquid/gas) flow situation in the porous catalyst and diffusion layers as well as in the flow channels (see section 1.1.4 for a detailed discussion on  $\text{BH}_4^-$  hydrolysis). This flow behaviour leads to complications in mass transfer for typical gas diffusion anode structures and fuel distribution methods, and it is further aggravated for larger stacks [129,171]. In a study on the effect of hydrogen evolution on the cell and stack performances of a DBFC, Liu et al. showed that the evolved hydrogen during fuel cell operation blocks the channels in the flowfield and may also impede the ion conductance at the interface between the catalyst layer and the membrane [129]. Therefore, improving the Faradaic efficiency of the direct  $\text{BH}_4^-$  oxidation to possibly 8 electrons has been the focus of many investigations [9,86,172]. Methods that have been investigated for Faradaic efficiency improvement include the use of additives such as TU, discussed in section 1.2.2, and alternative catalyst materials such as AgNi, Au, and Os [17,103,165,172].

Another method that may be used to moderate the problem of  $\text{BH}_4^-$  hydrolysis is to change the structure of the anode catalyst layer to accommodate the evolved  $\text{H}_2$ . The three-dimensional electrode consists of an electrically conductive porous substrate with thickness in a fuel cell setup from  $\sim 200$  to  $2000 \mu\text{m}$ , with deposited catalysts dispersed uniformly through all three dimensions of the substrate. The purpose of its original development for direct fuel cells by Gyenge, Oloman, Wilkinson and co-workers was to address problems associated with direct organic fuels such as  $\text{CO}_2$  disengagement, and

fuel crossover [173--185]. In addition, monolithic three-dimensional electrodes extend the reaction zone of the anode of the fuel cell, which can improve the catalyst load utilization and hence the fuel utilization.

## **4.1 Experimental Procedure**

### **4.1.1 Catalyst Ink Preparation**

The catalyst ink used to prepare the unsupported Pt black and PtRu black (2-3 nm metal particle size), and Vulcan<sup>®</sup> XC-72 supported PtRu/ C (2-3 nm metal particle size) catalysts consisted of a dispersion in a 2:1:4 mass ratio of: a) catalyst powder – 5 wt% Nafion<sup>®</sup> solution (3:2 catalyst powder to Nafion<sup>®</sup> dry weight ratio), b) 15 MΩ deionized water and c) 2-Propanol (Fisher Inc). The ink was stirred for 5 minutes then sonicated for 3 hours prior to use. The catalysts investigated in this study were: PtRu/ C (1:1 at. ratio) 20 %wt supported on Vulcan<sup>®</sup> XC-72 (purchased from E-TEK), PtRu (1:1 at. ratio) black (Alfa Aesar) and Pt black (Alfa Aesar).

### **4.1.2 Fuel Cell Experiments**

Sodium borohydride solutions were prepared using various concentrations of 98 wt% NaBH<sub>4</sub> (ACROS) and 2 M Certified A.C.S. NaOH (Fisher Scientific). Vulcan<sup>®</sup> XC-72 carbon supported and unsupported catalysts (1 mg cm<sup>-2</sup> metal loading) were sprayed onto the membrane side of commercial half membrane electrode assemblies (MEA) (Lynntech). The half MEA consisted of unsupported 4 mg cm<sup>-2</sup> Pt black cathode catalyst layer painted on one side of a Nafion<sup>®</sup> 117 (183 μm thickness) membrane (DuPont).

Untreated carbon cloth and ELAT<sup>®</sup> gas diffusion layers were positioned between the MEA and the flowfield plates at the anode and cathode respectively. Stainless steel flowfield plates with serpentine flow channels compressed the MEA. Teflon<sup>®</sup> coated fiberglass gaskets (McMaster and Carr) sealed either side of the MEA. Fuel cell tests were carried out using the Fuel Cell Methanol Test Kit and FC Power<sup>™</sup> software (Fideris). Additional information regarding the fuel cell test setup can be found in Appendix H.

### 4.1.3 PtRu Electrodeposition on Graphite Felt

A method devised by Bauer et al. for the electrodeposition of PtRu nanoparticles on fibrous carbon substrates using the non-ionic surfactant Triton X-100 was adopted in this study [176,178]. The surfactant assisted electrodeposition method generates evenly dispersed PtRu nanoparticles on graphite felts. In the present work a 350  $\mu\text{m}$  thick, 0.95 porosity, and 5  $\text{cm}^2$  geometric area compressed graphite felt GF-S3 (Electro Synthesis Company Inc.) was employed. The felt was cleaned with methanol (Fisher) and distilled water, and then dried at 333 K in air. The electrodeposition media consisted of 65 mM  $\text{H}_2\text{PtCl}_6 \cdot 6 \text{H}_2\text{O}$  (99.9 wt% Aldrich), 65 mM  $\text{RuCl}_3 \cdot 3\text{H}_2\text{O}$  (99.9 wt% Alfa-Aesar), and 40 wt% Triton X-100 [ $\text{C}_{14}\text{H}_{22}\text{O}(\text{C}_2\text{H}_4\text{O})_n$ ,  $n = 9.5$ ] (Aldrich). Electrodeposition was carried out at a constant superficial current density (galvanostatic mode) of 600  $\text{mA cm}^{-2}$  applied for 1.5 h using platinized titanium counter electrodes. The temperature was 333 K. After electrodeposition, the felt was rinsed with warm methanol and distilled water to remove the surfactant. The electrodeposited PtRu on graphite felt (PtRu/ GF) was then

electrochemically conditioned at -0.8 V vs. Hg/ Hg<sub>2</sub>SO<sub>4</sub> for 5 minutes in 0.5 M H<sub>2</sub>SO<sub>4</sub> to clean the electrode.

#### **4.1.4 Characterization of the PtRu on Graphite Felt**

Crystallography, particle size and phase of the deposited catalyst were identified via X-Ray Diffraction (XRD) using the D8 Advance Bruker diffractometer with Cu K $\alpha_1$  radiation. Transmission electron microscopy (TEM) was performed using the Hitachi H7600 microscope with an accelerating voltage of 120 kV. The TEM sample was composed of PtRu/ GF grounded into a powder using a mortar and pestle and suspended in ethanol (Fisher Inc.).

## **4.2 Effect of Support**

Figure 52A shows that the DBFC performance of PtRu black (i.e. not supported on Vulcan<sup>®</sup> XC-72 carbon) at 333 K is comparable to that of Pt black, reaching a peak power density of 35.1 mW cm<sup>-2</sup> versus 31.6 mW cm<sup>-2</sup> for Pt black. Previous electrochemical studies of the Lam and Gyenge showed the number of electrons for BH<sub>4</sub><sup>-</sup> electro-oxidation on PtRu/ C can vary from 2 to 8 depending on the OH<sup>-</sup>/ BH<sub>4</sub><sup>-</sup> concentration ratio, temperature, reaction time, electrode material, and potential [165]. A closer examination of the polarization curve in Figure 52B at cell potentials higher than 0.8 V reveals that BH<sub>4</sub><sup>-</sup> electro-oxidation is kinetically more favorable on PtRu black than Pt black. However, at current densities higher than 60 mA cm<sup>-2</sup> PtRu black becomes mass transport limited and the Pt black performance exceeds that of PtRu black. The

mass transport limitations of the PtRu black anode catalyst is due to the accumulation of hydrogen gas in the PtRu anode compartment [165].

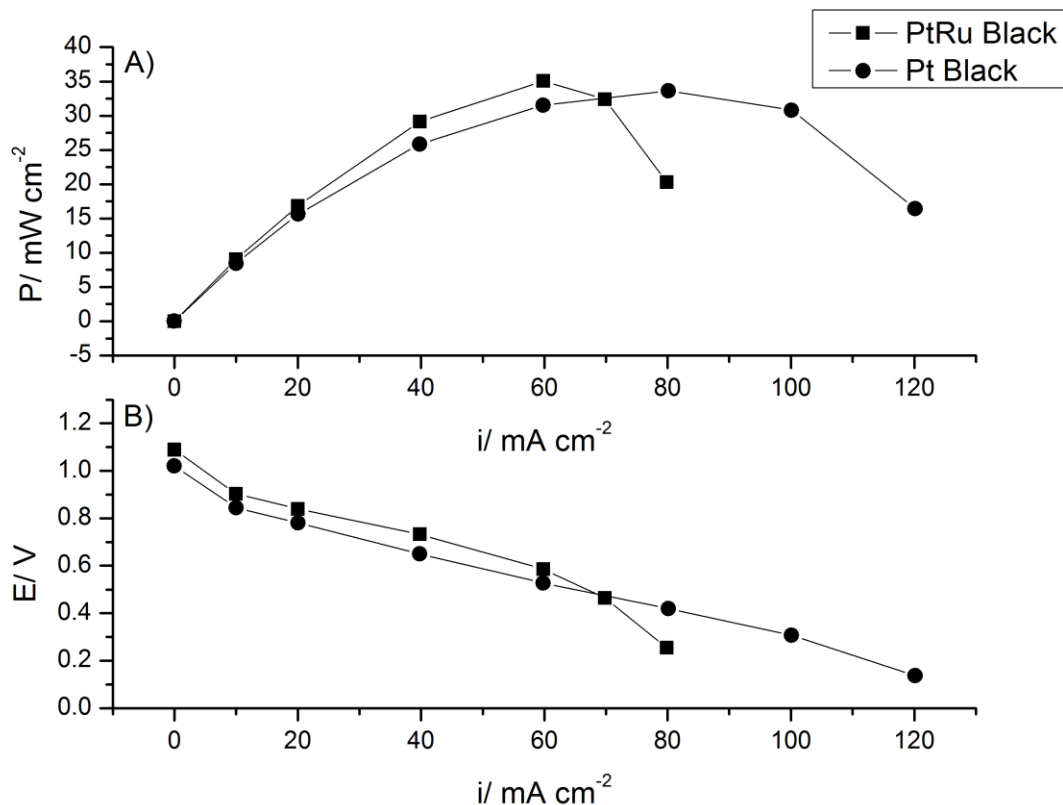


Figure 52. Non-supported Pt black and PtRu black anode catalyst comparison for DBFC. A) Power density curves B) Polarization curves. Anode loading: 1 mg cm<sup>-2</sup>, cathode loading: 4 mg cm<sup>-2</sup> Pt black, analyte: 0.5 M NaBH<sub>4</sub> – 2 M NaOH, analyte flow rate: 10 mL min<sup>-1</sup>, O<sub>2</sub> flow rate: 1.25 SLPM, O<sub>2</sub> pressure: 4.4 atm (abs); T: 333K. Reproduced with permission from [186], Copyright 2009, Springer.

In Figure 53 the polarization curves for PtRu black and PtRu/ C are compared, both with a 1 mg cm<sup>-2</sup> metal load. It is evident that the electrode kinetic performances are virtually identical at low current densities (up to 20 mA cm<sup>-2</sup>). At higher superficial current densities there is a significant drop in performance for the unsupported catalyst. Kim et al. investigated the effect of Vulcan<sup>®</sup> XC-72 carbon support for Pt/ C catalysts,

and found that an anode catalyst load four times higher was required for unsupported Pt black catalyst to match the fuel cell performance for Pt/ C catalyst [85].

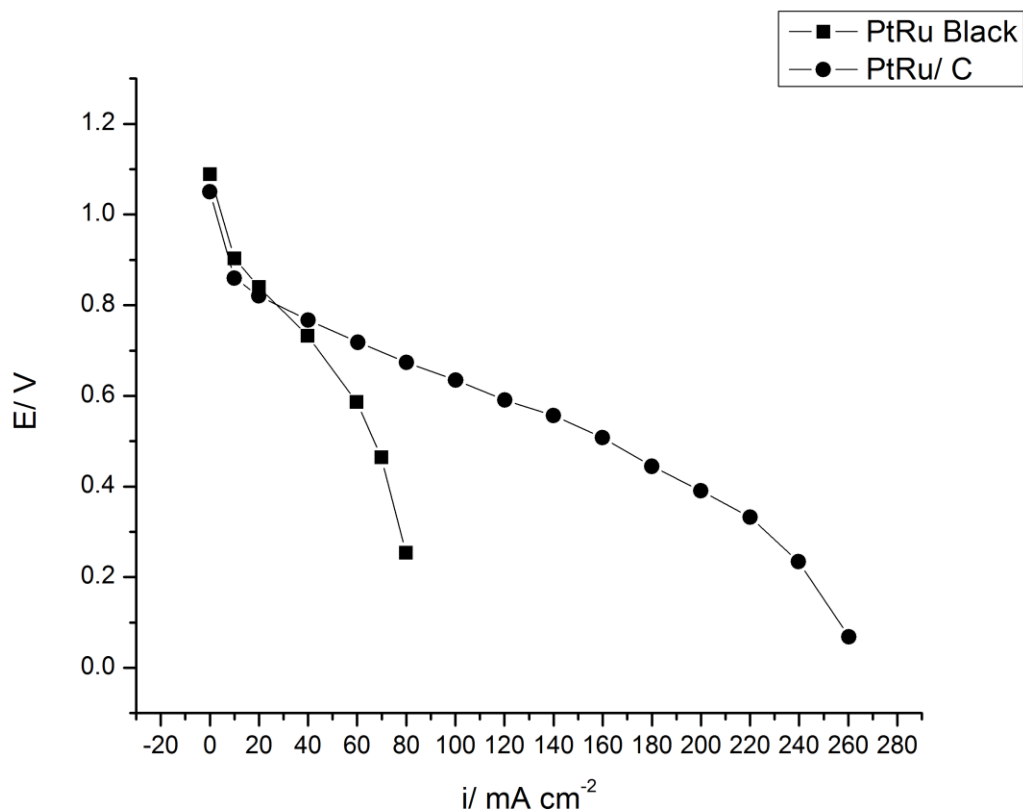


Figure 53. Comparison of 20% PtRu/ C and PtRu black catalyst performance. Anode loading:  $1 \text{ mg cm}^{-2}$ , cathode loading:  $4 \text{ mg cm}^{-2}$  Pt black, anolyte:  $0.5 \text{ M NaBH}_4 - 2 \text{ M NaOH}$ , anolyte flow rate:  $10 \text{ ml min}^{-1}$ ,  $\text{O}_2$ , flow rate:  $1.25 \text{ SLPM}$ ,  $\text{O}_2$  pressure:  $4.4 \text{ atm (abs)}$ ,  $T: 333\text{K}$ . Reproduced with permission from [186], Copyright 2009, Springer.

It is unlikely that in our case the intrinsic electrocatalytic activity of PtRu or catalyst-support electronic interaction effects were the primary contributors to the observed differences in performance in polarization curves at current densities higher than  $20 \text{ mA cm}^{-2}$  (Figure 53). The superior performance of the PtRu/ C catalyst could be attributed to effects associated with  $\text{H}_2$  generation by the hydrolysis reaction. The

supported catalyst layer is thicker in comparison to the unsupported catalyst layer due to both the carbon presence and the larger amount of Nafion<sup>®</sup>. The Nafion<sup>®</sup> content of the catalyst layer was measured against the total catalyst powder weight such that the final active layer dry composition was 60 wt% Nafion<sup>®</sup> and 40 wt% catalyst. The weight ratio of Nafion<sup>®</sup> to metal content differed for the unsupported and supported catalyst layers; it was 3:2 Nafion<sup>®</sup> to PtRu metal for the unsupported catalyst, and 15:2 for the supported catalyst.

We propose that the morphology of the thicker supported catalyst layer is such that the evolved hydrogen from the catalytic sites (mostly Ru) can be trapped more easily, because the path for the evolved hydrogen to escape would be tortuous. Thus, hydrogen will have a longer residence time inside the catalyst layer and a better chance to reach the oxidative catalytic sites (Pt). Hence, the electro-oxidation of hydrogen is more efficient in the supported catalyst layer. More specifically, the relative rate of hydrogen oxidation (on Pt) with respect to hydrogen generation (by BH<sub>4</sub><sup>-</sup> hydrolysis on Ru) is higher in the case of the supported catalyst due to both the different porous electrode structure and the higher Nafion<sup>®</sup> content. It must be also noted that the supported catalyst layer is more hydrophobic resulting in better H<sub>2(g)</sub> attachment and subsequent oxidation.

Visual observations (Figure 54) of the hydrogen evolution without polarization revealed the formation at a high rate of large gas bubbles on PtRu black compared to PtRu/ Vulcan<sup>®</sup> XC-72. Thus, the amount of Nafion<sup>®</sup> and carbon support can have a major effect on the rate of BH<sub>4</sub><sup>-</sup> hydrolysis. In future studies, a quantitative comparative measurement of the hydrogen evolution rate is required under both open-circuit and anodic polarization conditions.

Kim et al. investigated the effect of Nafion<sup>®</sup> content on the anode and found an optimal composition at 30 %wt which is in agreement with conclusions regarding the hydrogen polymer electrolyte fuel cells [85,187]. The Nafion<sup>®</sup> effect in the case of the alkaline BH<sub>4</sub><sup>-</sup> fuel cell was explained by the ability of the Nafion<sup>®</sup> to improve the wetting of the catalyst layer, while at higher than optimum Nafion<sup>®</sup> loadings, the ionic and electronic conductivities of the catalyst layer are diminished hence, the fuel cell performance is worse. In addition encapsulation of catalyst particles with Nafion<sup>®</sup> may hinder the mass transport of BH<sub>4</sub><sup>-</sup> anions to catalytic sites. Cheng et al. confirmed that the catalyst utilization was heavily dependent upon the Nafion<sup>®</sup> content and morphology [188].

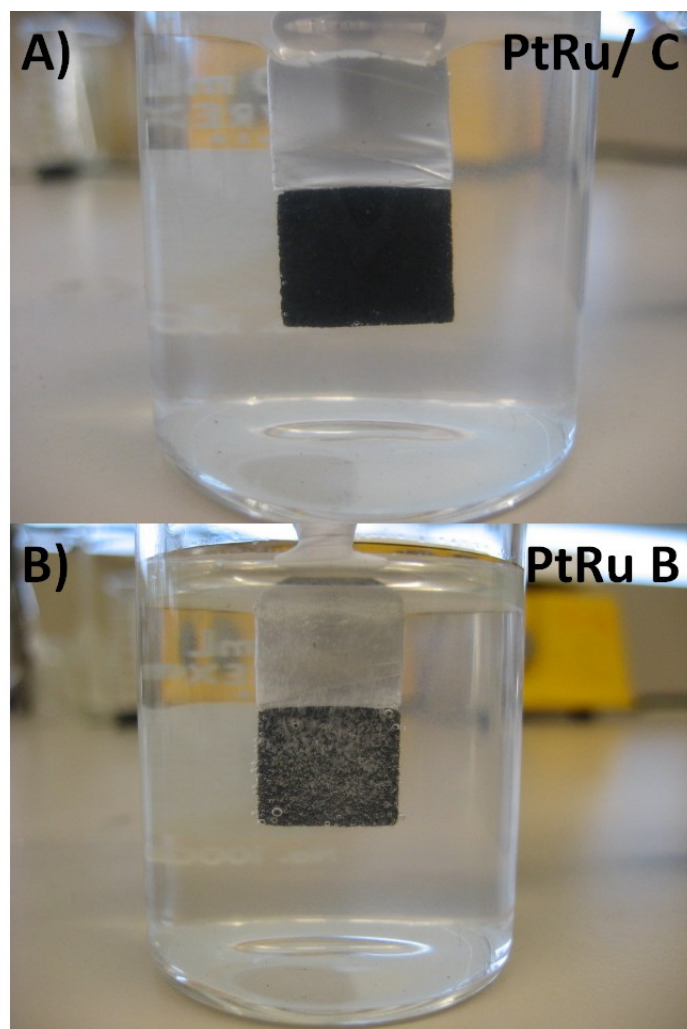


Figure 54. Heterogeneous catalysis of  $\text{BH}_4^-$  hydrolysis without electrode polarization.  $1 \text{ mg cm}^{-2}$  PtRu black and 20 wt%  $1 \text{ mg cm}^{-2}$  PtRu/ C. Catalyst sprayed on Toray carbon paper with 60 wt% Nafion<sup>®</sup> binder. Analyte: 0.5 M  $\text{NaBH}_4$  – 2 M NaOH; T: 293K. Reproduced with permission from [186], Copyright 2009, Springer.

### **4.3 Effect of the Anode Structure in Relation to PtRu electrocatalysts: Three-Dimensional Graphite Felt Support**

Hydrogen formation can hinder the mass transport of  $\text{BH}_4^-$  to the catalytic sites and diminish the effective ionic conductivity in the active layer [129] therefore, it must be efficiently oxidized on Pt. A major advantage of using a three-dimensional anode in DBFC besides providing an extended reaction zone for  $\text{BH}_4^-$  oxidation, is the high macro porosity of the felt (e.g.  $\geq 90\%$ ) that can aid in the disengagement of unconsumed hydrogen with lesser interference on the liquid mass transfer. Furthermore, ionic conductivity is provided by the concentrated NaOH. Thus, another advantage is the absence of Nafion<sup>®</sup> in the three-dimensional anode structure, which would mitigate such complications as electronic insulation of the catalyst particles, and potential mass transport limitations of  $\text{BH}_4^-$  anions diffusing through the Nafion<sup>®</sup> film. The graphite felt electrode may also help reduce the high  $\text{BH}_4^-$  crossover rate (e.g.,  $4.01 \times 10^{-3} \text{ mol m}^{-2}\text{s}^{-1}$  using the Nafion<sup>®</sup> 117 membrane (183  $\mu\text{m}$  thickness) at an assumed temperature of 298 K [14]) due to its extended reaction zone thickness of 300  $\mu\text{m}$  coupled with possibly higher catalyst utilization and activity.

#### **4.3.1 Characterization of PtRu Supported on Graphite Felt**

Figure 55A and Figure 55B shows the TEM pictures of PtRu on the graphite felt three-dimensional electrode produced by surfactant templated electrodeposition (Section 2.3). The larger deposits (e.g.  $\sim 160 \text{ nm}$  in diameter) (Figure 55A) are in fact agglomerates of much smaller particles with a narrow size distribution ranging from 2.9 to 4.6 nm creating a micro-porous catalyst structure (Figure 55B).

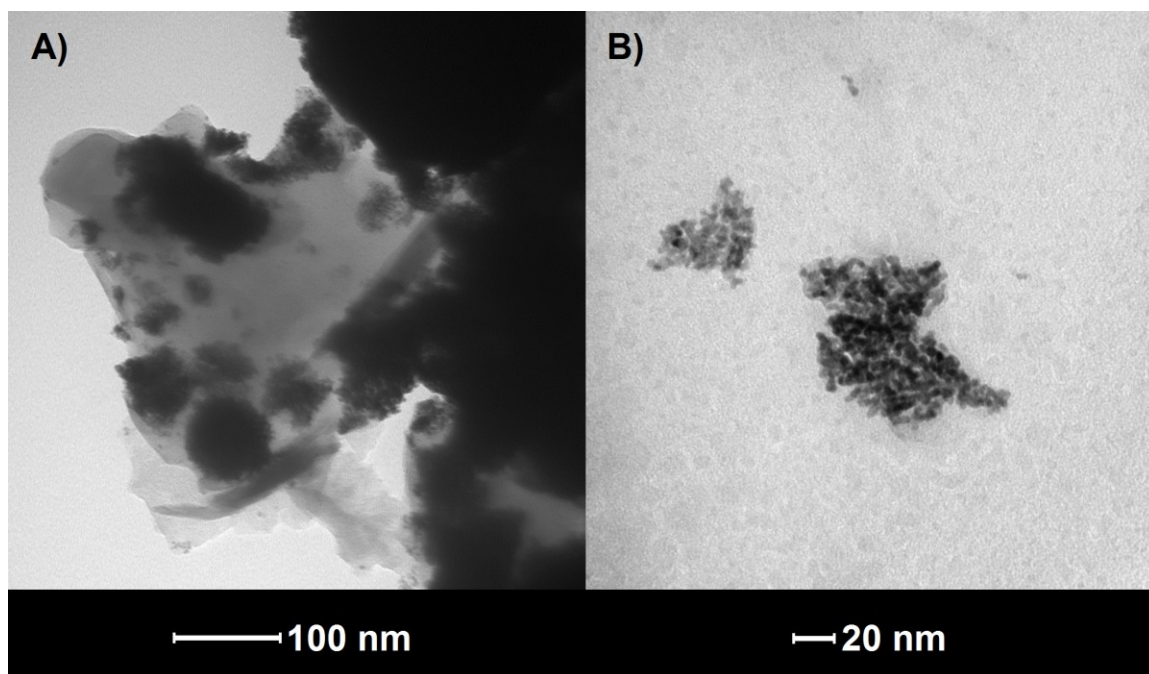


Figure 55. TEM picture of PtRu electrodeposited on compressed graphite felt. A)  $3 \times 10^5$  magnification. B)  $6 \times 10^5$  magnification. Reproduced with permission from [186], Copyright 2009, Springer.

Figure 56 shows the XRD pattern of the PtRu alloy. The crystallite sizes were calculated using:

$$d = \frac{\phi \lambda}{\beta \cos \theta} \quad (95)$$

where  $d$  is the crystallite diameter in  $\text{\AA}$ ,  $\phi$  is a coefficient equal to 0.88,  $\lambda$  is the x-ray wavelength equal to  $1.54058 \text{ \AA}$ ,  $\beta$  is the Full Width at Half Maximum (FWHM) in radians, and  $\theta$  is the angle at the maximum peak in radians

The crystallite sizes were found to range from 3.7 to 4.5 nm. Broadening of the XRD peaks, shift of the Bragg angle and decrease of the lattice parameter, may suggest the presence of PtRu alloy.

Based on ICP analysis, the Pt atomic composition was  $x = 0.583$ , corresponding to a lattice parameter of  $a_{\text{PtRu}} = 3.885 \text{ \AA}$  according to equation (96).

$$a'_{\text{PtRu}} = xa'_{\text{Pt}} + (1-x)a'_{\text{Ru}} \quad (96)$$

where  $a'$  is the lattice parameter and  $x$  is the atomic fraction of Pt.

$a'_{\text{PtRu}} = 3.885 \text{ \AA}$  from equation (96) is corroborated by the results of Lalande et al. [189]. Interpolating their bulk data for a  $\text{Pt}_{0.583}\text{Ru}_{0.417}$  alloy the PtRu lattice parameter at  $x = 0.583$  is  $3.881 \text{ \AA}$ .

Thus, there is good indication for the presence of PtRu alloy, but it cannot be considered conclusive evidence. The XRD results for PtRu alloy could also be confused with a mixture of *fcc* Pt and Ru catalysts, or a mix between PtRu alloy and *fcc* Pt and Ru catalysts. To prove the presence of PtRu alloy, several PtRu compositions have to be tested with a Ru content no greater than 0.62, due to the formation of the *hcp* phase where Ru atoms are replaced by Pt atoms [190]. The results must then obey the linearity of equation (96). Calculation of the specific surface area based on the crystallite size, yielded an average of  $82 \text{ m}^2 \text{ g}^{-1}$ .

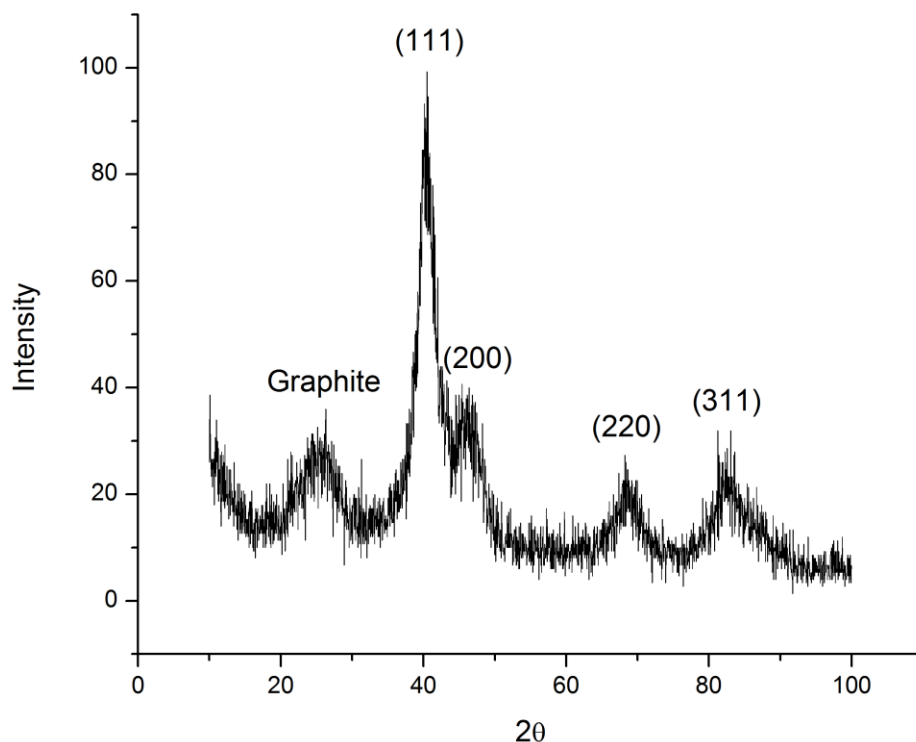


Figure 56. XRD spectra of PtRu electrodeposited on GF-S3. XRD scan of GF-S3 without Os deposit is shown in Appendix G. Reproduced with permission from [186], Copyright 2009, Springer.

### 4.3.2 PtRu on Graphite Felt Anode Performance in DBFC

Figure 57 compares the performance of unsupported PtRu (i.e., PtRu black), Vulcan XC-72 supported PtRu (i.e., PtRu/ C) and the PtRu/ GF. Generating a peak power density of  $130 \text{ mW cm}^{-2}$  the three-dimensional electrode enhanced the performance of the DBFC by approximately 33% compared to the conventional catalyst coated membrane (CCM) having a four times higher unsupported PtRu load. Compared to unsupported and Vulcan XC-72 supported PtRu at the same loading ( $1 \text{ mg cm}^{-2}$ ), the

performance improvement with PtRu/ GF based on peak power density was approximately 270% and 60% respectively.

The open circuit voltage was the lowest (i.e. 0.99 V) for the PtRu black with the highest load ( $4 \text{ mg cm}^{-2}$ ), followed by PtRu/ C at 1.05 V, and finally the PtRu/ GF at 1.11 V. This can be explained by the higher Ru content of the  $4 \text{ mg cm}^{-2}$  CCM. It is likely that such a high loading of Ru, approximately  $1.3 \text{ mg cm}^{-2}$ , promotes the hydrolysis to such an extent that the open circuit voltage becomes more dependent on the hydrogen reversible potential.

From Figure 57 it is clear that the  $\text{BH}_4^-$  electro-oxidation on the three-dimensional electrode was favorable to the CCM for all the investigated cases and over the entire polarization curve. The open structure of the three-dimensional electrode is better suited for the counter-current two phase gas-liquid flow regime and permits the unconsumed hydrogen gas to escape more easily without blocking the liquid feed pathways to the reaction sites. Furthermore, efficient gas evolution has the positive effect of enhancing the liquid mass transfer rate close to the electrode surface. All these factors contribute to the fact that as Figure 57 indicates, for PtRu/ GF clear mass transfer limitation is not apparent in the polarization curves at least up to  $450 \text{ mA cm}^{-2}$ , whereas for PtRu/ C and PtRu black with the same catalyst load of  $1 \text{ mg cm}^{-2}$  the mass transfer limiting superficial current densities are approximately  $260 \text{ mA cm}^{-2}$  and  $75 \text{ mA cm}^{-2}$ , respectively.

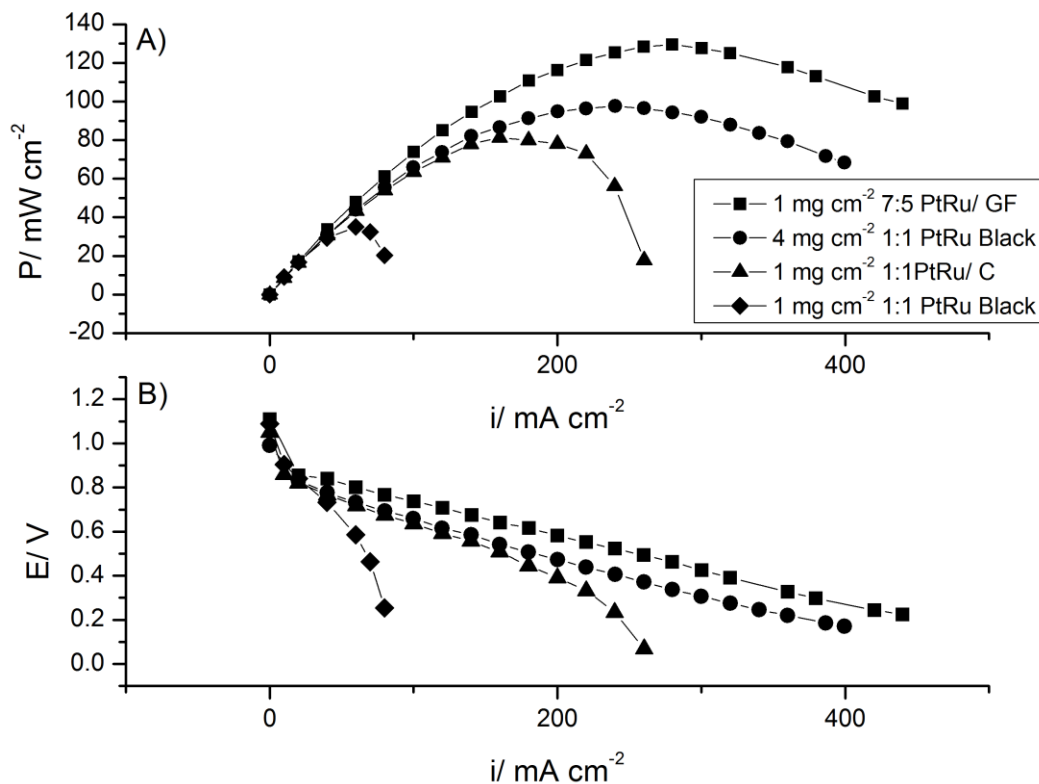


Figure 57. Effect of the three-dimensional anode structure on the DBFC. A) power density curves B) polarization curves. Cathode loading:  $4 \text{ mg cm}^{-2}$  Pt black, anolyte:  $0.5 \text{ M NaBH}_4 - 2 \text{ M NaOH}$ ; anolyte flow rate:  $10 \text{ ml min}^{-1}$ ;  $\text{O}_2$  flow rate:  $1.25 \text{ SLPM}$ ; oxidant pressure:  $4.4 \text{ atm (abs)}$ ; T:  $333 \text{ K}$ . Reproduced with permission from [186], Copyright 2009, Springer.

#### 4.4 Summary for Chapter 4.0

The improved performance of PtRu/ C (Vulcan<sup>®</sup> XC-72) versus PtRu black anode catalysts in DBFC was attributed to mass transport effects and different catalyst layer morphology due to the support. The PtRu/ C catalyst layer is characterized by more tortuous pathways for hydrogen evolution. Therefore, the hydrogen generated mainly by  $\text{BH}_4^-$  hydrolysis on the Ru sites is retained longer in the catalyst layer, where hydrogen electro-oxidation takes place on the Pt sites. In contrast, the thin PtRu black catalyst

layer is quickly saturated with evolved hydrogen gas, shielding the electrode surface and blocking the  $\text{BH}_4^-$  access. The  $\text{BH}_4^-$  electro-oxidation reaction mechanism on PtRu is dominated by indirect oxidation of  $\text{BH}_4^-$  (i.e., via hydrogen). Hence, PtRu is a bifunctional catalyst for  $\text{BH}_4^-$  oxidation.

In spite of the beneficial performance of PtRu/ C vs. PtRu black (i.e., unsupported) the hydrogen retention in the catalyst layer can cause a number of problems in the DBFC such as hampering the  $\text{BH}_4^-$  mass transfer leading to low fuel utilization efficiency, low effective ionic conductivity across the catalyst layer increasing the ohmic voltage loss and high anode pressure that could aggravate the  $\text{BH}_4^-$  crossover rate. In future studies the hydrogen evolution rate must be experimentally measured under both non-polarized and anodic polarization conditions.

The application of a monolithic three-dimensional graphite felt anode with electrodeposited PtRu (i.e., PtRu/ GF) increased significantly the peak power density of the DBFC. At 333 K the PtRu/ GF with  $1 \text{ mg cm}^{-2}$  PtRu generated a peak power of  $130 \text{ mW cm}^{-2}$  at  $275 \text{ mA cm}^{-2}$  while under similar conditions with the PtRu/ C (Vulcan<sup>®</sup> XC-72) the peak power was only  $80 \text{ mW cm}^{-2}$  corresponding to a superficial current density of  $150 \text{ mA cm}^{-2}$ .

The performance enhancement with the graphite felt three-dimensional support was attributed mainly to the enhanced two-phase (liquid  $\text{BH}_4^-$  / hydrogen gas) mass transfer in the anode compartment. Thus, the three-dimensional anode design in the context of the  $\text{BH}_4^-$  fuel cell constitutes a promising engineering advancement for increasing the power density while lowering the anode catalyst load. The next step of the investigation would therefore be to develop three-dimensional electrodes with Os

catalysts, which have previously been found to exhibit good catalytic activity for the direct electro-oxidation of  $\text{NaBH}_4$  as discussed in Chapter 3.0.

## 5 Development of Osmium Three-Dimensional Anodes\*

The objective of this chapter is to explore the three-dimensional anode concept for DBFC for the case of Os nanoparticle catalysts. The effectiveness for  $\text{BH}_4^-$  oxidation on Vulcan XC-72 supported Os nanoparticles synthesized by the Bönneeman was discussed in Chapter 3.0. Using cyclic voltammetry, a seven electron  $\text{BH}_4^-$  oxidation on Os/ C was determined, accompanied by a reduced hydrogen evolution rate compared to Pt/ C and PtRu/ C. Direct borohydride fuel cell experiments described in chapter 3.0 using Os/ C, catalyst layer coated on Nafion<sup>®</sup> 117 membrane, revealed that at 298 K the  $\text{BH}_4^-$  electro-oxidation on 20 wt% Os/ C was superior to commercial 20 wt% Pt/ C and PtRu/ C both in the electrode kinetic controlled and mass transport regions. A recent theoretical study of  $\text{BH}_4^-$  on Os (111) surface revealed strong undissociative adsorption [10], which could be favorable for direct electro-oxidation of  $\text{BH}_4^-$  as opposed to its hydrolysis followed potentially by oxidation of the evolved  $\text{H}_2$ .

To the author's knowledge, this is the first time three-dimensional Os anodes have been developed and tested in a DBFC system.

### 5.1 Experimental Procedure

Osmium was electrodeposited onto two different substrates: AvCarb<sup>™</sup> P75 (uncompressed thickness of about 210  $\mu\text{m}$  and porosity of 0.85, supplied by FuelCellStore.com) and GF-S3 (uncompressed thickness of 350  $\mu\text{m}$  and porosity of 0.95,

---

\* This chapter is based on the following submitted work:

V.W.S. Lam, D.C.W. Kannangara, A. Alfantazi, and E.L. Gyenge, J. Power Sources 212 (2012) 57.

supplied by Electro Synthesis Company Inc.). Prior to electrodeposition of the Os catalyst, the substrates were electrochemically pretreated in 2 M NaOH by potential cycling between 0 to 2 V for 50 cycles at  $50 \text{ mV s}^{-1}$  at 295 K using Ti counter electrodes and a Hg/ HgO/ 0.1M KOH reference electrode. The substrates were then thoroughly rinsed with 18 M $\Omega$  deionized water and air-dried at 333 K in an oven. The Os electrodeposition media consisted of a 10 mM  $(\text{NH}_4)_2\text{OsCl}_6$  (Alfa Aesar) solution prepared with 18 M $\Omega$  deionized water. A surfactant, 12.5 vol% Triton-X 102 (Sigma Aldrich), was added to control the deposit morphology and structure. The electrodeposition media composed of Triton-X 102 and  $(\text{NH}_4)_2\text{OsCl}_6$  solution was heated and stirred on a hot plate at 341 K for at least 30 minutes prior to deposition. Any evaporation of solution during the pre-heating procedure was replaced with 18 M $\Omega$  deionized water.

Electrodeposition was carried out at 341 K at a constant specified current density of  $4 \text{ mA cm}^{-2}$  for 30 minutes. Afterwards, the substrate was removed and soaked in acetone for 10 minutes at 330 K. Next, the substrate was refluxed in 50:50 v/v hexane and acetone for 1 h at 363 K to remove the surfactant Triton X-102 from the surface of the three-dimensional electrode. Afterwards, the substrate was dried in air at 295 K.

When more than one electrodeposition step was performed on the same substrate, the substrate was washed in acetone between depositions, for 10 minutes at 330 K. Reflux cleaning was only applied at the very end of the complete electrodeposition procedure.

The morphology and structure of the Os electrodeposit was characterized by XPS (Leybold Max 200 and Kratos AXIS Ultra), TEM (FEI Tecnai G2 200kV Transmission

Electron Microscope), XRD (D8 Advance Bruker diffractometer with Cu  $K\alpha_1$  source), SEM (Hitachi S-4700 and Hitachi S-4500 Field Emission Scanning Electron Microscopes.), and ICP-MS for Os loading determination.

For half-cell electrochemical evaluation of the electrocatalytic activity toward  $\text{BH}_4^-$  oxidation of the Os electrodeposited GF-S3 and AvCarb™ P75, solutions composed of 10 mM  $\text{NaBH}_4$  were prepared using a powdered form of 98 wt%  $\text{NaBH}_4$  (Acros Inc.) in 2 M NaOH. A three-electrode setup composed of the Os three-dimensional working electrode ( $6.45 \text{ cm}^2$  geometric area) with Ag/AgCl/3M KCl reference electrode (Cypress Systems Inc.) and a platinized titanium counter electrode ( $6.45 \text{ cm}^2$  geometric area) was connected to a PARSTAT 2263 potentiostat (Princeton Applied Research).

Fuel cell experiments were conducted using the Fideris MTK test station. The MEA was comprised of the Os electrodeposited AvCarb P75 or GF-S3 anode, respectively, and a Nafion® 117 membrane (183  $\mu\text{m}$  thickness) coated with  $4 \text{ mg cm}^{-2}$  Pt black on the cathode side (Lynntech Inc.). The flowfield plate material was stainless steel with a serpentine flow field. Additional information of the DBFC test setup can be found in Appendix H. Flow rates for the anolyte (0.5 M  $\text{NaBH}_4$  – 2 M NaOH) and oxidant ( $\text{O}_2$ ) were  $10 \text{ ml min}^{-1}$  and 0.25 to 1.25 SLPM, respectively. The  $\text{O}_2$  absolute pressure was 4.4 atm (abs), while the anode side pressure was about 1 atm (abs). Temperatures used during fuel cell performance testing were 298 K or 333 K.

## 5.2 Pretreatment of the Fibrous Carbon Substrates by Potential Cycling in 2M NaOH

The deposition substrates (AvCarb™ P75 and GF-S3) were analyzed using XPS before and after pretreatment (Figure 58). The pretreatment procedure is described in the Experimental section. Elemental analysis of the untreated AvCarb™ P75 substrate shows much lower content of heteroatoms (particularly oxygen and nitrogen) as compared to untreated GF-S3, which contains approximately 72 wt% graphitic carbon and 23 wt% oxygen (Table 7). After pretreatment, the surface oxygen content of AvCarb™ P75 increased to about 6-7.3 wt% , indicating oxidation of the substrate forming functional groups such as C-OH, C=O, COO, which were also separately identified by deconvolution of the carbon XPS spectra. The pretreatment of the GF-S3 substrate on the other hand resulted in a decrease of the oxygen content with about 4 wt% (Table 7), which suggest possible oxidation of functional groups on graphite felt (such as C-OH and C-O-C) to CO<sub>2</sub>. After pretreatment, the oxygen content of GF-S3 is approximately three times that of AvCarb™ P75 and also the former contains nitrogen in higher proportion (Table 7). The surface oxygen and nitrogen functional groups could act as active sites for Os nucleation and deposition.

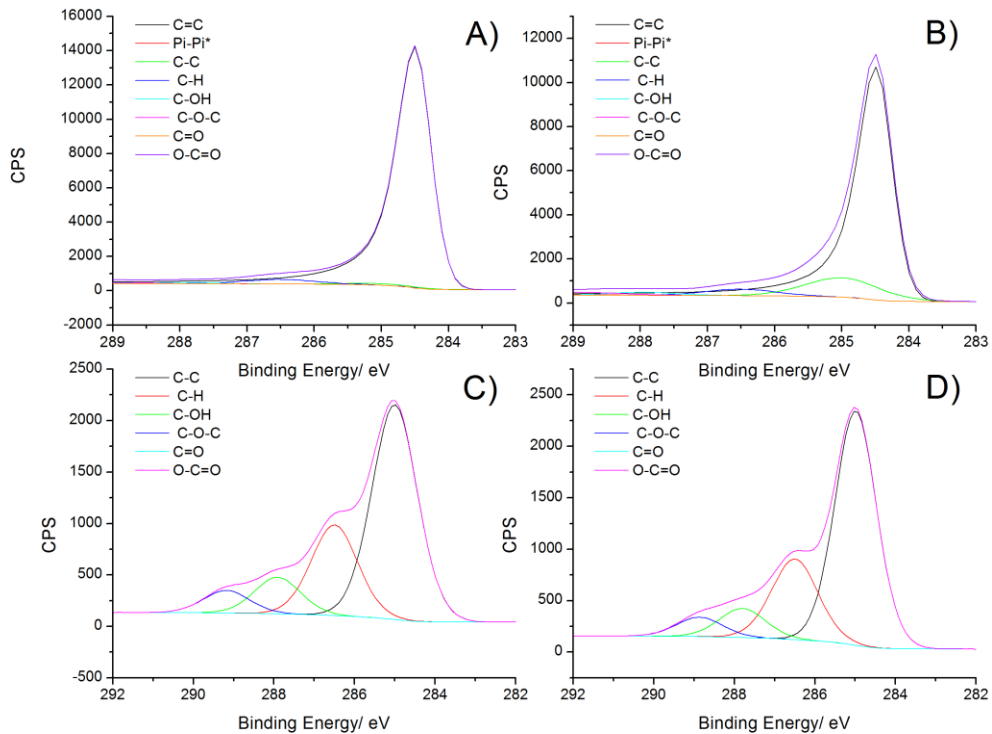


Figure 58. Deconvoluted XPS narrow scan on C 1s spectra. A) Untreated AvCarb™ P75, B) pretreated AvCarb™ P75, C) untreated GF-S3, D) pretreated GF-S3.

Table 7. Elemental analysis of deposition substrates before and after electrochemical pretreatment in weight percentage.

Sample	C	Ca	N	Na	O	S	Si
AvCarb™ P75	98.4-99.4	-		-	0.6-1.6	-	-
Pretreated AvCarb™ P75	90.7-91.4	-	0.2-0.5	1.6-2.3	6-7.3	-	-
GF-S3	70.7-72.2	0.5-0.8	3.1-3.2	1.0-1.2	21.7-23.4	0.6	0.2-0.6
Pretreated GF-S3	75.1-76.1	0.4-0.5	4-4.4	0.7-1.1	18.3-18.5	0.1	0.3-0.4

### 5.3 Os Electrodeposition and Structural Characterization of Os Three-Dimensional Electrodes

Figure 59 shows the cathode potential profile during the electrodeposition of Os on the AvCarb™ P75 substrate (reaction (97)) where the equilibrium potential can be calculated according to equation (98). The measured open circuit potential was 0.66 V compared to a calculated equilibrium potential of 1.2 V at 341 K; assuming an initial chloride concentration of 0.1 mM. Due to a lack of thermodynamic data in the literature, the equilibrium potential was calculated based on the four electron reduction of  $\text{OsCl}_6$  where  $\Delta S_{298\text{K}}^{\circ} = 104 \text{ J mol}^{-1} \text{ K}^{-1}$  and  $E_{298\text{K}}^{\circ} = 0.95 \text{ V}$ . There appears to be three deposition stages. The first stage, shown in the first 20 to 30 seconds in the inset of Figure 59, involves the nucleation of Os deposits on energetically favourable sites. From ~30 seconds onward, the second stage involves the bulk deposition of Os. At approximately 800 seconds of deposition, the potential profile indicates a limiting effect of the Os salt concentration. At deposition times much greater than 30 minutes (not shown here), severe mass transport limitation is imposed by the depletion of Os salt concentration within the deposition substrate. It should be noted that the electrodeposition media was not stirred during deposition. A similar profile was observed when depositing Os onto the GF-S3 substrate.



$$E_e = E_T^{\circ} - \frac{RT}{4F} \ln \frac{a_{\text{Cl}^-}^6}{a_{\text{OsCl}_6^{2-}}} \quad (98)$$

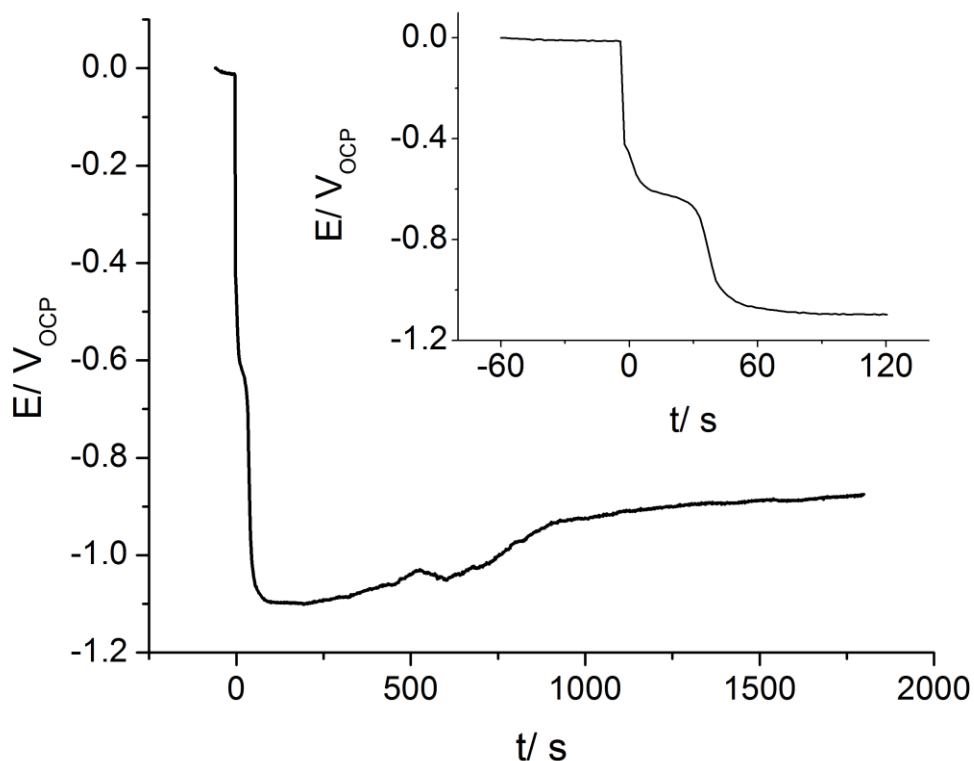


Figure 59. Cathode potential profile during Os electrodeposition on AvCarb™ P75 substrate at  $4 \text{ mA cm}^{-2}$  and 341 K. Inset: shows the cathode potential profile during the first 120 s of deposition. The bath was composed of 10 mM  $(\text{NH}_4)_2\text{OsCl}_6$  with 12.5 vol% of Triton-X 102. Typical  $E_{\text{OCP}} \sim 0.66 \text{ V}$ .

Scanning electron microscope images of AvCarb™ P75 and GF-S3 are shown in Figure 60A and B respectively. Figure 60C and D show the respective substrates with electrodeposited Os. The unique structural feature of the AvCarb™ P75 is the presence of interstitial carbon black deposit among the fibers (compare Figure 60A and B). The electrodeposited Os appeared as rough aggregates (Figure 60C and D). Low magnification SEM images (Figure 61) revealed a homogeneous distribution of the Os deposits throughout the thickness of the substrates.

Upon closer inspection of both electrodes with TEM (Figure 62A and Figure 62B), it was found that the large deposits are actually composed of nano-sized Os particles, with particle sizes less than 5 nm. A similar morphology was observed in our previous study of electrodeposited PtRu on GF-S3 in Chapter 4.0. The Os nanoparticle distribution within the aggregate was more uniform in case of GF-S3, which could be explained by the higher proportion of surface heteroatoms (particularly oxygen and nitrogen) (Figure 62B vs. 3A, and Table 7).

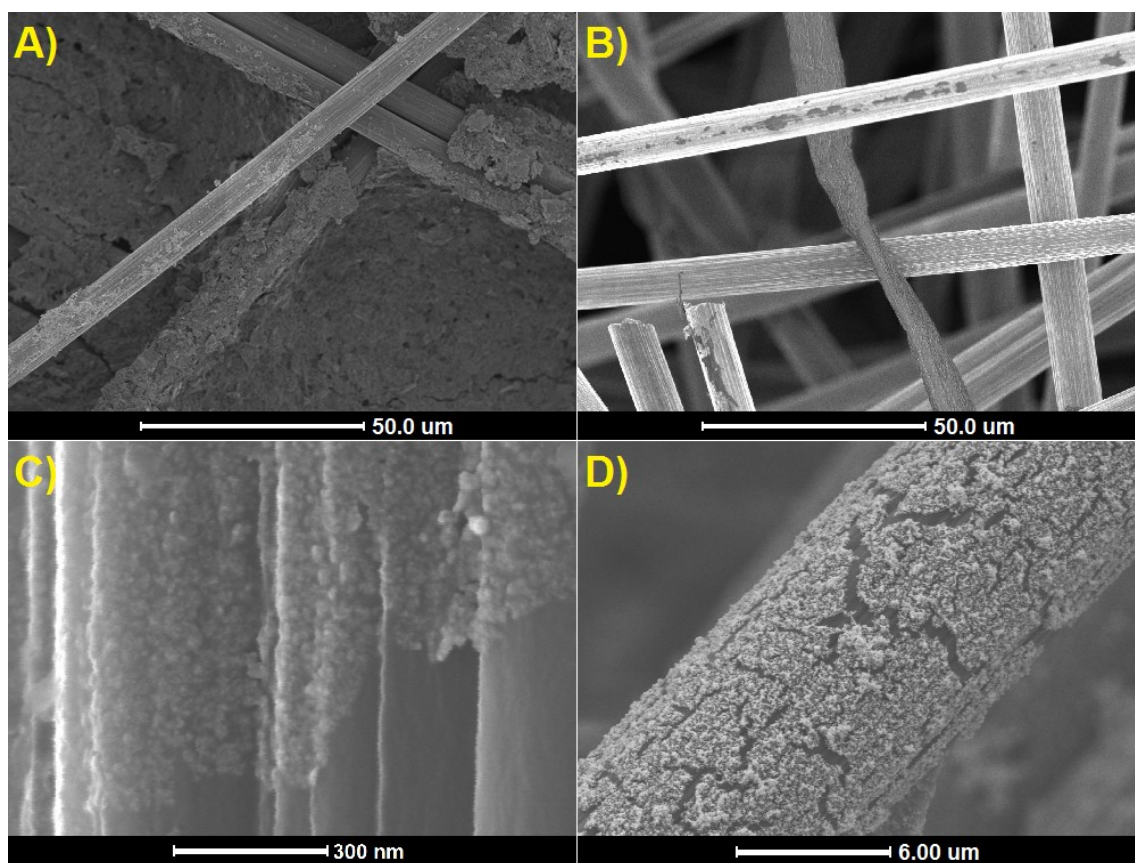


Figure 60. SEM images of A) AvCarb™ P75 without deposit, B) GF-S3 without deposit, and Os electrodeposited on: C) AvCarb™ P75 and D) GF-S3 substrates.

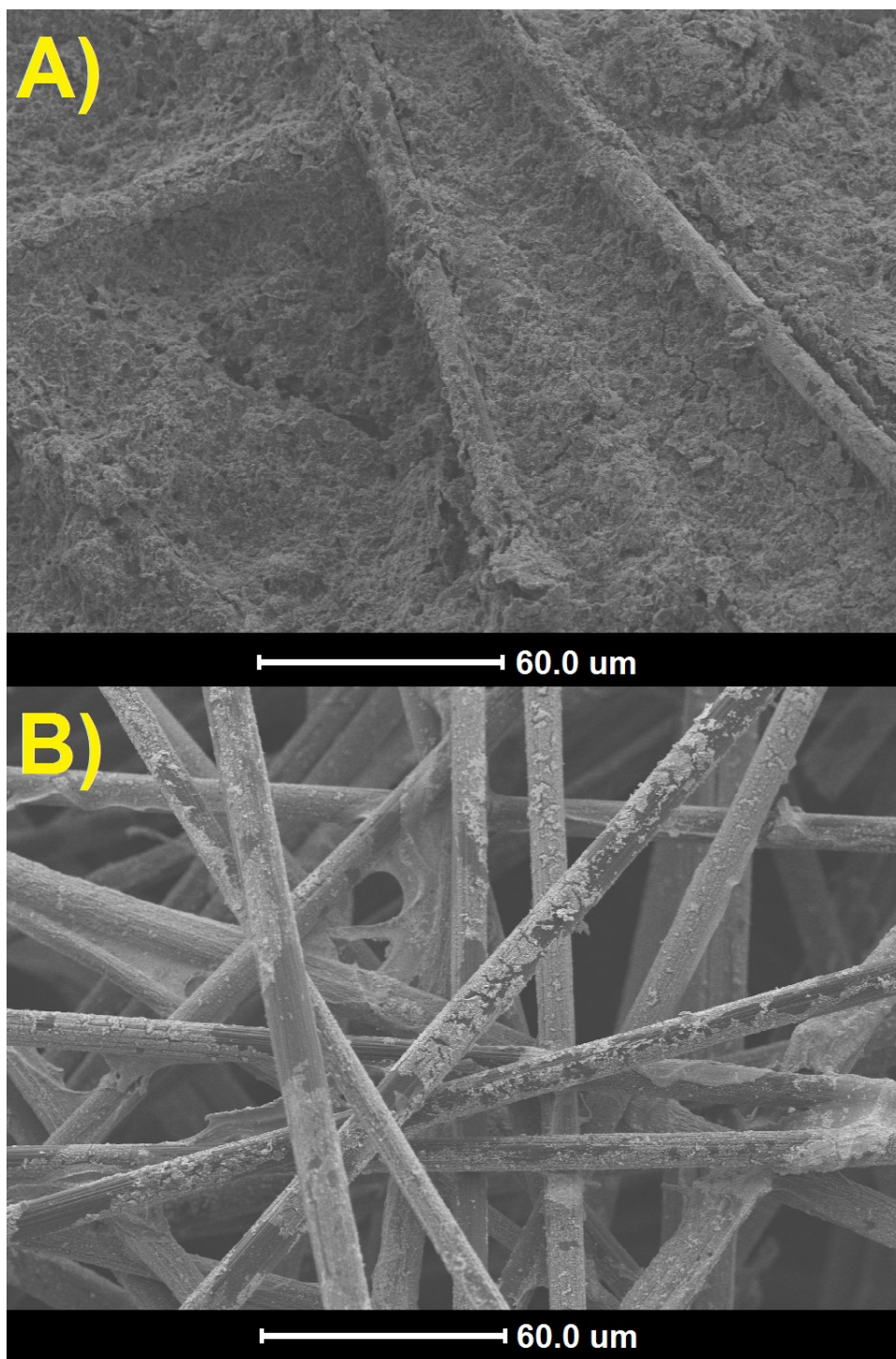


Figure 61. SEM Images of A) AvCarb™ P75 electrodeposited with Os and B) GF-S3 electrodeposited with Os.

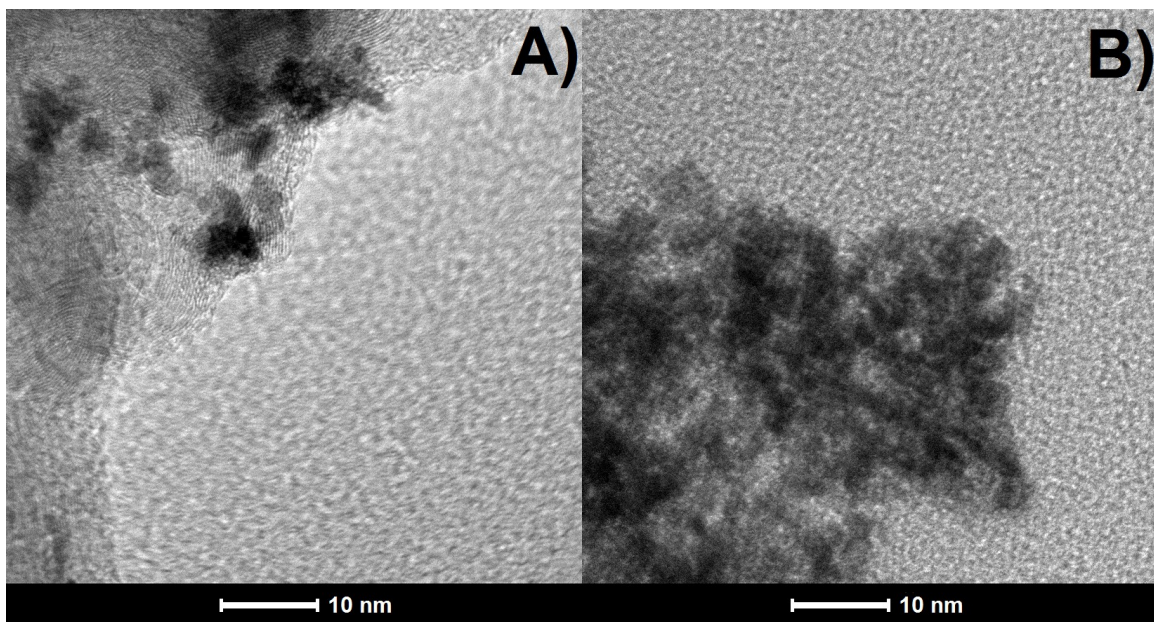


Figure 62. TEM images of Os deposits on: A) AvCarb™ P75 and B) GF-S3 substrates.

Figure 63 shows the XRD spectra from  $2\theta = 34^\circ$  to  $90^\circ$  for an Os/ AvCarb™ P75 electrode with a metal loading of  $0.3 \text{ mg cm}^{-2}$  and an Os/ GF-S3 electrode with a metal loading of  $0.2 \text{ mg cm}^{-2}$ . The spectra for the Os/ GF-S3 electrode indicates the presence of mainly the (101) plane with a low intensity compared to the strongly polycrystalline Os/ AvCarb™ P75 where the (100), (101), (103), (110) and (111) planes could be identified. Among the latter planes, the (101) plane generated the highest intensity. The crystallite sizes for the Os/ AvCarb™ P75 and Os/ GF-S3 electrodes were calculated to be approximately 2 nm and 1 nm, respectively. Another interesting distinguishing feature between the two electrodes is the strong graphite XRD signal from AvCarb™ P75 and its absence in case of GF-S3 (Figure 63). This shows significant structural differences between the two graphitic substrates, with possibly a high content of amorphous-like (less ordered) graphite in case of GF-S3.

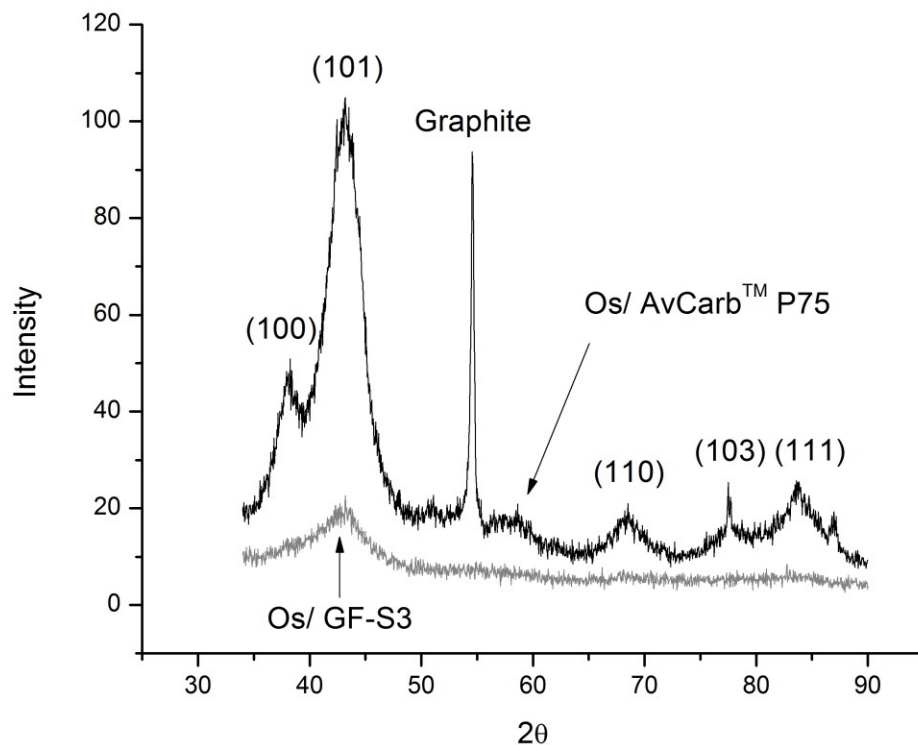


Figure 63. XRD wide scan of Os electrodeposited onto AvCarb™ P75 (Os loading: 0.3 mg cm<sup>-2</sup>) and GF-S3 (Os loading 0.2 mg cm<sup>-2</sup>). XRD scan of AvCarb™ P75 without Os deposit is shown in Appendix G.

#### 5.4 Cyclic Voltammetry Investigation of BH<sub>4</sub><sup>-</sup> Oxidation on the Electrodeposited Three-Dimensional Os Electrodes

Figure 64B and Figure 64D, show the cyclic voltammogram of Os/ AvCarb™ P75, and Os/ GF-S3 respectively, in 2 M NaOH in the absence of BH<sub>4</sub><sup>-</sup>. The broad peaks at -0.56 V (Figure 64B) and -0.59 V (Figure 64D) represent the electro-oxidation of H<sub>2</sub> generated on the cathodic scan. Figure 64B, also reveals that on Os/ AvCarb™ P75 weak underpotential formation of hydrogen occurred on the cathodic scan between approximately -0.57 V and -0.77 V, which was absent for the Os/ GF-S3 electrode

(Figure 64D). The strongly polycrystalline Os/ AvCarb™ P75 surface (Figure 63) is more likely to generate underpotentially deposited hydrogen atoms. Furthermore, there was no indication of the formation of any Os oxidation peaks within the potential range of the cyclic voltammograms, although the formation of OsO<sub>2</sub> is thermodynamically favourable at high pH and at potentials greater than -0.3 V [191].

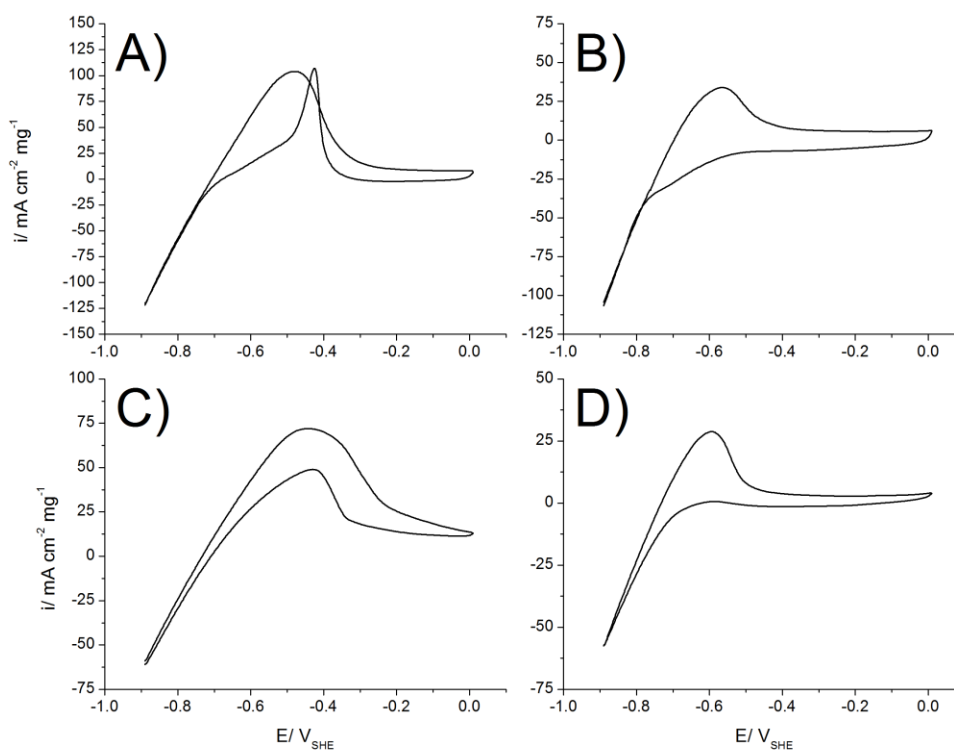


Figure 64. Cyclic voltammogram of: A) Os/ AvCarb™ P75 in 10 mM NaBH<sub>4</sub> – 2 M NaOH, B) Os/ AvCarb™ P75 in 2 M NaOH, C) Os/ GF-S3 in 10 mM NaBH<sub>4</sub> – 2 M NaOH, D) Os/ GF-S3 in 2 M NaOH, Os loading for each electrode: 0.2 mg cm<sup>-2</sup>. T: 298 K, scan rate: 10 mV s<sup>-1</sup>.

When 10 mM NaBH<sub>4</sub> was added to the 2 M NaOH solution, on the Os/ AvCarb™ P75 electrode two characteristic oxidation peaks were observed, one at -0.48 V in the

anodic direction and the other at -0.43 V on the return cathodic scan (Figure 64A). For the Os/ GF-S3 electrode, there was a slight positive shift for the forward oxidation peak to -0.44 V, whereas the cathodic return scan oxidation peak remained at -0.43 V (Figure 64C). The anodic peak current density in the presence of  $\text{BH}_4^-$  on both Os electrodes were up to about three times larger than the anodic peak current density measured in only 2 M NaOH. This shows clearly the activity of the electrodeposited Os electrodes toward  $\text{BH}_4^-$  electro-oxidation.

The observed peaks on Os/ AvCarb™ P75 in the presence of  $\text{BH}_4^-$  (Figure 64A) are similar to the characteristic dominant peaks “*aI*” (on the anodic scan) and “*cI*” (cathodic return scan) found on Pt discussed in Chapter 2.0. As may also be recalled from Chapter 2.0, The “*aI*” peak can involve the oxidation of both  $\text{BH}_4^-_{\text{ad}}$  and  $\text{H}_{\text{ad}}$ , the latter formed through partial hydrolysis of  $\text{BH}_4^-$ , with a total six electrons. On Os nanoparticles prepared by a modified Bönnehan method and supported on Vulcan XC-72, seven electron oxidation of  $\text{BH}_4^-$  corresponding to peak “*aI*” was found in Chapter 3.0.

A notable difference between the Os electrodes on AvCarb™ P75 and GF-S3 is the shape of the return, cathodic scan, oxidation peak “*cI*” (Figure 64A and C). For Os/ GF-S3, this peak is broader and its peak current density is over two times smaller than on Os/ AvCarb™ P75. The “*cI*” peak has been attributed to oxidation of strongly adsorbed intermediates such as  $\text{BOH}_{\text{ad}}$  and  $\text{BH}_2\text{OH}_{\text{ad}}$  as discussed in Chapter 2.0. The broader peak on Os/ GF-S3 could be indicative of a wider range of adsorbed species present on the surface compared to the Os/ AvCarb™ P75, where a sharp “*cI*” peak was observed. Furthermore, the large “*cI*” oxidation peak current density for Os/ AvCarb™ P75 (Figure

64A vs. C) suggests more effective oxidization of the adsorbed intermediates. For Os/GF-S3 the  $\text{BH}_4^-$  cyclic voltammogram was similar to that on Os nanoparticles prepared by a modified Bönnehan method and supported on Vulcan XC-72 [165].

To better understand the Os/ AvCarb™ P75 surface, XPS was performed after the electrode had been subjected to electrochemical half-cell tests (Figure 65). A narrow scan was performed on the Os 4f double peak. Deconvolution of the peaks revealed four peaks with binding energies at 50.8 eV, 51.7 eV, 53.5 eV, and 54.4 eV. It was found that the binding energies at 50.8 eV and 53.5 eV corresponded well to the literature indicating the presence of Os(0) ( $4f_{7/2}$  and  $4f_{5/2}$ , respectively) [192--196]. The binding energies at 51.7 eV and 54.4 eV likely indicate the presence of  $\text{OsO}_2$ , which is also supported by the literature [192--195,197]. The partial oxidation of the Os surface cannot be explained by anodic oxidation since the corresponding peak, expected at potentials greater than -0.3 V [191], was absent in the cyclic voltammograms (Figure 64A and B). Thus, it is surmised the partial surface oxidation ( $\text{OsO}_2$  formation) occurred during the electrode preparation procedure by exposure to ambient air.

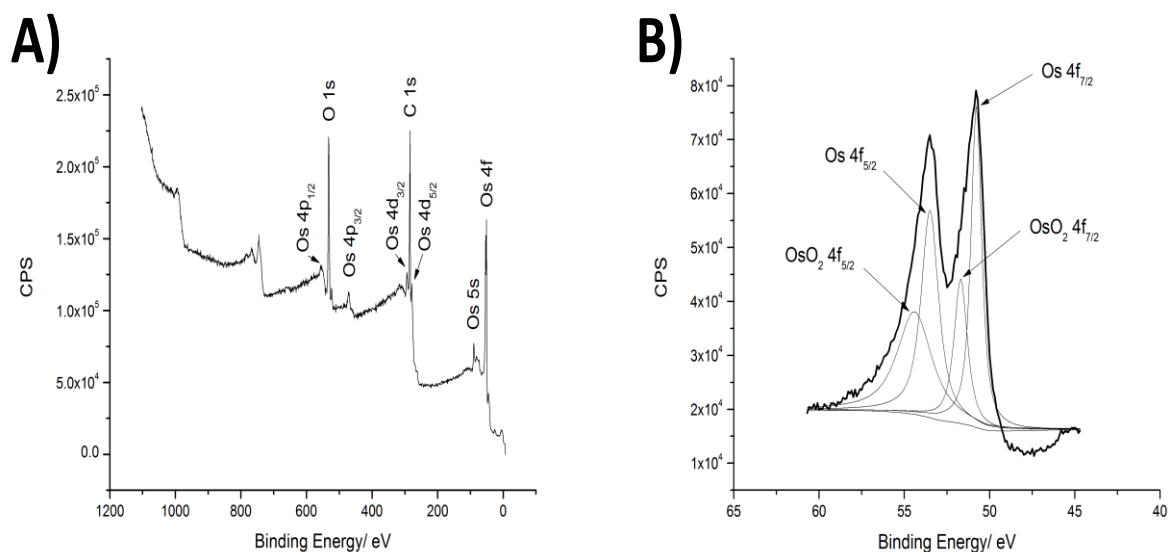


Figure 65. A) XPS wide scan of Os/ AvCarb™ P75 and B) XPS narrow scan of the same sample.

## 5.5 Direct Borohydride Fuel Cell Experiments

In Figure 66, the fuel cell performance at 333 K of the two Os three-dimensional anodes with AvCarb™ P75 and GF-S3 substrates, respectively, are compared at a low Os loading of  $0.2 \text{ mg cm}^{-2}$ . The AvCarb™ P75 electrode generated a superior peak power density compared to the GF-S3, namely  $25 \text{ mW cm}^{-2}$  versus  $18 \text{ mW cm}^{-2}$ . Both electrodes exhibited similar characteristics in the electrode kinetic region of the polarization curve, i.e., between cell voltages of 1.1 V (open-circuit) and 0.9 V. The polarization curves differ at cell voltages below 0.9 V (Figure 66), which is predominantly the Ohmic control region of the curves. Further explanation of this difference can be developed by calculating and comparing the effective ionic and electronic conductivities of the two three-dimensional electrodes.

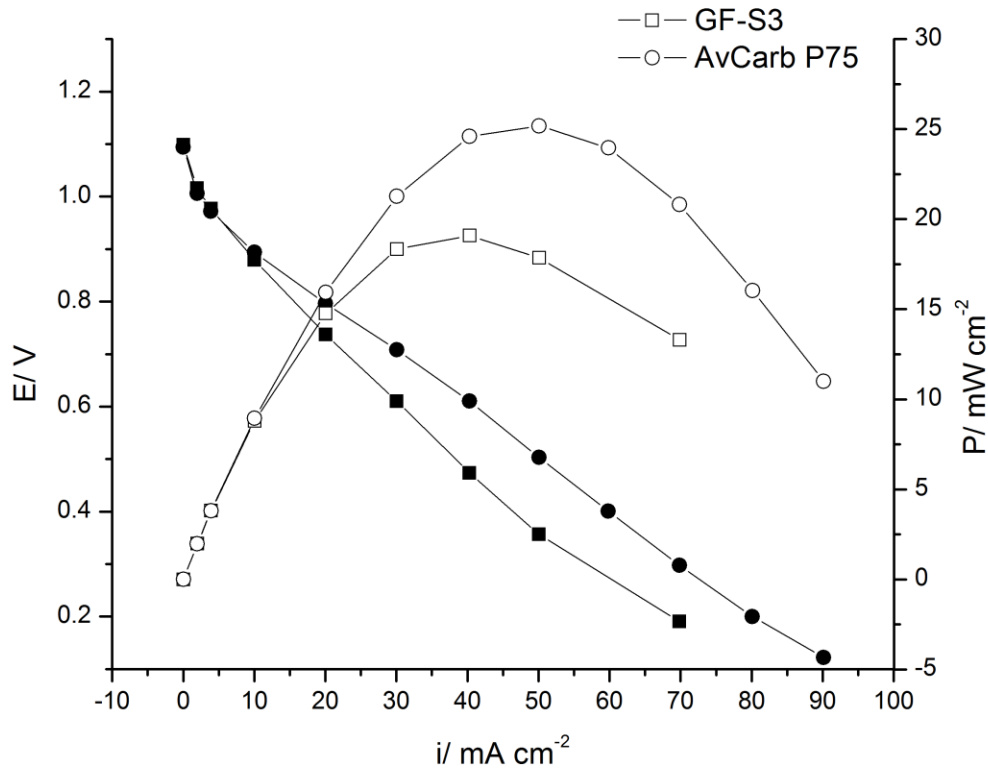


Figure 66. Comparison of DBFC performance with Os/ GF-S3 and Os/ AvCarb™ P75 anodes. Os loading:  $0.2 \text{ mg cm}^{-2}$  for both anodes. T: 333 K. Cathode catalyst:  $4 \text{ mg cm}^{-2}$  Pt,  $\text{O}_2$  pressure: 4.4 atm (abs),  $\text{O}_2$  flow rate 0.25 SLPM, anolyte: 0.5 M  $\text{NaBH}_4$  – 2 M NaOH, anolyte flow rate  $10 \text{ mL min}^{-1}$ .

The Bruggeman equation can be used to describe the effective ionic conductivity of a three-dimensional porous electrode:

$$\kappa = \kappa_o (\varepsilon)^2 \quad (99)$$

where  $\kappa$  is the effective ionic conductivity of the three-dimensional electrode [ $\text{S m}^{-1}$ ],  $\kappa_o$  is the conductivity of the electrolyte (2M NaOH) [ $\text{S m}^{-1}$ ], and  $\varepsilon$  is the porosity of the substrate.

The AvCarb™ P75 is a denser material, with an average porosity of 0.85 and a thickness of 210  $\mu\text{m}$  [198] whereas the GF-S3 has a porosity of 0.95 and a thickness of 350  $\mu\text{m}$  [180]. It was assumed that both electrodes were compressed in the fuel cell to the same final thickness (approximately 100  $\mu\text{m}$ ), which was determined by the thickness of the gasket (Table 8). The ratio of the effective ionic conductivities was calculated with equation (100) and the results are shown in Table 8.

$$\kappa' = \frac{\kappa_{GF-S3}}{\kappa_{AvCarbP75}} = \frac{(\varepsilon_{GF-S3})^{\frac{3}{2}}}{(\varepsilon_{AvCarbP75})^{\frac{3}{2}}} \quad (100)$$

where  $\varepsilon$  is the compressed porosity of the three-dimensional electrode calculated with:

$$\varepsilon = 1 - \frac{\tau'_o(1 - \varepsilon_0)}{\tau'} \quad (101)$$

where  $\tau'$ ,  $\tau'_o$  are the compressed and uncompressed thickness of the three-dimensional electrode, respectively.

Table 8. Calculation of the effective ionic ( $\kappa'$ ) and electronic ( $\sigma'$ ) conductivity ratios of the GF-S3 to AvCarb™ P75 three-dimensional electrodes under the employed experimental conditions.

	Uncompressed Electrode Thickness ( $\mu\text{m}$ )	Compressed Electrode Thickness ( $\mu\text{m}$ )	$\kappa$ ( $\text{S m}^{-1}$ )	$\sigma$ ( $\text{S m}^{-1}$ )	$\kappa'$	$\sigma'$
GF-S3	350	100	24.8	21.7	1.25	0.45
AvCarb™ P75	210	100	19.9	48.4		

From Table 8, it is clear that the GF-S3 three-dimensional electrode has a higher effective ionic conductivity than AvCarb™ P75. Therefore, the advantage of the Os/ AvCarb™ P75 over the Os/ GF-S3 electrode at fuel cell voltages lower than 0.9 V (Figure 66), is likely due to the higher electronic conductivity for AvCarb™ P75 and possibly other factors.

The effective transverse electronic conductivity of a graphite fiber matrix such as the GF-S3 and AvCarb™ P75 can be approximated by the following relationship [199]:

$$\sigma = 10 + 2800 \left( 1 - \frac{\varepsilon}{\varepsilon_0} \right)^{1.55} \quad 0.68 < \varepsilon/\varepsilon_0 < 1 \text{ at } 293 \text{ K} \quad (102)$$

where  $\sigma$  is the effective electronic conductivity of the graphite fiber matrix,  $\varepsilon$  is the compressed porosity, and  $\varepsilon_0$  is the uncompressed porosity.

It is likely that the parameters in equation (102) determined by fitting of experimentally measured electronic conductivity data [199], will differ based on the compositional and structural features of the employed carbon-based fiber matrix. In the absence of specific correlations for either AvCarb™ P75 or GF-S3, equation (102) can provide a preliminary estimate of the respective electronic conductivities as a function of porosity. The ratio of the electronic conductivities is:

$$\sigma' = \frac{\sigma_{GF-S3}}{\sigma_{AvCarbP75}} \quad (103)$$

The calculations reveal that compressed AvCarb™ P75 had about 2.2 times higher electronic conductivity compared to GF-S3, counteracting the approximately 25% lower effective ionic conductivity (Table 8). The higher effective electronic conductivity contributes to the superior fuel cell polarization performance of Os/ AvCarb™ P75 in the predominantly ohmic controlled region of the curve (Figure 66).

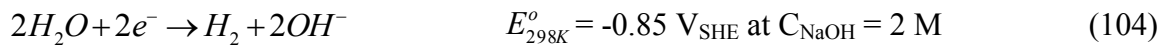
An additional effect that can be significant at cell voltages lower than 0.9 V is the accumulation of surface adsorbed intermediate species such as  $\text{BH}_2\text{OH}_{\text{ad}}$  and/ or  $\text{BOH}_{\text{ad}}$ . Since the fuel cell polarization data points are recorded in a sequential fashion, there is an in-built time factor in the polarization curves. The accumulation in time of strongly adsorbed species coupled with their sluggish oxidation will increase the anodic overpotential, and lower the power output. As discussed in relation to the cyclic voltammetry study and peak “c1” (Figure 64), Os/ AvCarb™ P75 was more effective in oxidizing the adsorbed intermediates. This beneficial effect could have contributed, in addition to the superior effective electronic conductivity, to the superior fuel cell performance of the Os/ AvCarb™ P75 anode.

Based on Figure 66, Os/ AvCarb™ P75 was retained as anode for further studies. The fuel cell performance was also investigated over longer time periods with shutdown and startup cycles and as a function of temperature. A significant performance improvement was observed when the fuel cell temperature increased from 298 K to 333 K (Figure 67). Improvements in electrode kinetics, ionic conductivity and the open circuit voltage were all evident.

The increased open circuit voltage with increased temperature is counter intuitive from thermodynamic point of view, which dictates that the equilibrium cell potential

(equation (5)) should decrease slightly with increased temperature. A decrease in the in the equilibrium cell potential from 1.65 V at 298 K to 1.63 V at 333 K is expected assuming precipitation of the NaBO<sub>2</sub>. The positive effect of the increased temperature on the open circuit voltage is due to reduced mixed potential polarization losses on the cathode and/or anode. Theoretically, a mixed potential between BH<sub>4</sub><sup>-</sup> and O<sub>2</sub> can establish on the cathode due to BH<sub>4</sub><sup>-</sup> crossover across Nafion<sup>®</sup> 117, whereas on the anode a mixed potential between BH<sub>4</sub><sup>-</sup> and O<sub>2</sub> can form due to O<sub>2</sub> crossover. The O<sub>2</sub> cathode pressure was kept at 4.4 atm (abs) while the anode operated at approximately atmospheric pressure. The pressure differential decreased the BH<sub>4</sub><sup>-</sup> crossover but it cannot be completely discounted.

In addition to the BH<sub>4</sub><sup>-</sup> - O<sub>2</sub> mixed potential, another possible complicating factor on the anode could be the H<sub>2</sub> generated either by thermocatalytic hydrolysis of NaBH<sub>4</sub> (equation (6)) or incomplete electro-oxidation of BH<sub>4</sub><sup>-</sup>. The presence of H<sub>2</sub> at the anode would lower the open circuit cell voltage by partially replacing the anodic reaction (3) with reaction (104). This effect is accentuated by the temperature increase that enhances the rate of BH<sub>4</sub><sup>-</sup> hydrolysis and H<sub>2</sub> evolution (reaction (6)).



The thermocatalytic H<sub>2</sub> evolution on Os/ AvCarb<sup>™</sup> P75 should be separately investigated in the future. The mixed potential loss on the Pt cathode however, is lessened at higher temperature because of enhanced hydrolysis on Pt of the BH<sub>4</sub><sup>-</sup> that crossed over to the cathode. As a result, the mixed potential polarization on the cathode

will involve  $\text{H}_2 - \text{O}_2$  as opposed to the  $\text{BH}_4^- - \text{O}_2$  couple. It is hypothesized that the positive effect of temperature on the mixed cathode potential overcomes the possible negative effect of temperature on the anode mixed potential, and therefore, the cell open circuit voltage increases with temperature.

Furthermore, the structure of the three-dimensional electrode could also play a role in raising the open circuit voltage by reducing the  $\text{BH}_4^-$  crossover flux. The ability for three-dimensional electrodes to decrease fuel crossover has been proven by Lam et al. in a direct methanol fuel cell (DMFC) system [182]. Lam et al. found that the open circuit voltage increased and methanol crossover decreased in their DMFC system with increased anode layer thicknesses.

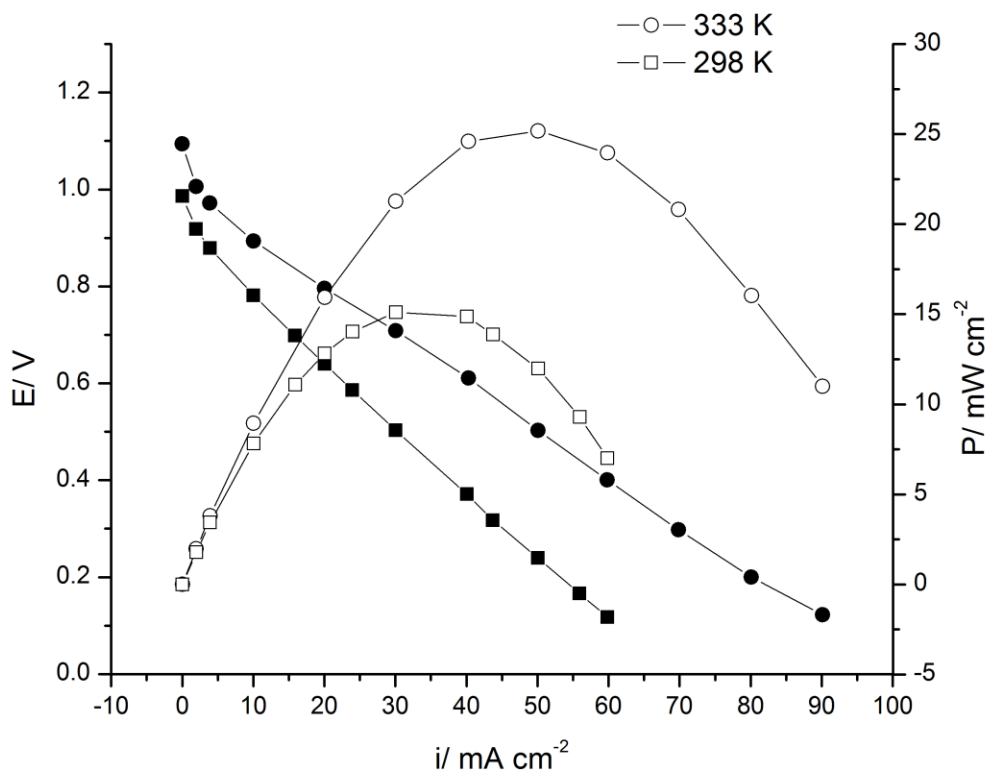


Figure 67. Effect of temperature on DBFC operation with Os/ AvCarb™ P75 anode with  $0.2 \text{ mg cm}^{-2}$  Os loading. Cathode catalyst:  $4 \text{ mg cm}^{-2}$  Pt,  $\text{O}_2$  pressure: 4.4 atm (abs),  $\text{O}_2$  flow rate 0.25 SLPM, anolyte: 0.5 M  $\text{NaBH}_4 - 2 \text{ M NaOH}$ , anolyte flow rate  $10 \text{ ml min}^{-1}$ .

The effect of Os loading was tested in the case of Os/ AvCarb™ P75 (Figure 68). Higher Os loadings were achieved by simply repeating the electrodeposition process on the same substrate a number of times, using a fresh bath for each deposition step (see Experimental Methods section). Thus, Os loadings of 0.3, 0.9, and  $1.7 \text{ mg cm}^{-2}$  were achieved with single (1x), double (2x) and quadruple (4x) depositions, respectively. The corresponding peak power densities were  $65 \text{ mW cm}^{-2}$ ,  $76 \text{ mW cm}^{-2}$ , and  $103 \text{ mW cm}^{-2}$ , respectively (Figure 68). It is important to note that the specific peak power densities per Os loading on the other hand, decreased with increased Os loading:  $204 \text{ mW mg}^{-1}$ ,  $89 \text{ mW mg}^{-1}$ , and  $61 \text{ mW mg}^{-1}$  for 1x, 2x, and 4x depositions, respectively. The most

probable explanation for this behavior is the increased agglomeration and reduced specific electrocatalytic surface area of Os as the loadings increased on the substrate.

Figure 68 also shows, that the electrode kinetic control region of the DBFC polarization curves remained virtually unchanged by the Os loading increase, and the majority of the performance improvements between different Os loadings appeared in the ohmic control region, i.e., from a cell voltage of 0.8 V and lower. Despite this observation, it is unlikely that the difference in ohmic resistance of the three dimensional anodes was responsible for the substantial difference in the three polarization curves in Fig. 9. Instead, it is proposed that the performance difference is due to the enhanced kinetics for  $\text{BH}_4^-$  electro-oxidation on the higher Os loaded anodes.

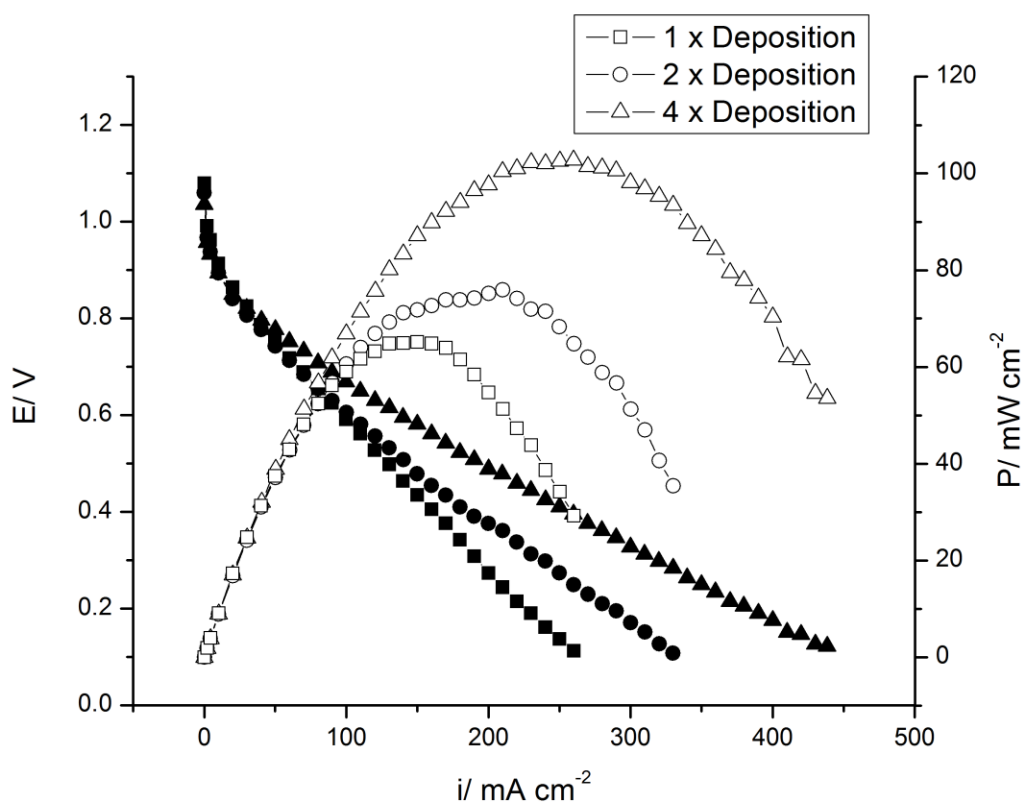


Figure 68. Effect of Os loading on the DBFC performance with Os/ AvCarb™ P75 anode. The Os loading was increased by repeating the electrodeposition process a number of times on the same substrate. Legend: (1x): single deposition, Os loading:  $0.3 \text{ mg cm}^{-2}$ , (2x): double deposition, Os loading:  $0.9 \text{ mg cm}^{-2}$ , (4x): quadruple deposition, Os loading:  $1.7 \text{ mg cm}^{-2}$ , T: 333 K, cathode catalyst:  $4 \text{ mg cm}^{-2}$  Pt,  $\text{O}_2$  pressure: 4.4 atm (abs),  $\text{O}_2$  flow rate 1.25 SLPM, anolyte:  $0.5 \text{ M NaBH}_4 - 2 \text{ M NaOH}$ , flow rate  $10 \text{ ml min}^{-1}$ .

The reproducibility of the anode performance was investigated by preparing three Os/ AvCarb™ P75 electrodes by quadruple electrodeposition (loading of  $1.7 \text{ mg cm}^{-2}$ ), and testing them under the same conditions in DBFC with the same cathode half-MEA each time (Figure 69). The cathode half-MEA were washed with deionized water and purged with air between the experiments.

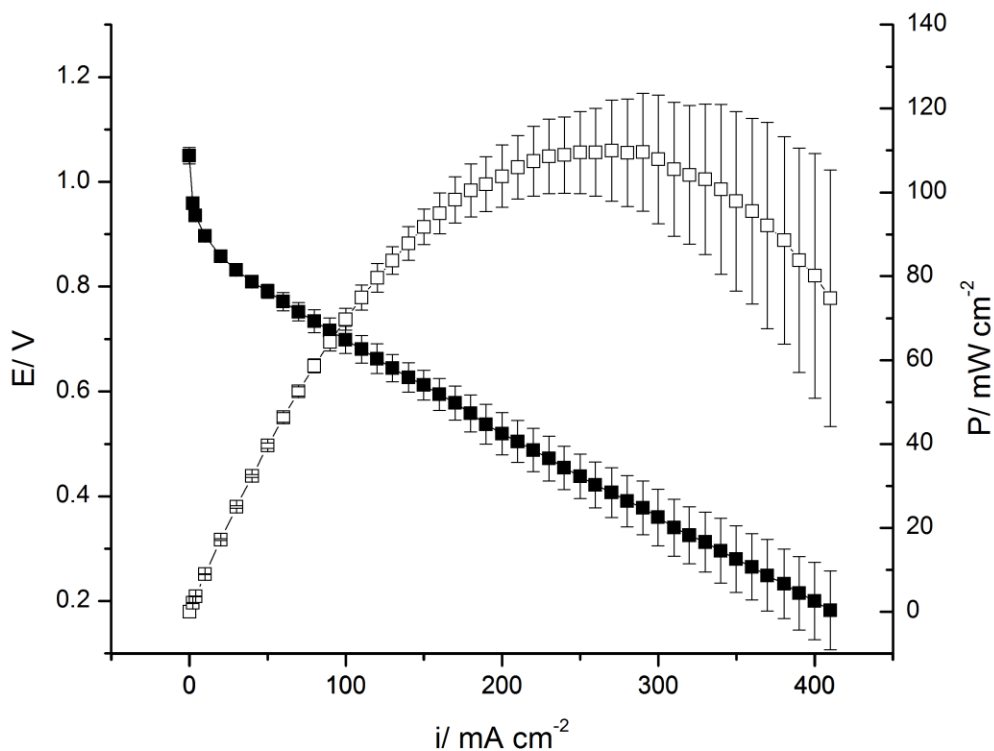


Figure 69. Reproducibility of the BFC performance with Os/ AvCarb™ P75 anode prepared by the quadruple (4x) deposition procedure. Error bars represent the standard error of the mean with 90% confidence level. T: 333 K, Cathode catalyst: 4 mg cm<sup>-2</sup> Pt, O<sub>2</sub> pressure: 4.4 atm (abs), O<sub>2</sub> flow rate 1.25 SLPM, anolyte: 0.5 M NaBH<sub>4</sub> – 2 M NaOH, anolyte flow rate 10 ml min<sup>-1</sup>.

The error bars in Figure 69 represent the standard error of the mean at 90% confidence level [200]. At low current densities the error was small, indicating that the electrodeposition procedure was generating reproducible Os catalytic surfaces with very similar electrode kinetic performance. The error in the measured cell voltage increased progressively with increasing current density, as ohmic and/ or mass transfer limitations gained an important role (Figure 69). This is likely due to the inherent morphological differences of the AvCarb™ P75 substrates, which causes differing Os morphologies (e.g., porous structure), that will affect the electronic conductivity and/or mass transport

characteristics of the anodes. The average peak power density was  $109 \text{ mW cm}^{-2}$  with a standard error of  $\pm 12 \text{ mW cm}^{-2}$  at 90% confidence level (Figure 69). This can be considered an acceptable level of reproducibility.

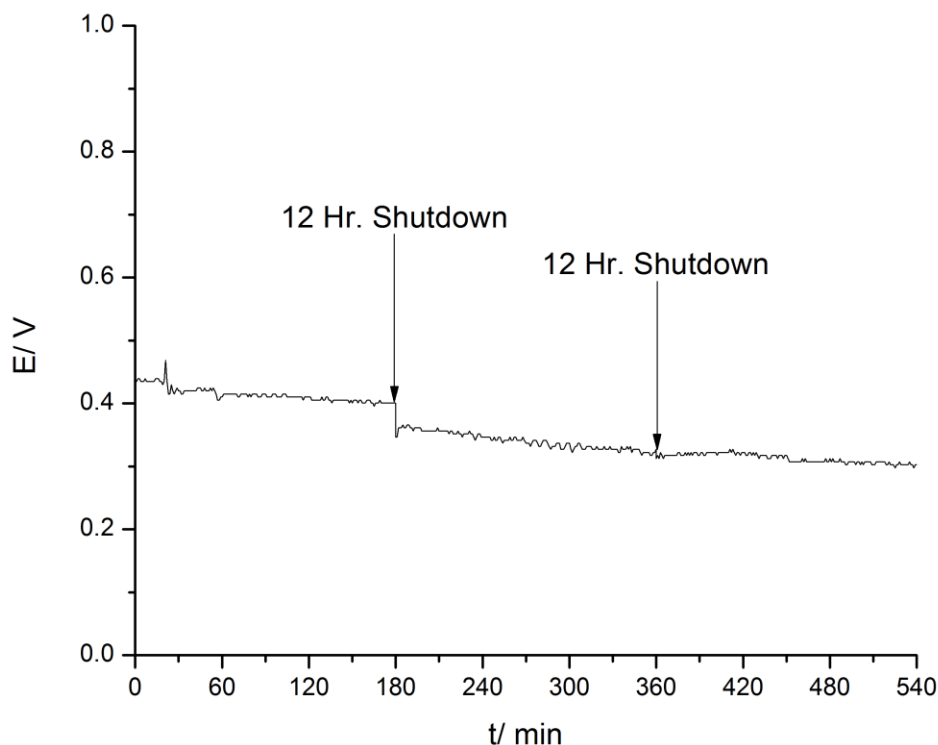


Figure 70. Longer-term performance evaluation of the DBFC with Os/ AvCarb™ P75 anode prepared by the quadruple (4x) deposition procedure. Os loading:  $1.7 \text{ mg cm}^{-2}$ . The DBFC was held at a constant current output of  $290 \text{ mA cm}^{-2}$ . T: 333 K, cathode catalyst:  $4 \text{ mg cm}^{-2}$  Pt, oxygen pressure: 4.4 atm (abs), oxygen flow rate 1.25 SLPM, anolyte:  $0.5 \text{ M NaBH}_4 - 2 \text{ M NaOH}$ , anolyte flow rate  $10 \text{ mL min}^{-1}$ .

The longterm performance of the DBFC equipped with Os/ AvCarb™ P75 anode prepared by the quadruple electrodeposition procedure (see Figure 68 and Figure 69), was investigated at a constant current density of  $290 \text{ mA cm}^{-2}$  over a total operational time of 540 minutes, which was interrupted by two shutdowns of 12 hrs each, after 180

and 360 min, respectively (Figure 70). After the first shutdown the fuel cell was not reconditioned in any form (such as by washing with distilled water or purging an inert gas at the cathode). During the first 180 minutes the DBFC cell voltage decreased by only about 30 mV. When the cell was started again, after the 12 hr shutdown, the voltage dropped by an additional 50 mV. It is hypothesized that the voltage (or power) loss at the first restart was due to crystallization and possibly carbonation of the NaOH electrolyte particularly in the gas diffusion cathode. This is a common occurrence in DBFC systems [73]. Therefore, after the second shutdown (i.e., after 360 minutes (Figure 70)) the cathode compartment was washed with copious amounts of deionized water followed by drying with high flow rate of air. Thus, following the second restart (between 360 and 540 min), the cell voltage was the same as in the last portion of the previous operation sequence and the rate of cell voltage decline remained constant relative to the 3 hour test prior to the second shutdown (Figure 70). Clearly, reconditioning the cathode was effective for recovering some of the performance. However, the original cell voltage from the beginning of the testing protocol (i.e., time zero) was not recovered, which can be attributed to a slight deactivation of the Os catalytic surface over the first 180 min, amounting to approximately  $10 \text{ mV h}^{-1}$  voltage loss. This low Os degradation rate, due probably to the incomplete removal of some of the strongly adsorbed intermediates (as discussed before in relation to the cyclic voltammograms), was also confirmed in our previous study of DBFC with Os nanoparticle anode catalyst prepared by the modified Bönneiman method and supported on Vulcan<sup>®</sup> XC-72 [165].

## 5.6 Summary for Chapter 5.0

Osmium three-dimensional electrodes were prepared by surfactant assisted electrodeposition on two graphite fiber substrates, AvCarb<sup>TM</sup> P75 and GF-S3, respectively. Due to the inherent morphological and compositional differences between the substrates, the Os deposit morphology and crystal structure was markedly different as well. On AvCarb<sup>TM</sup> P75, electrodeposition generated a polycrystalline Os with (100), (101), (103), (110) and (111) planes, whereas, on Os/ GF-S3 only a relatively weak response from the (101) plane was detected by XRD. Further inspection via SEM and TEM revealed clusters of nano-sized deposits of Os with particle sizes less than 5 nm for both cases. During cyclic voltammetry of Os in 2 M NaOH solution no evidence of OsO<sub>2</sub> formation was observed within the potential range of the cyclic voltammogram.

Cyclic voltammetry of the Os three-dimensional electrodes in 10 mM NaBH<sub>4</sub> – 2 M NaOH solution led to the conclusion that while both electrodes are efficient for BH<sub>4</sub><sup>-</sup> oxidation, Os/ AvCarb<sup>TM</sup> P75 was better especially with respect to oxidizing the strongly adsorbed intermediate species.

The performance of the Os/ AvCarb<sup>TM</sup> P75 and Os/ GF-S3 anodes was compared in DBFC polarization experiments. The major difference was noted in the ohmic control region of the polarization curve where Os/ AvCarb<sup>TM</sup> P75 was superior probably due to higher effective electronic conductivity. Increasing the temperature during fuel cell operation improved the overall performance of the AvCarb<sup>TM</sup> P75 electrode. At 333 K with 1.7 mg cm<sup>-2</sup> Os loading obtained by four successive electrodeposition steps on AvCarb<sup>TM</sup> P75, the average peak power density was 109 mW cm<sup>-2</sup> with a standard error of  $\pm 12$  mW cm<sup>-2</sup> at 90% confidence level.

## 6 Thesis Concluding Remarks

The level of interest in the development of DBFC's has increased within recent years. The potential of  $\text{NaBH}_4$  over carbonaceous fuel such as methanol, is that it overcomes many barriers that plague the development of direct fuel cells including CO poisoning and slow kinetics. The possibility of a direct fuel cell without any problems with catalyst poisoning is a significant advantage by itself. To the knowledge of the author, the experimental results discussed in Chapter 2.0 are the first to show via EQCM that  $\text{BH}_4^-$  electro-oxidation does not produce any reaction intermediates that may deactivate the Pt anode catalyst surface completely. There are, however, electro-oxidation reaction intermediates that adsorb on the surface of the Pt, which push the  $\text{BH}_4^-$  electro-oxidation onset potential higher and require higher oxidation potentials (relative to the direct electro-oxidation of  $\text{BH}_4^-$ ) to desorb. Comparing the EQCM and RDE results with DFT calculations in the literature, a reaction mechanism for  $\text{BH}_4^-$  electro-oxidation was proposed. These findings suggest that a stepwise dissociation of  $\text{BH}_4^-$  occurs upon electrosorption, where the mechanism is dictated by the number of available Pt surface sites. Eley-Rideal and Langmuir-Hinshelwood type electro-oxidation mechanisms involving  $\text{OH}^-$  and  $\text{OH}_{\text{ad}}$  are proposed to occur during  $\text{BH}_4^-$  electro-oxidation.

Direct borohydride fuel cells are a type of alkaline fuel cell, as basic conditions are required to stabilize the  $\text{BH}_4^-$ . Typical choices for supporting electrolytes are hydroxides such as NaOH and KOH. From the point of view of  $\text{BH}_4^-$  stability, there does not appear to be any dependence on the type of alkaline electrolyte, only that the solution pH must be high [46]. The alkaline environment of the fuel cell is an added benefit, as it

also allows for the use of cheaper non-noble metal catalysts in both the anode and cathode compartment.

However, the greatest barrier for DBFC development is the degradation of  $\text{BH}_4^-$  by hydrolysis. In addition to the mass transport issues that arise from  $\text{BH}_4^-$  hydrolysis during fuel cell operation,  $\text{BH}_4^-$  hydrolysis may also cause problems with fuel storage shelf life. Depending on the application and commercial shelf life requirements, one may need to consider the extra costs associated with  $\text{BH}_4^-$  degradation. It is very difficult to circumvent the problems associated with hydrolysis or even evade factors that promote the hydrolysis reaction. One method is to use thiourea (TU) to mitigate heterogeneous hydrolysis reactions on the anode catalyst surface. In chapter 2.0, it was proposed that at high TU concentrations, Lewis adduct type molecular associations between TU (weak Lewis acid) and  $\text{BH}_4^-$  (Lewis base) are possible when TU is added to the  $\text{BH}_4^-$  anolyte. This leads to a stable bi-layer build-up on the surface of the Pt. Stabilization of  $\text{BH}_{4,\text{ad}}^-$  and  $\text{BH}_{4,\text{ad}}$  in the TU intercalated bi-layer hampers  $\text{BH}_4$  dissociation, which explains the ability of TU to mitigate  $\text{BH}_4^-$  thermocatalytic hydrolysis.

Another method is to use an anode catalyst material that does not catalyze or is very poor in catalyzing the  $\text{BH}_4^-$  hydrolysis reaction such as Os. Supporting evidence for the viability of Os/ C as a DBFC anode catalyst was discussed in Chapter 3.0. Half-cell studies showed that  $\text{BH}_4^-$  electro-oxidation on Os/ C catalysts was very active, and preliminary calculations on the voltammetry data revealed that the Faradaic efficiency of  $\text{BH}_4^-$  electro-oxidation was high (~7 of a possible 8 electron reaction). Fuel cell studies also support this efficiency as the performance of Os/ C relative to Pt/ C and PtRu/ C anode catalysts appear to be less affected by  $\text{BH}_4^-$  hydrolysis at 298 K.

A novel anode design that allows for the efficient electro-oxidation of  $H_2$  may also be a good method to alleviate the negative effects of  $BH_4^-$  hydrolysis. This may be realized by changing the structure of the catalyst layer such that evolved  $H_2$  may have more time to react with the electro-active layer. In chapter 4.0, Vulcan<sup>®</sup> XC-72 carbon supported and unsupported PtRu anode catalysts were compared in a DBFC. The improved performance of the supported over the unsupported PtRu was likely due to structural differences in the respective catalyst layers. The supported PtRu catalyst layer was thicker than the unsupported PtRu layer due to the presence of Vulcan<sup>®</sup> XC-72 carbon support. As a result, the pathway for the hydrogen byproduct through the supported catalyst layer was more tortuous facilitating therefore the subsequent oxidation of  $H_2$  on the Pt sites. Mass transport characteristics were also improved due to the effect of the support.

In Chapters 4.0 and 5.0 three-dimensional DBFC Os and PtRu anodes were developed and investigated. The anodes were synthesized by surfactant assisted templated electrodeposition onto fibrous graphite substrates. Characterization of the PtRu and Os three-dimensional electrodes through microscopy and XRD revealed Os deposits of nano-sized particles/ crystallites of less than 5 nm.

It was proposed that the open structure of three-dimensional anodes would allow for the quick disengagement of evolved hydrogen from  $BH_4^-$  hydrolysis. Much greater limiting current densities from DBFC tests were achieved when using three-dimensional anodes compared to Vulcan<sup>®</sup> XC-72 carbon supported and non-supported catalyst coated membrane electrodes. For the PtRu three-dimensional electrode, mass transfer limitations were reached at current densities not less than  $450 \text{ mA cm}^{-2}$ , whereas for

PtRu/ C and PtRu black with the same catalyst metal load of  $1 \text{ mg cm}^{-2}$ , the mass transfer limiting superficial current densities are approximately  $260 \text{ mA cm}^{-2}$  and  $75 \text{ mA cm}^{-2}$ , respectively. The maximum peak power density achieved for the PtRu three-dimensional anode was also much greater at  $130 \text{ mW cm}^{-2}$  compared to  $80 \text{ mW cm}^{-2}$  and  $40 \text{ mW cm}^{-2}$ , for PtRu/ C and PtRu black, respectively. For the Os/ AvCarb™ P75 three-dimensional electrode, a limiting current density of  $350 \text{ mA cm}^{-2}$  and a peak power density of  $76 \text{ mW cm}^{-2}$  were reached with a  $0.9 \text{ mg cm}^{-2}$  catalyst metal loading.

The reproducibility of the Os/ AvCarb™ P75 three-dimensional anode was also tested. Three Os/ AvCarb™ P75 three-dimensional anodes were synthesized using the same procedure and experimental conditions and tested in a DBFC. It was found that the peak power density of the three electrodes varied with a standard error of  $\pm 12 \text{ mW cm}^{-2}$  from  $109 \text{ mW cm}^{-2}$ . The error in the cell voltage increased moving towards limiting current densities indicating differences in the ohmic drop and mass transport properties of the anodes. It was surmised that the differences in the anodes tested were due to morphological differences in the supporting AvCarb™ P75 substrates and subsequently morphological differences in the Os deposits.

Shut down and startup tests were performed to assess the longterm performance of the Os/ AvCarb™ P75 anode in a DBFC at a constant current density draw. The approximate rate of degradation of the DBFC cell voltage was  $10 \text{ mV hr}^{-1}$  in the first 3 hours of operation. It was surmised that the majority of the stability issues in the DBFC were attributed to the cathode compartment, which is prone to catalyst layer flooding,  $\text{BH}_4^-$  crossover, carbonate formation, and NaOH crystallization. An attempt was made to recondition the cathode in order to recover the original performance of the DBFC with an

Os/ AvCarb™ P75 anode, however the attempt was not successful. It is likely that the strong adsorption of intermediate electro-oxidation species on the Os contributed to the irrecoverable performance.

Another significant advantage of the three-dimensional electrode is the absence of Nafion® ionomer in the catalyst layer. Nafion® is a selective cation exchange ionomer, and therefore it will likely impede the  $\text{BH}_4^-$  anion from reaching catalytic sites. Most anion exchange materials do not appear to have a high enough chemical resistance to strong alkaline conditions ( $\text{pH} > 14$ ) [12,13]. The presence of Nafion® in the DBFC anode catalyst layer may also cause internal catalyst layer Ohmic resistances (both ionic and electronic). Due to the typically strong alkaline conditions in the DBFC anode ( $\text{pH} > 12$ ), the ionic conductance of Nafion® is not needed. It is proposed that the absence of Nafion® in the three-dimensional electrode has a beneficial influence on DBFC performance relative to supported and unsupported catalyst layers that require Nafion® as a binder. Furthermore, the absence of Nafion® simplifies the anode catalyst layer fabrication process.

## 7 Recommendations

- Studies on hydrogen adsorption onto single crystal Os lower Miller index planes need to be completed in order to establish a standard for the hydrogen desorption charge per real surface area on polycrystalline Os. By knowing the manner in which hydrogen adsorbs onto the Os surface, one would be able to determine the electrochemical surface area of Os catalysts. This is an important parameter when applying electrochemistry relationships to extract pertinent information regarding the electrochemical behaviour of  $\text{BH}_4^-$  on Os electrocatalysts. A preliminary attempt in approximating the electrochemical surface area of Os is shown in Appendix F.
- It is recommended that further fundamental studies on  $\text{BH}_4^-$  electro-oxidation on Os to be carried out, e.g., rotating disk electrode and EQCM studies. This will allow for the conclusive determination of the faradaic efficiency of  $\text{BH}_4^-$  electro-oxidation on Os, and the assessment of reaction intermediate species adsorption on Os.
- The effect of Os oxidation state and/ or the crystallographic structure of polycrystalline Os on  $\text{BH}_4^-$  electro-oxidation and hydrolysis should be explored. There are apparent differences in the cyclic voltammetry performed by Atwan et al. [16,109] on supported Os catalyst and the cyclic voltammetry performed by Lam et al.[165]. The differences are likely attributed to differing oxidation states or crystallographic features of the catalysts. Various post-catalyst synthesis treatments, or insitu catalyst synthesis treatments can be applied in an attempt to change the crystallinity and/ or oxidation state of the catalyst. XRD may be used

to check the crystallinity of the catalyst.  $\text{BH}_4^-$  hydrolysis can be measured by measuring the volume of  $\text{H}_{2(\text{g})}$  evolved at various temperatures and  $\text{BH}_4^-/\text{OH}^-$  concentration ratios [29].

- More extensive DBFC durability testing.
- The effect of the flowfield plate design on the performance of three-dimensional electrodes in a DBFC system should be explored. The serpentine flowfield design utilized in this dissertation may not necessarily be optimal for the performance of the tested three-dimensional electrodes. Bauer et al. did some preliminary work on exploring the effect of flow-by versus serpentine end plates on three-dimensional electrodes for a DMFC system [201].
- The effect of three-dimensional electrodes on  $\text{BH}_4^-$  crossover should be studied.
- A systematic study must be conducted in order to evaluate non-Pt air cathodes such as  $\text{MnO}_2$  for DBFC. Some preliminary evidence in the literature has already been published [102] and seem to indicate that  $\text{MnO}_2$  is almost completely inert for  $\text{BH}_4^-$  electro-oxidation. However, no improvement in the open circuit voltage has been found for tested DBFC systems utilizing  $\text{MnO}_2$  cathodes in the literature [22]. In addition to  $\text{MnO}_2$ ,  $\text{La}_{1-x}\text{Sr}_x\text{CoO}_3$  [24],  $\text{Eu}_2\text{O}_3$  [26],  $\text{LaNiO}_3$  [23], Fe TMPP [202] and CoPc [27] cathode catalysts have also been found to be tolerant to  $\text{BH}_4^-$  oxidation.
- In light of the discovery of cathode catalysts that are potentially immune to  $\text{BH}_4^-$  crossover, it is recommended that an in depth study be conducted to test the applicability of different separator materials including anion exchange membranes

and commercial battery diaphragms for the DBFC system. A preliminary study has been conducted in Appendix G.

- In the case of chlor-alkali membrane reactors where  $O_2$  is fed to the cathode compartment, it was found that humidifying the air stream led to greater improvements in the overall cell voltage [203]. By humidifying the  $O_2$  stream the local concentration of NaOH at the cathode active layer is reduced albeit flooding of the cathode catalysts would also occur [203]. The effects of cathode flooding however can be alleviated by the addition of Teflon<sup>®</sup> in the active layer and/ or controlling the degree in which the  $O_2$  feed is humidified. Although this method may be applicable for chlor-alkali membrane reactors, it is not necessarily suitable for DBFC systems as the presence of excess water in the cathode compartment may further complicate the DBFC system design.
- It is proposed that  $BH_4^-$  electrochemical systems may also function well as primary batteries. The high theoretical energy density of  $BH_4^- - O_2$  systems and their high theoretical cell voltage give them a competitive edge. In addition, relatively cheap anode and cathode catalysts and commercial battery diaphragms may be used to negate the typical system cost differences between commercial batteries and fuel cells.

## Bibliography

- [1] M. E. Indig and R. N. Snyder, *J. Electrochem. Soc.* 109 (1962) 1104.
- [2] R. Jasinski, *Electrochem. Technol.* 3 (1965) 40.
- [3] Z. P. Li, B. H. Liu, K. Arai, and S. Suda, *Journal of Alloys and Compounds* 404-406 (2005) 648.
- [4] S. C. Amendola, P. Onnerud, M. T. Kelly, P. J. Petillo, S. L. Sharp-Goldman, and M. Binder, *J. Power Sources* 84 (1999) 130.
- [5] S. Song, W. Zhou, W. Li, G. Sun, Q. Xin, S. Kontou, and P. Tsiakaras, *Ionics* 10 (2004) 458.
- [6] H. Cheng and K. Scott, *J. Power Sources* 160 (2006) 407.
- [7] E. Gyenge, *PEM Fuel Cell Electrocatalysts and Catalyst Layers: Fundamentals and Applications, *Electrocatalytic Oxidation of Methanol, Ethanol and Formic Acid**, (Springer London, 2008), p. 165.
- [8] J. Wee, *J. Power Sources* 161 (2006) 1.
- [9] E. Gyenge, *Electrochim. Acta* 49 (2004) 965.
- [10] M. Escano Clare Sison, E. Gyenge, R. L. Arevalo, and H. Kasai, *J. Phys. Chem. C* 115 (2011) 19883.
- [11] B. H. Liu, Z. P. Li, K. Arai, and S. Suda, *Electrochimica Acta* 50 (2005) 3719.
- [12] C. P. de Leon, F. C. Walsh, D. Pletcher, D. J. Browning, and J. B. Lakeman, *J. Power Sources* 155 (2006) 172.
- [13] C.P. de Leon, F. C. Walsh, R. R. Bessette, C. J. Patrissi, M. G. Medeiros, A. Rose, D. Browning, J. B. Lakeman, and R. W. Reeve, *ECS Trans.* 15 (2008) 25.

- [14] J. B. Lakeman, A. Rose, K. D. Pointon, D. J. Browning, K. V. Lovell, S. C. Waring, and J. A. Horsfall, *J. Power Sources* 162 (2006) 765.
- [15] M. H. Atwan, C. L. B. Macdonald, D. O. Northwood, and E. L. Gyenge, *J. Power Sources* 158 (2006) 36.
- [16] M. H. Atwan, D. O. Northwood, and E. L. Gyenge, *Int. J. Hydrogen Energy* 30 (2005) 1323.
- [17] H. Dong, R. Feng, X. Ai, Y. Cao, H. Yang, and C. Cha, *J. Phys. Chem. B* 109 (2005) 10896.
- [18] E. Gyenge, M. H. Atwan, and D. Northwood, *J. Electrochem. Soc.* 153 (2006) A150.
- [19] B. H. Liu, Z. P. Li, and S. Suda, *Electrochim. Acta* 49 (2004) 3097.
- [20] B. H. Liu, Z. P. Li, and S. Suda, *J. Electrochem. Soc.* 150 (2003) A398.
- [21] E. Sanli, H. Celikkan, B. Zuhtu Uysal, and M. L. Aksu, *Int. J. Hydrogen Energy* 31 (2006) 1920.
- [22] F. A. Coowar, G. Vitins, G. O. Mepsted, S. C. Waring, and J. A. Horsfall, *J. Power Sources* 175 (2008) 317.
- [23] J. Ma, Y. Liu, Y. Liu, Y. Yan, and P. Zhang, *Fuel Cells (Weinheim, Ger.)* 8 (2008) 394.
- [24] Y. Liu, Y. Liu, J. Ma, and J. Lai, *J. Power Sources* 195 (2010) 1854.
- [25] Y. Liu, J. Ma, J. Lai, and Y. Liu, *J. Alloys Compd.* 488 (2009) 204.
- [26] X. Ni, Y. Wang, Y. L. Cao, X. P. Ai, H. X. Yang, and M. Pan, *Electrochem. Commun.* 12 (2010) 710.
- [27] J. Ma, Y. Liu, P. Zhang, and J. Wang, *Electrochem. Commun.* 10 (2008) 100.

- [28] J. Wee, *J. Power Sources* 155 (2006) 329.
- [29] J. B. Brown and M. Svensson, *Journal of the Scientific Laboratories* 44 (1958) 117.
- [30] C. A. Lumsden and T. H. Evans, US 2003/0108832 A1 (USA, 2003) Patent.
- [31] G. Broja and W. Schlabacher, DE 1108670 (Germany, 1959) Patent.
- [32] F. Schubert, K. Lang, and W. Schlabacher, DE 1067005 (Germany, 1959) Patent.
- [33] H. Knorre and H. Kloepper, US 3379511 (USA, 1962) Patent.
- [34] E. E. Filby, US 3993732 A (USA, 1976) Patent.
- [35] Y. Zhou, US 7429368 B2 (USA, 2008) Patent.
- [36] Y. Zhou, WO 2002062701 A1 (USA, 2002) Patent.
- [37] S. C. Amendola, M. T. Kelly, and Y. Wu, WO 2002083551 A1 (USA, 2002) Patent.
- [38] S. C. Amendola, M. T. Kelly, J. V. Ortega, and Y. Wu, US 20030092877 A1 (USA, 2003) Patent.
- [39] S. Suda, JP 2004010446 A (Japan, 2004) Patent.
- [40] J. Snover and Y. Wu, US 6706909 B1 (USA; 2004) Patent.
- [41] D. N. Bingham, B. M. Wilding, K. M. Klingler, W. T. Zollinger, and K. M. Wendt, US 20050077170 A1 (USA, 2005) Patent.
- [42] H. I. Schlesinger, H. C. Brown, and A. E. Finholt, *J. Am. Chem. Soc.* 75 (1953) 205.
- [43] Y. Wu, M. T. Kelly, and J. V. Ortega, Review of Chemical Processes for the Synthesis of Sodium Borohydride ( 2004) Report No. DE-FC36-04GO14008.
- [44] Alibaba.com, <http://www.alibaba.com>, Date Accessed: January 2012.

- [45] E. H. Jensen, A study on sodium borohydride, with special reference to its analytical application in organic chemistry (Nyt nordisk forlag, Copenhagen, 1954) Thesis.
- [46] V. Minkina, S. Shabunya, V. Kalinin, and V. Martynenko, Russ. J. Appl. Chem., 81 (2008) 380.
- [47] S. Colominas, J. McLafferty, and D. D. Macdonald, Electrochim. Acta 54 (2009) 3575.
- [48] Rohm and Haas, *Sodium Borohydride Digest*, <http://www.rohmhaas.com>, Date Accessed: January 2012.
- [49] K. N. Mochalov, V. S. Khain, and G. G. Gil'manshin, Kinetika I Kataliz 6 (1965) 541.
- [50] Q. Zhang, G. Smith, Y. Wu, and R. Mohring, Int J Hydrogen Energy 31 (2006) 961.
- [51] K. Barral, Technical-Economical Assessment of Sodium Borohydride as an Energy Carrier, Air Liquid Claude Delorme Research Center, 2010 Presentation.
- [52] H. I. Schlesinger, H. C. Brown, A. E. Finholt, J. R. Gilbreath, H. R. Hoekstra, and E. K. Hyde, J. Am. Chem. Soc. 75 (1953) 215.
- [53] A. Gonçalves, P. Castro, A. Novais, V. R. Fernandes, C. M. Rangel, and H. Matos, Chem. Engg. Trans., 12 (2007) 243.
- [54] A. Gonçalves, P. Castro, A. Q. Novais, C. M. Rangel, and H. Matos, 18<sup>th</sup> European Symposium on Computer Aided Process Engineering, *Modeling of catalytic hydrogen generation from sodium borohydride* (Elsevier, 2008) 757.

- [55] J. Andrieux, U. B. Demirci, J. Hannauer, C. Gervais, C. Goutaudier, and P. Miele, *Int J Hydrogen Energy* 36 (2011) 224.
- [56] R. L. Pecsok, *J. Am. Chem. Soc.* 75 (1953) 2862.
- [57] R. E. Davis and C. G. Swain, *J. Am. Chem. Soc.* 82 (1960) 5949.
- [58] R. E. Davis, E. Bromels, and C. L. Kibby, *J. Am. Chem. Soc.* 84 (1962) 885.
- [59] W. H. Stockmayer, R. Miller R., and R. J. Zeto, *J. Phys. Chem.* 65 (1961) 1076.
- [60] W. L. Jolly and R. E. Mesmer, *J. Am. Chem. Soc.* 83 (1961) 4470.
- [61] R. E. Mesmer and W. L. Jolly, *Inorg. Chem.* 1 (1962) 608.
- [62] J. A. Gardiner and J. W. Collat, *J. Am. Chem. Soc.* 86 (1964) 3165.
- [63] S. S. Muir and X. Yao, *Int J Hydrogen Energy* 36 (2011) 5983.
- [64] B. H. Liu and Q. Li, *Int J Hydrogen Energy* 33 (2008) 7385.
- [65] S. Özkar and M. Zahmakıran, *J. Alloys Compd.* 404-406 (2005) 728.
- [66] U. S. Department of Energy, *Go/No-Go Recommendation for Sodium Borohydride for On-Board Vehicular Hydrogen Storage*, 2007), NREL/MP-150-42220.
- [67] A. Verma and S. Basu, *Journal of Power Sources* 145 (2005) 282.
- [68] R. K. Raman, N. A. Choudhury, and A. K. Shukla, *Electrochem. Solid-State Lett.* 7 (2004) A488.
- [69] Z. P. Li, B. H. Liu, K. Arai, and S. Suda, *J. Electrochem. Soc.* 150 (2003) A868.
- [70] F. Walsh, *A First Course in Electrochemical Engineering*, The Electrochemical Consultancy, Hants, England, 1993.
- [71] B. H. Liu, J. Q. Yang, and Z. P. Li, *Int J Hydrogen Energy* 34 (2009) 9436.
- [72] C. Celik, F. San Gul Boyaci, and H. I. Sarac, *J. Power Sources* 195 (2010) 2599.

- [73] R. Jamard, J. Salomon, A. Martinent-Beaumont, and C. Coutanceau, *J. Power Sources* 193 (2009) 779.
- [74] T. Maoka and M. Enyo, *Surface Technology* 9 (1979) 147.
- [75] C. Celik, F. G. Boyaci San, and H. I. Sarac, *Int. J. Hydrogen Energy* 35 (2010) 8678.
- [76] R. Jamard, A. Latour, J. Salomon, P. Capron, and A. Martinent-Beaumont, *J. Power Sources* 176 (2008) 287.
- [77] S. Towne, M. Carella, W. E. Mustain, V. Viswanathan, P. Rieke, U. Pasaogullari, and P. Singh, *ECS Trans.* 25 (2009) 1951.
- [78] B. H. Liu and S. Suda, *J. Power Sources* 164 (2007) 100.
- [79] G. Wang, Y. Gao, Z. Wang, C. Du, and G. Yin, *Electrochem. Commun.* 12 (2010) 1070.
- [80] B. H. Liu, Z. P. Li, and S. Suda, *J. Power Sources* 175 (2008) 226.
- [81] M. V. Mirkin, H. Yang, and A. J. Bard, *J. Electrochem. Soc.* 139 (1992) 2212.
- [82] H. Cheng and K. Scott, *Electrochim. Acta* 51 (2006) 3429.
- [83] C. Ponce-de-León, D. V. Bavykin, and F. C. Walsh, *Electrochem. Commun.* 8 (2006) 1655.
- [84] J. P. Elder and A. Hickling, *Trans. Faraday Soc.* 58 (1962) 1852.
- [85] J. Kim, H. Kim, Y. Kang, M. Song, S. Rajendran, S. Han, D. Jung, and J. Lee, *J. Electrochem. Soc.* 151 (2004) A1039.
- [86] J. I. Martins, M. C. Nunes, R. Koch, L. Martins, and M. Bazzouai, *Electrochim. Acta* 52 (2007) 6443.

- [87] M. H. Atwan, D. O. Northwood, and E. L. Gyenge, *Int. J. Hydrogen Energy* 32 (2007) 3116.
- [88] H. Cheng, K. Scott, and K. Lovell, *Fuel Cells* 6 (2006) 367.
- [89] H. Cheng and K. Scott, *J. Appl. Electrochem.* 36 (2006) 1361.
- [90] Z. P. Li, B. H. Liu, J. K. Zhu, and S. Suda, *J. Power Sources* 163 (2006) 555.
- [91] K. Wang, J. Lu, and L. Zhuang, *J. Phys. Chem. C* 111 (2007) 7456.
- [92] L. Wang, C. Ma, and X. Mao, *J. Alloys Compounds* 397 (2005) 313.
- [93] C. Wu, H. Zhang, and B. Yi, *Catal. Today* 93-95 (2004) 477.
- [94] Y. Bai, C. Wu, F. Wu, and B. Yi, *Mater. Lett.* 60 (2006) 2236.
- [95] U. B. Demirci and F. Garin, *Int. J. Green Energy* 5 (2008) 148.
- [96] D. Xu, H. Wang, P. Dai, and Q. Ye, *The Open Catalysis J.* 2 (2009) 92.
- [97] G. Guella, B. Patton, and A. Miotello, *J. Phys. Chem. C* 111 (2007) 18744.
- [98] J. A. Gardiner and J. W. Collat, *Inorg. Chem.* 4 (1965) 1208.
- [99] J. A. Gardiner and J. W. Collat, *J. Am. Chem. Soc.* 87 (1965) 1692.
- [100] D. A. Finkelstein, M. Da Nicolas, J. L. Cohen, and H. D. Abruna, *J. Phys. Chem. C* 113 (2009) 19700.
- [101] D. M. F. Santos and C. A. C. Sequeira, *J. Electroanal. Chem.* 627 (2009) 1.
- [102] R. X. Feng, H. Dong, Y. D. Wang, X. P. Ai, Y. L. Cao, and H. X. Yang, *Electrochem. Commun.* 7 (2005) 449.
- [103] E. Gyenge, *Electrochim. Acta* 49 (2004) 1875.
- [104] V. W. S. Lam, D. C. W. Kannangara, A. Alfantazi, and E. L. Gyenge, *J. Phys. Chem. C* 115 (2011) 2727.

- [105] B. M. Concha, M. Chatenet, C. Coutanceau, and F. Hahn, *Electrochem. Commun.* 11 (2009) 223.
- [106] M. Chatenet, F. H. B. Lima, and E. A. Ticianelli, *J. Electrochem. Soc.* 157 (2010) B697.
- [107] P.J. Loferski, U.S. Geological Survey, Interview: January 21, 2010.
- [108] Platinum Today, <http://www.platinum.matthey.com>, Date Accessed: March 23, 2012.
- [109] M. H. Atwan, D. O. Northwood, and E. L. Gyenge, *J. New Mater. Electrochem. Syst.* 8 (2006) 243.
- [110] A. E. Sanli, I. Kayacan, B. Z. Uysal, and M. L. Aksu, *J. Power Sources* 195 (2010) 2604.
- [111] V. A. Hernandez-Ramirez, A. Alatorre-Ordaz, M. L. Yopez-Murrieta, J. G. Ibanez, C. Ponce-de-Leon, and F. C. Walsh, *ECS Trans.* 20 (2009) 211.
- [112] C. Molina B. and M. Chatenet, *Electrochim. Acta* 54 (2009) 6130.
- [113] C. Molina B. and M. Chatenet, *Electrochim. Acta* 54 (2009) 6119.
- [114] Q. Yi and L. Li, *Huagong Xuebao (Chin. Ed.)* 60 (2009) 455.
- [115] E. Sanli, B. Z. Uysal, and M. L. Aksu, *Int. J. Hydrogen Energy* 33 (2008) 2097.
- [116] M. Chatenet, F. Micoud, I. Roche, and E. Chainet, *Electrochim. Acta* 51 (2006) 5459.
- [117] M. Chatenet, F. Micoud, I. Roche, E. Chainet, and J. Vondrák, *Electrochim. Acta* 51 (2006) 5452.
- [118] E. R. Savinova, D. Zemlyanov, B. Pettinger, A. Scheybal, R. Schlögl, and K. Doblhofer, *Electrochim. Acta* 46 (2000) 175.

- [119] D. M. F. Santos and C. A. C. Sequeira, *ECS Trans.* 16 (2009) 123.
- [120] D. M. F. Santos and C. A. C. Sequeira, *J. Electrochem. Soc.* 157 (2010) B13.
- [121] J. Hong, B. Fang, C. Wang, and K. Currie, *J. Power Sources* 161 (2006) 753.
- [122] London Metal Exchange, <http://www.lme.com>, Date Accessed: January 2012.
- [123] Ö. Metin and S. Özkar, *Journal of Molecular Catalysis A: Chemical* 295 (2008) 39.
- [124] X. Geng, H. Zhang, W. Ye, Y. Ma, and H. Zhong, *J. Power Sources* 185 (2008) 627.
- [125] G. Wang, Y. Gao, Z. Wang, C. Du, J. Wang, and G. Yin, *J. Power Sources* 195 (2010) 185.
- [126] J. Ma, Y. Sahai, and R. G. Buchheit, *J. Power Sources* 195 (2010) 4709.
- [127] J. Q. Yang, B. H. Liu, and S. Wu, *J. Power Sources* 194 (2009) 824.
- [128] M. Simoes, S. Baranton, and C. Coutanceau, *J. Phys. Chem. C* 113 (2009) 13369.
- [129] B. H. Liu, Z. P. Li, J. K. Zhu, and S. Suda, *J. Power Sources* 183 (2008) 151.
- [130] G. Wang, X. Wang, R. Miao, D. Cao, and K. Sun, *Int. J. Hydrogen Energy* 35 (2010) 1227.
- [131] B. H. Liu and S. Suda, *J. Alloys Compd.* 454 (2008) 280.
- [132] L. Wang, C. Ma, X. Mao, J. Sheng, F. Bai, and F. Tang, *Electrochem. Commun.* 7 (2005) 1477.
- [133] B. H. Liu, Z. P. Li, and S. Suda, *J. Power Sources* 185 (2008) 1257.
- [134] V. Kiran, T. Ravikumar, N. T. Kalyanasundaram, S. Krishnamurthy, A. K. Shukla, and S. Sampath, *J. Electrochem. Soc.* 157 (2010) B1201.

- [135] N. Duteanu, G. Vlachogiannopoulos, M. Shivhare, E. Yu, and K. Scott, *J. Appl. Electrochem.* 37 (2007) 1085.
- [136] G. Rostamikia and M. J. Janik, *ECS Trans.* 16 (2008) 1869.
- [137] G. Vatankhah, J. Lessard, G. Jerkiewicz, A. Zolfaghari, and B. E. Conway, *Electrochim. Acta* 48 (2003) 1613.
- [138] Y. Ratieuville, P. Viers, J. Alexandre, and G. Durand, *Electrochem. Commun.* 2 (2000) 839.
- [139] D. M. F. Santos and C. A. C. Sequeira, *J. Electrochem. Soc.* 156 (2009) F67.
- [140] J. I. Martins and M. C. Nunes, *Journal of Power Sources*, 175 (2008) 244.
- [141] F. Huerta, E. Morallón, C. Quijada, J. L. Vázquez, and L. E. A. Berlouis, *J. Electroanal. Chem.* 463 (1999) 109.
- [142] A. Bewick and J. W. Russell, *J. Electroanal. Chem.* 132 (1982) 329.
- [143] F. Gloaguen, J. - L. Léger, and C. Lamy, *J. Electroanal. Chem.* 467 (1999) 186.
- [144] D. M. Drazic, A. V. Tripkovic, K. D. Popovic, and J. D. Lovic, *J. Electroanal. Chem.* 466 (1999) 155.
- [145] A. V. Tripkovic, K. D. Popovic, and J. D. Lovic, *J. Serb. Chem. Soc.* 66 (2001) 825.
- [146] E. Morallón, J. L. Vázquez, and A. Aldaz, *J. Electroanal. Chem.* 288 (1990) 217.
- [147] H. Angerstein-Kozłowska, B. E. Conway, and W. B. A. Sharp, *J. Electroanal. Chem.* 43 (1973) 9.
- [148] A. J. Appleby, *J. Electrochem. Soc.* 120 (1973) 1205.
- [149] B. E. Conway, *Prog. Surf. Sci.* 49 (1995) 331.
- [150] G. Rostamikia and M. J. Janik, *Electrochim. Acta* 55 (2010) 1175.

- [151] M. T. M. Koper, *Faraday Discuss.* 140 (2009) 11.
- [152] M. Yan, K. Liu, and Z. Jiang, *J. Electroanal. Chem.* 408 (1996) 225.
- [153] D. Papapanayiotou, R. N. Nuzzo, and R. C. Alkire, *J. Electrochem. Soc.* 145 (1998) 3366.
- [154] G. García, J. L. Rodríguez, G. I. Lacconi, and E. Pastor, *J. Electroanal. Chem.* 588 (2006) 169.
- [155] J. O. Bockris, S. D. Argade, and E. Gileadi, *Electrochim. Acta* 14 (1969) 1259.
- [156] W. D. Kumler and G. M. Fohlen, *J. Am. Chem. Soc.* 64 (1942) 1944.
- [157] R. Parsons, *Proceedings of the Royal Society of London A* 261 (1961) 79.
- [158] S. Romanowski, T. M. Pietrzak, M. Skompska, M. Jurkiewicz-Herbich, and J. Jastrzębska, *J. Electroanal. Chem.* 345 (1993) 83.
- [159] J. Kua and W. A. Goddard, *J. Am. Chem. Soc.* 121 (1999) 10928.
- [160] G. Gokagac and B. J. Kennedy, *Z. Naturforsch.* 57b (2002) 193.
- [161] J. Huang, H. Yang, Q. Huang, Y. Tang, T. Lu, and D. L. Akins, *J. Electrochem. Soc.* 151 (2004) A1810.
- [162] H. Bönemann, W. Brijoux, R. Brinkmann, T. Joußen, B. Korall, and E. Dinjus, *Angew. Chem. Int. Ed Engl.* 30 (1991) 1312.
- [163] M. Götz and H. Wendt, *Electrochim. Acta* 43 (1998) 3637.
- [164] P. C. Yen, R. S. Chen, C. C. Chen, Y. S. Huang, K. K. Tiong, and P. C. Liao, *J. Alloys Compd.* 383 (2004) 277.
- [165] S. C. Amendola, S. L. Sharp-Goldman, M. S. Janjua, N. C. Spencer, M. T. Kelly, P. J. Petillo, and M. Binder, *Int. J. Hydrogen Energy* 25 (2000) 969.

- [166] A. J. Bard and L. R. Faulkner, *Electrochemical Methods: Fundamentals and Applications*, (John Wiley & Sons, New York, 2001).
- [167] K. Wang, J. Lu, and L. Zhuang, *J. Electroanal. Chem.* 585 (2005) 191.
- [168] J. Newman and K. E. Thomas-Alyea, *Electrochemical Systems, Mass Transfer* (John Wiley & Sons, New Jersey, 2004), 3rd Ed., p. 532.
- [169] J. W. Tsang and R. Prasad, US 20030143443 A1 (USA, 2003) Patent.
- [170] C. Kim, K. Kim, and M. Y. Ha, *J. Power Sources* 180 (2008) 154.
- [171] R. X. Feng, H. Dong, Y. L. Cao, X. P. Ai, and H. X. Yang, *Int. J. Hydrogen Energy* 32 (2007) 4544.
- [172] V. W. S. Lam and E. L. Gyenge, *J. Electrochem. Soc.* 155 (2008) B1155.
- [173] T. Cheng and E. Gyenge, *J. Appl. Electrochem.* 38 (2008) 51.
- [174] T. T. Cheng and E. L. Gyenge, *J. Appl. Electrochem.* 39 (2009) 1925.
- [175] T. T. Cheng and E. L. Gyenge, *J. Electrochem. Soc.* 155 (2008) B819.
- [176] A. Bauer, E. L. Gyenge, and C. W. Oloman, *J. Power Sources* 167 (2007) 281.
- [177] D. R. Lycke and E. L. Gyenge, *Electrochim. Acta* 52 (2007) 4287.
- [178] A. Bauer, E. L. Gyenge, and C. W. Oloman, *Electrochim. Acta* 51 (2006) 5356.
- [179] T. T. Cheng and E. L. Gyenge, *Electrochim. Acta* 51 (2006) 3904.
- [180] A. Bauer, C. W. Oloman, and E. L. Gyenge, *J. Power Sources* 193 (2009) 754.
- [181] A. Lam, B. Wetton, and D. P. Wilkinson, *J. Electrochem. Soc.* 158 (2011) B29.
- [182] A. Lam, D. P. Wilkinson, and J. Zhang, *Electrochim. Acta* 53 (2008) 6890.
- [183] A. Lam, M. S. Dara, D. P. Wilkinson, and K. Fatih, *Electrochem. Commun.* 17 (2012) 22.

- [184] R. G. Allen, C. Lim, L. X. Yang, K. Scott, and S. Roy, *J. Power Sources* 143 (2005) 142.
- [185] R. Chetty, K. Scott, S. Kundu, and M. Muhler, *J. Fuel Cell Sci. Technol.* 7 (2010) 031011.
- [186] V. Lam, A. Alfantazi, and E. Gyenge, *J. Appl. Electrochem.* 39 (2009) 1763.
- [187] V. A. Paganin, E. A. Ticianelli, and E. R. Gonzalez, *J. Appl. Electrochem.* 26 (1996) 297.
- [188] X. Cheng, B. Yi, M. Han, J. Zhang, Y. Qiao, and J. Yu, *J. Power Sources* 79 (1999) 75.
- [189] G. Lalande, M. C. Denis, D. Guay, J. P. Dodelet, and R. Schulz, *J. Alloys Compd.* 292 (1999) 301.
- [190] E. Antolini, L. Giorgi, F. Cardellini, and E. Passalacqua, *J. Solid State Electrochem.* 5 (2001) 131.
- [191] N. Takeno, *Atlas of Eh-pH Diagrams - Intercomparison of Thermodynamic Databases*, 2005), 419.
- [192] R. Liu, H. Iddir, Q. Fan, et al, *J. Phys. Chem. B* 104 (2000) 3518.
- [193] Y. Zhu and C. R. Cabrera, *Electrochem. Solid-State Lett.* 4 (2001) A45.
- [194] A. Hamnett and B. J. Kennedy, *Electrochim. Acta* 33 (1988) 1613.
- [195] Y. Hayakawa, K. Fukuzaki, S. Kohiki, Y. Shibata, T. Matsuo, K. Wagatsuma, and M. Oku, *Thin Solid Films* 347 (1999) 56.
- [196] R. Zanoni, V. Carinci, R. Abu-Samn, R. Psaro, and C. Dossi, *J. Mol. Struct.* 131 (1985) 363.

- [197] D. D. Sarma and C. N. R. Rao, *J. Electron. Spectrosc. Relat. Phenom.* 20 (1980) 25.
- [198] J. T. Gostick, M. W. Fowler, M. D. Pritzker, M. A. Ioannidis, and L. M. Behra, *J. Power Sources* 162 (2006) 228.
- [199] C. Oloman, M. Matte, and C. Lum, *J. Electrochem. Soc.* 138 (1991) 2330.
- [200] R. E. Walpole, R. H. Myers, and S. L. Myers, *Probability and Statistics for Engineers and Scientists* (6<sup>th</sup> Ed., Prentice Hall, USA, 1972).
- [201] A. G. Bauer, *Direct Methanol Fuel Cell with Extended Reaction Zone Anode: PtRu and PtRuMo Supported on Fibrous Carbon* (The University of British Columbia, Vancouver, 2008) Thesis.
- [202] H. Cheng and K. Scott, *J. Electroanal. Chem.* 596 (2006) 117.
- [203] J. Chlistunoff, *Advanced Chlor-Alkali Technology* (U.S. Department of Energy, Los Alamos, 2004) Report No. LAUR 05-2444.

## Appendix A Electrochemical Surface Area Calculation

The electrochemical surface area or real surface area of polycrystalline Pt was determined by the underpotential deposition (UPD) and desorption of a monolayer of  $H_{ad}$ . UPD refers to the deposition of hydrogen at potentials more positive than its thermodynamic equilibrium potential. The adsorption of a monolayer of H allows for the determination of the Pt electrochemical surface area by knowing the Pt-H stoichiometry of the monolayer. There are two underlying assumptions for this method [1]:

- 1) The electrode potential at which there is a full coverage of a monolayer of H is equal to the onset potential of  $H_2$  evolution
- 2) The stoichiometric relationship between Pt atoms and  $H_{ads}$  is one to one.

An additional assumption of the H-UPD method is that only the lower Miller index planes are considered when determining  $H^*$  adsorption on the Pt surface; namely (100), (110), and (111) [1--3].  $H^*$  adsorption onto higher index planes, which are also likely to be present on a polycrystalline Pt surface, are neglected.

Adsorption of the  $H^*$  monolayer occurs electrochemically via the following mechanism [2]:



At the point where a full monolayer is reached, the formation of diatomic hydrogen takes place on the Pt surface [2]:



At even lower reducing potentials,  $H_{2(g)}$  evolution will occur, thus freeing Pt sites via [2]:



The hydrogen charge density associated with reaction (A.1) to form a monolayer on polycrystalline platinum has been experimentally measured and universally accepted to be equal to 210  $\mu\text{C}$  per  $\text{cm}^2$  of real electrochemical area. This value is based on either the adsorption of H onto the predominant (100) plane or an equal distribution (33.3%) of (100), (110), and (111) [1--3].

A monolayer of  $H_{ads}$  on a Pt surface can be achieved by setting the potential of the Pt to 50 mV in 0.5 M  $\text{H}_2\text{SO}_4$  [1]. For determining the electrochemical surface area of the Pt disk and the Pt resonator in Chapter 2.0, the monolayer charge was measured from Pt cyclic voltammograms in 0.5 M  $\text{H}_2\text{SO}_4$  scanning from a minimum of 1.1 V to 50 mV with a scan rate of 20  $\text{mV s}^{-1}$ . The resulting voltammogram for the Pt disk is shown in Figure 71.

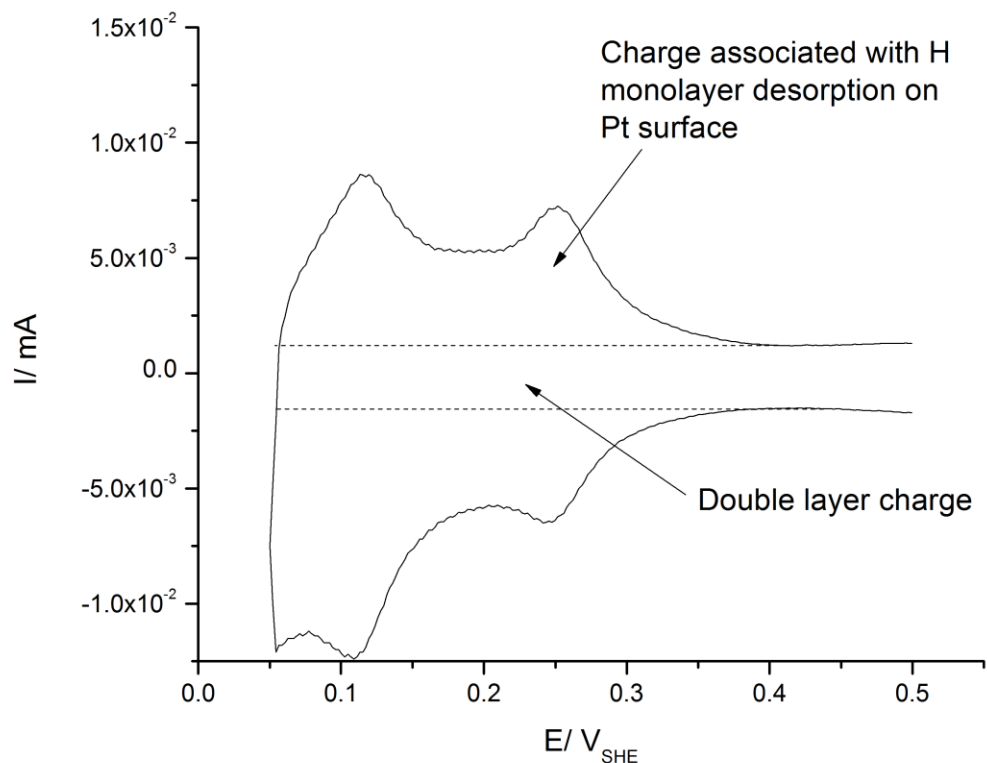


Figure 71. H-UPD on 0.5 cm diameter polycrystalline Pt disk. T: 298 K, Electrolyte: 0.5 M H<sub>2</sub>SO<sub>4</sub>, scan rate: 20 mV s<sup>-1</sup>

The H monolayer charge can be measured from the stripping of the monolayer in the forward scan of the cyclic voltammogram. In order to obtain the true charge, one must subtract from the total charge, the charge associated with the double layer. Calculation of the monolayer charge can be achieved as follows:

$$Q = \frac{1}{\nu} \int_{0.05}^{0.5} IdE - Q_{DL} \quad (\text{A.4})$$

where  $Q$  is the charge associated with the formation of a Pt-H monolayer in C,  $v$  is the scan rate in  $V s^{-1}$ ,  $I$  is the current in A,  $E$  is the voltage in V, and  $Q_{DL}$  is the double layer charging in C. The electrochemical surface area can then be calculated via the following relationship [1-2]:

$$A = \frac{Q}{Q_m} \quad (A.5)$$

where  $A$  is the real electrochemical surface area, and  $Q$  is the measured charge associated with the formation of a Pt-H monolayer, and  $Q_m$  is the charge density corresponding to a complete hydrogen monolayer on polycrystalline Pt which is equal to  $210 \mu C cm^{-2}$ . The electrochemical surface area for the Pt RDE disk was  $0.28 cm^2$ , and the Pt resonator was  $0.23 cm^2$ . The geometric surface areas of both electrodes were  $0.20 cm^2$ .

## References:

- [1] F.C. Nart, and W. Vielstich, in: W. Vielstich, H.A. Gasteiger, A. Lamm (Eds), Handbook of Fuel Cells: Fundamentals, Tehcnology, and Applications, *Normalization of Porous Active Surfaces*, John Wiley & Sons, Ltd. New Jersey, 2003, pp. 302-315.
- [2] J.M.D. Rodriguez, J.A.H. Melian, J.P. Pena, J. Chem. Educ. 77 (2000) 1195.
- [3] T. Biegler, D.A.J. Rand, R. Woods, J. Electroanal. Chem. 29 (1971) 269.

## **Appendix B      Electrochemical Quartz Crystal Microbalance**

The EQCM is an instrument capable of detecting small mass changes on conductive surfaces. The mechanism for this capability is primarily attributed to the unique properties of piezoelectric materials; mainly the ability to induce a stress in the material by inducing a charge imbalance across the material surface. Specifically for the EQCM used in this study, AT cut piezoelectric quartz wafers are utilized with a conductive material (typically an electrocatalytic material) sputtered on both sides of the wafer. This is referred to as a resonator.

Alternative to AT cut resonators are NT, MT, GT, CT, DT, BT, and SC cut resonators. The difference between the cuts is the angle from the quartz optic axis from which the quartz wafers are cut. For example AT cut wafers are cut at  $35.25^\circ$  from the optic axis of the quartz and BT cut wafers are cut at  $49^\circ$  from the optic axis. This results in differences in the temperature stability, mechanical stability, and the operable frequency range of the resonators.

During operation, an alternating charge is applied to the resonator by the EQCM such that the material is resonating at a specific frequency. Changes in the mass of the conductive material, either via a change in chemical state or adsorption of a chemical species results in a change in the resonator frequency. This frequency change can be associated with a change in the mass of the resonator surface. In this study, the resonant frequency of the AT cut resonator was 9 MHz. 5MHz and 10 MHz resonators are also available for EQCM.

The EQCM is theoretically capable of detecting low frequency changes (0.1 Hz). The actual mass changes on the resonator surface are calculated based on the proportional

relationship between the frequency change of a resonating piezoelectric material and its change in mass. The relationship between frequency and mass change is represented by the Sauerbrey equation:

$$\Delta f_0 = -C_f \Delta m \quad (\text{B. 1})$$

where  $\Delta f_0$  is the deviation from the resonant frequency of the piezoelectric material,  $C_f$  is the Sauerbrey constant, and  $\Delta m$  is the mass change.

Typically a potentiostat is coupled with the EQCM in order to study the mass changes accompanying a potential scan. For the reader's interest, a review by Buttry and Ward describes in detail the theory and operation of the EQCM [1].

## **B.1 Electrochemical Quartz Crystal Microbalance Cell Setup**

In this study, the QCA 922 (Seiko EG&G) EQCM was operated in conjunction with cyclic voltammetry. A representative schematic of the experimental setup is shown in Figure 72.

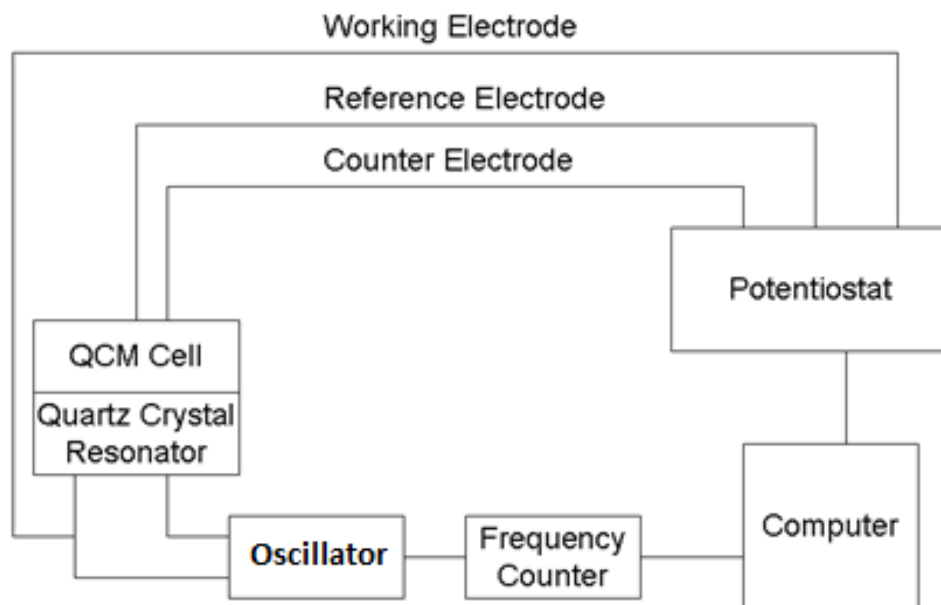


Figure 72. EQCM experimental setup.

A novel aspect of the experimental setup used in this study was the incorporation of a vertical cell design to allow the disengagement of gaseous species that could otherwise interfere with the EQCM measurements. In the case of the presence of a bubble on the surface of the resonator, the EQCM recognizes this effect as a displacement of the solution in contact with the resonator [1]. As a result, the response from the EQCM is a drop in mass. The accumulation of multiple bubbles on the surface of the resonator will result in a drop in mass beyond the lower detection limit of the instrument. In addition to the new cell design, in order to mitigate the effect of accumulated bubbles on the surface of the resonator prior to running an experiment with the EQCM, a micropipette was used to remove any bubbles that may have formed on the resonator surface. These precautions were especially important for studying  $\text{BH}_4^-$  electro-oxidation as  $\text{H}_{2(\text{g})}$  may form from  $\text{BH}_4^-$  hydrolysis. A diagram of the original cell

setup is depicted in Figure 73A, and a picture of the vertical cell setup is shown in Figure 73B.

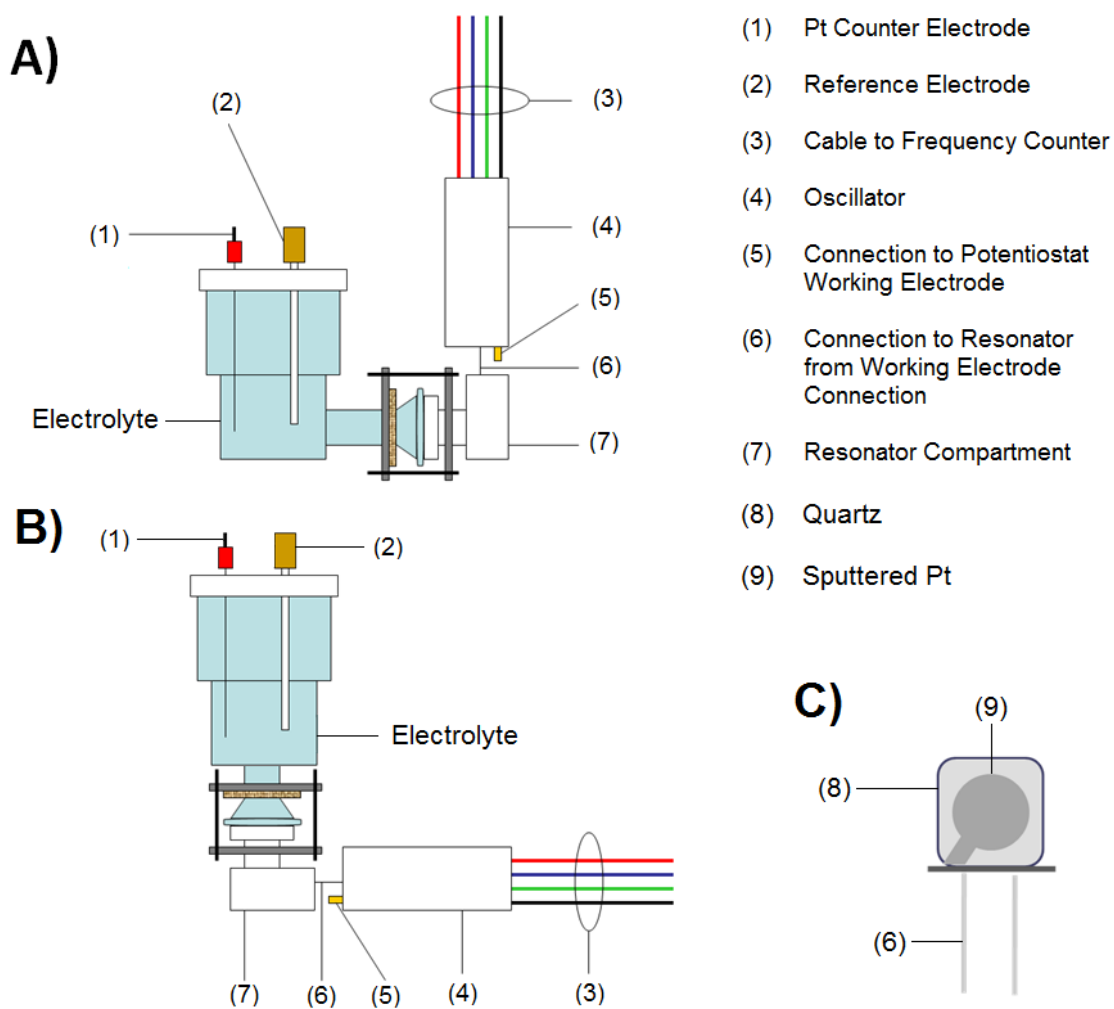


Figure 73. EQCM A) original cell design B) improved vertical cell design c) Pt resonator.

### References:

[1] D.A. Buttry, and M.D. Ward, Chem. Rev. 92 (1992) 1335.

## Appendix C Determination of the Sauerbrey Constant

Determination of the Sauerbrey constant and calibration of the EQCM was carried out by voltammetric stripping of an underpotentially deposited (UPD) Cu layer on the Pt resonator. Underpotential deposition of Cu refers to the deposition of Cu at potentials more positive than its thermodynamic equilibrium potential. This technique results in the deposition of a Cu monolayer on the Pt resonator [1--3]. Cu UPD was performed using a 2 mM CuSO<sub>4</sub> and 0.1 M H<sub>2</sub>SO<sub>4</sub> solution at 0.3 V for 20 min. The deposited Cu was anodically stripped off and the charge was measured relative to the blank cyclic voltammetry scan of Pt in 0.1 M H<sub>2</sub>SO<sub>4</sub>. Figure 74 shows both the blank cyclic voltammetry scan of Pt in 0.1 M H<sub>2</sub>SO<sub>4</sub> and the Cu stripping curve while, Figure 75 presents the QCM response generated by Cu stripping. After correcting the QCM measurement of the Cu stripping with the response from a blank scan, the frequency change was plotted versus the charge associated with the anodic Cu dissolution (Cu → Cu<sup>2+</sup> + 2e<sup>-</sup>) (Figure 76) and the Sauerbrey constant was calculated from the slope of equation (C.1) [4,5].

$$\Delta f = -10^6 C_f \frac{\eta \Delta Q MW}{nF} \quad (\text{C.1})$$

where F is the Faraday constant (96485 C mol<sup>-1</sup>), MW is the atomic weight of Cu (g mol<sup>-1</sup>), n is the number of electrons transferred (n = 2), ΔQ is the charge due to anodic Cu stripping (C cm<sup>-2</sup>) and η is the current efficiency (assumed to be 1). The factor 10<sup>6</sup>

accommodates the commonly used unit for  $C_f$  of  $\text{Hz cm}^2\mu\text{g}^{-1}$ . A sample calculation is shown below:

$$\text{Slope} = -2.8 \times 10^5 \frac{\text{Hz}}{\text{C}}$$

$$\text{Slope} = \frac{C_f MW}{nF}$$

$$C_f = \frac{-\text{Slope} * nF}{MW} = \frac{2.8 \times 10^5 (2)(96485)}{63.54} = 8.6 \times 10^8 \frac{\text{Hz}}{\text{g}}$$

or

$$C_f = 8.6 \times 10^8 \frac{\text{Hz}}{\text{g}} (0.196 \text{cm}^2) \left( \frac{1 \text{g}}{10^6 \mu\text{g}} \right) = 168.2 \frac{\text{Hz}(\text{cm}^2)}{\mu\text{g}}$$

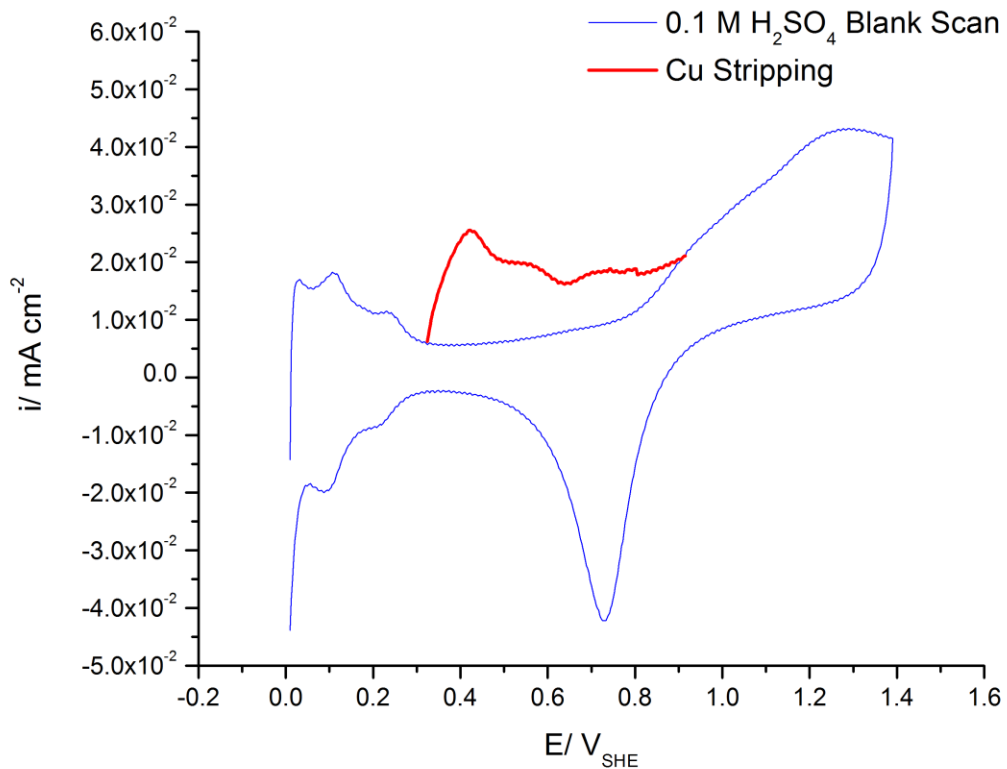


Figure 74. Cyclic voltammetry scan of Pt in 0.1 M H<sub>2</sub>SO<sub>4</sub> (20<sup>th</sup> scan) and the Cu stripping curve. T: 293 K, scan rate: 10 mV s<sup>-1</sup>. Reproduced with permission from [6], Copyright 2011, American Chemical Society.

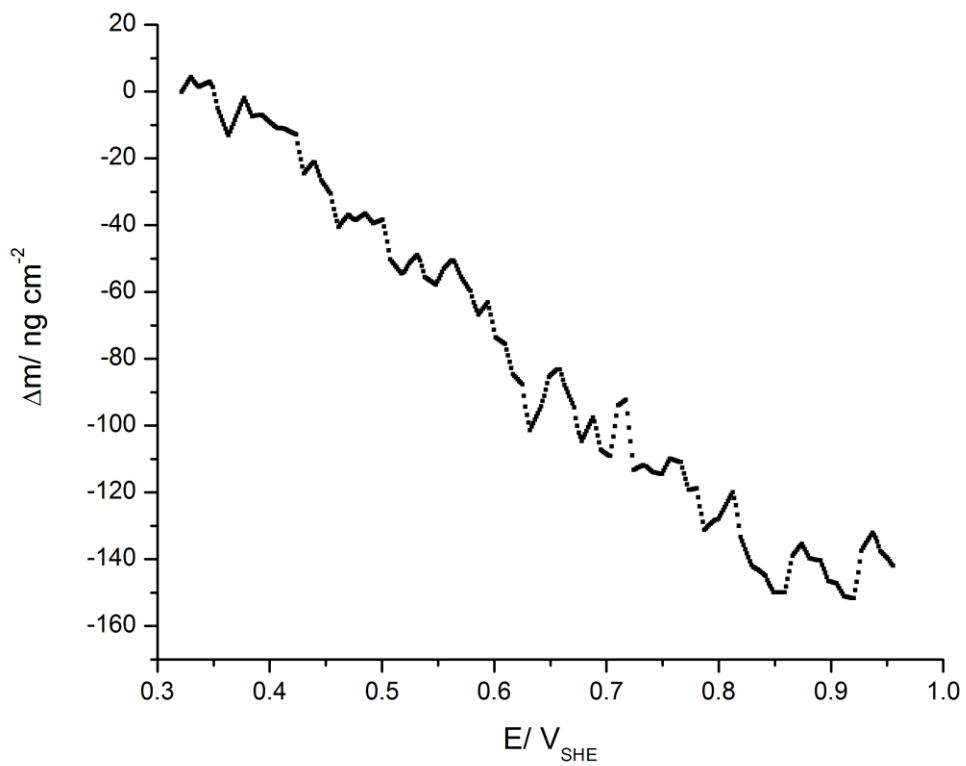


Figure 75. EQCM mass response from Cu stripping. Reproduced with permission from [6], Copyright 2011, American Chemical Society.

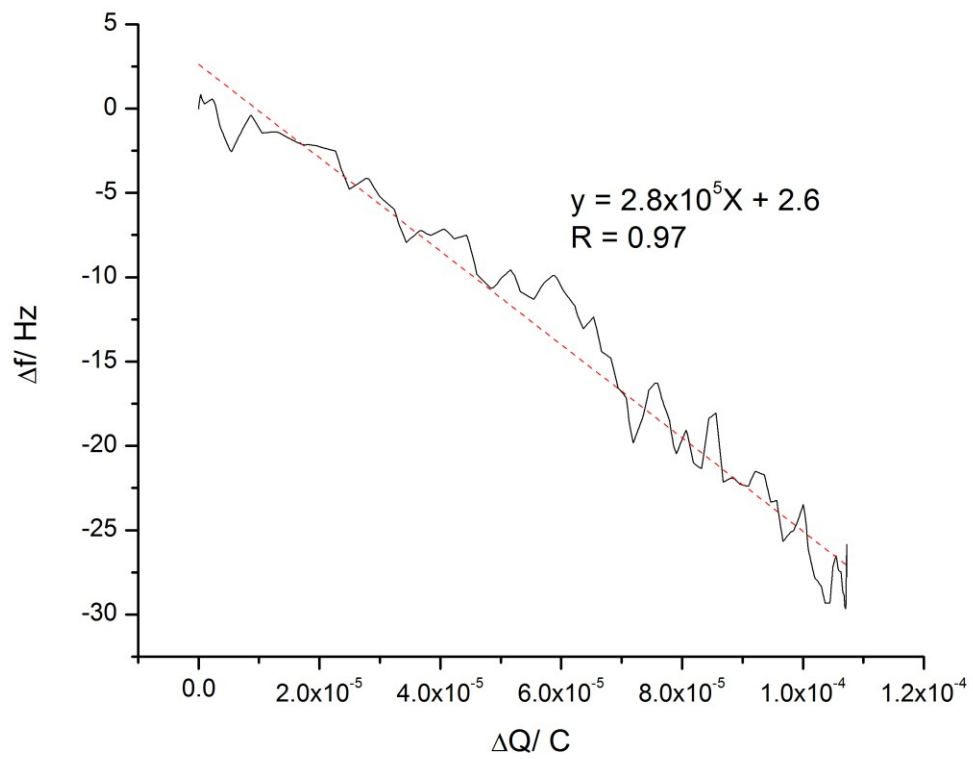


Figure 76. Change of resonator frequency versus change in Cu stripping charge.

## References:

- [1] C.L. Green, and A. Kucernak, *J. Phys. Chem. B* 106 (2002) 1036.
- [2] C.L. Green, and A. Kucernak, *J. Phys. Chem. B* 106 (2002) 11446.
- [3] E. Herrero, L.J. Buller, H.D. Abruna, *Chem. Rev.* 101 (2001) 1897.
- [4] Q. Xie, Z. Li, C. Deng, M. Liu, Y. Zhang, M. Ma, S. Xia, X. Xiao, D. Yin, and S. Yao, *J. Chem. Educ.*, 84 (2007) 681.
- [5] D.A. Buttry, and M.D. Ward, *Chem. Rev.*, 92 (1992) 1355.
- [6] V.W.S. Lam, K.C.W. Kannangara, A. Alfantazi, and EL. Gyenge, *J. Phys. Chem. C.*, 115 (2011) 2727.

## Appendix D Surface Coverage Estimation

The surface  $\text{BH}_4^-$  coverage change with respect to the start of the anodic scan on Pt in Chapter 2.0 was estimated from:

$$\Delta\theta' = \frac{\hat{\sigma}}{A} N_A \frac{\Delta m}{MW} \quad (\text{D.1})$$

where  $\Delta m$  is the mass change measured by QCM per unit electrochemical Pt area,  $MW$  is the molecular weight of the adsorbed species,  $N_A$  is Avogadro's number,  $\hat{\sigma}$  is the surface area occupied per molecule, and  $A$  is the electrochemical area.

The surface coverage change  $\Delta\theta'$  obtained from equation (D.1) is expressed as ( $\text{cm}^2_{\text{molecule}} \text{cm}^{-2}_{\text{Pt}}$ ), and is referred to as the number of monolayers (ML). The surface area occupied per molecule was approximated with the cross-sectional area of the hypothetical spherical van der Waals volume of the molecule. Obviously, this approximation does not take into account the dynamic situation on the surface, various possible configurations and inter-molecular interactions. However, it can offer an indication and starting point for the quantitative characterization of adsorbates.

$$\hat{\sigma} = \pi r^2 \quad (\text{D.2})$$

where the apparent molecular radius is expressed in terms of the van der Waals volume:

$$r = \left( \frac{3\hat{V}_{vdW}}{4\pi} \right)^{1/3} \quad (D.3)$$

The van der Waals volumes  $\hat{V}_{vdW}$  of the molecules and molecular fragments of relevance in the present work, was calculated with the equation developed by Abraham and co-workers for non-cyclic molecular structures [1]:

$$\hat{V}_{vdW} = \frac{4\pi}{3} \sum_{j=1}^N r_j^3 - 5.92(N-1). \quad (D.4)$$

In equation (E.4)  $\hat{V}_{vdW}$  is expressed in ( $\text{\AA}^3 \text{ molecule}^{-1}$ ), N is the total number of atoms in the structure and  $r_j$  is the atomic van der Waals radius [2]. Table 9 presents relevant values for  $\hat{V}_{vdW}$  and  $\hat{\sigma}$ .

Table 9. van der Waals volumes and cross-sectional areas for selected relevant molecules and molecular fragments [2,3].

Species	$\hat{V}_{vdW}$ ( $\text{\AA}^3 \text{ molecule}^{-1}$ )	$\hat{\sigma}$ ( $\text{\AA}^2 \text{ molecule}^{-1}$ )
BH <sub>4</sub>	28.2	11.2
OH	14.3	7.1
BH <sub>2</sub> OH	37.4	13.5
SC(NH <sub>2</sub> ) <sub>2</sub>	57.0	17.9
(SC(NH <sub>2</sub> ) <sub>2</sub> ) <sub>2</sub> (OH) <sub>2</sub>	142.7	33.0

## References:

- [1] Y.H. Zhao, M.H. Abraham, A.M. Zissimos, *J. Org. Chem.* 68 (2003) 7368.
- [2] M. Mantina, A.C.Chamberlin, R. Valero, C.J. Cramer, *J. Phys. Chem. A* 113 (2009) 5806.
- [3] V.W.S. Lam, D.C.W. Kannangara, A. Alfantazi, and E.L. Gyenge, *J. Phys. Chem. C* 115 (2011) 2727.

## Appendix E Standard Error Calculation

The standard error of the mean was calculated according to [1]:

$$\bar{z}' - t_{\alpha/2} \frac{s}{\sqrt{n'}} < \mu < \bar{z}' + t_{\alpha/2} \frac{s}{\sqrt{n'}} \quad (\text{E.1})$$

$$s = \sqrt{\frac{1}{n'} \sum_{i=1}^{n'} (z'_i - \mu)^2} \quad (\text{E.2})$$

where  $\bar{z}'$  is the mean of a sample of the total population of data points,  $\mu$  is the mean of the total population of data points,  $t_{\alpha/2}$  is the critical value for a t-distribution of data points equal to 1.886 [1],  $s$  (equation (E.2)) is the standard deviation,  $z'$  is the data point, and  $n'$  is the number of data points in the sample population which is equal to 3. The sample population number is taken as equal to the total population number in this case therefore  $\bar{z}'$  is assumed to be equal to  $\mu$ .

### References:

- [1] R.E. Walpole, R.H.Myers, S.L.Myers, Probability and Statistics for Engineers and Scientists, 6<sup>th</sup> ed., Prentice Hall, New Jersey, 1972.

## Appendix F Os Electrochemical Surface Area

The determination of the electrochemical surface area of Os via hydrogen underpotential adsorption has not yet been investigated in the literature. As may be recalled in Appendix B, the electrochemical surface area can be expressed as the charge associated with the deposition/ stripping of a monolayer of UPD hydrogen, divided by the hydrogen charge density of a complete monolayer for the catalyst material (equation (A.5)). In the case of polycrystalline Os, key pieces of information, particularly the hydrogen adsorption behaviour on lower Miller index single crystal Os has not yet been experimentally determined. Therefore the hydrogen charge density of complete monolayer Os coverage is not known. The hydrogen charge density in a complete monolayer can be calculated as follows [1]:

$$Q_m = ed_m \quad (F.1)$$

where  $e$  is the elementary charge equal to  $1.602 \times 10^{-19} \text{ C atom}^{-1}$ , and  $d_m$  is the density of a complete monolayer of hydrogen atoms on the lower Miller index planes of the catalyst surface in  $\text{atoms cm}^{-2}$ .

The value of  $d_m$  can be estimated. Pinto and Paniago [2], and Babenkova et al. [3] have both published data on the adsorption of hydrogen onto polycrystalline Os. Through temperature programmed desorption (TDP), Babenkova et al. determined the hydrogen monolayer density on Os to be  $2.3 \times 10^{15} \text{ atoms cm}^{-2}$  [3] at adsorption temperatures from 333 K to 723 K. Calculation of the of the hydrogen monolayer density from hydrogen adsorption experiments performed by Pinto and Paniago yielded an

average value of  $\sim 2.63 \times 10^{15}$  atoms  $\text{cm}^{-2}$  [2], which is in close agreement to the results by Babenkova et al.. As the results by Pinto and Paniago were experimentally supported by  $\text{N}_2$  BET, the value for  $d_m$  in this study was taken to be equal to  $2.63 \times 10^{15}$  atoms  $\text{cm}^{-2}$  and the value for  $Q_m$  was therefore calculated using equation (F.1) to be  $421 \mu\text{C cm}^{-2}$ .

In the ideal scenario, one would simply calculate the electrochemical surface area of Os using equation (A.5). However characterization of the electrochemical adsorption of hydrogen is complicated by the manner in which hydrogen is adsorbed onto the Os surface. Peinado and Colum [4] found that hydrogen desorption from Os during potential cycling in  $\text{H}_2\text{SO}_4$  can be very difficult due to diffusion of hydrogen into the bulk Os. These results are supported by Pinto and Paniago [2] where they found that successive experiments for hydrogen adsorption in Os powder results in decreasing hydrogen uptake. Koponen et al. [5] completed some studies on electrochemical adsorption/desorption of hydrogen on electrodeposited Os catalysts. They estimated that hydrogen coverage on Os was only 40%. In other words, during electrochemical stripping of underpotentially deposited hydrogen, only 40% of the hydrogen is desorbed from the surface. Equation (A.5) then becomes:

$$A = \frac{Q}{0.4Q_m} \quad (\text{F.2})$$

The specific surface area  $A_s$  can be calculated by dividing the electrochemical area by the total mass,  $m$  of the Os catalysts as follows:

$$A_s = \frac{A}{m} \quad (\text{F.3})$$

Figure 77 shows the cyclic voltammogram of a three-dimensional Os anode on AvCarb™ P75 with an Os loading of  $0.32 \text{ mg cm}^{-2}$  in  $0.5 \text{ M H}_2\text{SO}_4$ . The charge of the hydrogen stripping was calculated by integration of the hydrogen desorption peak in the cyclic voltammogram. The specific electrochemical surface area of a three-dimensional Os anode, from equations (F.3) and (F.4), was estimated to be  $310 \text{ cm}^2 \text{ mg}^{-1}$ .

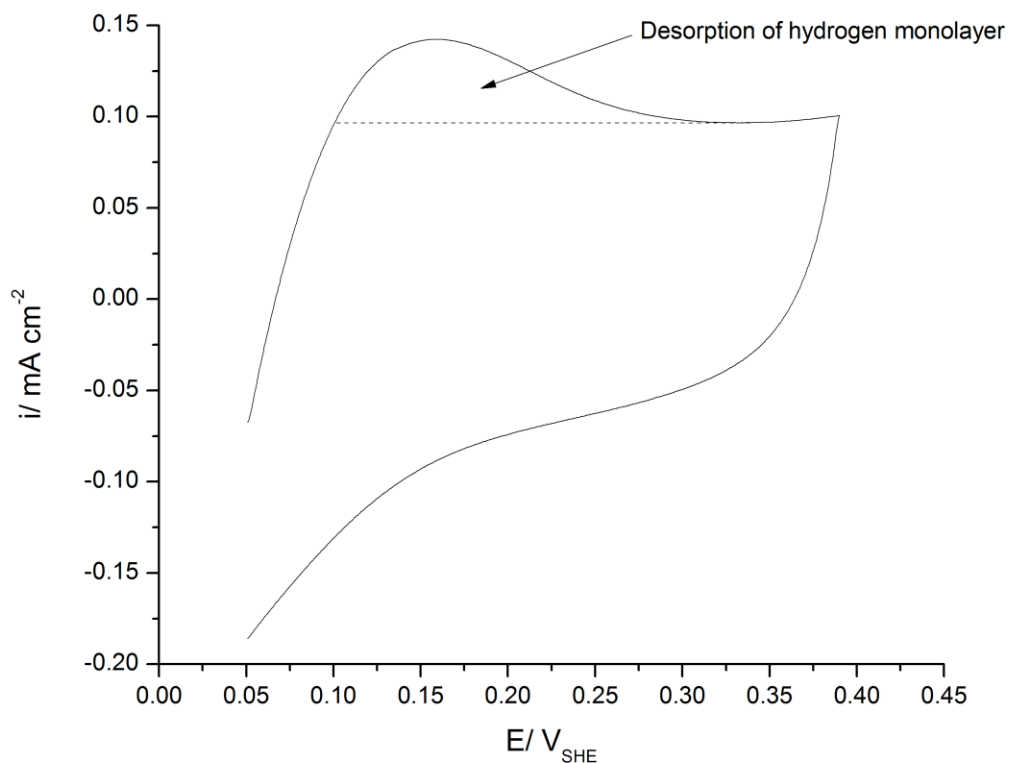


Figure 77. Three-dimensional Os electrode cyclic voltammogram in  $0.5 \text{ M H}_2\text{SO}_4$ . T: 298 K, scan rate:  $30 \text{ mV s}^{-1}$ .

## References:

- [1] J.M.D. Rodriguez, J.A.H. Melian, J.P. Pena, *J. Chem. Educ.* 77 (2000) 1195.
- [2] J.M.G. Pinto, A.R. Paniago, *Stud. Surf. Sci. Catal.*,10 (1982) 361
- [3] L.V. Babenkova, N.M. Popova, Y.G. Kulevskaya, *React. Kinet. Catal. Lett.*, 4 (1979) 325.
- [4] J. Peinado, F. Colom, *Anales de Quimica*, 74 (1978) 390.
- [5] U. Koponen, M. Bergelin, and M. Wasberg, *J. Electroanal. Chem.*, 531 (2002) 87.

## Appendix G XRD Scans on GF-S3 and AvCarb™ P75

### Blank Substrates

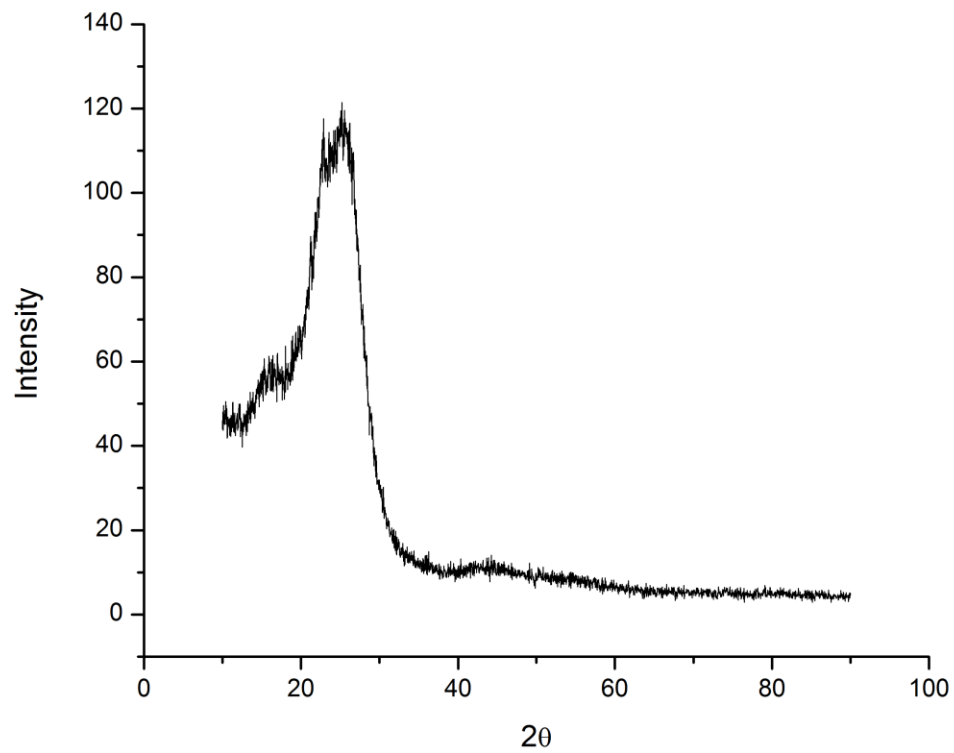


Figure 78. XRD scan of GF-S3 blank substrate.

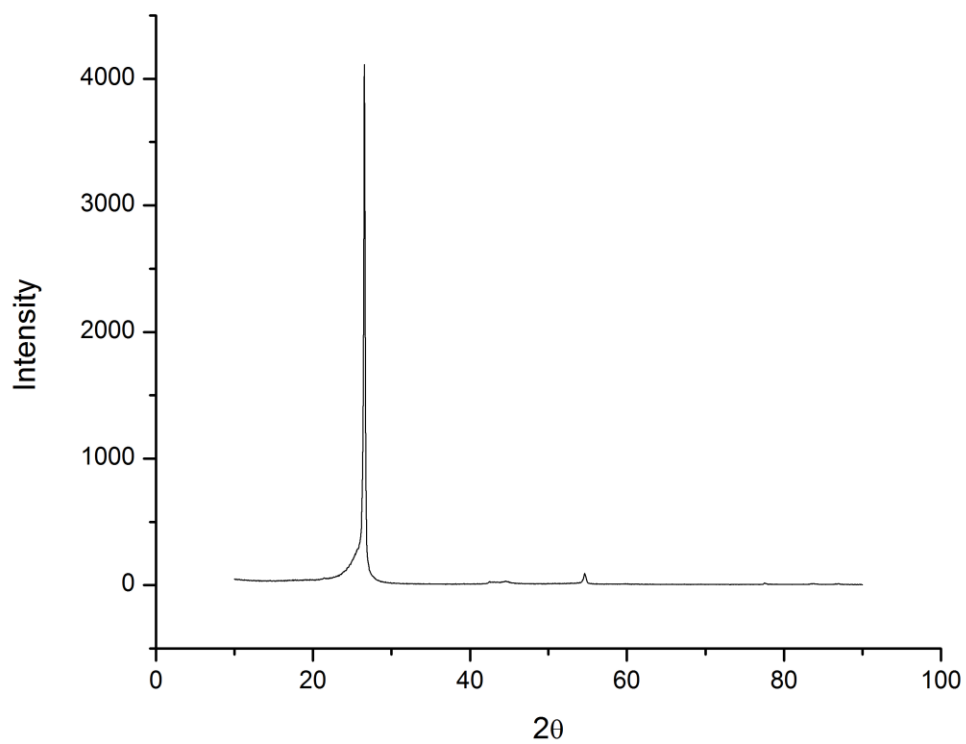


Figure 79. XRD scan of AvCarb™ P75 blank substrate.

## Appendix H Fuel Cell Setup

Description:

- Stainless steel endplates with serpentine channels
- Area of serpentine channel pattern = 645.2 mm<sup>2</sup>
- Channel depth ~ 0.9 mm
- Channel width ~ 1.5 mm
- Flowfield plates were compressed via 4 bolts torqued at 5 Nm by a digital torque wrench (Cedar)
- Electrical connection to test station was facilitated via gold plated connectors
- Stack was aligned vertically during testing as depicted in Figure 80 and Figure 81
- Fuel was supplied via an external peristaltic pump at room temperature
- All fuel cell tests were conducted using the Fideris Fuel Cell MTK test station

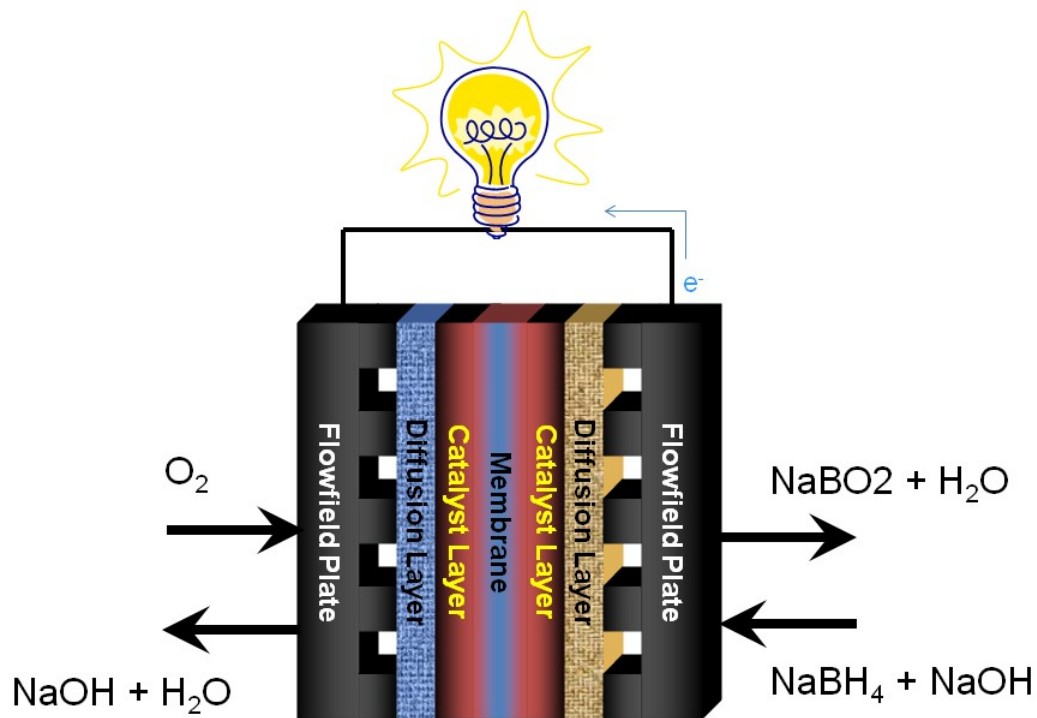


Figure 80. Schematic of DBFC cell used for single cell tests.

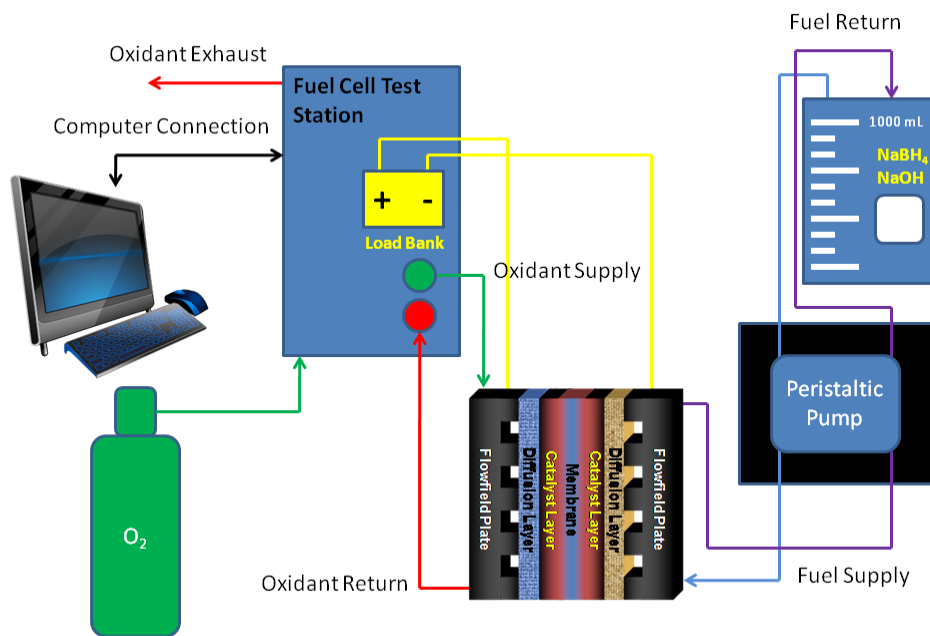


Figure 81. DBFC system testing setup

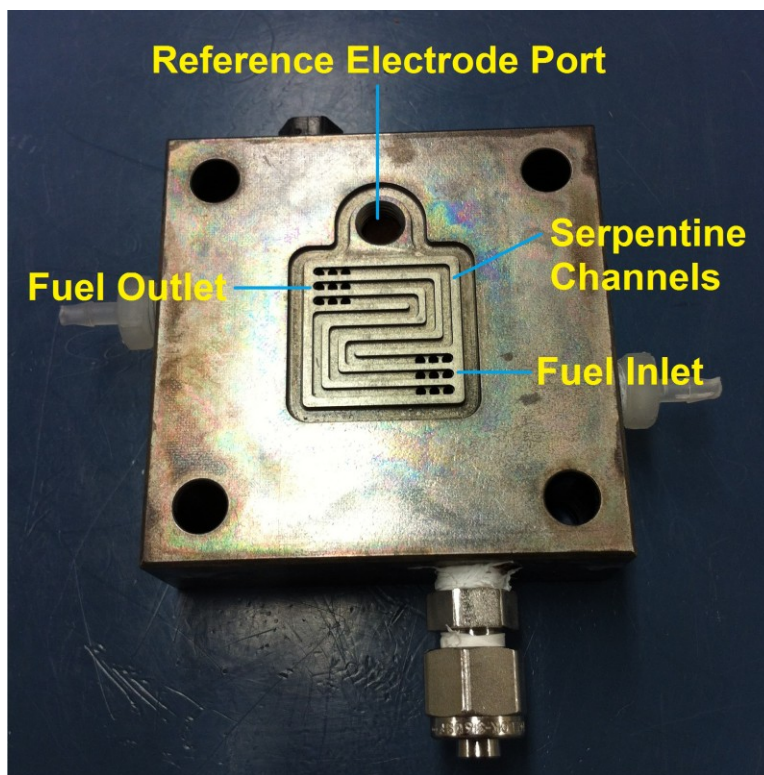


Figure 82. Stainless steel flowfield plate

## Appendix I      Effect of Diaphragms, and Anion and Cation Exchange Membranes on Direct Borohydride Fuel Cell Performance

A preliminary study was conducted on assessing the applicability of some commercial separators for the DBFC and described here. The DSM Solupor<sup>®</sup> diaphragm was obtained from DSM, but is now manufactured by Lydall Inc.. Fumapem membranes are manufactured by FuMA-Tech GmbH, and Nafion<sup>®</sup> membranes are manufactured by Dupont.

Table 10. Properties of various separators. AEM: anion exchange embrane, CEM: cation exchange membrane.

Separator	Type	Conductivity (mS cm <sup>-1</sup> )	Material	Chemical Stability**	Dry Thickness (μm)
DSM Solupor <sup>®</sup>	Diaphragm	N/ A	UHMWPE	Ok	28-35
Fumapem <sup>®</sup> FAA*	AEM	7-10*	N/ A	Poor	55-65
Fumapem <sup>®</sup> F-930	CEM	90-100	PFSA/ PTFE	Ok	30
Nafion <sup>®</sup> 117	CEM	83-100	PFSA/ PTFE	Ok	183
Nafion <sup>®</sup> 112	CEM	83-100	PFSA/ PTFE	Ok	51

\* OH<sup>-</sup> form in H<sub>2</sub>O at T = 298 K

\*\* 2 M NaOH at 333 K

## **I.1 Procedure**

### **I.1.1 Electrode Preparation**

40 wt% Pt/ Vulcan XC-72, 5 wt% Nafion<sup>®</sup> ionomer solution (Alfa Aesar), 2-propanol (Fisher Scientific), and 18 MΩ deionized water were mixed and sonicated for 2 hours. The catalyst weight and Nafion<sup>®</sup> weight were measured such that the final composition of the electroactive layer would be 70 wt% catalyst and 30 wt% dry Nafion<sup>®</sup>. The catalyst ink composition weight ratio was 2:1:60 of catalyst and wet Nafion<sup>®</sup> to 18 MΩ water to 2-propanol. After sonication, the catalyst ink was sprayed using an atomizing spray nozzle onto pretreated TGPH-60 (Toray) for the anode and TGPH-60 with 30wt% PTFE (Etek) for the cathode. The pretreatment was necessary to decrease the hydrophobicity of the TGPH-60 and consisted of boiling the TGPH-60 in 1 M nitric acid (Fisher Scientific) for 1 hour, then rinsing with copious amount of water and drying in air. The final anode and cathode loadings were 1 mg cm<sup>-2</sup> Pt each. During fuel cell testing, the electrodes were pressed to the diaphragms only by the pressure of the end plates.

### **I.1.2 Fuel Cell Tests**

Fuel cell tests were performed using a Fideris MTK test station. The stack temperature was maintained at 333 K and the cathode compartment pressure was maintained at 4.4 atm (abs) during fuel cell tests. The oxidant (O<sub>2</sub>) flow rate was 1.25 SLPM and the anolyte (0.5 M NaBH<sub>4</sub> – 2 M NaOH) flow rate was 10 mL min<sup>-1</sup>. Stainless steel end plates with a serpentine flowfield were used. Prior to the stack

assembly, the membranes and diaphragms were activated by soaking in 2M NaOH at 333 K for 1 hour.

## I.2 Discussion

Figure 83 and Table 11 shows the results from the fuel cell tests. The Fumapem<sup>®</sup> FAA anion exchange membrane was found to be unstable under the employed fuel cell operating conditions despite the high chemical resistance claimed in the product specifications (pH 1 to 14). It should be noted that during pretreatment in 2 M NaOH (pH 14) there were no signs of the membrane degradation due to chemical attack. Examination of the membrane after failure showed a complete loss in ductility of the membrane resulting in “flaking” and subsequent complete structural failure of the membrane. Failure was likely caused by the high pressure of the cathode compartment (4.4 atm (abs)), combined with pressure points from the serpentine flowfield, relatively high temperature of the fuel cell stack (333 K), chemical attack from the highly alkaline conditions (pH ~14.3), and perhaps chemical attack from the NaBH<sub>4</sub> present in the anolyte (0.5 M NaBH<sub>4</sub>). Other Fumatech anion exchange membranes that are commercially available are the Fumasep<sup>®</sup> FAP-1 and FAP-0. However, neither of the membranes are chemically stable in environments with a pH > 6. Prior to failure, an initial but unstable OCV of ~1.3 V was achieved with the Fumapem<sup>®</sup> FAA anion exchange membrane. This OCV is very high for a NaBH<sub>4</sub> – O<sub>2</sub> DBFC system, and has not been reported in the literature to the knowledge of the author. A high OCV is indicative of decreased crossover of the BH<sub>4</sub><sup>-</sup> anion to the cathode compartment. This high OCV may be explained by the properties of the Fumatech anion exchange

membrane under high alkaline conditions. The product specifications of the Fumasep<sup>®</sup> FAP-1 and FAP-0 anion exchange membranes state that a significant loss in conductivity of the membranes occur at  $\text{pH} > 6$ . It is therefore likely in the case of the Fumapem<sup>®</sup> FAA anion exchange membrane, at a  $\text{pH}$  of 14.3, a significant loss in the membrane conductivity occurred.

The Fumapem<sup>®</sup> F-930 cation exchange membrane showed the best chemical stability of all the Fumatech membranes tested. The OCV of the fuel cell stack using Fumapem<sup>®</sup> F-930 was surprisingly comparable to that of the Nafion<sup>®</sup> 117 membrane, despite the much lower dry thickness of the Fumapem<sup>®</sup> F-930, see Table 10. A much thinner membrane would normally generate greater  $\text{BH}_4^-$  crossover which is reflected in the case of the Nafion<sup>®</sup> 112 membrane where the OCV was significantly lower at 0.95 V compared to 1.04 V for the Nafion<sup>®</sup> 117 membrane. It is surmised that the performance advantage of the Fumapem<sup>®</sup> F-930 is attributed to its superior ion selectivity over the Nafion<sup>®</sup> membranes.

The power density output of the DBFC operated with the Fumapem<sup>®</sup> F-930 membrane was greater compared to Nafion<sup>®</sup> membranes. In comparison to the Nafion<sup>®</sup> 117 membrane, this advantage is clearly attributed to the higher ohmic drop associated with the thickness of the Nafion<sup>®</sup> 117 (183  $\mu\text{m}$  (Figure 83)). In the case of the Nafion<sup>®</sup> 112 membrane, where the thicknesses were comparable, the advantage of the Fumapem<sup>®</sup> F-930 over the Nafion<sup>®</sup> 112 membrane was likely due to differences in the ion selectivity of the membranes and also the marginally higher (manufacturer rated) conductivity of 0.09 – 0.1  $\text{S cm}^{-1}$  for the F-930 compared to 0.083  $\text{S cm}^{-1}$  for the Nafion<sup>®</sup> 112.

A high power density of  $60 \text{ mW cm}^{-2}$  was also achieved when employing the DSM Solupor<sup>®</sup> battery diaphragm, however the open circuit voltage of this system was the lowest among the tested diaphragms at 0.87 V. The relatively low open circuit voltage was expected, as the DSM diaphragm is among the thinnest of the tested diaphragms likely resulting in high  $\text{BH}_4^-$  crossover rates. It should be noted, that due to the high porosity of the DSM Solupor<sup>®</sup>, it was not possible to employ the gas diffusion electrodes in the configuration stated in the above procedure due to severe crossover of  $\text{O}_2$  to the anode compartment at an  $\text{O}_2$  pressure of 4.4 atm (abs). Therefore it was necessary to spray the catalyst layer directly onto the separator for both the anode and cathode active layers. In place of the unteflonated TGPH-60 backing, carbon cloth was used as a diffusion layer in the anode compartment, and ELAT<sup>®</sup> (teflonated carbon cloth) was used in the cathode compartment.

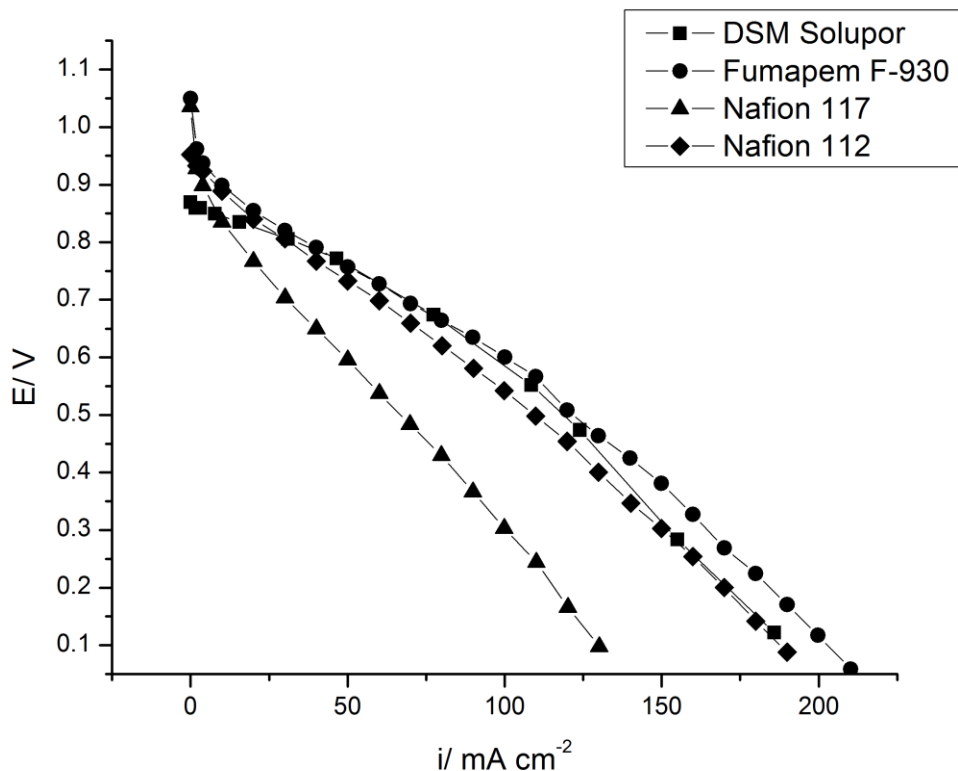


Figure 83. Polarization curves of diaphragms. T: 333 K, anode catalyst:  $1 \text{ mg cm}^{-2} \text{ Pt/ C}$ , cathode catalyst:  $1 \text{ mg cm}^{-2} \text{ Pt/ C}$ , oxidant:  $\text{O}_2$ , oxidant pressure: 4.4 atm (abs), oxidant flow rate: 1.25 SLPM, anolyte:  $0.5 \text{ M NaBH}_4 - 2 \text{ M NaOH}$ , anolyte flow rate:  $10 \text{ ml min}^{-1}$ .

Table 11. Performance comparison of separators under the conditions of Figure 83.

Separator	Open Circuit Voltage (V)	Peak Power Density ( $\text{mW cm}^{-2}$ )	Temperature (K)
DSM Solupor <sup>®</sup>	0.87	60	333
Fumapem <sup>®</sup> FAA*	1.3	N/A	333
Fumapem <sup>®</sup> F-930	1.05	62	333
Nafion <sup>®</sup> 117	1.04	33	333
Nafion <sup>®</sup> 112	0.95	55	333

## Appendix J      **Recyclability of Sodium Borate**

Due to the high cost of  $\text{BH}_4^-$  (\$55  $\text{kg}_{\text{NaBH}_4}$  [1]), it is of interest to regenerate spent  $\text{BH}_4^-$  fuel. Currently there are no known methods to regenerate the  $\text{BH}_4^-$  insitu in a DBFC, however several methods have been devised as a post treatment process including organic based reactions, and inorganic synthesis. For the reader's interest, Cloutier provides an extensive review on these processes [2]. In general, the recycling of sodium borate is difficult and costly. This is in part attributed to the multiple number of chemical reaction steps required to regenerate  $\text{NaBH}_4$ , the cost of reagents, and in part due to the high temperatures and pressures required to achieve high yields of  $\text{NaBH}_4$  in some processes.

More recent methods involve the regeneration of  $\text{NaBH}_4$  through the reaction of  $\text{NaBO}_2$  with a metal hydride. Kemmitt and Gainsford describe a method for generating  $\text{NaBH}_4$  with a high yield of 80%, through a two step process wherein  $\text{NaBO}_2$  is alkoxyated by refluxing with MeOH, then hydrogenated by reacting the alkoxyated product with  $\text{NaAlH}_4$  [3]. Kojima and Haga describe another method in which  $\text{NaBO}_2$  is reacted with  $\text{MgH}_2$  to form a high yield (97% at 823 K and 69.1 atm) of  $\text{NaBH}_4$  [4]. A low temperature method is also known where  $\text{NaBO}_2$  is ball milled with  $\text{MgH}_2$  to produce  $\text{NaBH}_4$  at room temperature with a 76% yield [5].

Electrochemical methods for  $\text{BH}_4^-$  synthesis have also been investigated [6--9]. Electrochemical regeneration could greatly simplify the production of  $\text{BH}_4^-$  at potentially low temperatures. At the moment, there are no known  $\text{BH}_4^-$  electrochemical regeneration methods that are practiced on the industrial scale.

## References:

- [1] J. Wee, *J. Power Sources* 155 (2006) 329.
- [2] C.R.C. Cloutier, *Electrochemical Recycling of Sodium Borohydride for Hydrogen Storage: Physicochemical Properties of Sodium Metaborate Solutions* (The University of British Columbia, Vancouver 2006) Thesis.
- [3] T. Kemmitt, and G.J. Gainsford, *Int. J. Hydrogen Energy*, 34 (2009) 5726.
- [4] Y. Kojima, and T. Haga, *Int. J. Hydrogen Energy*, 28 (2003) 989.
- [5] C.L. Hsueh et al., *Int. J. Hydrogen Energy*, 34 (2009) 1717.
- [6] H.B.H. Cooper, US 3734842 (USA, 1973) Patent.
- [7] C.H. Hale, and H. Sharifian, US 4931154 (USA, 1990) Patent.
- [8] S.C. Amendola, US 6497973 (USA, 2002) Patent.
- [9] E.L. Gyenge, and C.W. Oloman, *J. Appl. Electrochem.*, 28 (1998) 1147.